Frequency Containment using Voltage Source Converters in Future Power Systems

A thesis submitted to The University of Manchester for the degree of

Doctor of Philosophy

In the Faculty of Science and Engineering

2019

John Fradley

Department of Electrical and Electronic Engineering

Table of Contents

Word Count: 49, 561

Table of Figures

Table of Tables

Nomenclature

List of Acronyms

AC	Alternating Current
AVR	Automatic Voltage Regulator
BESS	Battery Energy Storage Systems
COI	Centre of Inertia
DAE	Differential Algebraic Equation
DC	Direct Current
DSR	Demand Side Response
EFR	Enhanced Frequency Response
EMF	Electro Magnetic Field
EV	Electric Vehicle
FCR	Frequency Containment Response
FFR	Fast Frequency Response
FFT	Fast Fourier Transform
FS	Frequency Stabiliser
GB	Great Britain
HVAC	Heating Ventilation Air Conditioning
HVDC	High Voltage Direct Current
IEEE	Institute of Electrical and Electronic Engineers
IGBT	Insulated Gate Bipolar Transistor
INELFE	Interconexión Eléctrica Francia-España
LCC	Line Commutated Converter
MMC	Modular Multilevel Converter
MPC	Model Predictive Control
MVDC	Medium Voltage Direct Current
NETS	New England Test System
PCC	Point of Common Coupling
PE	Power Electronic
PI	Proportional Integral
PLL	Phase Locked Loop
PMU	Phasor Measurement Unit
POD	Power Oscillation damping
PSO	Particle Swarm Optimisation

RES	Renewable Energy Sources
RMS	Route Mean Square
ROCOF	Rate of Change of Frequency
SCADA	Supervisory Control and Data Acquisition
SG	Synchronous Generator
SM	Sub Module
SMIB	Single Machine Infinite Bus
SO	System Operator
SRF	Synchronous Reference Frame
SVC	Static Var Compensator
VSC	Voltage Source Converter
VSG	Virtual Synchronous Generator
VSM	Virtual Synchronous Machine
WPP	Wind Power Plant

List of Symbols

C_{cable}	DC cable capacitance
C_{sm}	Sub module capacitance
$e_{a,b,c}$	Phase voltages of the VSC AC terminal
E	Energy
E_{cable}	DC cable electrostatic energy
E_{mmc}	MMC electrostatic energy
E_f	Excitation emf
E_{fd}	Excitation field voltage
E_s	Converter average stored energy
E_{sm}	Energy per sub module
f	Frequency
$\boldsymbol{f}$	Differential equation vector
f_a	Desired maximum output frequency
f_{coi}	Centre of inertia frequency
f_d	frequency dead band setting
f_d^{act}	Dead band activation
f_d^{deact}	Dead band deactivation
f_d^{op}	Dead band output

f_{meas}	Measured frequency
f^{n}	Noise component in the measured frequency
$f^{n\alpha}$	Noise amplitude in the measured frequency
$f^{n\beta}$	Noise component frequency of change in the measured frequency
f_{nadir}	Frequency nadir
f_n^{Area1}	Frequency nadir when operating VSC frequency response in Area1
f_n^{Area4}	Frequency nadir when operating VSC frequency response in Area4
$f_n^{non-VSC}$	Frequency nadir when operating without VSC frequency response
f_n^{VSC}	Frequency nadir when operating using VSC frequency response
f_o	Initial operating frequency
f_{pod}	Power oscillation frequency
f^{ref}	Frequency reference
f_s	Sampled frequency rate
f_{set}	Settling frequency
F	Fast Fourier transform output
$\boldsymbol{g}$	Algebraic equation vector
$\boldsymbol{h}$	Machine algebraic equation vector
H	Inertia constant
$H_{GVA.s}$	Quantity of system inertia
H_{sys}	System inertia constant
I	Current
$I_{a,b,c}$	Phase current
I_{cc}	Circulating current
I_d	d-axis current
I_d^*	d-axis current control signal
I_d^{max}	d-axis current maximum
I_d^{min}	d-axis current minimum
I_d^{ref}	Inner current reference signal pre ramp limiter
I_d^{rr}	d-axis current ramp rate limit
I_{DC}	DC side converter current
$I_{l,u}$	Lower and upper arm current
I_q	q-axis current
I_q^*	q-axis current control signal
I_{sm}	Sub module current

J	Moment of inertia
$\boldsymbol{J}$	Jacobian matrix
k	Average node degree or individual sample in FFT
K	Proportional gain
K_d	Derivative gain
K_E	Stored kinetic energy
K_{i1}	Outer loop integral gain
K_{i2}	Inner loop integral gain
K_{p1}	Outer loop proportional gain
K_{p2}	Inner loop proportional gain
$\mathrm{K_{p3}}$	Supplementary frequency controller proportional gain
K_{pf}	Frequency sensitivity coefficient
K_p^{PLL}	Phase locked loop proportional gain
K_i^{PLL}	Phase locked loop integral gain
K_t	Derivative adjustment factor
l	Length
L_{arm}	Converter arm inductance
m	Modulation index
n_{arms}	Number of converter arms
$\mathrm{n_{on}}$	Number of sub modules switched on
n_{sm}	Number of sub modules in a converter arm
N	Number of devices providing fast frequency response
P	Active power
P^*	Active power control signal
$\hat{P}$	Maximum available energy from POD
P_{AC}	AC active power
P_{actual}	Actual system power response
P_{ideal}	Ideal system power response
P_{ag}	Three phase air gap power
P_{DC}	DC system power
P_e	Electrical power
P_{gi}	Active power injection
P_l	Active power demand
P_{loss}	DC side converter losses

P_{Low}	Active power low limit
P_m	Mechanical power
P_{max}	Maximum active power injection
P_{meas}	Measured active power
P_n	Nominal power
P_o	Initial operating power
P_r	Rotor power
P^{ref}	Active power reference
P_{zip}	Active power demand from the ZIP model
PE_{ratio}	Ratio of synchronous to non-synchronous frequency response
Q	Reactive power
Q_{gi}	Reactive power injection
Q_l	Reactive power demand
Q^{ref}	Reactive power reference
r	Sub module ripple factor or Pearson correlation coefficient
R	Resistance or droop coefficient
R_{arm}	Converter arm resistance
R_{pe}	Synchronous generator droop coefficient
S	Apparent power
S_{dif}	Apparent power rating of the devices providing the difference response
S_{mmc}	Apparent power rating for an MMC
S_{total}	Total rating of all synchronous generators
T_A	Excitation operation time constant
T_e	Electrical torque
T_m	Mechanical torque
T_G	Turbine governor equivalent value
T_{max}	Frequency time period
u	Input variables
V	Voltage
V_c	Average voltage across a sub module capacitor
V_o	Initial operating voltage
$V_{a,b,c}$	AC phase voltages
V_{AC}	AC voltage
V_C	Voltage across the sub module capacitor

V_{cable}	DC cable voltage
$V_{d,q}$	d-q axis voltage
V_{DC}	DC voltage
$V_{DC\ meas}$	Measured DC voltage
V_{DC}^{min}	Minimum DC link voltage
$\mathrm{V}_{l,u}$	Converter arm voltage
V_{meas}	Measured voltage
V_{sm}	Sub module voltage
V_{sm}^{max}	Maximum sub module voltage
V_{sm}^{min}	Minimum sub module voltage
V_{sm}^{on}	Sum of voltages from the discharging sub modules
V_p	Turbine governor valve position
V^{ref}	Voltage reference
V_{AC}^{ref}	AC voltage reference
V_{DC}^{ref}	DC voltage reference
x	State variables
Y	Admittance
Y_{bus}	System admittance matrix
Z	Impedance
Z_{bus}	System impedance matrix
Z_{dd}	Self-impedance in the area of disturbance
α	Synchronous generator loading reference
$\alpha 1,2$	Combined controller contribution coefficients
δ	Rotor angle
$\varepsilon_{\Delta P}^{rms}$	Route mean square difference between ideal and actual power response
θ	Voltage angle
λ	Network topology measure
λ_{Area4}	Network topology measure for Area4 of the generic test system
σ	Crucial rate of change of frequency
φ	Primary response quantity
τ_{conv}	Converter operating time constant
τ_p	Load recovery time constant
τ_s	Supplementary frequency controller first order filter time constant
τ_{SG}	Synchronous generator operation time constant

τ_{sys}	Primary response operating time constant
ω	Rotor angular speed
ω_n	Nominal rotor speed
ω_o	Rotor speed set point
ω_r	Measured rotor speed
$\Delta\beta$	Active and reactive power mismatches
Δf	Frequency deviation
ΔP	Supplementary frequency controller output
$\Delta\hat{P}$	Maximum sinusoidal power injection
$\Delta P_{desired}$	Desired output power
$\Delta\omega$	Deviation in angular speed

Abstract

Name of University: The University of Manchester
Candidate's name: John Fradley
Degree title: Doctor of Philosophy
Thesis title: Frequency Containment using Voltage Source Converters in Future Power Systems
Date: September 2019

Maintaining the frequency stability in future power systems is a concern for system operators due to the reduction of synchronously connected kinetic energy and the subsequent loss of traditional response schemes. New renewable energy sources will be required to provide frequency response ancillary services, and a suitable candidate for facilitating this is the voltage source converter (VSC). This thesis investigates frequency stability contributing factors, VSC frequency response improvements including any resulting detrimental impacts, and the impact VSC frequency response schemes have under various operating conditions.

Traditionally, frequency stability studies have primarily focused on assessing the impact of the system inertia as the main factor dictating system frequency behaviour. This thesis expands this analysis to assess the role that additional factors including topology, power flow and inertia distributions play in frequency stability studies. This research highlights the influence the different factors have on frequency stability.

Fast frequency response requires the availability of energy that can rapidly be injected into, or absorbed from, the power system. A potential solution is to use the stored energy within a VSC system. This thesis will evaluate the impact that this stored electrostatic energy could have for ancillary services.

To improve the responsiveness of a VSC proportional frequency containment controller, the use of a discontinuous dead band implementation is presented. Proportional control is commonly proposed and this thesis exploits the fact that VSC devices can operate faster than traditional synchronous generators. To advance and provide a targeted response from the VSC, an innovative frequency controller is presented. This controller operates to provide the energy that is delayed from traditional synchronous generator primary response due to the mechanical and thermal delays. The controller provides the difference between an ideal system response, that has no mechanical or thermal delays, and the estimated actual system response. This controller provides a response that is analogous to an inertial response without using a derivative control element that can be problematic to realise in practice.

The need for fast frequency response is essential following large disturbances where the response provides a large quantity of power in a short timeframe to contain the frequency. However, the detrimental impacts of using fast frequency response schemes following a small disturbance could lead to unwanted converter behaviour. The incorporation of a large capacity of fast frequency response under small disturbance behaviour is investigated. A feedback based scheme is incorporated into the frequency controller that allows the VSC to respond un-hindered and reduces the responsiveness if any oscillatory behaviour is detected.

The deployments of four different VSC frequency control schemes are investigated under different operating situations that derive from the network factors analysis. The operation is analysed to inform the deployment and improve the frequency stability.

Overall the research in thesis has contributed to a greater understanding of frequency stability and the role that VSC devices can play in improving the frequency stability.

Declaration

No portion of the work referred to in the dissertation has been submitted in support of an application for another degree or qualification of this or any other university or other institute of learning.

Copyright Statement

The author of this thesis (including any appendices and/or schedules to this thesis) owns certain copyright or related rights in it (the "Copyright") and s/he has given The University of Manchester certain rights to use such Copyright, including for administrative purposes.

Copies of this thesis, either in full or in extracts and whether in hard or electronic copy, may be made **only** in accordance with the Copyright, Designs and Patents Act 1988 (as amended) and regulations issued under it or, where appropriate, in accordance with licensing agreements which the University has from time to time. This page must form part of any such copies made.

The ownership of certain Copyright, patents, designs, trademarks and other intellectual property (the "Intellectual Property") and any reproductions of copyright works in the thesis, for example graphs and tables ("Reproductions"), which may be described in this thesis, may not be owned by the author and may be owned by third parties. Such Intellectual Property and Reproductions cannot and must not be made available for use without the prior written permission of the owner(s) of the relevant Intellectual Property and/or Reproductions.

Further information on the conditions under which disclosure, publication and commercialisation of this thesis, the Copyright and any Intellectual Property and/or Reproductions described in it may take place is available in the University IP Policy (see http://documents.manchester.ac.uk/DocuInfo.aspx?DocID=24420), in any relevant Thesis restriction declarations deposited in the University Library, The University Library's regulations (see http://www.library.manchester.ac.uk/about/regulations/) and in The University's policy on Presentation of Theses

Acknowledgement

I would first like to express my sincere gratitude to my supervisors Dr Robin Preece and Prof Mike Barnes. Their support and guidance over the past four years has enabled me to fulfil potential that I never dreamed of achieving. It has been a privilege and an honour working with them and I will be forever indebted to them.

This would not have been possible without the financial support from the UK Engineering and Physical Sciences Research Council and Siemens. I would particularly like to thank Nigel Platt and Ervin Spahic from Siemens for their valuable insights.

I am appreciative for all of the fruitful discussions that I've had with my colleagues with special thanks to Theodor Heath and Surat Asvapoositkul for developing ideas and James Hill for his entertaining debates.

I would like to thank my family for their support and encouragement throughout my studies.

Finally and most importantly, I want to thank Rosanna for her unconditional support and patience. This would not have been possible without her encouragement and baking to keep me motivated and progressing.

1 Introduction

1.1 Background

Although carbon dioxide (CO_2) emissions from electricity generation in the UK have fallen 68% since 1990, mainly due the decommissioning of coal power stations, the sector in the UK still produced an estimated 98.3 Mt of CO_2 in 2018 [1]. CO_2 from electricity generation has been reducing, but the electrical demand is forecast to increase [2], which will require more generation to be connected to the system. In order to continue reducing greenhouse gas emissions from electricity generation and supply the increasing demand, traditional fossil fuel power plants are being replaced with renewable energy sources (RES). The production of electricity from RES in the UK was reported to be 33.3% of the overall produced electricity in 2018 [3].

The integration of more RES introduces new challenges for a system operator (SO) and creates the three way dilemma, known as the energy trilemma, made up of: *energy security*, *energy equity*, and *environmental sustainability* [4]. The RES impact on the energy security component due to them being intermittent and not possessing the same physical characteristics as a synchronous generator (SG); predominantly in the form of inertia. In order to achieve the mandated targets set out in the Paris Agreement and increase the amount of RES, the SO needs to be confident that it can maintain the energy security. A part of the energy security component is the ability to ensure a reliable energy supply, but the RES will impact on the stability of the power system which jeopardizes the energy security.

The stability of the power system can be classified into three main categories: *rotor angle stability*, *voltage stability*, and *mid/long term stability* [5]. The mid/long term stability occurs where there are severe system upsets such as the disconnection of a large SG. The severe system upsets lead to large excursions of frequency, which are currently controlled by slow responding processes over a time frame of seconds to minutes. This can be further sub classified as *frequency stability* and it is this classification of stability that is the focus of this research. Frequency stability is becoming a prominent issue because the RES do not possess the same physical or operational characteristics as the conventional synchronous generators they are displacing, making it harder to retain frequency stability.

1.2 Frequency Stability Overview

The SO uses the system frequency as a measure of the balance between generation and demand and to ensure sufficient generation is dispatched. Of concern is the need to contain the rate of change of frequency (ROCOF) and the maximum frequency drop following a disturbance to prevent rate of change relays and under frequency relays from operating. These normally operate to protect the SG and the network when the machine has become asynchronous. The network disturbance could cause a SG to disconnect from the system and potentially lead to further cascading failures as the remaining generators are required to supply the load. Although there are proposed plans to alter relay settings to cope with the change in network conditions (for example in the UK as given in [6]), the settings or the relay detection schemes may lead to SGs disconnecting during frequency excursion events.

In a traditional power system, frequency stability issues occur when there is insufficient power balancing between the mechanical power input (P_m) into a SG and the electrical power generated (P_e) by the SG, where P_e is the load demand. Mechanical input power cannot change instantly, whereas, electrical power demand can change very quickly compared to the mechanical power. When there is a change in electrical power generated or mechanical power input, the initial imbalance is covered by the inherent angular kinetic energy present in the SG rotors, known as the inertia. The inertia of the SG prevents any rapid deviations in system frequency when large changes in demand or generation occur. It determines the initial rate of change of frequency (ROCOF) and provides time for the ancillary frequency response controls to operate. The impact of the inertial response on the ROCOF can be described by determining the inertia constant (H) of a SG given by (1.1) where S is the rating of the machine, J is moment of inertia, and ω is the angular speed of the machine. This can then be applied to the well-known swing equation in (1.2) that determines the trajectory of the frequency. A low value of H describes that there is a lower value of stored energy and as this energy starts to be extracted the rotor will slow down faster causing an increased ROCOF and a greater frequency deviation.

$$H = \frac{1}{2}\frac{J\omega^2}{S} \tag{1.1}$$

$$\frac{d\omega}{dt} = \frac{\omega^2}{2HS}\,(P_m - P_e) \tag{1.2}$$

Following the natural inertial response, primary frequency control starts to operate and is achieved by regulating the mechanical input (torque input) into the turbine via the governor valve. This action adjusts the mechanical power input which reduces the difference between the mechanical and electrical power $(P_m - P_e)$ until equilibrium has been restored and the frequency excursion has been arrested, resulting in the nadir. There is a time delay between a disturbance occurring and the primary control action leading to a non-instantaneous response from the primary response. An approximate frequency response to a severe upset is depicted in Fig. 1.1. The timescales displayed in Fig. 1.1 are approximate and are dependent on the type of generation in the system and the quantity of ancillary services. There may be different frequency responses or variations that occur around the system following a disturbance [7].

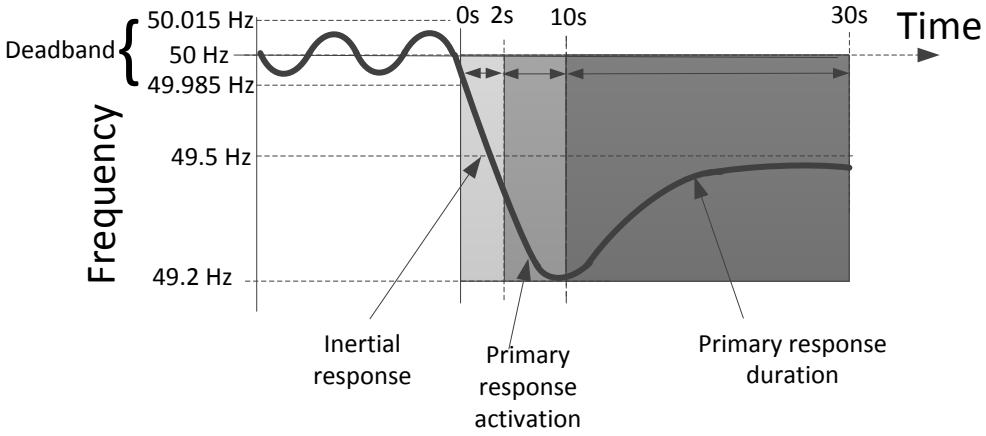

Fig. 1.1. Illustrative frequency response

The importance of power system inertia is described in [8-10] where the frequency dynamics are shown to be faster with larger resulting frequency deviations as the inertia reduces. Research provided in [11, 12] attempts to determine the minimum system inertia required to retain frequency stability by using the maximum values of ROCOF and nadir as input parameters to determine a dispatch profile. In addition, there is research aiming to estimate the actual value of system inertia as in [13, 14] that use synchrophasor measurements. The SOs have highlighted the numerous frequency stability challenges and concerns that the system faces in [15-18]. These concerns are focused around the reduced inertia contribution, reduced flexibility, and different operating characteristics caused by the incorporation of more RES. A major overall concern is to prevent blackouts from occurring such as those ones documented in [19, 20] due to insufficient frequency response. In [16], National Grid attempt to specify what they believe will be required in order to maintain the frequency stability as the

system evolves. Key requirements highlighted in [16] are the need for faster acting products that meet the system needs, greater transparency in the products that are specified for frequency response, and lowering barriers to entry into the product markets. This also includes different frequency response markets that can operate over different timeframes with various quantities of power injection.

Research in [21-24] determines how certain factors, including SG governor control, dead band size, and inertia, influence the frequency stability. The studies demonstrate how crucial the various factors are, especially when operating the system with a high penetration of RES. Further to this, the impact of the demand side inertia is evaluated and quantified in [25] and displays how it impacts the frequency at various loading levels. The damping effect from the load is shown to be an important factor and can lead to different frequency responses [26].

Even with all of the previous research, the diminishing levels of system inertia and traditional primary response that cannot operate in a suitable time frame, are making it difficult to maintain the frequency stability. Therefore, fast frequency response schemes have become a necessity and are a key component for future frequency stability highlighted in [16]. This creates the potential for fast controlled devices that can inject power into the network to contain the frequency after severe disturbances. A suitable candidate to achieve this comes from the power electronic devices that interface the RES to the network.

1.3 Power Electronic Converters

It is increasingly common for RES to be interfaced to the power system using power electronic (PE) converters. The use of PE converters allows DC transmission instead of AC in instances where there are long transmission distances or where two asynchronous networks are connected [27]. The use of PE converters also allows greater control of the RES and for the intermittent energy sources to be coupled to the network by regulating the power injection to minimise the impact to the network such as with wind power plants (WPP). One of the negative impacts of using a PE interface is that it decouples the inertia between the energy source and the network, therefore any high inertia energy sources or networks connected using PE will provide no natural inertial response. PE converters are used to connect different sized RES assets to the network: the low/medium voltage DC connections occur with low energy or decentralised assets, whereas high voltage DC (HVDC) connections occur with large energy asset connections such as interconnectors. It will be the HVDC connections that are focused

on in this research because there are already several projects in operation and numerous projects proposed that could be used to provide the frequency response services. The use of HVDC assets also enables a larger quantity of power without the need to coordinate multiple smaller rated assets.

The two types of PE converter used in HVDC applications are line commutated converters (LCC) and voltage source converters (VSC). An LCC uses high power current source switching devices such as thyristors. This enables high power transfer of up to 8 GW (with a bipolar configuration) and has been used in projects such as the Tian-Guang project in China [28]. Control of the device switching is limited in an LCC because they can only be turned on, requiring external commutation (usually by the AC network) to turn them off. This means LCC schemes typically require a strong AC network to enable correct commutation of the thyristors making them less applicable for low inertia systems. A VSC uses voltage source switching devices such as insulated gate bipolar transistors (IGBTs) that do not need a strong network to ensure correct commutation. This enables full control of the switching device, particularly the turn on and turn off states, and subsequently this enables control of the active and reactive power separately. This makes them beneficial for projects that require additional flexibility as in the INELFE back-to-back link between Spain and France [29]. An overview of the main benefits for each converter type is displayed in Table 1.1[30, 31].

Table 1.1. Benefits of LCC and VSC converters

LCC	VSC
• Higher conduction levels • Lower on state losses • Higher current overload	• Control of P, Q, independently • Power flow reversal • Black start capability • Lower harmonic filtering • Reduced converter station footprint

This ability of a VSC to control the active and reactive power independently makes it possible for them to provide multiple ancillary network services such as: power oscillation damping, frequency response, and reactive power support. There are an increasing number of VSC projects that are interfacing WPPs, asynchronous networks, PV, and battery storage. In particular, the future HVDC interconnector projects in GB have all been proposed using VSC technology. A list of the interconnector projects is provided in Appendix Section A.1. This increases the potential number of HVDC

controllable assets and creates the opportunity to enable and control the VSC-HVDC assets to provide ancillary services, with a focus on providing frequency response in this research.

1.4 Past Research on Frequency Containment

A review of proposed frequency response control methods is provided in this subsection.

1.4.1 General Overview of Non-PE Frequency Response Schemes

The non-PE frequency control methods are presented to highlight some alternative methods that are being proposed or implemented in order to retain the frequency stability. In order to maintain a certain level of directly connected inertia (kinetic energy) and provide short circuit current, the use of synchronous condensers are utilised in [32-34]. The synchronous condenser provides the system with similar characteristics to a SG and can provide similar ancillary services. Although they provide inertia, they require an energy input which impacts on the economics of this scheme and they are limited by the mechanical properties similar to a SG [35]. The mechanical limitations prevent an increase in the speed of primary response services from a synchronous condenser and this would limit the use of them in systems that require fast response.

The ability to shed load following a disturbance in order to reduce the power imbalance can be achieved using demand side response (DSR). A comprehensive review of DSR is provided in [36]. Through the use of smart devices and IoT, DSR could now be provided by domestic users and various implementations of DSR are investigated in [37]. The use of aggregation may be crucial for DSR as described in [37] to ensure there is sufficient response in the regions of tens of megawatts from each aggregator. The amount of DSR required for a disturbance is evaluated in [38] displaying the complexities of calculating the amount of DSR required. A promising solution is to control a building's heating ventilation and air conditioning (HVAC) system such as described in [39]. All DSR schemes require complex communication and operating schemes where there is currently no standard operating methodology, making it hard for the SO to predict how the system will respond following a disturbance. The ability to partake at a domestic customer level at the moment is limited but the benefits of DSR are presented in [40] with the use of it potentially reducing the system operating costs and the need to curtail WPPs. In a similar manner to DSR, load shedding schemes can be used to disconnect load when the system frequency exceeds statutory limits [41-43]. This brief evaluation of DSR has highlighted the difficulties in

ensuring that there is sufficient response available and that the correct amount of response is operated following a disturbance.

1.4.2 VSC Grid Following Control Schemes

A grid following or supporting converter injects a set quantity of active and reactive power and aligns itself to the frequency of the grid [44]. Enabling a grid following VSC to provide frequency containment requires the addition of a supplementary frequency control loop. The supplementary loop facilitates the converter to inject (or absorb) active power based on the active power set point and the state of the system frequency. An overarching review of the myriad available options is provided in [45-48] and will be expanded on in this section. The use of the terms synthetic inertia and fast frequency response are often used to describe the operation of the frequency control operation and these terms are discussed and addressed in [49], however, there is no set standard definition for them between SOs. Within this thesis the term fast frequency response (FFR) will refer to frequency response that can be delivered faster than traditional primary response schemes.

The simplest option to enable a VSC to provide frequency response is to implement a proportional controller, known as droop. This type of control has been extensively investigated or used in [50-70]. The proportional controller is implemented in the same way as the primary response control structure of a SG, and acts on the frequency deviation (Δf) that is determined using the difference between the measured and the reference frequency. This type of control provides a response that is similar to a SG but is not inhibited by mechanical and thermal process delays that limit the speed of operation in a SG. Comparison between DC voltage-frequency and active power-frequency droop is provided in [51] and displays that both methods improve frequency response. However the use of active power-frequency droop is shown to be superior compared to altering the DC voltage to initiate the power exchange. The ability to overload the VSC when providing droop based frequency support is investigated in [63] and concludes that the converter can be overloaded by up to 27.5% above its nominal rating. The overload period would depend on the percentage that the converter is overloaded and is stated at being in the region of 5 s when setting the temperature margin at 5 °C, making it feasible and beneficial for frequency response. There may be additional concerns about transferring disturbances to attached networks through an interconnector when providing frequency response [55]. Due to the coupling of networks through HVDC interconnectors, the use of frequency control schemes that

extract energy from the attached network will cause a power deficit in the attached network. The deficit is dependent on the quantity and speed of the energy extraction and further prevention of disturbance propagation is required in the future. Proportional control schemes provide limited benefit to the initial ROCOF because they rely on the absolute frequency deviation.

To address the issue of high ROCOF due to inertia reduction, there is also a focus on being able to provide a large initial quantity of energy unlike a proportional control scheme. This type of control is required to act on the rate of change of the frequency (df/dt) or the rate of change of the frequency deviation $(d\Delta f/dt)$, rather than on the absolute frequency deviation (Δf). This control is implemented using derivative control schemes and is often referred to as inertial response or synthetic inertia. This type of frequency control has been investigated in [46, 54, 60, 71-76]. An inertial response scheme may use a gain value that mimics the inertia constant of a SG to provide a similar response profile. Two possible operating approaches for this type of scheme are *continuous* and *one shot* [46]. The continuous method continually calculates the rate of change of the frequency for use in the response and is highly adaptive to the changing network frequency, but requires more complex filtering. Conversely, one shot control response is based on the initial ROCOF calculation and is simpler to implement but does not continually adapt as the ROCOF changes. These type of schemes depend on the use of derivative action which adds complexity to the control scheme, making them harder to implement due to the calculation of the derivative and making them more susceptible to noise [77].

The effects of different phase locked loop (PLL) bandwidths used for frequency measurement in a derivative scheme is evaluated in [76], showing that low bandwidth values (ω_n) result in unsatisfactory oscillatory behaviour. To reduce the complexity of the derivative calculation, the derivative action may be added as a lead-lag filter [60]. Implementing the derivative or inertial response as a lead-lag filter not only reduces the complications of derivative calculation, it also provides greater control over the damping provided, and the rise and settling time of the frequency. Parameter tuning is also highlighted as a concern in [78] where an objective to minimize cost of the energy used for the frequency response is added.

The use of inertial support requires the utilisation of energy in short time frames which is difficult when using WPPs, as the turbines pitch or set points have to be adjusted, which delays the speed of response. To overcome this when using VSC technology, research presented in [79-83] proposes the use of the intrinsic stored energy

within the converter or the addition of integrated energy storage in the converter to provide the inertial frequency containment service. Using the intrinsic energy stored within the converter's sub modules (SM) and DC link cable is shown to enable a faster frequency response. However, the studies do not state the quantity of intrinsic energy available or apply it over the specific frequency response requirements and timeframes set by the SO. Although the converter does possess electrostatic stored energy, the use of it needs to satisfy the SO requirements without compromising the converter operation.

The ability to control and operate the converter with energy storage integrated into its structure (such as added into the structure of the power electronic converter) is provided in [84]. The ability to add additional storage whilst maintaining the safe operability of the converter would allow the owner and operator to provide a more diverse range of ancillary services, one being inertial support. Without the use of the additional storage, it has been proposed that the electrostatic capacitive energy could be extracted to provide the energy for the inertial response [81]. To achieve this, and depending on how the converter stations are setup, the DC voltage set point would need to be adjusted [85].

A combination of droop and derivative frequency control schemes is provided in [81, 86, 87]. Utilising both droop and derivative components allows an initial fast response from the derivative control that uses the limited intrinsic stored energy, allowing time for the proportional control to operate [87]. The use of a combined scheme is shown to reduce the nadir over a proportional control scheme on its own. A comparison between droop and virtual inertia schemes is undertaken in [44, 77] concluding that the synthetic inertia control has performance limitations due to the derivative behaviour. The use of proportional and derivative control has been implemented to simply inject power based on the system frequency. However, the use of the VSC frequency control scheme is not limited to simply using proportional or derivative schemes. Different styles of response could be achieved such as providing a large initial quantity of power that decays as the primary response from SGs operates. This could be valuable because the SG primary response is delayed by mechanical processes which restrict the initial quantity of energy injected.

With the increase in VSC interfaced energy sources and the construction of markets for capacity and enhanced frequency response, there is now an opportunity for the WPP asset owners to provide the ancillary services. Enabling a VSC grid connected WPP to provide frequency containment has been investigated in numerous research articles with

a selection of the research provided in [88-93]. In [90], they aim to provide an inertial response by releasing the energy in the turbines and this is achieved by increasing the power reference signal. To overcome the communication delays between main grid frequency detection and wind power plant control, research presented in [91] uses a communication-less scheme where the DC link transfers the system imbalance information. In this control operation, following the disturbance and the activation of the response scheme, the DC link voltage is perturbed from its steady state operating range. These perturbations are measured by the sending end converter and it responds to adjust the DC voltage by extracting energy from its attached energy source. The use of gain scheduling [93] is utilised to adjust the response characteristics to improve a WPP response as its operational characteristics change. Several of these schemes have gone to market including the WindInertia controller from GE [94].

Battery energy storage systems (BESS) used for frequency response are investigated in [95-98] with several proposals to operate them as virtual inertia within the system. BESS have reduced control complexity compared to a WPP, as the energy is already available and does not have to be extracted from the turbine and transferred. Another benefit of battery storage is that it can be located within the network and at locations that experience severe frequency stability issues. The energy can be injected in shorter time scales and is only inhibited by the discharge limitations of the device [99]. The use of a super capacitor storage unit designed by Siemens (SVC +FS) is controlled to provide frequency response using step action in [100-102]. The control operates in a step control mode where the unit provides maximum power if the frequency deviation or detected rate of change of frequency exceeds stated limits. This type of response ties in with requirements from SOs such as Eirgrid where they require the response from PE in steps dependant on the frequency excursion [103]. In addition to bulk storage units, electric vehicles (EV) could be used to provide frequency response by disconnection if they are charging or by injecting power if they have sufficient charge as detailed in [104, 105]. The influence of the network location of distributed energy resources evaluated in [98] concludes that the system inertia needs to be significantly reduced for placement to become a concern.

The ability to co-ordinate a response from distributed energy sources that are interfaced using VSC technology or from a multi terminal DC grid will become crucial in future low inertia power systems, and several schemes are presented in [106-108]. In [107] islanded microgrid inverter control is surveyed with detection of an islanded system noted as being important to schedule the operation of inverters. In [108] a multi-

agent microgrid control system, that adjusts the droop characteristics of each controller depending on the availability and state of charge of the other connected sources, is presented. Multiple agents may not communicate with VSCs in the time frames required to enable fast frequency response, but they could be used to provide more optimal coordinated control between VSCs over longer timescales, perhaps through appropriate gain scheduling such as [93]. More complex centralised control strategies in the form of model predictive control (MPC) and particle swarm optimisation (PSO) are presented in [109] and [110]. These methods aim to determine the power injections required by each converter and also attempt to determine the optimal parameters for each converter. However, the practical applicability of such methods is severely limited by the processing time required for optimal decisions to be reached and the timescales in which this occurs in.

To reduce the impacts of diminishing levels of inertia on frequency stability, research provided in [111-113] presents methods to determine the optimal location of virtual inertia services. Conclusions drawn state that the locations of least inertia benefit the most from virtual inertia services and that the disturbance location plays a significant role in the determination.

All of the methods presented in the literature improve the frequency stability under large disturbances. A number of the schemes are designed to provide a fast response that will not only operate during severe disturbances, but it is expected that they will also operate when smaller disturbances occur. No studies presented in this literature evaluated the frequency stability under small disturbances when the network has a large quantity of fast response VSC units connected.

1.4.3 Grid Forming VSC Control Schemes

A grid forming converter sets the system frequency and voltage based on reference set points. An overview of grid forming converters known as virtual synchronous generators (VSG) or virtual synchronous machines (VSM) is provided in [114, 115]. A VSM uses voltage, power, and frequency measurements to generate its frequency, phase angle, and voltage magnitude. The control structure of a VSM is designed around the SG machine equations, notably the swing equation, and this allows them to emulate the effects of rotational inertia or provide inertial support [116-119]. Additional primary response can also be incorporated into the control architecture through a representation of a turbine governor model. The use of a VSM allows the existing generator dynamics to be simplified and implemented into the converter's control structure, reducing the

need for additional frequency control schemes. On-going research in the area of grid forming converters is addressing the issue of AC current limiting such as in [120], and this will be crucial for the operation when multiple VSMs are connected to a system. At the moment, the GB power system does not operate with any grid forming converters but there is significant interest in this type of technology. VSM converter implementations provide a possible solution (or part of the solution) for maintaining the frequency stability in the future. However, there are still several implementation issues that require resolving before they can be successfully deployed. In addition, the VSM schemes are designed to mimic traditional SG operation and this may limit or constrain the operation of the converter. As the power system evolves, there may different requirements imposed on the power electronics that go beyond mimicking SG operation.

1.4.4 VSC Frequency Control Summary

All of the reviewed VSC control options were shown to improve the frequency stability. From the literature, it is apparent that local droop-based strategies have proved most popular in this research area. The complexities highlighted with derivative control make it difficult to implement in a real world environment where the measured variables contain noise and measurement error components. It was highlighted that converters can be operated in shorter timeframes making them desirable for frequency response.

From the literature review several areas have been identified which need further research, and these can be summarised as follows:

- There exists the need for further research to investigate how frequency stability will be affected in future power systems. This knowledge can be used to inform the VSC frequency response requirements in order to provide enhanced frequency containment schemes.
- Further evaluation is required to determine if it is possible to use the intrinsic energy from a VSC for ancillary network services. The quantity of feasible extractable energy may limit the type of ancillary service it can be used for. A study is required that evaluates the impact of the services from an energy injection viewpoint.
- No studies investigate how the fast frequency response schemes would operate under low inertia conditions combined with a small network disturbance. Past research has focused on providing fast frequency response

when the system is subject to a large disturbance. Research is required to determine if the speed and quantity of fast frequency response schemes under small disturbance scenarios could lead to unwanted system behaviour and how this could be mitigated.

- No frequency response schemes presented were specifically designed to operate in-line with existing SG primary response schemes. The VSC could be operated to inject a large initial quantity of power that decays as the primary response increases. This would enable the power that is delayed by the measurement and mechanical processes in the SG primary control loop to be provided by the VSC. A method that evaluates the limitations of existing primary response and acts to reduce the limitations would be beneficial for the SO, so that they could be confident about the quantity of response they have by a given frequency deviation.
- As the system characteristics and network operation changes, different forms or implementation of VSC frequency control may be more suitable. Therefore a comprehensive evaluation of VSC frequency control implementation for varying network operating scenarios is required.

1.5 Research Objectives

This research aims to address several of the issues and gaps identified within the existing literature. The primary aim of this thesis is to evaluate and present methods that can improve frequency stability through the use of power electronic converters. In order to assess and further improve the frequency stability of future power systems, the following objectives have been identified:

1) Develop a generic test system model that can be used to evaluate frequency stability and allow for discrete and quantifiable network alterations.
2) Evaluate how network factors and system operating condition impact frequency stability beyond the well-established impact of inertia.
3) Determine the quantity of intrinsic energy within a VSC-HVDC system and assess whether it is viable for ancillary services.
4) Develop frequency control methods that improve the responsiveness of the VSC proportional control schemes.
5) Investigate detrimental system impacts created by incorporating fast frequency response schemes.
6) Develop a frequency control method that operates based on the delays and limitations of traditional primary response schemes.
7) Thoroughly investigate the impact of fast frequency response implementations under various network scenarios in order to provide operation guidance.

1.6 Main Contributions of the Thesis

The main contributions of the thesis can be summarised as:

- Development of a generic four-area test system that can be used to evaluate frequency stability. A unique measure for the topology has been developed within this work that takes into consideration the number of connections per node and the electrical distance between nodes. The new measure enables any network topology to be quantified numerically and allows comparison between different types of topology. This contribution completes objective 1.
- An extensive evaluation of network factors and how they influence the frequency stability has been performed. The evaluation determines how a change in network topology, power flow, inertia distribution, and droop gain distribution impact the ROCOF and the frequency nadir around the system. The influence of power flow and the mechanisms that cause power flow to influence

frequency stability are presented. The contribution of this component completes objective 2.

- The structure of a modular multilevel converter (MMC) is reviewed and the intrinsic energy stored within the sub modules is calculated. The calculated intrinsic energy is applied to power oscillation and frequency containment scenarios to determine the impact and the viability of its use for these services. This contribution completes objective 3.
- Development of an enhanced droop control scheme that enables it to respond faster by altering the dead band implementation. The adaptation of the dead band from a continuous to a discontinuous one is implemented to allow it to provide greater quantities of energy without introducing hunting behaviour. Objective 4 is completed by this contribution.
- Hunting or cyclic behaviour around the dead band when large quantities of fast frequency response and a small disturbance occur simultaneously is highlighted. To reduce the impact of the cycle limiting behaviour an adaptive control scheme is presented. The adaptive controller detects oscillations in the VSC frequency control loop output and reduces the influence of the FFR loop using an adaptive algorithm. This contribution completes objective 5.
- Development of a frequency response scheme that co-ordinates a frequency response with existing SG primary response schemes. The VSC frequency response is designed to provide the energy that is delayed from the SG response due to its physical and thermal limitations. The scheme provides an inertia analogous response that decays as the primary response governors operate. Objective 6 is achieved with this contribution.
- A comprehensive evaluation to determine how different implementations of VSC frequency response impact the frequency stability. The VSC frequency response is evaluated under various network scenarios and at different locations in the system. This will produce operating recommendations that can be used effectively deploy the VSC frequency response services. This work completes objective 7.

1.7 Summary of Publications

The following publications have arisen from this research. Details for each publication are provided in the following subsections

1.7.1 Conference papers

[C1] J. Fradley, R. Preece, M. Barnes, "VSC-HVDC for Frequency Support (a review)" *13th IET Conference on AC and DC Power (ACDC)*, Manchester, UK, 14-16 February 2017.

[C2] J. Fradley, R. Preece, M. Barnes, "Fast Frequency Response From MMC-HVDC with Varying Dead Band Implementation" *10th IFAC Symposium on Control of Power and Energy Systems (CPES)*, Tokyo, Japan, 4- 6 September 2018.

[C3] J. Fradley, R. Preece, M. Barnes, "Adaptive Fast Frequency Response for Power Electronic Connected Energy Sources " *13th IEEE Powertech*, Milano, Italy, 23 - 27 June 2019.

[C4] S. Asvapoositkul, J. Fradley, R. Preece, "Incorporation of Active Power Ancillary Services VSC-HVDC Connected Energy Sources" *21st Power Systems Computation Conference*, Porto, Portugal, 29 June - 3 July 2019. (Will be submitted)

1.7.2 Journal Papers

[J1] J. Fradley, R. Preece, M. Barnes, "Assessment of the Impact of MMC-HVDC Intrinsic Energy on Power System Stability" *IET Journal of Engineering*, vol. 2019 pp 4012-4016, 2019.

[J2] J. Fradley, R. Preece, M. Barnes, "The Influence of Network Factors on Frequency Stability" submitted to *IEEE Transactions on Power Systems*, Accepted for publication on the 30th November 2019.

1.8 Thesis Overview

This thesis comprises of eight chapters in total. The chapters that follow the introduction can be summarised as:

Chapter 2 – Network Modelling and Associated Considerations

The test systems used within this research are presented in this chapter. The development of the generic four area test system is presented along with the component models. An evaluation of the importance of specifying certain generator and load models is highlighted to describe how they can influence the frequency stability analysis.

Chapter 3 – Factors Affecting Frequency Stability Within Networks

The influence that specific network factors have on the frequency drop and the ROCOF are investigated in this chapter. The network factors that include network topology, power flow, inertia reduction, and droop gain increase are presented. The analysis is performed using the generic four-area test system and a unique topology measure is developed to quantify the topology changes. In addition, the mechanism explaining how the power flow influences the frequency stability is introduced.

Chapter 4 – MMC-HVDC Technology and Its Intrinsically Stored Energy

In this chapter the VSC MMC physical structure and control architecture are described and the reduced mathematical models applicable to this research are presented. This chapter will introduce how the supplementary frequency control loop is incorporated into the main cascaded control structure for the VSC. Using the mathematical equations of an MMC, the value of intrinsic energy inherent in the converter sub module design is calculated. The subsequent value of intrinsic energy is applied to power oscillation damping and frequency response scenarios to determine its usefulness for these ancillary services.

Chapter 5 – Fast Frequency Response Using MMC-HVDC Technology

Development of a VSC droop control scheme that uses a discontinuous dead band and enables the converter to respond faster is presented and evaluated in this chapter. The detrimental system impacts caused due to fast frequency response are also investigated and a mitigation strategy is presented that uses an adaptive control scheme.

Chapter 6 – Innovative Frequency Containment Control

This chapter evaluates the quantification of frequency response and highlights the difference between the expected and the actual values. An innovative VSC frequency controller is presented that is designed to reduce the difference between the expected

and the actual quantity of primary response that is created by the delays in traditional SG primary response.

Chapter 7 – Evaluation of VSC-HVDC Frequency Response Scheme Deployment

Building on the work presented in the aforementioned chapters, this chapter evaluates the impact that different VSC frequency control schemes have on a specific frequency metric under various network scenarios and at different network locations. The analysis is used to provide operating recommendations for the deployment of VSC frequency control.

Chapter 8 – Conclusions and Future Work

This chapter brings together and discusses the main conclusions from the research that has been presented. Suggestions for future development and improvement of the research are presented in this chapter.

2 Network Modelling and Associated Considerations

This chapter will define the AC models that are used and will present the test systems that are employed in this research to perform the time domain analysis. Frequency metrics and system quantities used throughout this thesis will also be provided in this chapter. All modelling is undertaken in Powerfactory DIgSILENT 2017 with the additional use of MATLAB 2016a and Python 3.6. The VSC models and their associated control will be presented in chapter 4.

2.1 Synchronous Generator and Load Modelling

When undertaking frequency stability studies, the models that are used to represent the various network components and their control can positively or negatively impact the evaluated frequency stability. The use of certain models could lead to the frequency stability appearing less severe, yielding incorrect or insufficient mitigation strategies. Two important models for frequency stability studies are the synchronous generator (SG) and load because they dictate power injection and consumption, which vary post disturbance depending on model type. SG and load models will be presented and evaluated to justify the models selected. In this research models that could lead to less desirable frequency stability conditions will be used to create worst case scenarios and consequently lead to more robust analysis.

2.1.1 Synchronous Generator and Control

The synchronous generator model and its associated control are presented in this sub section. A comparison between two SG models is performed to view how the models impact the reported machine speed and the frequency stability, following disturbances.

2.1.1.1 Synchronous Generator Model

In power system stability studies, SGs are a vital system component as they provide the largest contribution to the system dynamics in current power systems. Because of this, care should be taken when determining the models and the parameters used. The basic components of a SG are the prime mover (turbine), and the electrical generator which consists of the rotor with a field winding, and the stator with an armature winding. Much work has been done in the area of understanding and describing the operation of the SG for example in [10, 121, 122]. A description of SG operation is provided here in order to visualise the forces that govern the dynamic behaviour, which are relevant in frequency stability studies.

In principle, thermal energy is provided to the prime mover which is a turbine. The turbine is rotated and creates a mechanical torque T_m which is determined by the rotor speed (ω) and mechanical input power (P_m). The mechanical torque can be given by (2.1) that describes the relationship between the mechanical power, mechanical torque, and the rotor speed. The electrical generator rotor, which is connected to the turbine, has a field winding incorporated into it that is used to generate a magnetic field. When the turbine is rotated it induces a current into the stator winding. Induced current into the stator winding can be viewed as forces acting on the stator conductors and this sets up an opposing electrical force.

The electromagnetic torque developed between the rotor and stator can be derived from the magnetomotive forces (mmfs) of the rotor and stator. The electromagnetic torque can be calculated based on the power of the air gap (P_{ag}) and is dependent on the attractive forces between the stator and rotor mmfs. The air gap power can be derived from the electrical form as given by (2.2) where I is the current, E_f is the excitation emf, and β is the angle between the two components. From the electrical form of P_{ag}, this results in equivalence between electrical power (P_e) and P_{ag} [10]. Electrical torque (T_e) can then be given by (2.3).

$$T_m = \frac{P_m}{\omega} \tag{2.1}$$

$$P_{ag} = 3E_f I \cos\beta \tag{2.2}$$

$$T_e = \frac{P_e}{\omega} \tag{2.3}$$

During steady state operation where the electrical power requirements equal the mechanical power input, the mechanical and electrical torques are equal and opposing each other. In this condition, P_{ag} is equal to the mechanical power input which is provided by the prime mover. To maintain a non-changing rotor speed, the mechanical torque produced must be equal to the opposing electrical torque. This condition is depicted in Fig. 2.1(a).

If the electrical energy demand (P_e) from the network on the generator changes, the electrical torque (T_e) will change in accordance. The extra energy delivered to or absorbed from the network comes from the generator rotor following the disturbance and can be given by (2.4) where P_r is the power injected or absorbed from the rotor.

Mechanical input power cannot change as fast as electrical power demand and is assumed constant for a period following a disturbance.

$$P_e = P_m + P_r \tag{2.4}$$

If the electrical demand from the SG increases, then using (2.1) and (2.3), it is possible to determine the torques at the instance of the disturbance. The change in mechanical and electrical torque is visually displayed in Fig. 2.1(b). At this instance, the rotor speed has not changed but the imbalance in torques will cause the rotor to begin to decelerate and start to change the angular velocity (ω). As the rotor decelerates and the velocity changes, T_e and T_m will increase while the mechanical and electrical powers remain constant. This is displayed in Fig. 2.1(c). The increase in T_e and T_m is not uniform and T_e will start to diverge and become larger at a faster rate than T_m . This will lead to an increase in the torque imbalance on the rotor, resulting in faster (non-linear) rotor deceleration. The rate of rotor deceleration is determined by the inertia constant of the machine and can be examined further by using the swing equation.

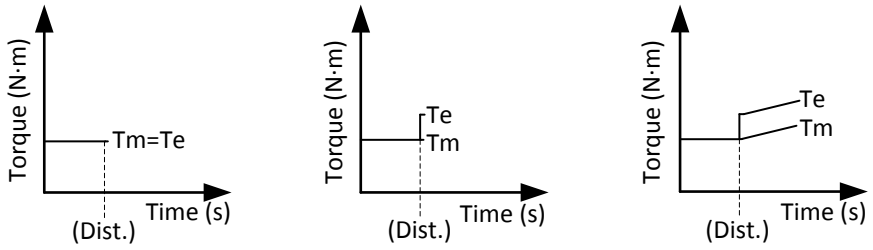

(a) (b) (c)

Fig. 2.1. Mechanical and electrical torque visualisation. (a) pre-disturbance, (b) initiation of disturbance, (c) post fault evolution

There are various SG models that can be used during simulation studies and these incorporate different levels of detail with respect to the machine dynamics. The sixth order model and the second order model are presented in this subsection and compared. The first order differential equations for each model are provided in Appendix Section B.2.

The second order model (classical model) is a simplified model that represents a constant voltage behind a transient reactance and assumes a constant flux. This reduces the level of machine dynamics compared to the sixth order model that incorporates the effects of the damper windings and leakage reactance. The two versions of SG model are compared using a single machine infinite bus setup shown in Fig. 2.2, where the

generator is connected to bus 1 and the infinite bus is connected to bus 2. Both scenarios (i.e. different SG models) are subjected to the same disturbance: a 10% load increase at the infinite bus. The SG models do not incorporate any turbine governor control or voltage control.

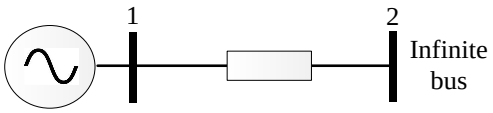

Fig. 2.2. Single machine infinite bus test system

In this simplified analysis test case, it can be seen in Fig. 2.3 that the resultant rotor speeds of the models diverge. The disturbance is initiated when time equals zero. The divergence in speed is due to the difference in evolution of the torques imposed on the rotor. In the second order model following the disturbance, the electrical torque remains constant because of the simplified constant flux assumption. The mechanical torque change is based on the mechanical torque equation given by (2.1). The resultant torque evolutions for the second order model are displayed in Fig. 2.4(a), and the resultant torque evolutions for the sixth order model are displayed in Fig. 2.4(b). When using the sixth order model, the mechanical and electrical torques are both affected by the rotor speed In this model the electrical torque starts to change faster than the mechanical torque, causing a greater difference in net torque imbalance (ΔT) resulting in faster ROCOF.

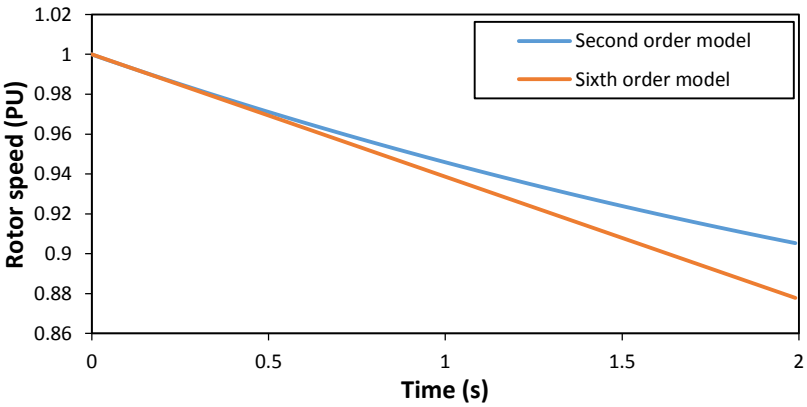

Fig. 2.3. Comparison between second and sixth order SG model following a disturbance

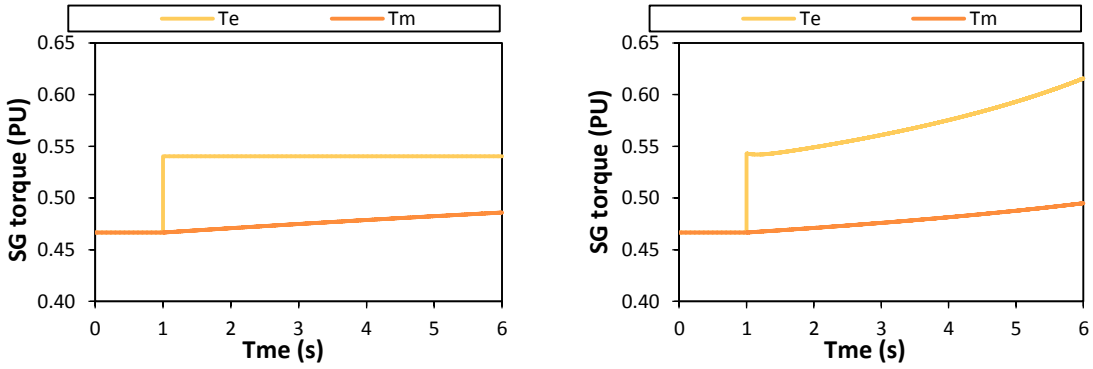

(a) (b)

Fig. 2.4. SG torque evolution. (a) second order model, (b) sixth order model

To improve the accuracy of the results for the RMS time series frequency stability analysis, the sixth order SG model is used throughout this research. The exact simulation model and the equation solving method is provided in [123] and the parameters used during the analysis for the SG components are provided in Appendix Section B.2.

2.1.1.2 Turbine Governor Control

A crucial component for frequency stability studies is the governor control system that is used to provide the primary response from the SG. A turbine governor or speed governor is used to control the active power of the generator. The turbine governor controls the flow into the generator turbine via a control valve using the control signal V_p, as illustrated by the simplified representation in Fig. 2.5 [122]. The governor acts to maintain the active power output of the generator as demand changes by monitoring the speed of the turbine rotor (ω_r). Two types of governor may be used and these are the *isochronous* governor or the *speed droop* governor.

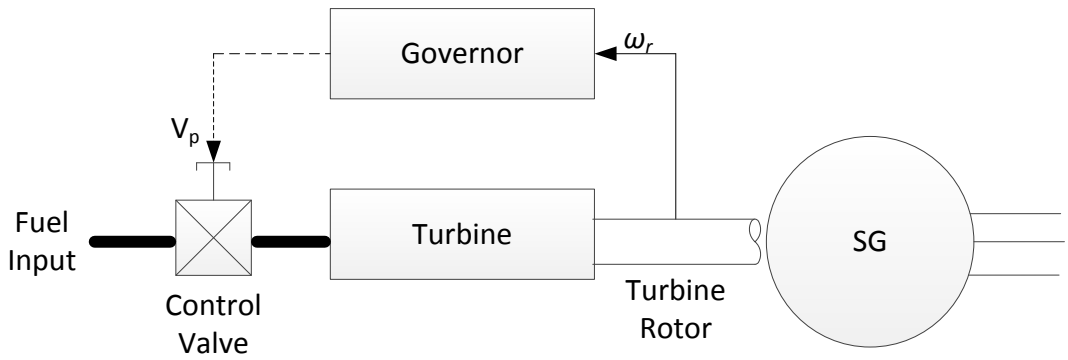

Fig. 2.5.Turbine governor representation

Isochronous governor

This type of governor attempts to ensure a constant speed is achieved and adjusts the control valve until the frequency is back at the nominal value. An error signal is produced by comparing the measured rotor speed (ω_r) to the speed set point (ω_o), this error signal is then amplified and integrated to produce the control valve reference signal. An isochronous block diagram is displayed in Fig. 2.6(a). This type of governor is only applicable if a generator is supplying a single load or only one generator is required to respond when there is a change in network demand. An isochronous control is used when only a single generator is required to provide a response to prevent both generators attempting to restore the frequency to their own reference points. If two machines were operating using isochronous control it may lead to the situation where the two machines are both attempting to be dominant, which leads to interactions and oscillations between the machines.

Speed droop governor

To enable all generators to respond to a network disturbance, the use of speed droop is incorporated into the governor control loop. The speed droop also overcomes multiple generators fighting to control the system frequency to their own reference [122]. To provide the load sharing functionality a steady state feedback loop is introduced around the proportional integral control as represented by the function block diagram in Fig. 2.6(b). In Fig. 2.6(b) the symbol R is the droop coeffcient and the parameter K is the gain of the feedback. The speed droop model may be simplified to the governor function displayed in Fig. 2.7, where $\Delta\omega$ is the difference in angular speed and T_G is equivalent to $1/KR$. The speed droop governor produces the characteristics shown in Fig. 2.8(b) where the value of R determines the slope of the droop characteristics and subsequently the change in power given by (2.5). For multiple generators operating in parallel, a load reference value is added to adjust the output of the SG to a given system frequency. This can be altered to return the frequency back to its nominal value [124]. This is a secondary frequency control action and the use of this type of frequency restoration is not investigated in this research.

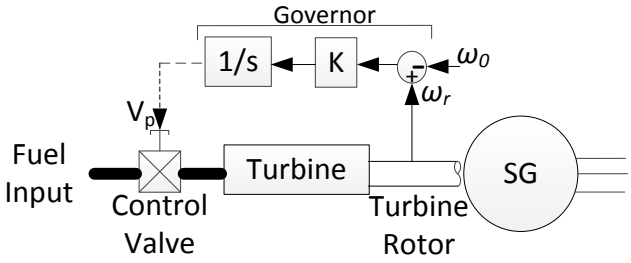

(a)

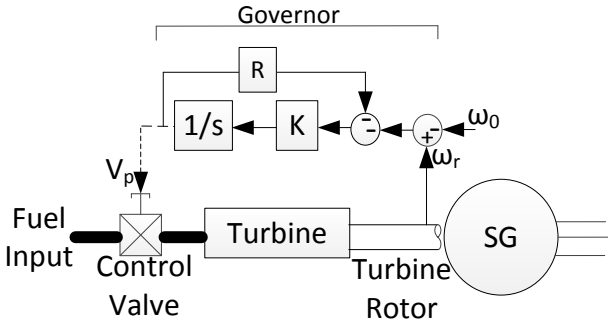

(b)

Fig. 2.6. Governor models. (a) isochronous block diagram,
(b) speed droop function block diagram

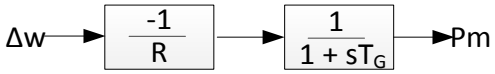

Fig. 2.7. Simplified and reduced governor block diagram

$$\frac{\Delta\omega_r}{R\ \omega_n} = -\frac{\Delta P}{P_n} \tag{2.5}$$

Typical values of droop coefficient (R) are between 0.03-0.09 (3-9%) [10] which for example means that a 0.03 (3%) or a 0.09 (9%) change in the nominal frequency leads to a 100% change in SG output. A range of values are depicted in Fig. 2.8(a), where P_n is the nominal power output of the generator and the steeper the ramp slope, the lower the droop coefficient value. The minimum value of droop coefficient (causing a faster response) is limited by the mechanical limitation of the generator in order to prevent any detrimental stress being applied to the rotor. The role of the intentional dead band within the governor control loop is to prevent the generator output from continually adjusting during normal operation. In the GB system the dead band size should be ≤ 0.03 Hz [125] and the influence of changing the dead band size is depicted in Fig. 2.8(b) emphasizing that a larger dead band will result in the maximum output being reached at a lower frequency deviation.

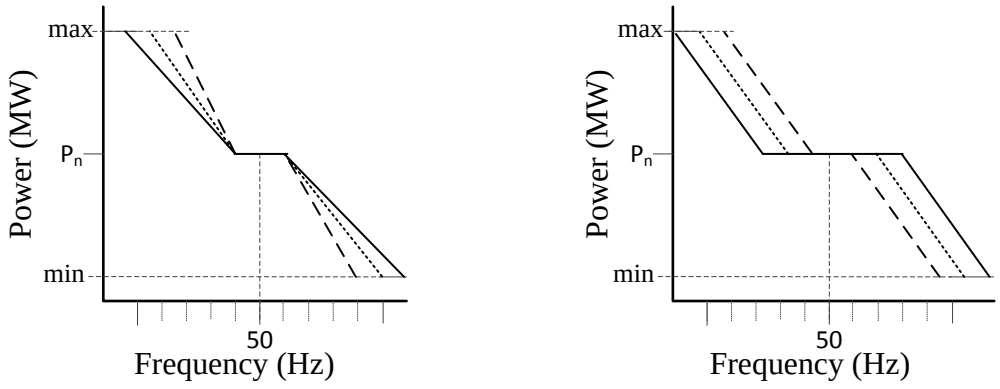

(a) (b)

Fig. 2.8. Speed-power droop characteristics. (a) influence of droop gain, (b) influence of dead band

The exact turbine governor model is dependent on the type of generator and the mechanical input energy type, such as steam, hydro, or gas. The most common types of turbine governor model are TGOV1, GAST, IEEESGO, and IEEEG1 [126]. An in-depth review of turbine governor modelling is provided in [127]. As highlighted in [128], the intentional dead bands that are implemented into governor control loops in order to prevent excessive operation have an impact on the frequency response. Typical turbine governor models in software simulation packages such as DIgSILENT PowerFactory may not have the dead band implemented. Taking this in to account, an augmented version of the IEEEG1 which has a dead band on the speed input is the WIESG1 in DIgSILENT. The WIESG1 turbine governor model incorporates a dead band function on the input measured variable as displayed in Fig. 2.9, and the parameters of the four most common turbine governors can be converted to this model as described in [126]. The dead band setting is chosen to be 15 mHz because the grid code states that it should be no greater than 30 mHz but to avoid doubt it should be set to 15 mHz [125]. Throughout this research the dead band will be set to 15 mHz unless stated otherwise. The nominal droop gain is set at 20 pu (5% droop). The remaining governor parameters are configured using parameter values detailed in [129] and provided in Appendix Section B.2.

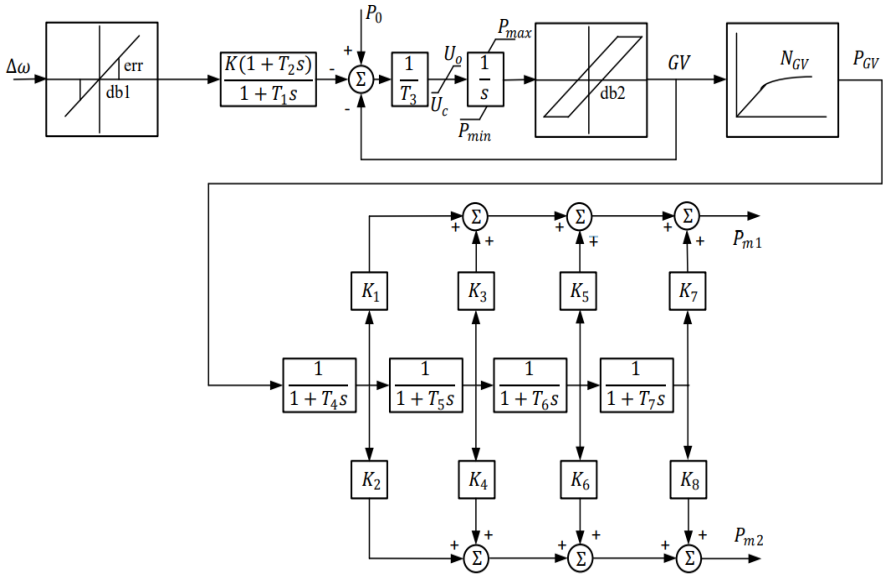

Fig. 2.9. WIESG1 governor model [126]

2.1.1.3 Excitation and Automatic Voltage Control

In a SG the excitation control should be capable of adjusting the field current automatically to maintain the terminal voltage as that SG's active and reactive power outputs change due to disturbances or alterations in the network. During frequency stability studies that involve severe disturbances, the electrical power from a SG changes almost instantaneously when the disturbance occurs. This sudden change in electrical power output from a SG leads to a change in its terminal voltage. The excitation system is a crucial component that is used to maintain the terminal voltage following a disturbance where it may have changed due to a different active power transfer from a SG. Maintaining the terminal voltage also enables effective transfer of active power.

Excitation systems can be classified as DC, AC, or Static. The different excitation system models are discussed in detail in the IEEE standard available in [130]. In a DC excitation system, DC current is supplied to the field winding to produce a magnetic field. Generally, DC excitation systems are slower to respond than AC types. An increase in excitation field voltage (E_{fd}) produces an increase in emf that results in a higher terminal voltage. The addition of an automatic voltage regulator (AVR) allows control of the excitation field current which non-AVR excitation systems do not have. The use of an AVR provides control of the generator output voltage which enables it to contribute to the stability of the power system [10]. By adjusting the excitation current to adjust the output voltage, reactive power transfer may also be affected. A simplified

version of the IEEE Type DC1A (IEEE type1) excitation control is displayed in Fig. 2.10. In order to maintain the required reference voltage, the measured voltage (V_{meas}) is compared to the reference voltage (V^{ref}) and the signal from the power system stabiliser (V_{pss}). The model consists of five main components. The first component is a transducer for the measured variable which incorporates a measurement delay modelled as a first order lag with the time constant T_G. There is then an amplifier (AVR) function with the time constant of operation given by T_A followed by the excitation function that is represented by the function $1/(K_E + sT_E)$. There is also a compensation element consisting of the derivative function $sK_F/(1 + sT_F)$, and a saturation function.

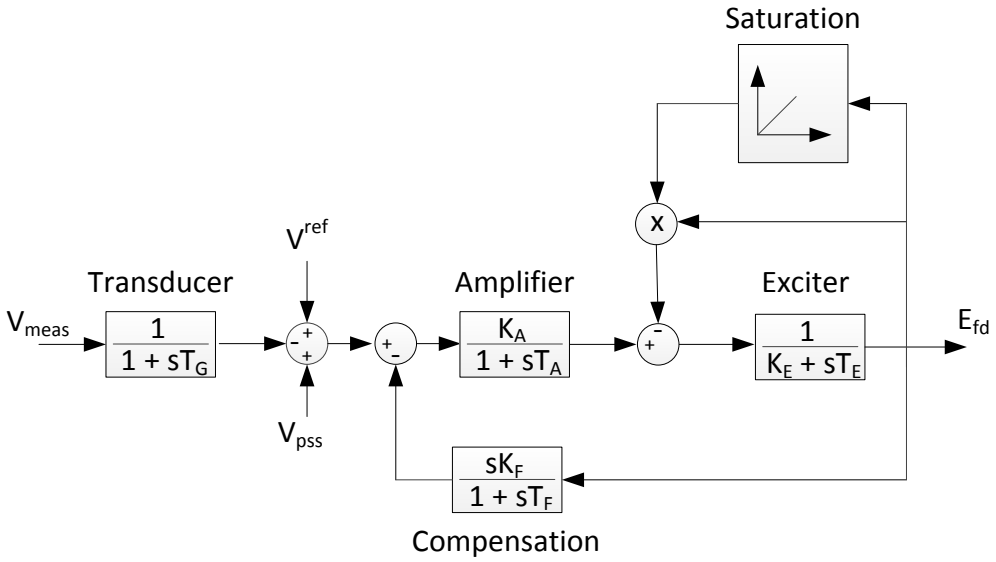

Fig. 2.10. IEEE DC1A (IEEE Type 1) excitation system

2.1.2 Load Modelling

Different types of load model may be represented within the analysis depending on the desired load. The simplest implementations are constant impedance, constant power, and constant current, that can be described using the polynomial impedance-current-power (ZIP) model given by (2.6) where P is the power demand from the load [10]. The ZIP model may be used to create a composite model where different weightings for each element can be set using the parameters P_1, P_2, P_3. In the ZIP model P_o is the initial operating power, V_o is the initial operating voltage, and V is the actual system voltage. For a constant impedance load, the variables P_2, P_3 are set to zero and for a constant power load the variables P_1, P_2 are set to zero.

More complex load models can be implemented that incorporate frequency dependant elements given by (2.7) where Δf is the difference between nominal and measured frequency, and K_{pf} is the frequency sensitivity parameter. When the use of static load models is insufficient to describe the behaviour of the load, a dynamic load model may be required. This may incorporate an element of dynamic recovery and this type of dynamic load recovery model is described by the set of equations in (2.8). The dynamic load recovery model uses the initial operating frequency (f_o) and the actual system frequency (f), along with the state variable of the load power (x_1) and recovery time constant (τ_p). This model can be simplified and linearized as (2.9) [131, 132].

$$P = P_0 \left(P_1 \left(\frac{V}{V_0}\right)^2 + P_2 \left(\frac{V}{V_0}\right) + P_3 \right) \tag{2.6}$$

$$P = P_0 \left(P_1 \left(\frac{V}{V_0}\right)^2 + P_2 \left(\frac{V}{V_0}\right) + P_3 \right) \left(1 + k_{pf} \Delta f\right) \tag{2.7}$$

$$\left.\begin{aligned} \tau_p \frac{dx_1}{dt} + x_1 = P_0 \left(\left(\frac{f}{f_o}\right)^{\alpha s} - \left(\frac{f}{f_o}\right)^{\alpha t} \right) \\ P = x_1 + P_o \left(\frac{f}{f_0}\right)^{\alpha t} \end{aligned}\right\} \tag{2.8}$$

$$P = \frac{k_p + s\,T_1}{1 + s\,\tau_p} \left(\frac{\Delta f}{f_0}\, P_0 \right) \tag{2.9}$$

Extensive work has been done to evaluate the impact the load type has on the voltage stability as in [132, 133]. A simple study provided here evaluating the impact the load type has on frequency stability, confirms that the constant power load model leads to a worst case scenario for frequency stability studies. The response of the load power consumption following the disturbance is displayed in Fig. 2.11(a) and the resultant speed of the SG (frequency) is displayed in Fig. 2.11(b). The constant power load demand is shown to be invariant following the disturbance which leads to an unchanging ROCOF because the electrical torque of the SG does not reduce. As more loads are being connected using PE interfaces, that can be viewed as constant power loads [134], these will create worst case loading scenarios. Due to this trend and the results shown in Fig. 2.11, constant power loads will be used as the load models for all studies undertaken.

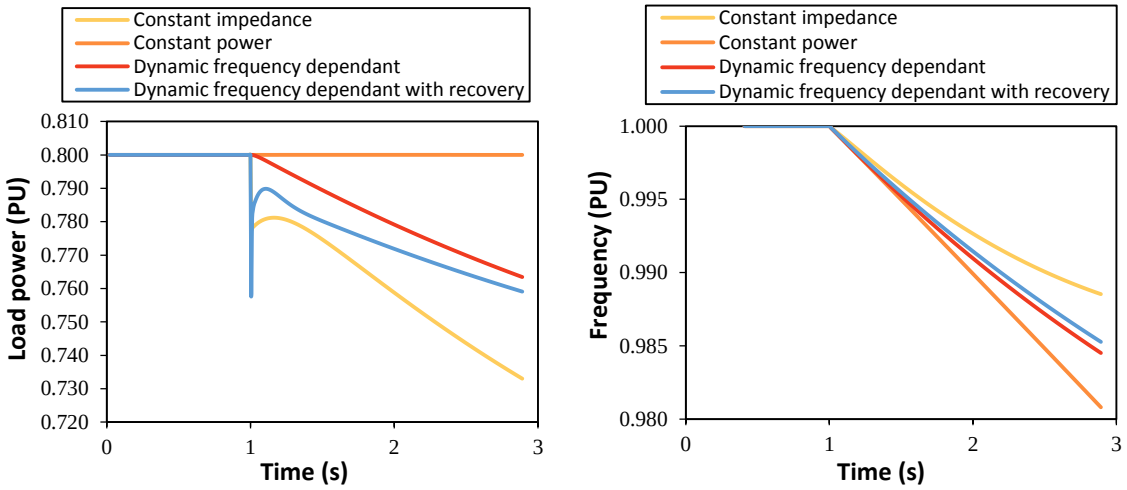

(a) (b)

Fig. 2.11. Influence of load model, (a) load power consumption, (b) SG speed

2.2 Wind Power Plant Modelling

The wind power plants (WPP) may be represented using different model types and with different levels of dynamics incorporated into their RMS models. In this research the WPPs are operated as constant power injection devices that represent Type 4 full converter wind turbines (FCWT) [135, 136]. No dynamic response is incorporated into the control architecture of the WPPs, this enables the HVDC control and response to be evaluated in isolation without the WPP interacting with the HVDC converters.

2.3 Network Models

Three network models will be used to perform the analysis in this research. The first network is simple to enable preliminary studies to be undertaken. The second network is the widely known New England Test System which has applications in stability studies. The third network has been designed uniquely to allow discrete quantifiable network and frequency control changes which allow the resulting frequency stability to be evaluated with a greater degree of flexibility and control than is possible using established test systems.

2.3.1 Single Machine Infinite Bus Test System

The diagram of a single machine infinite bus system that includes a WPP to enable non synchronous generation to be incorporated is displayed in Fig. 2.12 and consists of an infinite bus supplied by a single SG (G1) and a single WPP (W1). The use of a SG and WPP allow the synchronous to non-synchronous generation ratio to be adjusted.

The network and generation are connected via a single transformer (T1) and a single transmission line. The SG operates with the WEISG1 turbine governor and the IEEE type 1 exciter. The system parameters are provided in Appendix Section B.3.

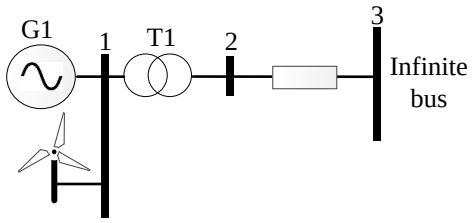

Fig. 2.12. System diagram for the updated single machine infinite bus system (SMIB)

2.3.2 New England Test System (NETS)

The New England Test System (NETS) is detailed in [137] with the full parameters used provided in [138]. It comprises of 10 SG machines, 19 loads, and 39 buses as displayed in Fig. 2.13. The loads have been converted to constant power from constant impedance models. The nominal system frequency in this system is 60 Hz. The IEEEG1 governor parameters are configured using parameter values detailed in [129]. The system data is provided in Appendix Section B.3.

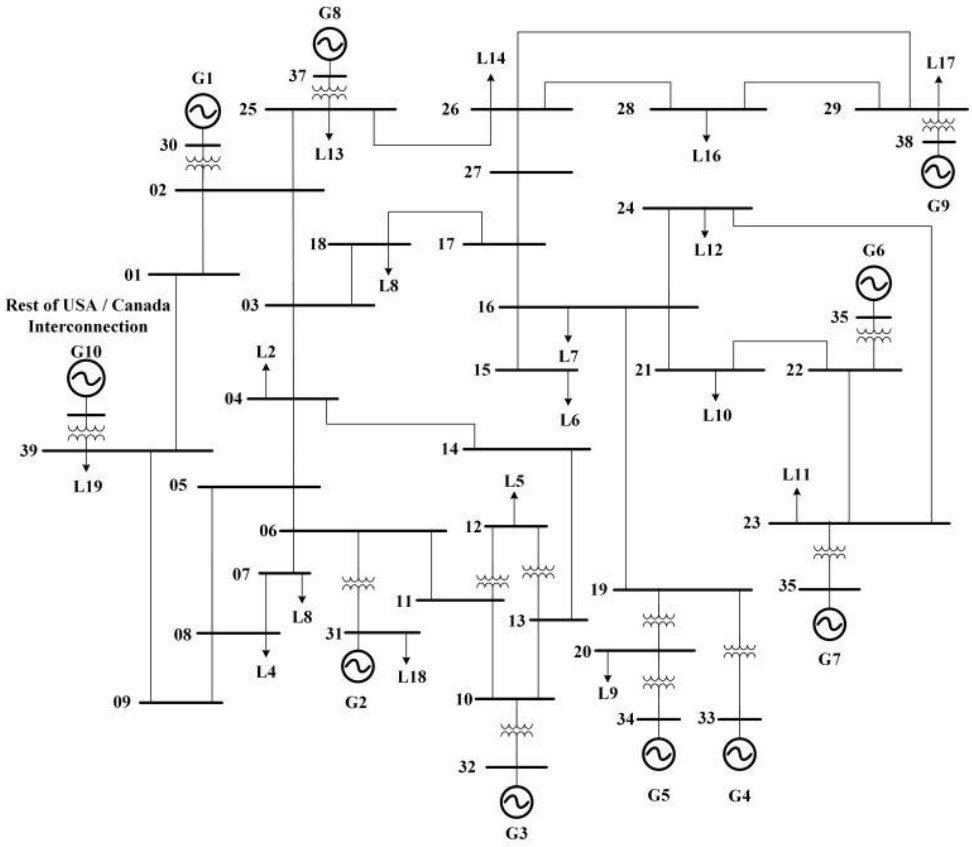

Fig. 2.13. System diagram for the New England Test System (NETS)

2.3.3 Four Area System

In order to assess the impact that various network conditions and VSC-HVDC frequency control implementations have on the frequency stability, a generic four area power system model has been developed. The aim of the model is to allow discrete quantifiable network parameter changes and allow alterations to frequency response controls to isolate their impact on frequency stability. The model is designed to enable simple but precise topology changes without the need for laborious quantification as would occur in a larger system. The model will also allow different VSC-HVDC frequency control schemes to be implemented and their impact investigated around the system. The model consists of four areas (nodes) as depicted in Fig. 2.14 and each area is connected using a double circuit transmission line. The disturbance is created by disconnecting a static generator in Area4 and the disturbance size used is 1.8 GW unless stated otherwise.

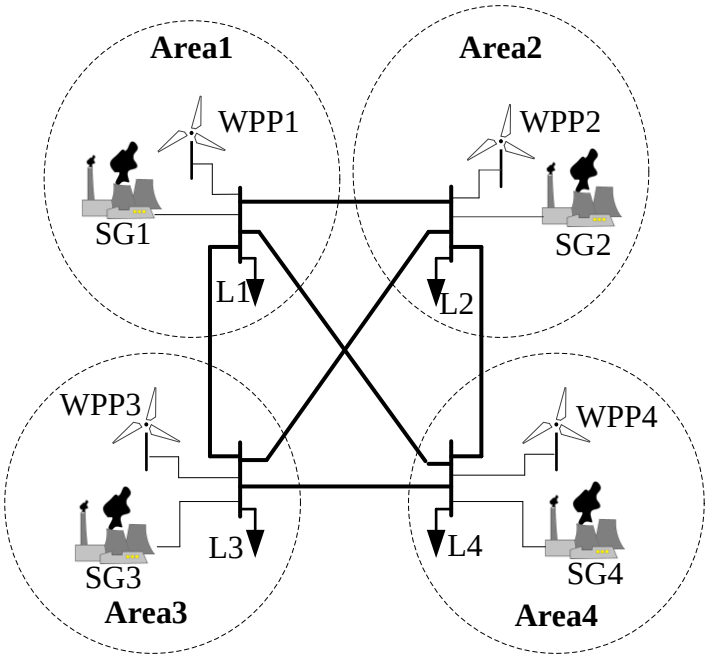

Fig. 2.14. System diagram for the generic four-area test system

A number of topologies (graphs) used for connecting all areas is given by Fig. 2.15. The set of graphs is not an exhaustive set but presents the variants used in this research. Many other variants of connection using the same topologies are non-isomorphic graphs as they are rotated versions of the presented isomorphic graph. The different topologies allow a logical investigation into how the coupling of the power system affects frequency stability. The different topologies are created by setting lines in or out of service.

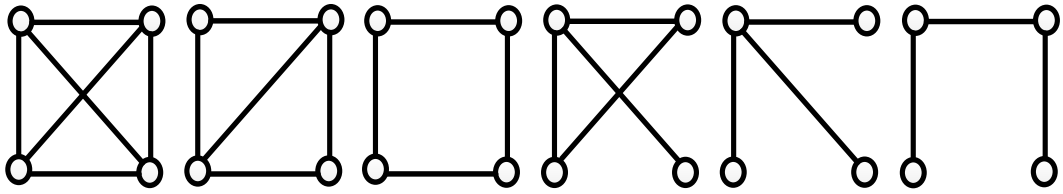

(T1) (T2) (T3) (T4) (T5) (T6)

Fig. 2.15. Selected network topologies

Each area consists of an aggregated SG and an aggregated WPP. All SGs have an IEEE type 1 exciter with voltage set points of 1.01 pu and a turbine governor of type WIESG1. Each area has a constant power load. Different loading scenarios can be set to produce different power flow solutions. The SG in Area4 is set as the slack generator for the power flow analysis. The dispatch, loading, and governor control parameters are representative of a winter profile in the GB system of 50 GW demand [139]. The dispatch and model parameters are provided in Appendix Section B.3 but several of these factors will be explored further and varied in Chapter 3.

2.4 Frequency Analysis Metrics and System Wide Quantification

During frequency stability studies the metrics of nadir and ROCOF are used to evaluate the severity of the frequency stability because it is these values that are used in the system to operate protective devices. During system wide frequency analysis studies there becomes a need to aggregate the quantity of machine parameters (such as inertia constants) in order to represent the average system behaviour or trends in this behaviour, because the frequency will be different around the system following a disturbance. In large power systems, the nadir and ROCOF experienced can be different around the system [140] and the unique oscillatory behaviour of each machine means that the resulting post fault time series frequency plot is not the same at every location within the system. This necessitates a method to remove the rotor angle oscillations from the frequency plots and create a single frequency plot to produce a general system response. This section will present the frequency evaluation methods and provide useful quantification and aggregation methods that will be used throughout this thesis.

2.4.1 Frequency metrics

The following metrics are required to report and analyse the frequency stability.

2.4.1.1 Frequency Nadir

The frequency nadir (f_{nadir})is the lowest frequency value experienced at a specific location during a disturbance simply given as (2.10) where $f(t)$ is the frequency at a given time. During the power system operation this value becomes a critical factor for the disconnection of load that is controlled using under frequency load shedding schemes. Automatic load shedding occurs in stages [141] and each stage is triggered when the frequency deviation exceeds a predefined value. Automatic load shedding is an extreme measure taken because it results in consumers being disconnected and a less reliable system, but it minimizes the chance of cascading failure and so is still necessary.

$$f_{nadir} = \min(f(t)) \tag{2.10}$$

2.4.1.2 ROCOF

The ROCOF is used to describe how fast the frequency changes following a disturbance. This metric is crucial to the system because some generation assets have rate of change of frequency relays that are used to disconnect the generation if the value measured in Hz/s exceeds a predefined set point for a set period of time. The actual ROCOF detection method and process in the relays will vary and so will the settings used. In the UK the predefined tripping values have been proposed to be changed to 0.5 Hz/s or 1 Hz/s depending on the size and age of the machine [6]. During the analysis of the frequency stability events, the ROCOF may be calculated as (2.11) where the subscript 0 is the initial value and the subscript 1 is the current sampled value. Although ROCOF relays have strict predefined settings, the reporting of the ROCOF during simulation studies has no preferred standard to the best of the author's knowledge. Thus the ROCOF could be reported over a 500 ms or 1 s period, both of which will result in different reported values. During this research, the ROCOF will be reported in different ways depending on the studies being performed: using the worst 200 ms period experienced post fault, or over the first 500 ms or 1000 ms period starting at the initiation time of the disturbance. This will be clearly stated whenever the ROCOF is reported in this thesis.

$$\frac{df}{dt} = \frac{f_1 - f_0}{t_1 - t_0} \tag{2.11}$$

2.4.1.3 Centre of Inertia of Frequency

The nadir and ROCOF experienced around the system are not uniform and the local frequency at any bus contains rotor angle oscillations. To obtain a single system frequency plot, the system response requires the aggregation of all SG responses. This can be achieved using the centre of inertia frequency (f_{coi}) calculation as given by (2.12) that calculates the aggregated frequency responses of the SGs weighted by their specific inertia constants (H_i) and machine ratings (S_i).

$$f_{coi} = \frac{\sum_{i=1}^{n}(fSH)_i}{\sum_{i=1}^{n}(SH)_i} \tag{2.12}$$

2.4.2 Inertia

The system inertia has two major roles for frequency stability as described in Chapter 1 and recapped here as: 1) it limits the initial ROCOF experienced, 2) this subsequently allows time for traditional SG primary response control to operate (due to constraining the initial ROCOF). Some frequency stability studies only report the value of H or the system inertia constant (H_{sys}) that have the units of seconds. These values can be determined using (1.1) and (2.13) where S_{total} is the total ratings of all SGs [8]. This is not a useful measure for describing system inertia as it is the ratio between the kinetic energy and rating of the machine which is fairly consistent for all similar types of machine, and is independent of rating. A more accurate representation of the system inertia involves the ratings of the machines and their inertia constants given by (2.14) where $H_{GVA.s}$ represents the quantity of system inertia. This provides an indication of how much inertial energy is available in the system and this value allows for direct comparison between cases.

$$H_{sys} = \frac{\sum_{i=1}^{N} H_i S_i}{S_{total}} \tag{2.13}$$

$$H_{GVA.s} = \sum_{i=1}^{n}(S \times H)_i \tag{2.14}$$

2.5 Simulation Details

The power system analysis package used for all studies in this research is DIgSILENT PowerFactory 2017a. The time series analysis is performed using RMS analysis because the faster electromagnetic transients are not of interest in this research. The network is setup as a balanced three phase representation and the integration simulation time step is 10 ms.

To increase the functionality of certain models, the use of MATLAB has been used. In the instances where MATLAB is used, PowerFactory interacts with MATLAB at every simulation time step and MATLAB returns the updated parameter values before the next time step iteration is completed.

To enable a vast number of simulations to be performed in an automated manner, the use of Python scripting has been used. The Python script is used to populate the simulation parameters and initial conditions, initiate the simulation, extract the simulation data, and analyse the data. This process is looped to run a vast number of automated simulations. The possible process flows used within this thesis are displayed in Fig. 2.16.

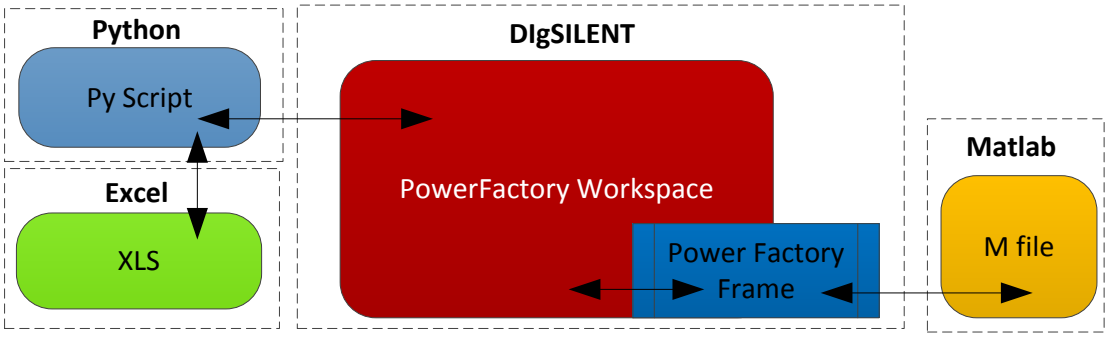

Fig. 2.16. Simulation process flows

2.6 Summary

This chapter has presented the models that are used to represent the AC network components and the associated SG controls that are used in this research. The chapter has presented models that are important to frequency stability analysis which include SG, turbine governor, excitation control, and load composition. The use of a sixth order SG model has been evaluated over the second order model. The analysis displayed how the second order model leads to a reduced impact on the frequency stability metrics. This section has also evaluated the impact that different load compositions have on the frequency stability. Constant power loads were shown to produce the worst case

frequency stability setup. In this thesis, constant power loads will be used for all of the analysis because of their detrimental characteristics and because they represent the trend in future loads. The use of the WEISG1 turbine governor control will be used because the literature highlights that the dead band is a crucial factor. The IEEE DC1A type 1 exciter will be used throughout the research to represent the legacy excitation systems.

The test system models applicable for this research have been presented and will be used throughout this thesis in the following chapters.

3 Factors Affecting Frequency Stability Within Networks

The frequency stability and the corresponding post disturbance response are heavily determined by the system inertia, and the reason for this has been discussed in the previous two chapters. Although the inertia is a key frequency stability component in traditional power systems, there may be other factors that influence the frequency stability and the response in the system. The aim of the analysis in this chapter is to highlight which network factors are of concern when assessing frequency stability. A change in a certain network factor may have a profound influence on either the frequency drop, ROCOF, or both. Determining which factors are of concern for each metric will allow the speed and quantity of the limited frequency response services to be better allocated in order to target a specific metric more strongly. The factors highlighted can be used to better inform the frequency containment services in the network. Furthermore, this analysis can be used to determine the most favourable type of VSC frequency controller and the location within the network for that specific type. Chapter 7 will build on this analysis by incorporating the different VSC frequency controllers presented in this research into various network operating scenarios.

The contribution from this chapter can be summarised as:

1) Identifying and quantifying the variable impact that network factors have on the frequency drop and ROCOF in multi-area power systems.
2) Providing an explanation of the mechanism through which power flow impacts frequency stability.
3) Developing a new measure that is used to quantify network topology. The measure can be used to characterize different network connectivity which is shown to have a strong relationship with the resultant system ROCOF.

3.1 Frequency Stability and Containment

As introduced in Chapter 1, frequency stability is governed by the swing equation given in (1.2). Changes in electrical power around the system occur almost instantaneously, whereas, mechanical power changes are limited by the governor controls. Mechanical power cannot change instantly or in large quantities as this would cause excess stress to be placed on the generator's rotor. A visual depiction of how the torque imbalance $(T_m - T_e)$ on the rotor changes as time progresses following a system disturbance is given in Fig. 3.1. The torque imbalance is compared to the mechanical and electrical power changes during the same time frame and the resultant frequency

evolution. It displays the sudden initial large torque imbalance due to the pick-up followed by the slower acting torque balance restoring force of the primary response. The stages of interest for frequency stability in this component of research are: *initial torque imbalance* (generator pick up), *inertial response*, and *Primary response*. The initial torque imbalance occurs instantaneously following a disturbance. The inertial response occurs from the time of the disturbance and lasts until the turbine mechanical power has started to increase, which is approximately 2-3 s after the onset of a disturbance. The primary response starts to operate after approximately 2 s and lasts for several seconds following this until equilibrium has been achieved. The timescales for each response in Fig. 3.1 would be dependent on the system setup and conditions and are shown for illustrative purposes to highlight the different response types.

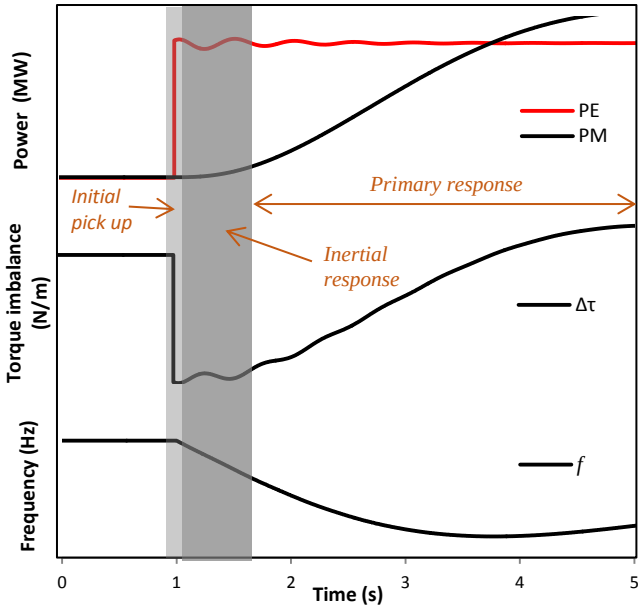

Fig. 3.1. SG power imbalances and mechanics following a disturbance

3.1.1 Initial Torque Imbalance

The quantity of additional load that each generator initially picks up following a disturbance is important because it determines the initial torque imbalance on the machine. The amount of power injected by each SG can be determined through the solution of the system differential-algebraic equations (DAEs) that are provided in detail in [121, 142]. This has been extensively covered in literature and is fundamental to time domain simulation analysis. The implications of these equations and solutions for frequency stability have not yet been explored. It is for this reason that they are included here to fully describe what happens following a disturbance as they have implications for how different network factors affect frequency stability.

The solution is obtained using the differential vector $\boldsymbol{f}$, the algebraic vector $\boldsymbol{g}$, and the machine algebraic vector $\boldsymbol{h}$ as displayed by the standard notation given in (3.1)-(3.3). These include the state variables (x) the input variables (u) which incorporates voltage (V) and voltage angle (θ), and the stator algebraic variables (I_d, I_q). The initial pick up is particularly concerned with solving the algebraic equations at the time of disturbance. The state variables, that consist of variables that are time dependent, in the differential equations in $\boldsymbol{f}$ do not change instantly and will be ignored for the timescales of interest. Applying a partitioned solving method and using a Newton-Raphson (N-R) approach, the algebraic variables in $\boldsymbol{g}$ are updated by (3.4), where $\Delta\beta$ is a vector of active and reactive power bus mismatches and $\boldsymbol{J}$ is the Jacobian matrix which determines the gradient change to a given algebraic variable. The superscript n denotes iteration number and the values of the algebraic variables at that iteration, whilst $n+1$ denotes the values at the next iteration.

$$\dot{\boldsymbol{x}} = \boldsymbol{f}(x, u) \tag{3.1}$$

$$\mathbf{0} = \boldsymbol{g}(x, u, I_d, I_q) \tag{3.2}$$

$$(I_{d,} I_q) = \boldsymbol{h}(x, u) \tag{3.3}$$

$$\begin{bmatrix} \theta \\ V \\ I_d \\ I_q \end{bmatrix}^{n+1} = \begin{bmatrix} \theta \\ V \\ I_d \\ I_q \end{bmatrix}^{n} - \boldsymbol{J}^{-1}\, \Delta\beta \tag{3.4}$$

The network node equations given in current form by (3.5) where $\boldsymbol{Y}$ is the admittance matrix, $\boldsymbol{V}$ is the node voltage matrix, and $\boldsymbol{I}$ is the node current injection matrix are used to determine the node mismatches. Using the power balance form, the active power (P_{gi}) and reactive power (Q_{gi}) injected from a generator into the network at bus i are determined from the stator algebraic equations as in (3.6)-(3.7) with the subscript $i = 1, 2, \ldots, N$.

$$[\mathbf{0}] = [\boldsymbol{Y}][\boldsymbol{V}] - [\boldsymbol{I}] \tag{3.5}$$

$$P_{gi} = I_{di} V_i \sin(\delta_i - \theta_i) + I_{qi} V_i \cos(\delta_i - \theta_i) \tag{3.6}$$

$$Q_{gi} = I_{di} V_i \cos(\delta_i - \theta_i) - I_{qi} V_i \sin(\delta_i - \theta_i) \tag{3.7}$$

Combining these into the active and reactive power balance equations for a generator bus produces the equations in (3.8)-(3.9) [121], where the general bus values are denoted by the subscripts i, j and the difference between two busses is denoted by the subscript ij where $i = 1,2, \dots, N$. Completing the set of algebraic equations are the active and reactive power balance equations for a load bus as given by (3.10)-(3.11) where P_l and Q_l are the active and reactive load values.

$$0 = I_{di}V_i \sin(\delta_i - \theta_i) + I_{qi}V_i \cos(\delta_i - \theta_i) - \sum_{j=1}^{N} V_i V_j Y_{ij} \cos\left(\theta_i - \theta_j - \theta_{ij}\right) \tag{3.8}$$

$$0 = I_{di}V_i \cos(\delta_i - \theta_i) - I_{qi}V_i \sin(\delta_i - \theta_i) - \sum_{j=1}^{N} V_i V_j Y_{ij} \sin\left(\theta_i - \theta_j - \theta_{ij}\right) \tag{3.9}$$

$$0 = -P_l + \sum_{j=1}^{N} V_i V_j Y_{ij} \cos\left(\theta_i - \theta_j - \theta_{ij}\right) \tag{3.10}$$

$$0 = -Q_l + \sum_{j=1}^{N} V_i V_j Y_{ij} \sin\left(\theta_i - \theta_j - \theta_{ij}\right) \tag{3.11}$$

The Jacobian matrix consists of the partial derivatives for each active and reactive power equation with respect to the algebraic variables as given by (3.12). The Jacobian can be considered as four separate matrices when the stator variables are removed and form their own Jacobian.

$$J = \begin{bmatrix} \frac{\partial P}{\partial \theta} & \frac{\partial P}{\partial V} \\ \frac{\partial Q}{\partial \theta} & \frac{\partial Q}{\partial V} \end{bmatrix} \tag{3.12}$$

When the algebraic equation solutions are updated through a new iteration denoted by $\theta^{n+1}, V^{n+1}, I_d^{n+1}, I_q^{n+1}$, they lead to new active and reactive power flows determined by (3.8)-(3.11), that in turn update the vector $\Delta\beta$. These updated mismatch values drive the N-R method until the mismatch errors are suitably reduced and then the differential equations can be solved. This is the basic format and well known method of the power

flow solution. During this solution, the partial derivatives in J determine the gradient or sensitivity at that specific operating point. Isolating the partial derivative for the active power of a generator bus with respect to the voltage angle in (3.13), it can be seen that the gradient is determined by the algebraic variables, $V,\ \theta,\ I_d,\ I_q$, state variable δ, and network impedance Y.

$$\frac{\partial P_i}{\partial \theta_i} = I_{di}V_i \cos(\delta_i - \theta_i) + I_{qi}V_i \sin(\delta_i - \theta_i) + \sum_{j=1}^{N} V_i V_j Y_{ij} \sin(\theta_i - \theta_j - \theta_{ij}) \tag{3.13}$$

These gradients determine how the algebraic variables change and subsequently how the power flow changes in (3.8)-(3.11). Following a SG disconnection, the voltage angles and magnitudes along with the active and reactive power flows start to change around the system according to the described equations governing the power flow solution. The bus voltages and angles are in turn determined by the active and reactive power flows. The sensitivities of voltage to active power (dV/dP) and reactive power (dV/dQ) can be obtained by rearranging (3.4) to determine how the voltages change in the system. Certain busses have greater sensitivity to changes in the algebraic variables, particularly busses that are operating with a greater voltage angle. This increased sensitivity creates the situation where as the power flow solution starts to evolve and increase the power injection at that bus, this increased power leads to a greater reduction in voltage.

At the next iteration of the power flow solution, this reduced voltage magnitude at the bus now impacts the power transfer. In essence, it is during the power flow solution that the voltage magnitudes at busses that are operating with greater initial voltage angles experience the greatest reduction, because they have greater sensitivity to changes in power flow. The resultant voltage changes now impact the active power transfer and the power injection in the algebraic solution that ultimately determine the initial imbalance before the differential equations are solved.

This previous point is highlighted using the network setup given by Fig. 3.2 using two different test case scenarios. The network consists of two SG that are labelled SG1 and SG2, a load, and a static generator $(G3)$ used as the disturbance. During both test case scenarios the rating of the SGs does not change from 1400 MVA. The disconnection size is 50 MW in both cases and the location remains fixed. Both

generators are symmetrically located from the disturbance and the load (i.e., $Z_{B1-B3} = Z_{B2-B3}$).

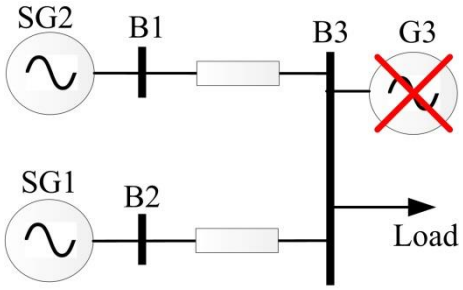

Fig. 3.2. Pick up test system

The first test scenario represents a condition where both SGs pick up the same initial power following the disturbance. In this scenario both SGs are operating with the same pre-fault active power, voltage magnitude, and voltage angle with relation to bus 3. The second scenario represents an operating situation where the two SG are providing different initial active power injections and have different terminal voltage angles with respect to bus 3. The pre-fault values for each scenario are provided in Table 3.1.

Table 3.1. Pick up test scenario pre fault values

	G1			G2		
	θ_0 (°)	V_0 (pu)	P_0 (MW)	θ_0 (°)	V_0 (pu)	P_0 (MW)
Scenario 1	2.59	1	725	2.59	1	725
Scenario 2	4.30	1	1200	0.86	1	250

In scenario 1, it can be seen that the initial pickup from both SGs in the test network is identical as displayed in Fig. 3.3(a). The resulting terminal voltage reduction following the disturbance is also identical for both SGs displayed in Fig. 3.3(b).

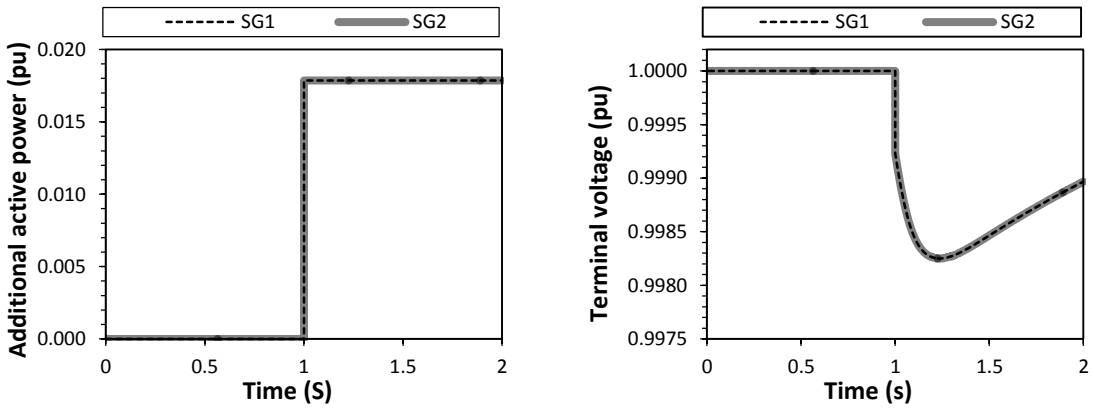

(a) (b)

Fig. 3.3. Test case scenario 1 results. (a) active power pickup, (b) terminal voltage

For scenario 2 where the post fault active power injection and resulting terminal voltage angle in relation to bus three is different, leads to unbalanced pick up. The initial additional electrical power injected from both SGs is displayed in Fig. 3.4(a). The terminal voltages for both SGs are displayed in Fig. 3.4(b). In this scenario it can be seen that SG1 that was initially providing a larger quantity of active power picks up slightly less power following the disturbance – shown at time $t = 1$ s in Fig. 3.4(a). The terminal voltage for SG1 is seen to experience a greater reduction as predicted by the power flow equations.

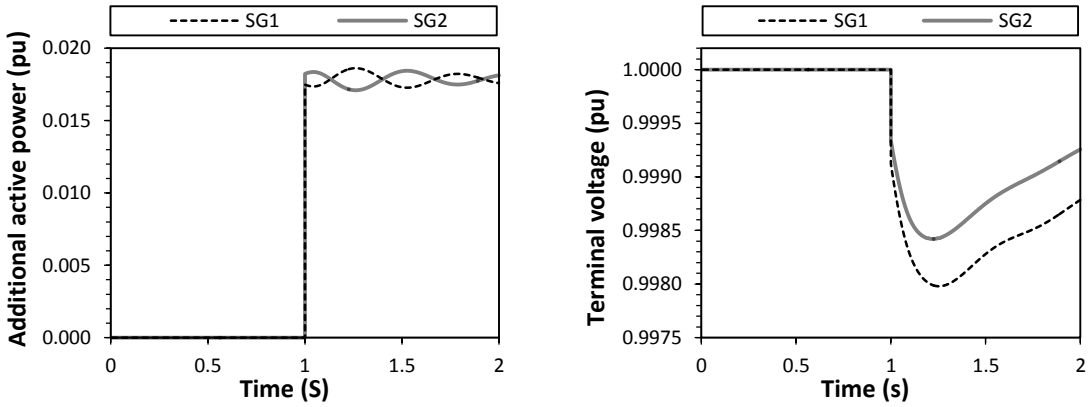

(a) (b)

Fig. 3.4. Test case scenario 2 results. (a) active power pickup, (b) terminal voltage

It can be concluded from this basic analysis that if two identical generators are operating with the same active and reactive power output when a disturbance occurs at a symmetrical distance of Z from the load, then the initial pick up will be identical. However, if the two machines are operating at different power angles, or a machine is connected to a bus with a different voltage angle, then they would not pick up an identical amount of load. The machine that is operating at a larger power angle or that is connected to a bus with a greater voltage angle would subsequently experience a greater change in voltage drop. This resultant voltage drop leads to a reduced active power transfer from that SG.

This analysis has explained the resultant quantity of load that the each generator picks up and, more importantly, it determines the electrical torque on the machine and therefore the rotor acceleration – which is of interest in this research.

3.1.2 Inertial Response

The inertial response is a natural response where the energy from the turbine rotor is released providing the additional electrical energy following the disturbance. The required amount of energy is released immediately and constantly over the time period to provide a step in electrical power (P_E). The inertial response does not reduce the torque imbalance, but it does determine how fast the rotor will constantly decelerate based on the rotor energy extraction rate. This is predominantly determined from the well-known swing equation given by (1.2). The numerical solution requires the solution of differential equations and the update of the machine states for each time step. The evolution of the machine's response is dependent on the torques imposed on the machine, machine damping, and the inertia of the machine. The inertia constant for a machine is the ratio of the stored angular kinetic energy of a generators rotor (K_E) to the size or rating of the machine (S) given by K_e/S. The time evolution of the frequency deviation is dependent on H and the net torque (ΔT). To reduce the ROCOF requires either an increase in inertia or a reduction in the net torque imbalance.

3.1.3 Primary Response

The primary response in a typical SG is implemented into the turbine governing system and is a proportional control scheme, commonly known as droop control. The primary control response increases the mechanical power (P_m) into the turbine and this reduces the torque imbalance. The reduction in torque imbalance reduces the deceleration of the rotor until equilibrium has been reached when P_m has been increased sufficiently to equal P_e. The droop characteristic determines the change in power for a given change in machine speed given as (3.14) where R is the droop coefficient and P_n is the nominal power [122]. The primary response is contracted to start within a set timeframe by the system operator, but due to the physical constraints of the machine, it cannot start instantly nor have an excessive droop characteristic. As this response is proportional to the frequency deviation and delayed due to measurement and activation, it has limited impact on the initial ROCOF and has a stronger impact on the frequency containment. The primary response acts to create equilibrium between the electrical and mechanical torques by increasing the mechanical power and therefore increasing the mechanical torque .

$$\frac{\Delta\omega_r}{R\ \omega_n} = -\frac{\Delta P}{P_n} \tag{3.14}$$

3.2 Frequency Stability Contributing Factors

Following a disturbance, certain factors affect the instantaneous changes (algebraic equations) and certain factors influence the time varying state changes (differential equations). The instantaneous changes following a disturbance are associated with the voltages, voltage angles, and currents. These determine the initial pick up of the SGs in the system. However, the time series evolution of the frequency is determined by the differential equations. Changes in the factors that influence the algebraic and differential equations can be given as:

- Algebraic equations: *Network topology* & *Power flow*.
- Differential equations: *Inertial response* & *Primary response*.

3.2.1 Network Topology

In order to understand how the network topology influences the frequency stability and post disturbance response, it is beneficial to create a unique numerical measure for any given topology in order to be able to compare it against another topology. To distinguish each topology, the number of node connections, known as the average node degree (from graph theory) for each area and the electrical distance from the area where the disturbance occurs to every other area has been used in this research. This measure is used to capture how connected the network is and, therefore, how easily power can be transferred to the area of disturbance.

The average node degree is given by (3.15) where k is the average node degree parameter, k_i is a network node, and N is the number of connections into the node [143]. The electrical distance as viewed from the disturbance area is given by (3.16) where Z is the network impedance and $\mathrm{Z_{dd}}$ is the self-impedance in the area where the disturbance occurs. The subscript j refers to a network node or area in this case and Z_{dj} refers to the connection between the area where the disturbance occurs and the next connected area. To obtain the impedance values between areas, the system admittance matrix (Y_{bus}) can be inverted as (3.17) to produce the impedance matrix (Z_{bus}). The Y_{bus} changes for each topology and becomes sparser as the network becomes more radial. Together they are used to create the overall topology measure (λ) given by (3.18) that comprises of how connected and how distant the areas are from each other. The parameter λ is the ratio between the impedance of a network and the connectivity of all nodes within the network. A high value of λ implies either a high impedance (distant

areas) or low nodal connectivity. A low value of λ is indicative of either a highly meshed or a low impedance network.

$$k = 1/N \sum_{i=1}^{N} k_i \tag{3.15}$$

$$Z = \sum_{j=1}^{N-1} \left(Z_{dd} + Z_{jj} - 2Z_{dj}\right) \tag{3.16}$$

$$Z_{bus} = (Y_{bus})^{-1} \tag{3.17}$$

$$\lambda = Z/k \tag{3.18}$$

The network topology strongly affects the system voltage angles and magnitudes that in turn determine the resultant generator pick up and post disturbance power flow. The topology also determines the rotor angle stability, where certain topologies cause greater rotor swings that are superimposed onto the frequency excursion. A weakly coupled system or an area that has a high electrical distance from the rest of the system will experience larger rotor angle swings. When these are superimposed over the frequency excursion, some machines will experience periods where the frequency rate of change is higher than the centre of inertia (or system) ROCOF, as displayed in Fig. 3.5. This phenomenon can result in highly localized frequency behaviour. As ROCOF measurement techniques improve or the detection window reduces, these oscillations will need to be mitigated during the measurement process to prevent excessive or unwanted tripping.

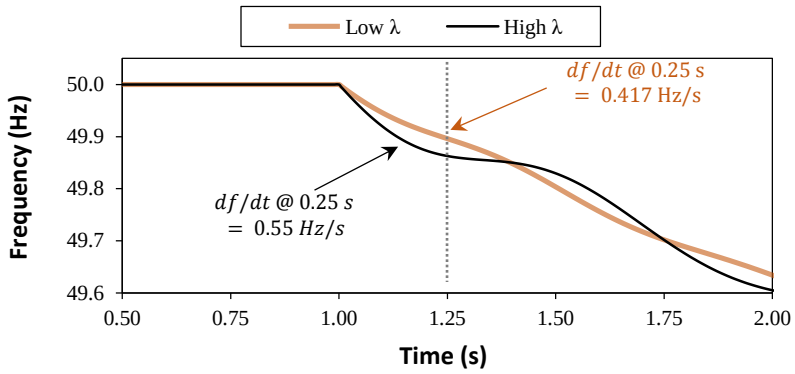

Fig. 3.5. Impact of topology on frequency response

3.2.2 Network Power Flow

The location and magnitude of the generation and the load determine the power flow around a network and subsequently determine the voltage magnitudes and angles. As outlined in section 3.1.1, the frequency stability and response of different synchronous machines will be different depending on the network operating points. The power flow into the area of the disturbance can be used as a quantity that indicates the voltage angle differences in relation to the area of disturbance. It can be extrapolated that the greater the power flow into the disturbance area, the greater the voltage angle differences will be with respect to the other areas due to the greater power transfer. Using the power flow instead of calculating the actual voltage angles requires less system information and would be less complex in a large scale system. This could be achieved using supervisory control and data acquisition (SCADA) data without the need for numerous phasor measurement units. As described in section 3.1.1, this resultant larger angle difference due to a greater power transfer into the disturbance area is expected to have a detrimental impact on frequency stability and lead to larger frequency drop and ROCOF.

3.2.3 Inertial and Primary Response Distribution

Reducing inertia will decrease the frequency stability due to faster ROCOF. Increasing primary response droop gain will improve frequency stability as synchronous machines will actuate a greater response to frequency changes. However, when these factors are changed in different areas in relation to the disturbance area, they may lead to dissimilar frequency responses. Reducing inertia in the area where a disturbance occurs may lead to greater ROCOF than if the same inertia reduction occurs in another area. Similarly, increasing the primary response may be more beneficial in the disturbance area, or where the system experiences its worst frequency stability. Changing these factors in certain areas, could either provide system benefits or have limited impact on the overall frequency stability. The option may exist to target specific response types in specific areas depending on connected resources and operational conditions, particularly where the system is identified as weak with respect to frequency stability.

3.3 Simulation Configuration and Data Analysis Techniques

In order to investigate the various network factors described above in detail entails a large number of system simulations, where each simulation or scenario is created from a combination of different system factor setups. This process is enhanced through the use of Python scripting and the use of correlation analysis to extract meaningful results from the large data set obtained.

3.3.1 Simulation Configuration

The test system used is the generic four area test system that is presented in Chapter 2. The generation dispatch remains unchanged throughout these studies, and the 1.8 GW disturbance always occurs in Area4 by disconnecting the static generator that does not possess any inertia. An exhaustive simulation methodology is used in which data is obtained from all cases involving six topology configurations, nine inertia distributions, eight load distributions, and nine droop gain distributions. The parameter values for each setup are given in Appendix Section C.1, and the resulting total number of simulations is 3888.

For each scenario the maximum frequency drop and ROCOF is recorded for every area. These maximum values of frequency drop and ROCOF from each unique scenario are used during the analysis phase. The maximum ROCOF is detected over a 200 ms sliding window in this chapter to capture the influence of the rotor angle stability on the frequency metrics. The six network topologies depicted in Chapter 2 are used and the values of electrical distance to all areas from Area4 (Z), average node degree (k), and unique topology measure (λ) for each topology are displayed in Table 3.2. It can be seen that as the topology becomes less meshed (T1 → T6) the value of λ increases. The value of λ will be used during the analysis to investigate topology impact.

Table 3.2. Average node degree, impedance, and λ values for each topology

	T1	T2	T3	T4	T5	T6
Z	4.7	7.5	8.4	11.6	14.1	22.6
k	3	2.75	2	2	1.5	1.5
λ_{Area4}	1.56	2.72	4.2	5.8	9.4	15.06

Python scripting is used within DIgSILENT in this chapter in order to automate the vast number of scenario simulations. Python is used to populate the initial system setup and parameters, and initiate the simulation. Following each simulation, Python is used

to extract and analyse the data before populating and initiating the next scenario. To achieve all combinations involving the factors presented, the Python code is setup using a nested loop approach. A pseudo implementation of the nested loop code is presented below:

```
For: inertia_setting in range (1:9)
   Inertia setup (inertia_setting)
   For: load_setting in range (1:8)
        Load setup (load_setting)
        For: topology in range (1:6)
             Topology setup (topology)
             For: droop_gain in range (1:9)
                  Droop setup (droop_gain)
                  Initiate simulation ( )
                  Extract data/analysis data ( )
```

3.3.2 Correlation Analysis

Initial analysis of the results for all scenario combinations is undertaken using a Pearson multiple input linear regression correlation approach as outlined in [144]. The correlation is used to determine how a change in a certain factor affects the frequency drop and ROCOF. It is used specifically to calculate the degree of linear dependence between the variables and each metric. This highlights which parameters have a significant linear correlation with the given metrics. The premise of the linear correlation is derived from the equation of a straight line and can be extended to multiple variable regression analysis. The input variables denoted by X are standardised using the standard deviation values to enable comparison between variables. The output variables denoted by Y relate to the frequency drop and the ROCOF.

The Pearson correlation coefficient (r) that is given by (3.19) is used to determine the strength of the linear relationship between the pair of variables where the subscript i refers to the sample point [144].

$$r = \frac{\sum_{i=1}^{n}(X_i - \overline{X})(Y_i - \overline{Y})}{\sqrt{\sum_{i=1}^{n}(X_i - \overline{X})^2}\sqrt{(Y_i - \overline{Y})^2}} \tag{3.19}$$

3.4 Results of Simulation Analysis

This section presents a selection of the key results obtained from analysing the data set produced from undertaking all combinations of the possible network scenarios.

3.4.1 Correlation Analysis

The variables used for the correlation analysis are:

- Topology measure.
- Power flow into Area4 (that is altered using different load profiles).
- Inertia distributions in Area1-Area4.
- Droop gain distribution in Area1-Area4.

This gives a total of 10 input (*X*) variables that are used in the correlation process. There are two output (*Y*) variables of interest in the correlation analysis and these are the frequency drop and ROCOF. Note that the symbols of X, Y are used in this section to denote input and output parameters in the correlation analysis, and do not refer to the reactance or admittance. Frequency drop is used as a measure instead of nadir so that both output variables increase to display worse frequency stability conditions.

The procedure to perform the correlation analysis starts by extracting the time series data for each scenario as illustrated in Fig. 3.6 (with an arbitrary selection of topology T1 and load L7 configuration). From the time series data the frequency drop and ROCOF for that simulation can be calculated as highlighted in Fig. 3.6. In order to evaluate how correlated the power flow variable is to the ROCOF, the power into Area4 is calculated by taking the sum of the active power into Area4. The values for frequency drop and ROCOF can now be plotted against power flow individually. The resultant ROCOF calculation and the power flow calculation for scenarios that only involve a change in load conditions are displayed in Fig. 3.7. It can be seen how a change in the load produces a change in the power flow and ROCOF and furthermore this allows the correlation between the two variables to be assessed. The power flow and ROCOF data collection description is extended for a change in all variables to produce the scatter plot in Fig. 3.8. The scatter plot displays the data sampled for all variations in the network factors for the variables of power flow and ROCOF. The main factor that changes the power flow into Area4 is a change in loading. These changes in loading are modelled using discrete steps which lead to a plot that appears quantized in appearance for the power flow variable. A set of similar plots can be achieved for frequency drop versus power flow. This method is undertaken for each *X* variable against each *Y* variable. The

topology variable value is the value given by λ provided in Table 3.2. The variables for droop gain and inertia distribution are taken straight from the SG machines in each area.

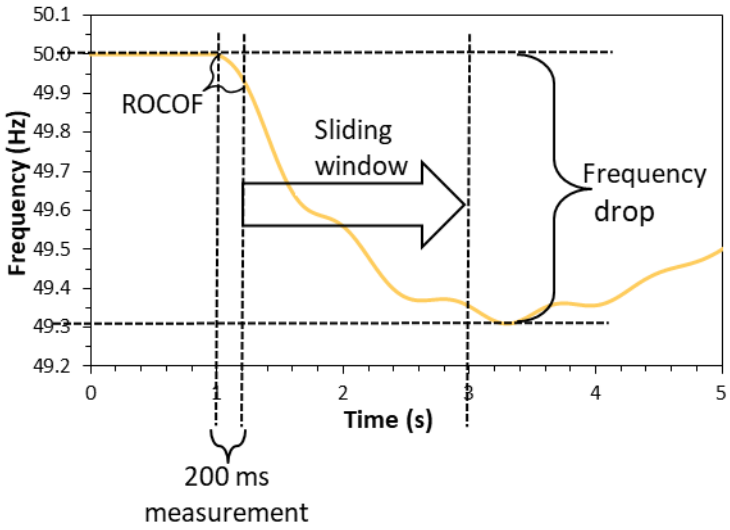

Fig. 3.6. Example time series plot displaying the ROCOF and frequency drop calculation

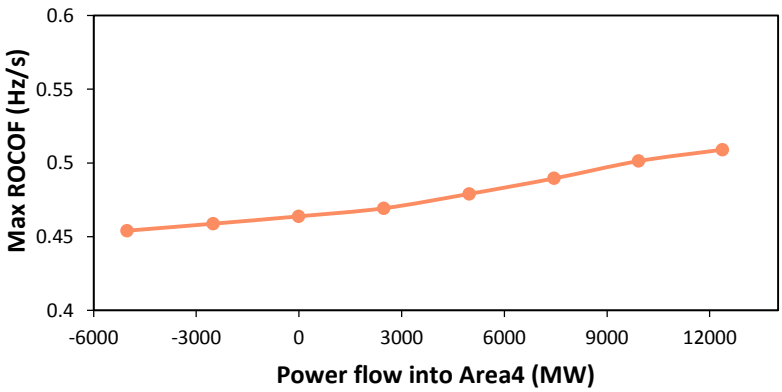

Fig. 3.7. Power flow versus ROCOF for a change in load demand

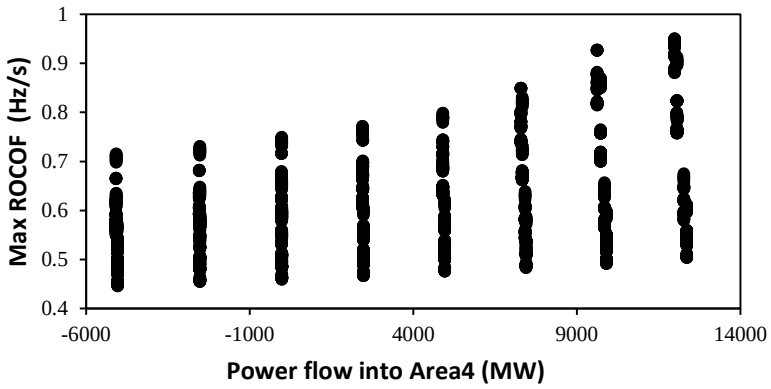

Fig. 3.8. Power flow versus ROCOF for a change in all variables

The complete correlation results for each variable are displayed in Fig. 3.9. Positive values of standardised coefficient value in Fig. 3.9 relate to a positive correlation between the variable and the frequency drop and ROCOF (where positive value implies worse frequency stability). A negative value of standardised coefficient value means that there is a negative correlation between the variable and the frequency drop and ROCOF (where negative equals an improvement in the frequency metric).

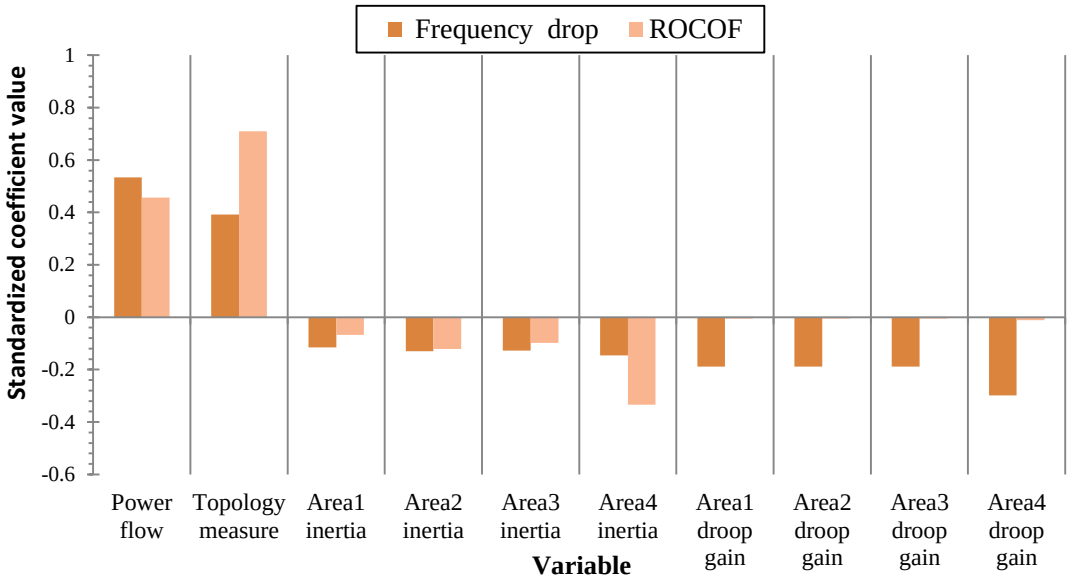

Fig. 3.9. System level factor correlation

The correlation analysis confirms the knowledge that the primary response has limited impact on ROCOF because there is insufficient time for it to respond sufficiently in the immediate moments following the disturbance. The results also display that an increase in Area4 inertia has the strongest effect on reducing ROCOF. A high value of λ (i.e., a less connected system or one with larger electrical distances), is shown to have a strong positive correlation with ROCOF. The results also confirm the theory that changes in power flows into Area4 lead to changes in frequency drop and ROCOF. These specific aspects will be examined in further detail in the remainder of this chapter.

3.4.2 Impact of Topology and Power Flow

The impact topology and power flow have on the frequency stability is investigated in this section. The frequency drop and ROCOF for each topology is analysed under the same load, inertia, and primary response distribution. The values of frequency drop and ROCOF for each topology is provided in Table 3.3. The maximum ROCOF observed in the network is plotted against the maximum frequency drop in Fig. 3.10. Picking this

identical system setup for each topology shows that changing topology has a negligible impact on maximum frequency drop (y-axis of Fig. 3.10) but that there is a significant change in ROCOF of 0.132 Hz/s between the best and worst ROCOF values (x-axis of Fig. 3.10). A closer examination of the cause reveals that topology T6 (the fully radial topology) causes larger rotor angle oscillations that are superimposed onto the frequency drop as displayed in Fig. 3.11. The results display that a larger value of λ (as in the case of T6) causes a greater ROCOF; however, there is negligible impact on the frequency drop as λ increases. It is noted that the impact of these superimposed oscillations is dependent on the ROCOF window measurement.

Table 3.3. ROCOF and frequency drop values for each topology

Network topology	Max ROCOF (Hz/s)	Max frequency drop (Hz)
T1	0.459	0.547
T2	0.459	0.548
T3	0.504	0.548
T4	0.582	0.549
T5	0.581	0.550
T6	0.591	0.556

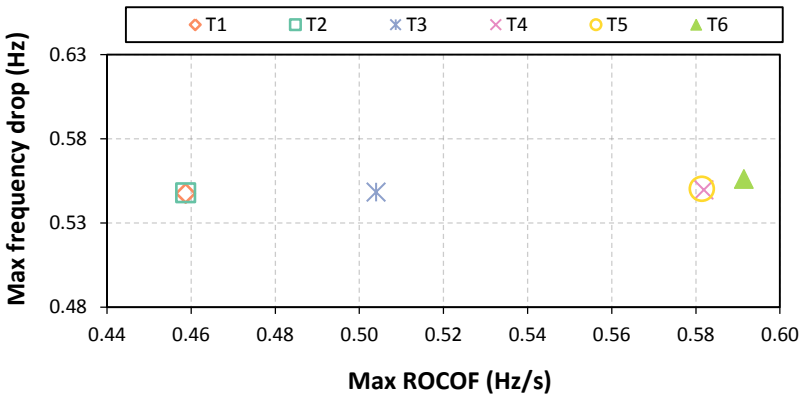

Fig. 3.10. Impact of topologies on ROCOF and frequency drop.

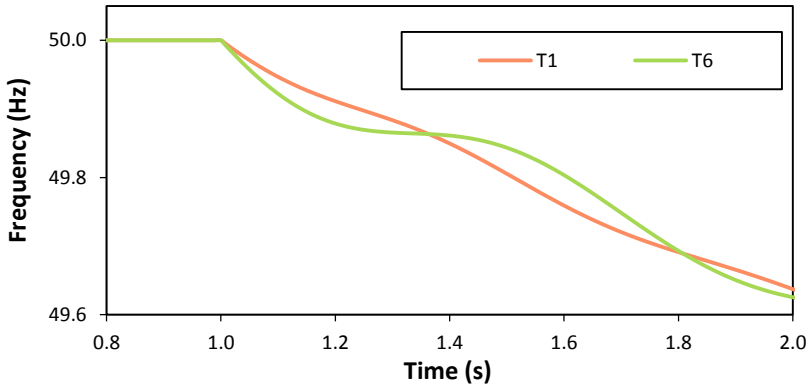

Fig. 3.11. Time series comparison between topology T1 and T6

Using the power flowing into Area4 as an indicator of the system operating point enables analysis of frequency drop and ROCOF as displayed in Fig. 3.12(a) and Fig. 3.12(b). The power flow into Area4 is calculated as described earlier in this chapter. The results display that for topology T1 there is a slight increase in both metrics when the power flow into Area4 increases. Conversely for topology T6, there is a significant increase in both metrics as the power flowing into Area4 increases.

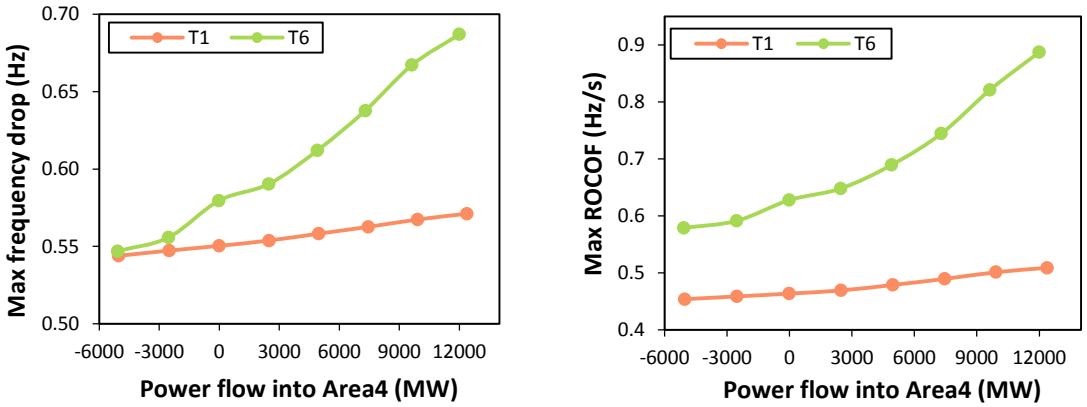

(a) (b)

Fig. 3.12. Comparison between topology T1 and T6. (a) maximum frequency drop, (b) max ROCOF

It was discussed in section 3.1 how a larger voltage angle operating point with respect to Area4 will lead to greater voltage drops at those specific buses following system load disturbances. The reason for this is because a larger voltage angle between two busses or between a SG and a bus leads to greater voltage sensitivity to changes in power flow. This increased sensitivity causes a greater voltage change following the disturbance, which impacts the power transfer capability. In a case where there is a loss of generation, this leads to a reduction in voltage at the SG bus terminal and subsequently reduces the active power transferred. This in turn leads to less power being transferred. Considering topology T1, the post fault voltage drops for different power flow scenarios

are shown in Fig. 3.13(a) where it can be seen that the greater the power flow into Area4, the higher the voltage drop following the sudden generator disconnection. Furthermore, Fig. 3.13(b) displays the voltage drops plotted against the pre-disturbance voltage angles with reference to Area4. It can be seen that a greater pre-disturbance voltage angle leads to greater voltage drops, indicating that the power transferred for a given change in angle during the updated power flow solution will be reduced.

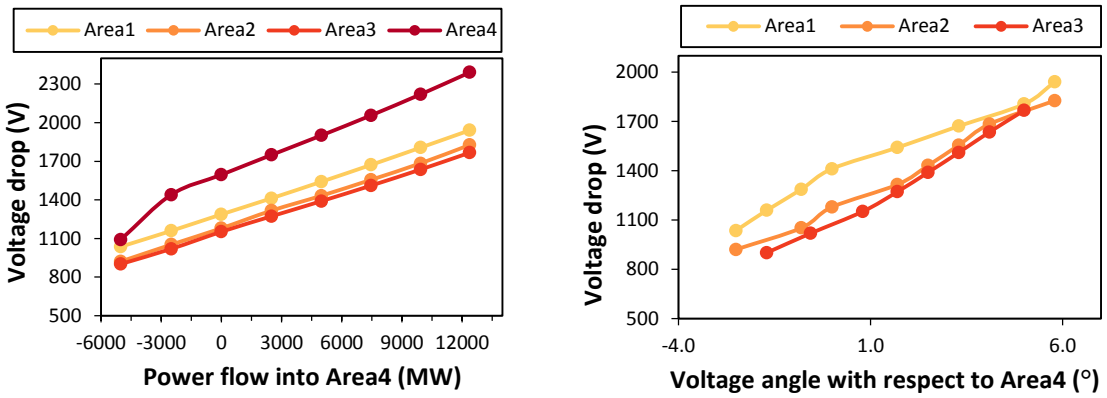

(a) (b)

Fig. 3.13. Voltage drop analysis. (a) voltage drop for a pre disturbance power flow into Area4, (b) voltage drop vs pre fault voltage angle with respect to Area4

A time domain comparison between load distributions L7 and L8 using topology T1 is shown in Fig. 3.14(a), confirming the resultant increase in frequency drop. The frequency drop is further exacerbated when loading scenario L7 is combined with topology T6 as displayed in Fig. 3.14(b). This is due to even greater voltage angles between areas as this highly radial topology (with high λ) increases the impedance, and therefore the initial voltage angle differences, between areas.

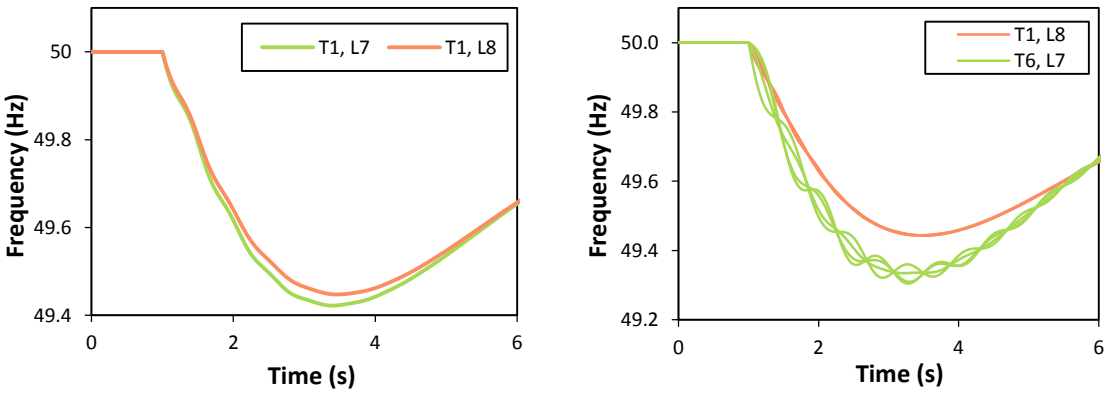

(a) (b)

Fig. 3.14. Time series comparisons. (a) time series comparison for T1 with loading L7 and L8, (b) time series comparison for T1, L8 and T6, L7

3.4.3 Impact of Inertia and Primary Response Distribution

The impact of inertia reduction in a single specific area (without reducing it in other areas) is displayed in Fig. 3.15(a) and Fig. 3.15(b). This is equivalent to decommissioning or temporarily disconnecting SGs from different areas of the network. The total system inertia before a reduction in a specific area is 120 GVA.s and the primary response remains unchanged in each area. The system inertia is reduced by adjusting the inertia time constant value of a SG. This leaves the primary response quantity unaffected because it depends on the rating of the SG not the inertia time constant. The analysis uses topology T1 and loading L1 to create the base case conditions.

Reducing the same amount of inertia in any area causes the same increase in frequency drop as shown in Fig. 3.15(a). Note that the y-axis here is scaled to be comparable to other plots included in this chapter on frequency drop. It is acknowledged that the lines are essentially indistinguishable between different areas. In contrast, with respect to ROCOF, a reduction of inertia in Area4 results in a much greater change occurring. This is because the SG in Area4 will experience the greatest torque imbalance due to it being electrically closest to the disturbance. Changes in inertia will therefore have a greater relative impact with respect to the resultant SG acceleration. This set of results highlights that fast acting response analogous to an inertial response should be incorporated into areas that experience a reduction in inertia. This is also applicable for areas that could be susceptible to large disturbances (e.g. areas with large interconnector in-feeds or large SG in-feeds) while also having sensitive ROCOF relays operating.

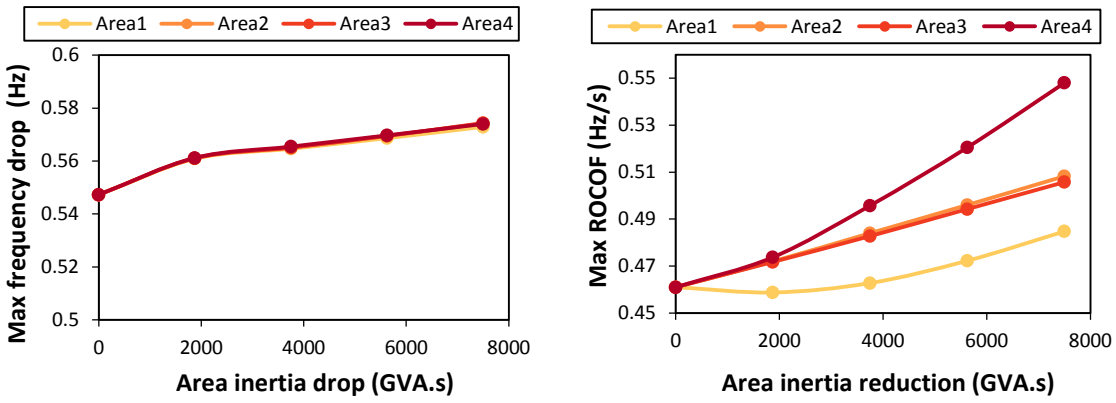

(a) (b)

Fig. 3.15. Inertia reduction analysis. (a) frequency drop for an inertia reduction in a specific area (N.B. lines are coincident as the y-axis is scaled to be comparable to other frequency drop plots), (b) ROCOF for an inertia reduction in a specific area

Simulation cases where the droop gain is increased in different areas one-at-a-time are analysed in this subsection using topology T1 and loading L1 similar to the previous results presented. The increase of the droop gain in Area4 is shown to be more effective at reducing the nadir over cases where the same droop gain increase is applied to SGs in the non-disturbance area as displayed in Fig. 3.16(a). The droop gain increase does not reduce the severity of the initial maximum ROCOF seen in the system when the value is adjusted in any area as displayed in Fig. 3.16(b). This is due to the fact that the most severe ROCOF occurs immediately following the disturbance before the primary response has had time to detect and act. These results highlight that the primary response should be made more responsive (i.e. higher gain) in areas susceptible to large disturbances or in areas that have a high percentage of under frequency disconnection relays.

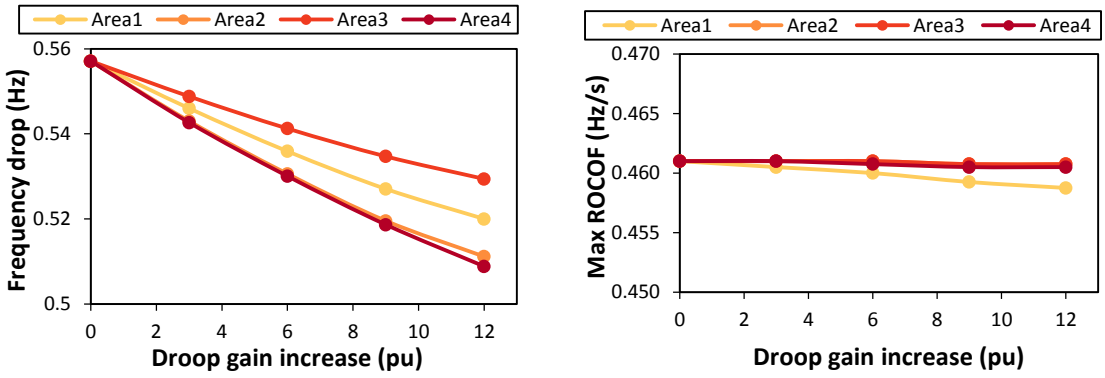

(a) (b)

Fig. 3.16. Droop gain increase analysis. (a) frequency drop for a droop gain increase in a specific area, (b) ROCOF for a droop gain increase in a specific area (N.B. some lines are coincident as the y-axis is scaled to be comparable to other plots ROCOF plots).

3.4.4 Review of Factor Influence

A general summary displaying the influence that an increase in a factor has on the frequency metrics is presented in Table 3.4. An increase in a singular factor may only cause a negligible or slight increase in a certain metric. However, when there is an increase in multiple factors conjointly, such as the topology and power flow, the combination leads to a greater deterioration in both metrics.

Table 3.4 Summary of Factor Influence on frequency Metrics

Factor (increase)	Frequency drop	ROCOF
Topology (λ)	Negligible impact	Strong deterioration
Power flow (into disturbance area)	Slight deterioration	Slight deterioration
Topology and Power flow	Strong deterioration	Strong deterioration
Inertia reduction	Slight deterioration	Strong deterioration
Droop gain increase	Improvement	Negligible impact

3.5 Summary

This chapter has explored frequency stability in greater depth with relation to the mechanisms and factors that govern the frequency drop and ROCOF in a power system. It has revealed how different network factors affect the time evolution of the frequency response and how specific parameters impact different frequency metrics. Network topology, described through the new metric λ that combines connectivity and impedance, has been shown to influence the ROCOF. Frequency stability is further influenced by the power flow around the system in relation to the area where the disturbance occurs. Moreover, the topology and power flow influence the operating points around the system which in turn determines the post fault torque imbalances (load pick up) for each SG. It has been shown that the power flow into the disturbance area can be used as an elementary indicator of subsequent frequency performance. The greater the power flow into the area of disturbance, the greater the frequency drop.

The location of the inertia reduction or the droop gain increase has also been shown to have a strong impact on the ROCOF and the frequency drop respectively. This work has shown the location-specific nature of these aspects and highlights that consideration should be given when deciding where to change these network factors.

Overall the contribution of research in this chapter highlights that the frequency drop and ROCOF are influenced separately. It also displays that the factors governing them should be taken into consideration when allocating frequency response resources. This chapter of research completes objective 2.

The implications highlighted in this research build the foundations for future VSC frequency response schemes and how they can be used to target a specific metric. The use of inertia style control to reduce ROCOF or droop style to reduce frequency drop may be specifically required, depending on the location that they are incorporated into the network. Analysis provided later in Chapter 7 will incorporate different types of VSC frequency control schemes to determine the benefits they provide under different

system conditions. The network factor analysis from this chapter will be used to create different scenarios where the VSC frequency response schemes can be evaluated.

4 MMC-HVDC Technology and Its Intrinsically Stored Energy

For early HVDC systems such as interconnectors, traditional two-level VSC technology was suitable but this technology has a number of shortcomings for high voltage and power situations.. VSC two-level shortcomings for high power and high voltage situations can be summarised as: a) high switching power losses, b) limited voltage blocking capability, and c) high stresses on the semiconductors caused by high rate of change of current (di/dt) due to the switching occurring between the positive and negative rails of the DC link [145]. To address these shortcomings when using VSC power electronics in HVDC situations, the modular multilevel converter (MMC) becomes applicable. The use of MMC technology overcomes the shortcomings through its construction that comprises the use of multiple two-level converters that are termed submodules (SMs) and are combined together. Advances in semiconductor technology combined with the use of the MMC has increased the power rating capability of the converters as highlighted in the Ultranet project in Germany that uses MMC technology and has a rating of 2 GW at 380 kV DC [146].

Due to the construction and characteristics of MMC technology, there may be additional features that could be added to the control system that enable the MMC to provide network support for frequency response or power oscillation damping. The services may be provided by transferring the energy from the connected energy source or by using the naturally stored electrostatic energy within the submodules. The most commonly reported methods for achieving this in the literature were found to be droop control techniques that transfer the energy from the attached energy source. The MMC has a greater quantity of stored electrostatic energy than the 2 level PWM topology converter. As will be described in this chapter, each submodule has stored electrostatic energy that has the potential to be utilised for ancillary network services. The utilisation of the intrinsic electrostatic energy may be able to provide support and damping if power can be injected into the network quickly and without disturbing the additional energy source connected. The advantages of intrinsic energy response over transferring the energy from the attached energy source is the reduced time it would take to provide the response and the reduced impact on the attached network.

This chapter will firstly provide details about the construction of an MMC. The simulation models and control principles are then presented. In addition to the standard

MMC control, the two most common types of supplementary frequency control loops are presented. Finally, this chapter will use the construction of the MMC to investigate the use of the naturally (intrinsically) stored energy that is present in the submodules. This analysis will apply the energy for power system ancillary services in the form of frequency containment and power oscillation damping (POD). The aim of this chapter is to present the DC models that will be used throughout this thesis and to determine the potential impact that the intrinsic energy has on ancillary services. The main contribution from this chapter is the quantification and evaluation of MMC intrinsic energy for power system ancillary services. This analysis determines the effectiveness of the intrinsic energy for support schemes and shapes the direction of the future frequency control design.

4.1 MMC Design and Operation

Within this section, the physical construction of the MMC is discussed and the relevant simulation models are presented. To accompany the MMC model, the standard cascaded vector control that is required to operate the converter, is presented. In addition to the standard models and operational control, supplementary frequency control loops that enable the MMC to provide frequency response are also introduced.

4.1.1 MMC Physical Design

A point-to-point MMC-HVDC system comprises of two converter stations where one station is configured as the rectifier and the other is set as the inverter. There is the option to reverse the direction of the power flow when using such a system. An MMC station uses VSC technology and is built up using submodules (SMs) in a modular construction allowing easy scalability [147]. Each half bridge SM is a two-level VSC converter and contains two IGBTs and a single parallel capacitor. For safety, each SM contains a bypass switch to remove it from the circuit following a component fault [148]. Each phase of an MMC is made up of one leg which consists of two arms as depicted in Fig. 4.1. The resistance per arm is given by R_{arm}. An inductor L_{arm} is connected in each arm to supress circulating currents, reduce switching ripples, and limit fault current [149]. This MMC construction supplies the three phase output given by $I_{a,b,c}$ and the SMs are charged using the DC link voltage V_{DC} where I_{DC} is the DC current that flows through the converter legs. The number of SMs per arm is determined by the required levels in the output voltage and the harmonic requirements. For HVDC projects the number of SMs per arm is usually in the hundreds to reduce the switching

losses and to create an output voltage that is closer to a sinusoidal waveform that does not require excessive filtering.

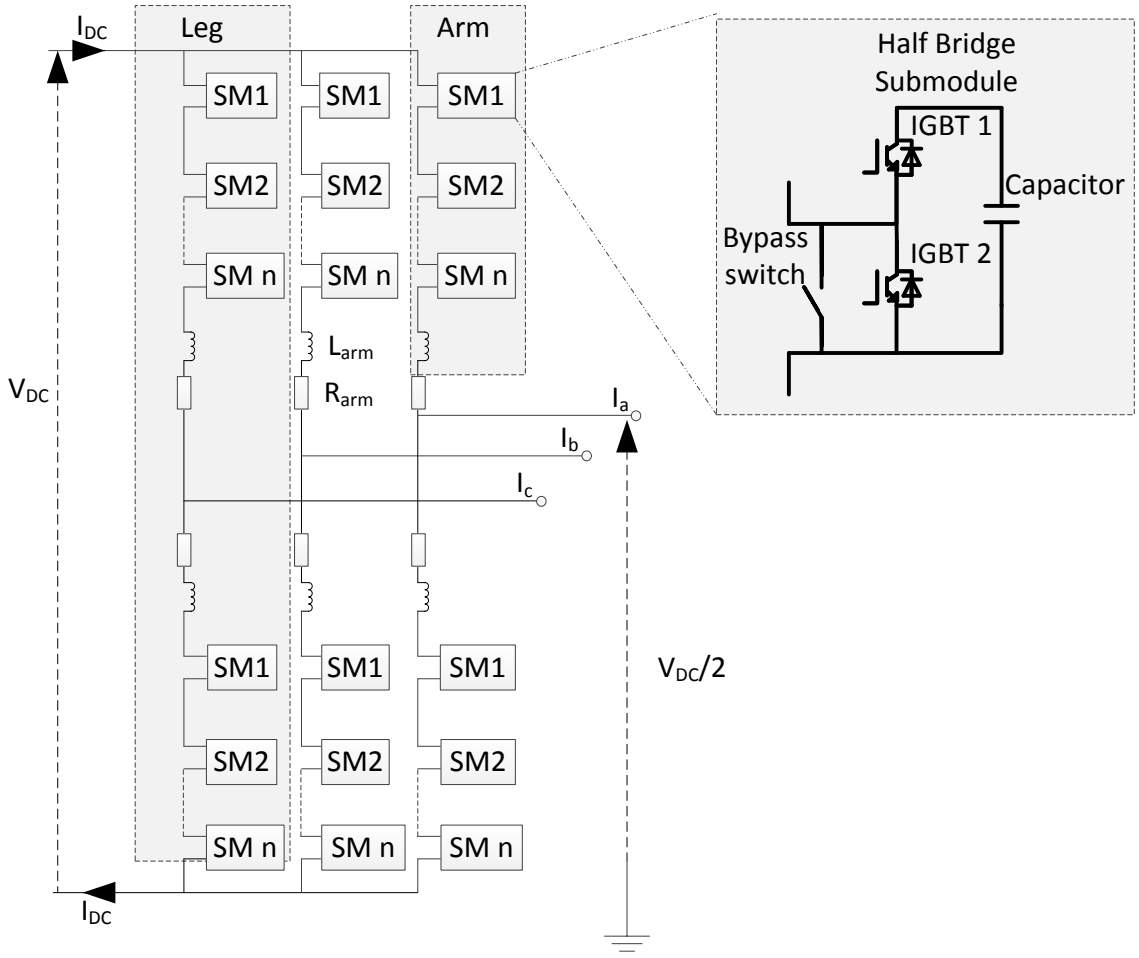

Fig. 4.1. Structure of an MMC and a half bridge submodule

The voltage across each SM depends on which state it is being operated in. A SM capacitor may be charging, discharging, or bypassed, depending on the switching arrangement of the IGBTs and the direction of current flow in the arm. If arm current is positive and IGBT1 and IGBT2 are Off, then the SM will charge as displayed in Fig. 4.2(a). The red dashed line represents the current flow through the SM and the direction is given by the arrow indication. If arm current is negative and IGBT 1 is On and IGBT 2 is Off then the SM will discharge as shown by Fig. 4.2(b). The SM will be bypassed if arm current is positive and IGBT 1 is Off and IGBT 2 is ON as in Fig. 4.2(c) or if arm current is negative and IGBT 1 OFF and IGBT 2 OFF. A comprehensive review of operation is provided in [145] and discusses all SM operating states.

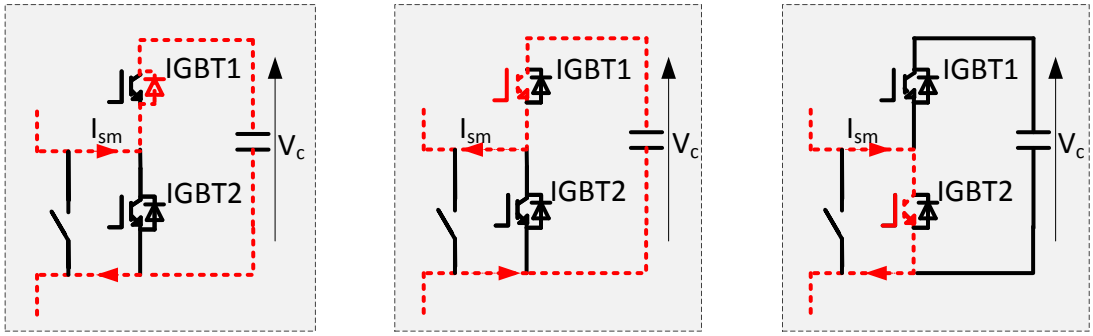

(a) (b) (c)

Fig. 4.2. Basic submodule conduction states. (a) charging, (b) discharging, (c) bypassed

The DC voltage at the inverter end (V_{DC}) should ideally equal the sum of voltages across all SMs that have their capacitor as given by (4.1) where V_{sm}^{on} is the voltage produced by the SM [145]. The output voltage is given by the upper arm voltage subtracted from the upper arm voltage rail and should also equal the lower rail voltage with the lower arm voltage added to it. Each arm voltage is determined by the sum of voltages of SMs that are turned on (discharging) (V_{sm}^{on}) in that specific arm, as given by equation (4.2) where l and u denotes the lower and upper arms, $\mathrm{n_{on}}$ is the number of SMs turned on and V_c is the average voltage across the sub module capacitor.

$$V_{DC} = \sum V_{sm}^{on} \tag{4.1}$$

$$\mathrm{V}_{l,u} = \mathrm{n}_{on\ l,u}\, V_{\mathrm{c}} \tag{4.2}$$

These ideal cases may not always be met, due to the sub-modules switching in and out for example, the arm inductances 'absorb' any difference in voltage. There are a number of models that have been designed to simulate the operation of an MMC and a detailed description of all seven types is provided in [150]. The models range from the Type-1 that is a full physics model through to the Type-7 that is a load flow model. In this research the average value model (Type-5) that models the AC and DC sides as controlled current and voltage sources is used. This model allows different control strategies to be implemented and most importantly it allows various frequency control schemes to be implemented and evaluated without the need for large amounts of computational processing power. Full detail is provided in [150-152].

4.1.1.1 AC Side Model

The AC side output voltage (V_a) for a single phase comprises of the upper and lower arm voltage components that are given by (4.3)-(4.4). The upper and lower arm currents given by (4.5)-(4.6) are made up of three components. The DC current (I_{DC}), which is shared equally between the three legs, the AC phase current (I_a) generated by the phase voltages, and the circulating currents (I_{cc}) caused by unequal voltages in each arm that occurs due to the switching. In a practical system I_{cc} is regulated through the use of a circulating current controller that reduces the arm current distortion. In the average value model, the interior dynamics of the model are not considered which eliminates the need to model the circulating current component (I_{cc}): an alternative way to view this is that the average value model assumes very effective circulating current control has been implemented which effectively reduces I_{cc} to zero.

$$V_a = \frac{V_{DC}}{2} - V_u - L_{arm}\frac{dI_u}{dt} - R_{arm}I_u \tag{4.3}$$

$$V_a = -\frac{V_{DC}}{2} + V_l - L_{arm}\frac{dI_l}{dt} - R_{arm}I_l \tag{4.4}$$

$$I_u = \frac{I_{DC}}{3} + \frac{I_a}{2} + I_{cc} \tag{4.5}$$

$$I_l = \frac{I_{DC}}{3} - \frac{I_a}{2} + I_{cc} \tag{4.6}$$

By substituting the arm currents given in (4.5) and (4.6) into the arm voltages given in (4.3) and (4.4), the converter voltage for phase ***a*** can be given by (4.7). The internal voltage of the converter (e_a) is given by (4.8). Similar equations can be written for phase b and c.

$$V_a = e_a - \frac{L_{arm}}{2}\frac{dI_a}{dt} - \frac{R_{arm}}{2}I_a \tag{4.7}$$

$$e_a = \frac{V_l - V_u}{2} \tag{4.8}$$

4.1.1.2 DC Side Model

The DC side components can be derived by starting with the power balance equation between the AC and DC sides given by (4.9) [152], where P_{AC} and P_{DC} are the AC and DC side powers and P_{loss} is the DC side converter losses. The AC side power P_{AC} can be substituted for the sum of the phase voltages and currents and the DC side can be represented by the DC side quantities as (4.10). The modulation index given by (4.11) can be used to determine the DC side current (I_{DC}) as (4.12) where I_{loss} is determined from the converter resistance [152].

$$P_{AC} = P_{DC} + P_{loss} \tag{4.9}$$

$$\sum_{j=a,b,c} V_j I_j = V_{DC} I_{DC} + P_{loss} \tag{4.10}$$

$$m = 2V_{AC}/V_{DC} \tag{4.11}$$

$$I_{DC} = \left(\frac{1}{2} \sum_{j=a,b,c} m_j I_j\right) - I_{loss} \tag{4.12}$$

4.1.2 MMC Control Structure

An advantage of VSC technology over LCC is the ability to control real and reactive power independently. In an MMC HVDC system, a terminal typically acts to control active power (P) or DC voltage (V_{DC}) and reactive power (Q) or AC voltage (V_{AC}). The MMC is controlled using a cascaded control structure that has been widely used for VSCs as illustrated in the cascaded control structure overview in Fig. 4.3. The MMC is a variant of a VSC because an MMC uses voltage controlled switching devices, therefore requiring a similar control structure. Similar to standard VSC control, the MMC control structure can be broken down into Dispatch or station control, High level, which comprises outer and inner structures, and Low Level control [150]. The Low Level control of an MMC differs from two level VSC control as highlighted later.

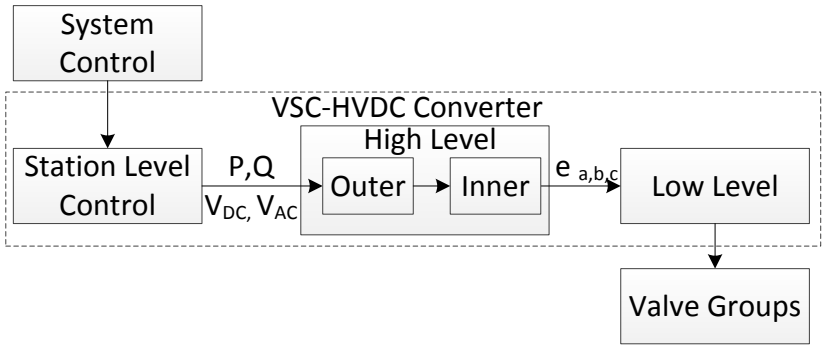

Fig. 4.3. General VSC cascaded control structure overview

An overview of the High Level and Low Level control structure used for a VSC is displayed in Fig. 4.4 to highlight the basic control operation when a vector control scheme is used. It can be seen that the active and reactive power components are controlled individually using a direct-quadrature (dq) reference frame. System measurements and converter angle coupling for use in the vector control (dq control) method is achieved through a phase locked loop (PLL), and by using Clarke and Park transforms. The Clarke and Park transforms enable the three phase sinusoidal measurements to be converted to DC quantities using the reference provided from the PLL (θ). The parameters of the PLL determine how fast it tracks the system. The dq control receives the active and reactive power current control signals $I^*_{d,q}$ and the measured values of $I_{d,q}$ and $V_{d,q}$. These signals are used to produce the phase voltage reference signals $e_{a,b,c}$ for the Low Level control. The operation of the different control levels is expanded below.

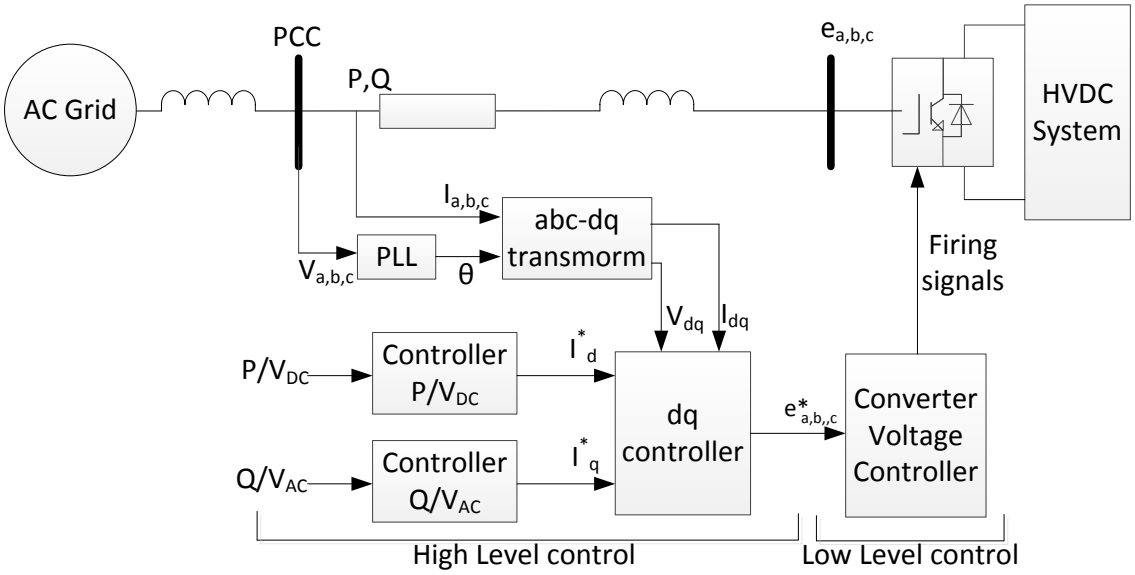

Fig. 4.4. VSC control structure overview

Dispatch Level control is used to configure and adjust operating set points and includes reference signals for active power P^{ref}, reactive power Q^{ref}, AC voltage V_{AC}^{ref} and the DC voltage V_{DC}^{ref}. Dispatch control could also be responsible for altering settings within the control structure such as limits or permissible rates of change if required. For instances of islanded operation, the converter may also be configured to control the connected AC system frequency and AC voltage.

The High Level control can be split into the *outer* and *inner* control. Outer control receives the references and grid measured variable quantities which it responds to without allowing any sudden changes to be applied to the converter. The active and reactive power components are controlled in the outer loop based on operating reference signals. The active power of the converter may be controlled using active power control as displayed in Fig. 4.5(a) or using DC voltage control in Fig. 4.5(b). The outer control loop consists of a proportional-integral (PI) function and uses the gain values K_{p1} and K_{i1}. A current limiter function is also incorporated to limit the maximum current reference and to limit the change in current reference signal. The maximum and minimum inner current reference values are limited by I_d^{max} and I_d^{min} and the ramp rate is limited by I_d^{rr}. This function will be discussed later in this section. The reactive power is controlled in the outer loop similarly using reactive power control or AC voltage control.

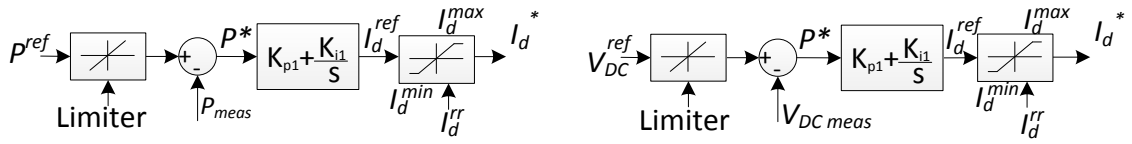

(a) (b)

Fig. 4.5. Outer control active power control. (a) active power control, (b) DC voltage control

The reference signal I_d^* is input into the inner current control loop. Here, different control techniques including direct, vector, and power synchronisation exist but vector current control (commonly known as dq) appears most in the literature and will be used as the basis for the control in this research. The inner current control loop uses a PI function where K_{p2} and K_{i2} are the gain parameters. A simplified representation of the inner current control loop where no cross coupling terms are included is displayed in Fig. 4.6 [153, 154] and the MMC is considered as an ideal unity transfer function where

the output is equal to the input. The converter arm dynamics are given by the first order transfer function that includes converter resistance (R) and inductance (L).

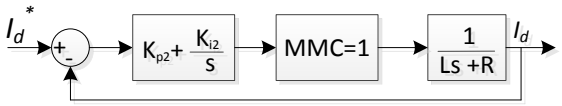

Fig. 4.6. Simplified d-axis inner current control loop

Low Level control of an MMC is different compared to the standard two-level VSC. In an MMC, Low Level control is not only concerned with modulation, but also with capacitor voltage balancing, and circulating current suppression. Different switching algorithms such as pulse width modulation, space vector, or nearest level control may be used in the low level control depending on the operational characteristics required from the converter [150]. An overview of low level control is provided in [149]. Low Level control is not modelled in this work as it is assumed to be ideal within the Type-5 average value model, but the low level control operation can be represented by a first order lag.

A simplified implementation of the complete control structure to control active power adopted from [155] is displayed in Fig. 4.7 with time variant functions transformed into the Laplace domain (hence the use of the s variable). A similar control structure would be required to control the reactive power or AC voltage depending on converter operation.

To ensure speed of operation does not overlap between the inner and outer loops, the proportional and integral parameters should be set accordingly and the tuning of these parameters is discussed in [156]. In Fig. 4.7 the Low Level control operation is displayed as a first order time delay function using the modulation time constant τ_{mod} as the detailed low level control is out of scope for this research. To complete the control structure, a simplified representative network model function given by $I = YV$ is included and the measurement delays are represented with a time delay function and a first order function using the parameters θs and τ_2 respectively. The measured d-axis voltage V_{dmeas} and the q-axis mutual inductance term ωL are incorporated to remove the cross coupling terms. The parameters used for the MMC stations and network components are provided in Appendix Section D.1.

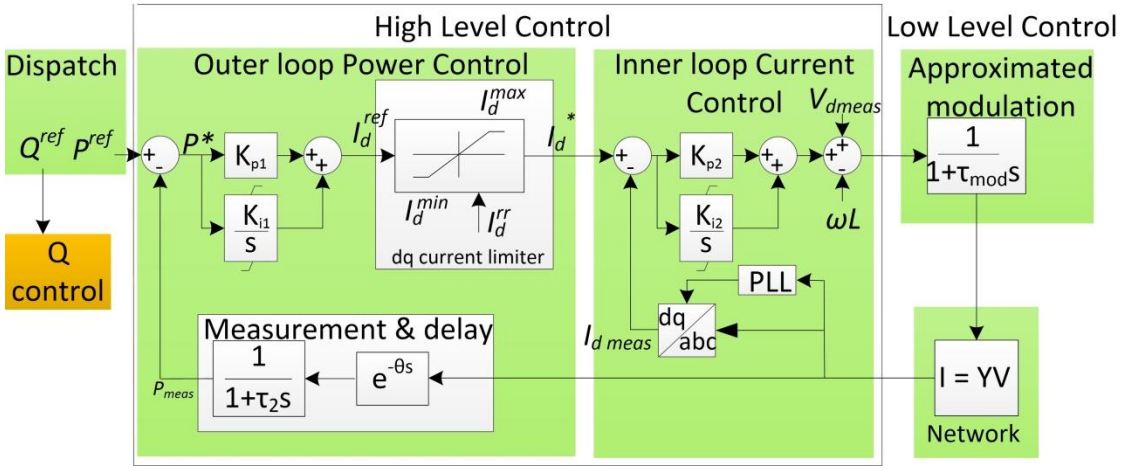

Fig. 4.7. Active power MMC simplified control structure

It is also important to note that the dq current limiter within the outer active power control loop limits how the inner current control signal (I_d^*) changes when the active power reference signal is changed or the supplementary frequency control is operating. The active power input signals are used to construct the inner current reference signal (I_d^{ref}), and it is this signal that the ramp rate limiter is applied to. From a device perspective, the limiter function prevents extreme thermal events occurring from large sudden changes in current, and from a system perspective it prevents large sudden power injections into the network from occurring. The ramp rate limiter is given in the units of active power (W/s or GW/s) but is converted into the units of A/s as it is applied to the current reference signal I_d^{ref}. For the remainder of this thesis, the ramp rate limiter will be described using GW/s as this is considered more meaningful from a system perspective, but the reader should note that its implementation within the control structure is in A/s. The rate of change of I_d^* needs to be limited as given by (4.13) where I_d^{rr} is the ramp rate limit. If I_d^{ref} exceeds the allowed ramp rate for that given simulation time step (Δt), then the output is determined as the maximum allowed difference for one time step added to the previous output value given by $(i-1)$. The ramp rate limiters that are incorporated into MMCs at the moment are estimated to be operating at around 1 GW/s [153] but with the advances in technology, this could be higher and up to 2 GW/s and possibly higher in the future providing there are no detrimental impacts on the system. In addition to the ramp rate limit, there are maximum and minimum value limits that prevent the current reference signal (I_d^*) from exceeding operating limits given by I_d^{max} and I_d^{min}. Any delays present in the control architecture due to signal processing or communication are ignored in this research as they are consistent and do not alter for the range of operation changes proposed.

$$I_d^* = \begin{cases} I_d^{ref}, & \dfrac{dI_d^{ref}}{dt} < (I_d^{rr} \times \Delta t) \\ (I_d^{rr} \times \Delta t) + I_d^*(i-1), & \dfrac{dI_d^{ref}}{dt} \geq (I_d^{rr} \times \Delta t) \end{cases} \tag{4.13}$$

4.1.3 MMC FFR Control Structure

In order for the converter to be able to provide frequency containment response, this functionality must be incorporated in the form of an supplementary frequency control loop. The output from the supplementary control loop is added into the MMC's outer control loop as a change in the active power reference (ΔP). The two most commonly reported forms are the proportional controller (droop) and the derivative control. This section will present the standard controller models for proportional and derivative control that will be used in this thesis. The term fast frequency response (FFR) in this thesis refers to the frequency response that is faster than traditional SG primary response. The RMS models in this thesis assume a balanced three phase network with PLL configured to track the positive sequence voltage.

4.1.3.1 Proportional Control

The supplementary frequency control loop output is added to the summation block in the outer control loop in the high level control structure shown in Fig. 4.8. This type of frequency control loop responds in a similar manner to a traditional proportional controller that is implemented in a SG to provide primary response. The measured frequency (f_{meas}) obtained through a PLL is compared to the system reference frequency (f^{ref}) to produce the frequency error signal Δf. The error signal is then subject to a dead band function and a gain function given by K_{p3}.

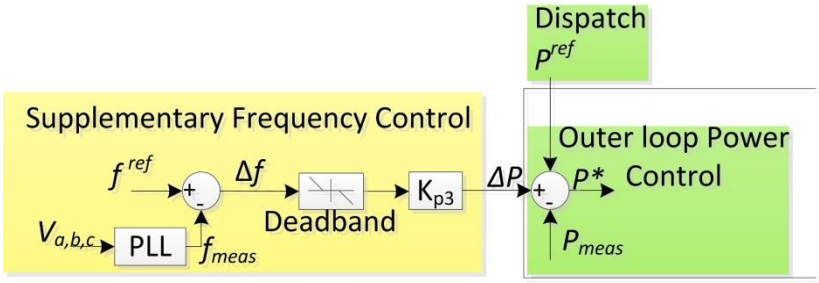

Fig. 4.8. Supplementary proportional frequency control loop for an MMC

The system frequency is measured at the point of common coupling using a synchronous reference frame phase locked loop (SRF-PLL) which is implemented as Fig. 4.9. This PLL has a lower bandwidth than the inner control measurement PLL and is expected to have a bandwidth in the range of 50-100 Hz. The per unit values for the PLL are set as K_p^{PLL} = 12.56 pu and K_i^{PLL} = 39.47 pu and are determined from [157] based on a fixed bandwidth and damping factor.

The value of K_{p3} is determined from the required droop characteristic as $^1/_R$. Both the dead band and gain in the proportional controller can be varied to achieve the desired response. The operation of the dead band will be discussed and explored in Chapter 5.

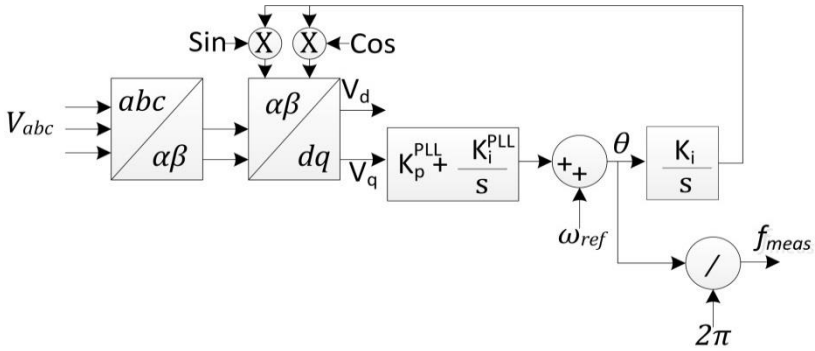

Fig. 4.9. Phase locked loop implementation

4.1.3.2 Derivative Control

Derivative control has usually been implemented to emulate an inertial response. As discussed in the literature review, the derivative controller may be implemented by taking the direct derivative (df/dt) of the frequency or it may be implemented as a filter function. The inherent difficulties implementing a derivative scheme are outlined in [71] where measurement noise and the selection of suitable PLL parameters are highlighted as potential issues.

Instead of emulating an inertial response, this research proposes a method based on a predetermined maximum rate of change of frequency that is analogous to the operation of droop control. As a recap, droop response is designed to fully operate the SG by a given deviation in frequency, usually 3-5%. Inertia emulation strategies may be operated to provide a response based on a virtual inertia constant as in [119]. This methodology could limit the speed and quantity of the response following a disturbance. To overcome this, the response in this research is scaled based on the maximum rate of change of the frequency. If the maximum rate of change is measured then this causes a maximum output from the converter. First, to ensure repeatability, the derivative

component in this research is determined using a fixed time value instead of a derivative function block that operates every simulation time step. The reason for this is that using a basic derivative function block, where the derivative is taken every time step of the simulation, may produce different behaviours depending on the simulation time step size. Due to this, replicating derivative control operation is difficult because researchers may be using slightly different simulation time steps depending on the level of detail required in their studies. Also depending on simulation package or user settings, it may be unrealistic for implementation or realisation into real world control software packages unless there are fixed parameters used.

The derivative implementation in this research is given by Fig. 4.10. There is a dead band that is used to operate the control as given by (4.14) where f_d is the dead band setting and K_d is the gain parameter.

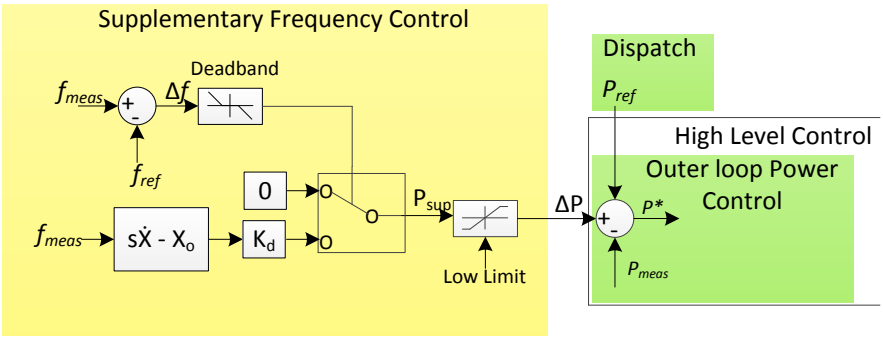

Fig. 4.10 Derivative control structure overview

$$\Delta P = \begin{cases} 0, & |\Delta f| < f_d \\ (df/dt)K_d, & |\Delta f| \geq f_d \end{cases} \tag{4.14}$$

The value of K_d is dependent on the required output action of the controller when subjected to a given rate of change. The crucial rate of change value given by σ can be used in conjunction with the desired frequency control output (ΔP) to determine the value of K_d as given by (4.15). For example, the crucial ROCOF value for σ could be 0.5 Hz/s and if this was detected, the operator may want the converter output to be fully operating. This is analogous to the droop value that is determined using a certain percentage change in frequency causing a 100% change in the output.

$$K_d = \frac{\Delta P}{\sigma} \tag{4.15}$$

The time frame that the derivative is taken over in the controller requires careful consideration because a short time step would capture more noise that is present in the measured signal. However a large step would lead to a slower response from converter. The value of σ (always given as Hz/s) requires adjusting down to the time frame of the derivative action as given by (4.16) where K_t is the unitless adjustment factor and Δt is the time frame that the derivative is taken over. Using K_t, the controller gain value K_d can be determined by (4.17) to ensure that the converter fully operates by the given ROCOF value σ when the derivative time frame is not taken over a 1 s time period (this scales the derivative output to the required Hz/s unit from Hz/ms). The outer control functions of ramp rate limiter and PI values play an important role in limiting any sudden derivative changes that occur due to noise.

$$K_t = \frac{1}{\Delta t} \tag{4.16}$$

$$K_d = \frac{\Delta P}{\sigma} K_t \tag{4.17}$$

4.2 Calculation of MMC Intrinsically Stored Energy

The previous sections have presented the physical design and control of the MMC along with the proportional and derivative frequency control loops. In the pursuit to provide frequency containment services using an MMC, it is worthwhile evaluating the capability of the intrinsic energy at this point. Going forward this will determine if the use of the intrinsic energy should be considered in the proceeding frequency control schemes.

An MMC-HVDC system has intrinsic energy stored within the SM capacitors and the HVDC cable. Energy extracted from an MMC-HVDC system and used to provide ancillary services would not be an inertial response, as additional sensing and control would be required. However it could potentially be extracted quickly within 2 s and could present an opportunity to enhance AC network support. In an MMC system, the value of stored energy is continually changing depending on the voltage of each SM and how accurately the control systems maintain the nominal voltage. Control systems are required to manage the circulating currents and the charging and discharging of the SMs through balancing controls. A SM is operated to be charging or discharging based on its level of charge. A certain amount of energy is required in order for the MMC system to

provide the required voltage and active power levels to the AC system. The electrical energy stored within a SM of an MMC can be seen as analogous to the kinetic energy of a generators rotating shaft. Total MMC energy is calculated using (4.18), where C_{sm} is SM capacitance and V_{sm} is SM voltage. n_{sm} is the number of SMs per arm and n_{arms} is the number of arms per converter.

$$E_{mmc} = n_{arms}\, n_{\mathrm{sm}} \left(\frac{1}{2}\, C_{sm} {V_{sm}}^2 \right) \tag{4.18}$$

SM capacitor sizing is a trade-off between component physical size, ripple voltage, and cost of adding additional SMs. According to [153], the average stored energy in the converter (E_s) required to produce a ripple voltage of no more than ± 5% is 30-40 kJ/MVA. An estimate of the energy storage required per SM (E_{sm}) can be derived which allows the calculation of capacitor size. Nominal SM voltage (V_{sm}) is required which is given by (4.19). SM energy is calculated using (4.20) where S_{mmc} is the converter rating. Based on the required energy storage value per SM, the SM capacitance (C_{sm}) can be determined by (4.21).

$$V_{sm} = V_{DC}/n_{sm} \tag{4.19}$$

$$E_{sm} = \frac{E_s S_{mmc}}{n_{arms}\, n_{sm}} \tag{4.20}$$

$$C_{sm} = \frac{E_{sm}}{\frac{1}{2}{V_{sm}}^2} \tag{4.21}$$

The DC cable connecting the rectifier and inverter has electrostatic energy stored due to the electric charge. Energy for a single pole (E_{cable}) can be calculated using (4.22) where V_{cable} is the DC voltage of the pole and (l) is the cable length with C_{cable} the capacitance rating per/km for the cable.

$$E_{cable} = \frac{1}{2} l C_{cable}\, {V_{cable}}^2 \tag{4.22}$$

The equations presented in this section will be used in the following sections to investigate how beneficial the stored intrinsic energy could be for frequency containment and POD ancillary services.

4.2.1 Frequency Containment

The quantity of power available for frequency containment support depends on the total available energy, which can be a combination of the SM energy and cable energy, and also on the time over which the energy is released. A longer sustained requirement for energy release leads to a reduced level of power attainable from the system.

4.2.2 Power Oscillation Damping

In order for an MMC to provide power oscillation damping by releasing and absorbing energy, the inverter must operate within pre-defined boundaries and the SM energy must not exceed the limits. A generic comparison between normal SM operation and POD SM operation is displayed in Fig. 4.11. It should be remembered that no modulation of power at the other end of the HVDC system is required; energy is released and absorbed within the MMC itself to enable POD.

In order to determine the amount of energy available for POD, the allowable energy deviation must be calculated. The minimum DC link voltage $\left(V_{DC}^{min}\right)$ required to produce the desired AC output voltage can be determined by rearranging (4.9) and substituting e_a for the required AC output voltage amplitude. Minimum SM voltage (V_{sm}^{min}) is determined using (4.23) where r is the ripple factor of the SM (usually ± 5%). SM energy difference (ΔE_{sm}) is determined by (4.24) and is used to determine total MMC energy available for POD (ΔE_{mmc}) in (4.25).

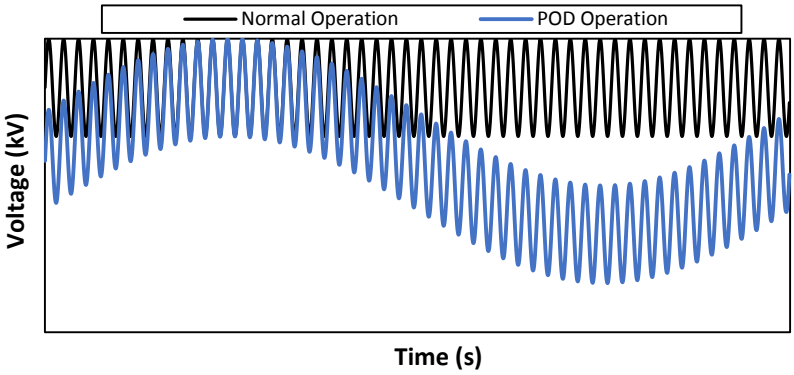

Fig. 4.11. Normal and POD SM operation

$$V_{sm}^{min} = \left(V_{DC}^{min}/n_{sm}\right) r \tag{4.23}$$

$$\Delta E_{sm} = \left(\frac{1}{2} C V_{sm}^{max\,2}\right) - \left(\frac{1}{2} C V_{sm}^{min}\right) \tag{4.24}$$

$$\Delta E_{mmc} = n_{arms}\, n_{sm}\, \Delta E_{sm} \tag{4.25}$$

In order to provide POD, the additional energy is released and absorbed in a sinusoidal manner to counteract typically sinusoidal electromechanical oscillations. The maximum power injected and absorbed ($\Delta\hat{P}$) into the system is given by (4.26) and depends on the amount of available energy from the MMC and also on the period of the modulating signal.

$$\int_0^{\pi} \Delta\hat{P} \sin \omega t \; d(\omega t) = \Delta E_{mmc} \tag{4.26}$$

4.2.3 Enhancement of Power

To enhance the capabilities of an MMC for the purpose of improving power system stability, certain parameters may be adjusted. Obtaining the general solution of (4.26) for $\Delta\hat{P}$ and assuming that the energy would always be injected between 0 and π produces (4.27). Equation (4.27) allows different system parameters to be adjusted to view the affect they have on energy available for POD. The power oscillation frequency in Hz (f_{pod}) is also incorporated. Financial implications may make certain parameter changes impractical in reality.

$$\Delta\hat{P} = \left\{0.5C_{sm} \left[(V_{sm}r)^2 - \left(V_{sm}^{min}r\right)^2\right]\right\} n_{sm}n_{arms}\,\pi f_{pod} \tag{4.27}$$

4.3 Analysis of MMC Intrinsically Stored Energy

In order for an MMC-HVDC system to provide network support to the AC system, there has to be sufficient power for the tendered service. To assess the level of intrinsic energy available within an MMC-HVDC system for network support, frequency response and POD scenarios are investigated. System parameters displayed in Table 4.1 based on the Transbay interconnector project [158] have been used and an estimated SM capacitance value was determined using (4.19)-(4.21).

Table 4.1. System parameters [159]

Parameter	Value
Power	400 MW
DC Voltage	400 kV (± 200kV)
Number of SMs	200 per arm
SM capacitance	5 mF
Number of arms	6
Cable length	85 km
Cable capacitance	0.1908 μF/km
RMS Output Voltage	115 kV

4.3.1 Frequency Containment

This section determines the amount of power an MMC-HVDC system could theoretically and hypothetically provide during a disturbance. This section aims to highlight what impact the *total* intrinsic electrostatic energy could provide the network in terms of power injection. It is noted and fully appreciated that the extraction of all electrostatic energy would not be a practical solution as this would cause further detrimental system impacts. This is purely illustrative. The energy within the HVDC cable and the MMC are considered and combined to produce a total value of energy. Estimating the energy stored within the HVDC cable can be deduced from Table 4.1 and (4.22). Similarly, an estimate of MMC energy can be produced using (4.18). Total cable energy for both poles is 0.644 MJ and total converter energy is 12 MJ, producing a system total of 12.644 MJ.

A *hypothetical* situation is considered in which all of the energy within the converter is released in a uniform manner to provide network support. Power is determined by the speed of energy release, therefore, the longer the energy release the lower the available power as given using dE/dt. The time over which energy is released (Δt) can be determined by dividing the converter energy by the required power output (E/P). E.g. power deliverable for 1 s is 12.644 MW as displayed in Fig. 4.12.

Practical application of the stored energy within the converter to provide frequency support in this situation can be determined using minimum contracted support services tendered by National Grid (the Great Britain transmission system operator). If the converter was contracted for mandatory primary response, the power output must be sustainable for 20 s. An enhanced frequency response (EFR) contract requires a sustainable power output for 9 s [160] (since undertaking this analysis, the frequency

response requirements set by the SO have changed). Table 4.2 displays the level of power that would be provided by the system for both tendered services.

Table 4.2. Tendered service response

Service	Power
Mandatory primary response	0.616 MW
EFR	1.369 MW

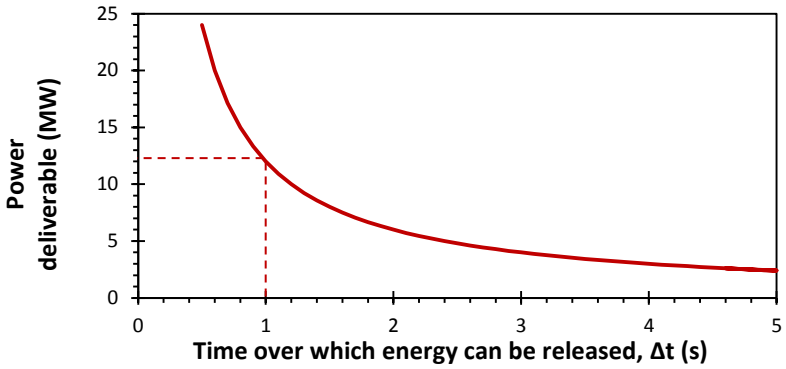

Fig. 4.12. Power deliverable for specific time periods

Under these illustrative assumptions where all of the energy within the converter system is extracted, it can be seen that there is a minimal amount of power available for system support. The extraction of intrinsic electrostatic energy from within MMC converters for the purpose of frequency containment following disturbances is therefore not possible without the addition of *significant additional* energy storage.

4.3.2 Power Oscillation Damping

In this section, the energy available for POD is quantified and applied. The required control architecture is omitted from this research but could be investigated if deemed viable.

4.3.2.1 Power Oscillation Damping Method

The method entails injecting and absorbing power to and from the AC network by dynamically changing SM voltage operating points. By reducing SM voltages, stored energy can be gradually released until the SMs are operating at their minimum accepted voltage level. The minimum acceptable DC voltage level has to be capable of producing the desired output AC voltage. Once SM voltages are at their minimum acceptable level, energy can be absorbed from the AC network by charging SMs back up to their maximum level. This method excludes the use of redundant SMs and does not take into

account SM rotation in the switching sequence. This method would impact on the DC link potentially causing higher current to flow from the rectifier to the inverter and would impact the converters ability for AC fault ride through as nearly all the SM's voltage margin would be used. This would have to be carefully considered against grid-code requirements, and the benefits to be gained.

The quantity of power available for injection and absorption is calculated using parameters in Table 4.1 and equations (4.23)-(4.25). The assumed peak AC output voltage based on an RMS voltage of 115 kV (and assuming a transformer turns ratio of 1:1) is 162 kV. The DC link voltage minimum is 324 kV. A SM ripple voltage of ±5% is also taken into consideration. The difference in energy per SM (ΔE_{sm}) is calculated as 3.8 kJ and the total energy deviation of the MMC is calculated as 4.56 MJ. When this energy is applied to a 1 Hz power oscillation where power is injected over half of the period (0.5 s), maximum power injection is 14.32 MW as given by (4.27). This is the peak of a sinusoidal power injection that could be injected and then absorbed from the AC network. As a percentage of the test scenario converter rating, this equates to 3.58%. The quantity of power injected or absorbed at a specific time is displayed in Fig. 4.13.

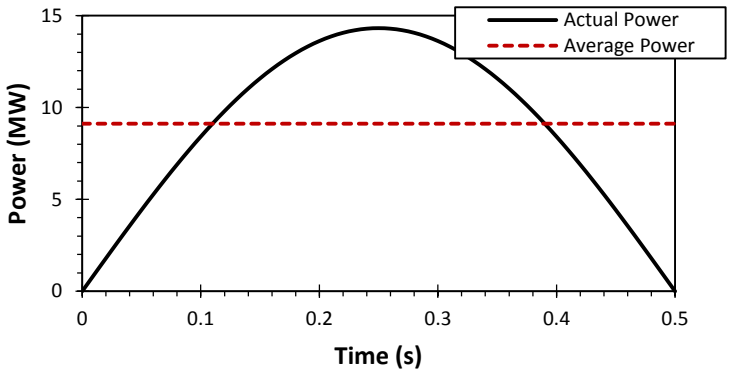

Fig. 4.13. Power injected

4.3.2.2 Power Oscillation Damping Analysis

To ascertain if the available energy from an MMC could improve POD, a number of simulations are undertaken. The test system chosen is a single machine infinite bus (SMIB) system, which allows easier interpretation of network dynamics. The synchronous generator is modelled with constant excitation and does not incorporate any additional control; governor or power system stabiliser. The power from an MMC ($\Delta\hat{P}$) is attached to bus1 of the SMIB test system from Fig. 2.12 using a controllable load. The load is operated to mimic the power system stabilising capabilities of the

MMC and does not absorb or inject power during steady state. The controllable load power injection and absorption is the value of $\Delta\hat{P}$ e.g. the peak sinusoidal value of 14.32 MW. The timing signal offset of $\Delta\hat{P}$ in relation to the power oscillation can be controlled as well as the amplitude.

The aforementioned test system has been used to determine what level of impact the electrostatic energy could provide for power oscillation damping. As the amplitude of $\Delta\hat{P}$ increases, it is expected that system damping would increase as it can absorb and inject higher levels of power to damp the oscillations. Five amplitudes for $\Delta\hat{P}$ were chosen and are based on the rating of system generation. A 1% value for $\Delta\hat{P}$ represents 1% of the installed system generation e.g. a 2 GW installed capacity would give $\Delta\hat{P}$ a value of 20 MW. The angular phase offset of the $\Delta\hat{P}$ in relation to the power oscillation was investigated to view how it influenced the damping factor. Results obtained from analysis where the angular phase offset of $\Delta\hat{P}$ is altered in relation to the power oscillation, determined that to achieve greater levels of damping the angular offset for $\Delta\hat{P}$ should be 90° leading the power oscillation. In this component the damping is calculated empirically from the time series data obtained from the simulations. The average damping difference with respect to the natural system damping and rated power of the system is displayed in Fig. 4.14. Similarly, Fig. 4.15 displays the change in damping with respect to the short circuit level of the system.

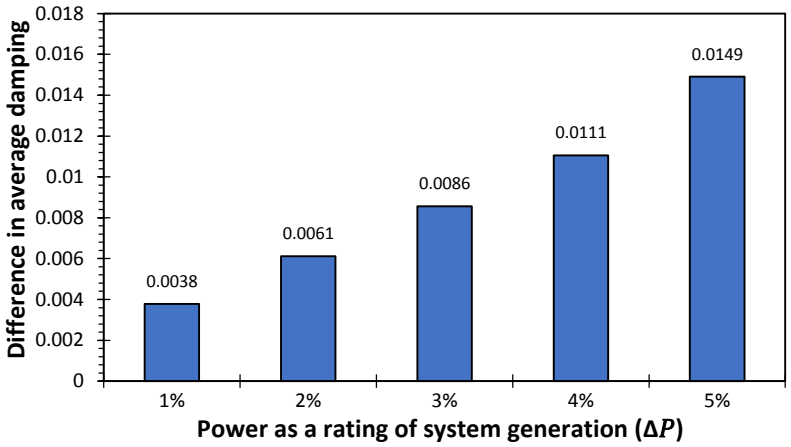

Fig. 4.14. Damping factor versus $\Delta\hat{P}$ as a percentage of system rating

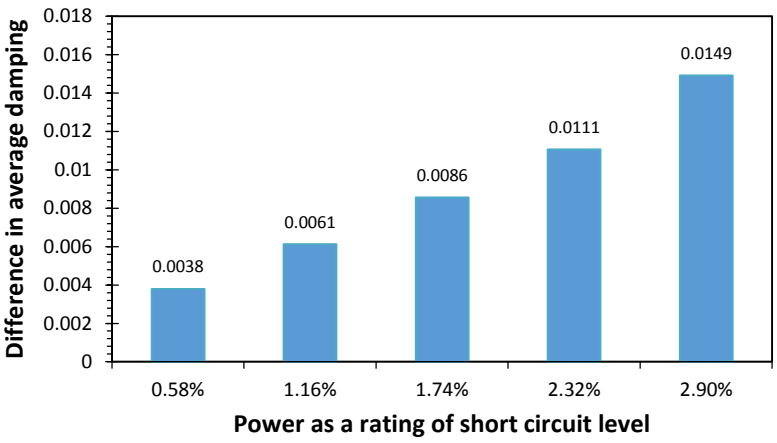

Fig. 4.15. Damping factor versus $\Delta\hat{P}$ as a percentage of short circuit rating

Results in Fig. 4.15 show an approximate linear increase in damping as the amplitude of $\Delta\hat{P}$ increases as a percentage of the system rating. Fig. 4.14 also displays that the damping increase does exist but is marginal. Although there is only a marginal increase displayed in this analysis that represents a single or a small number of aggregated converters, as more are eventually connected into the network, this will increase the impact they can provide for system stability. The impact of a 2% amplitude for $\Delta\hat{P}$ on power oscillation damping for the test system is compared against the natural system damping in Fig. 4.16 and confirms that $\Delta\hat{P}$ has a noticeable effect on damping. The results obtained confirm that the use of the electrostatic energy deviation in an MMC can marginally increase system damping. However, the value of damping increase is dependent on the energy deviation that the MMC can withstand and the number of converters connected to the network providing the POD service.

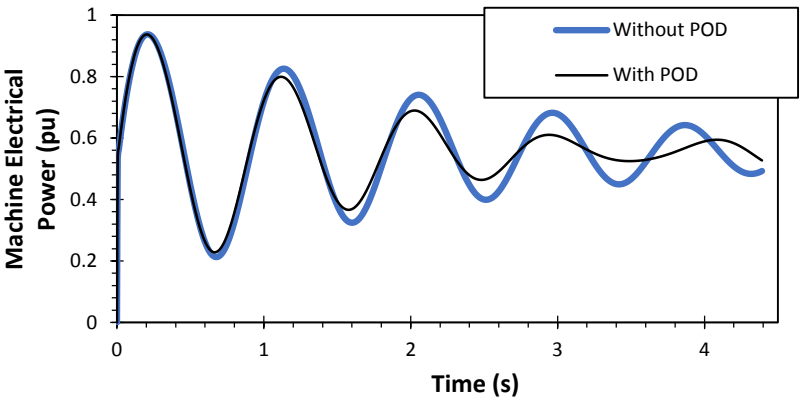

Fig. 4.16. Comparison of natural damping versus controllable load providing 2% of system power

From this simplified analysis it can be seen that the intrinsic energy has the potential to provide ancillary POD services. The damping effect from a single MMC is seen to be small but this could be increased by aggregating a response from multiple converters.

4.4 Summary

This chapter has presented the construction of the MMC and the associated controls required for its operation. The supplementary frequency controls loops for proportional and derivative control types that are incorporated into the cascaded control structure have also been presented.

In addition to the MMC models, the value of the intrinsic stored energy within an MMC has been calculated in order to determine its effectiveness for power system ancillary services of frequency containment and POD. When applied to frequency response situations, it is shown that even if all stored MMC energy was utilised to provide network support, the level of response would be negligible. Furthermore, when converter operating limits and considerations are incorporated, the level of support for frequency response would be greatly reduced. Therefore there is no feasible viability of using the intrinsic MMC energy to provide support in this area.

For POD however, theoretical calculations suggest that from an AC system viewpoint, an MMC could assist with POD in a small way if internal submodule voltage variations are permissible. Using a simple SMIB test system, the use of the electrostatic energy and energy deviation within the MMC has been shown to increase damping. Although the level of damping is relatively small from a single MMC, a coordinated approach using multiple MMCs could increase the level of damping on the system.

The major contribution from this chapter is the evaluation of the capability of the intrinsic energy within the converter, which was set by objective 3 in the research objectives Research presented in this chapter shows that the use of intrinsic energy was negligible and would not be able to provide the minimum quantity of energy required by the system operator. Therefore, the proposed MMC frequency control designs presented in the remaining body of this research will omit any use of intrinsic energy support. The outcomes of this chapter enable a focus to be placed on MMC frequency support schemes that rely on an attached energy source.

5 Fast Frequency Response Using MMC-HVDC Technology

The most common type of VSC supplementary frequency controller reported in Chapter 1 is proportional control, and in the literature it has been proven to be beneficial to improve the frequency. A proportional controller is simpler to incorporate than a derivative controller, possibly making it more favourable but it has several reported drawbacks. The main drawback is the quantity of response provided, which is initially low when the frequency deviation starts. In low inertia systems the frequency excursions are expected to deviate faster and further following severe disturbances. This means frequency control schemes will be required to operate as fast as possible and provide large quantities of energy to stabilise the frequency excursion. In order to improve the responsiveness of proportional control schemes a simple alteration is to increase the value of the gain component (reduce the droop percentage). Although this will improve the speed of the response, the initial response is still low due to the controller output being proportional to the frequency deviation.

This section will build on past research such as in [66, 68] to investigate improvements that can be applied to the supplementary proportional frequency controller of an MMC in order to improve its responsiveness. This type of control has traditionally been presented similarly to the SG governor primary control loops that are restricted from sudden and discontinuous changes. However the MMC is not subject to the same limitations as a SG which allows flexibility in the frequency control implementation. Traditional proportional control schemes provide a limited initial response because the proportionality of frequency to power output starts when the frequency exits the dead band operating range. This reduces the initial power injection which leads to a reduced impact from these control schemes on the initial frequency containment process.

In addition to improving the frequency following large disturbances, fast frequency response from power electronics could lead to unwanted behaviour under small disturbance situations. The phenomena of fast frequency response occurring in a low inertia system will be investigated under small disturbance scenarios. This analysis will investigate the frequency controller response to determine if cycle limit behaviour occurs due to the recovery of the frequency back above frequency control operating limits. Mitigation strategies will be presented that could be used to prevent this phenomenon from occurring and becoming a concern.

The first objective of this chapter is to provide improvements to the proportional frequency control scheme, with a particular focus on the dead band implementation. The second objective of this chapter is to identify detrimental system behaviour that can occur in low inertia systems when using vast quantities of fast frequency response. Additional control elements will be introduced to reduce unwanted fast frequency response issues. This chapter addresses thesis objectives 4 and 5.

5.1 Proportional Controller Improvements

During normal operation the system frequency will inherently deviate within a narrow band as slight changes in generation and demand occur. To prevent excessive operation and adjustment of generation through the primary control schemes, the schemes are typically fitted with a dead band. When the frequency is outside of this dead band, the control schemes start to operate. With a high inertia system, the dead band can be narrow, as typical variations will be small and at present the dead band incorporated into SGs should be no greater than ±0.03 Hz in the GB system [125]. In a low inertia system, the normal operational deviations will become larger as there will be less kinetic energy stored in SG rotors. As it is this kinetic energy which covers the energy shortfall between the mechanical input power and the electrical output power, with less available, disturbances will cause a greater deviation in synchronous rotor speed. The issue of normal operational deviations could also become greater due to volatile energy sources such as WPP and photovoltaics. The combination of reduced inertia and volatile energy sources may require the dead bands of the frequency control schemes to be extended beyond their current limits to prevent unwanted or excessive operation.

This section will investigate alternative approaches to the VSC supplementary frequency control dead band implementation and the impact of the current ramp rate limiter to ascertain which combination is most beneficial.

5.1.1 Controller Dead Band Options

The role of the dead band is discussed in the previous section and highlights that there may be a requirement to increase the dead zone due to larger normal deviations in frequency. The consequence of increased dead band limits could be that when the system does experience a large disturbance, any required frequency containment response does not operate as quickly as it will not be triggered until the dead band limits have been exceeded. This will potentially lead to lower frequency nadirs or an

insufficient quantity of response for the system to recover. The factors described suggest the need for a review of dead band implementation and its operation to assess the impacts of different designs on system stability. The dead band may be implemented in two ways, denoted in this research as *continuous* given by (5.1) and *discontinuous* given by (5.2) where f_d^{op} is the dead band output value, and f_d is the dead band value. A comparison of the two operating techniques is displayed in Fig. 5.1[161].

$$f_d^{op} = \begin{cases} \Delta f + f_d & \Delta f < -f_d \\ 0 & -f_d \leq \Delta f \leq f_d \\ \Delta f - f_d & \Delta f > f_d \end{cases} \tag{5.1}$$

$$f_d^{op} = \begin{cases} \Delta f & \Delta f < -f_d \\ 0 & -f_d \leq \Delta f \leq f_d \\ \Delta f & \Delta f > f_d \end{cases} \tag{5.2}$$

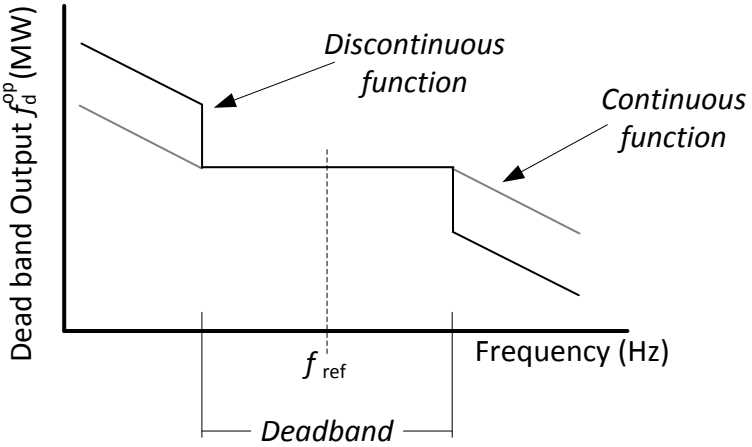

Fig. 5.1. Continuous and discontinuous dead band operation

5.1.1.1 Continuous Dead Band

Continuous dead bands have typically been implemented into the primary control schemes of SGs as a consistent slope output commonly known as droop control. The output from the control scheme can be given by (5.3) where ΔP is the output power and K_p is the generic gain of the frequency controller. Adjusting the dead band creates a shift in controller output, which retains the same slope (droop) value independent of dead band value as displayed in Fig. 5.2(a). This would lead to a reduced response at lower frequencies as the dead band limits are increased. To overcome this, the gain value can be modified to be a function of the dead band size so that a desired output is achieved by a given frequency deviation, as given by (5.4). In (5.4), $\Delta P_{desired}$ is the

desired output value and f_a is the frequency when the output should be achieved. Implementing this strategy would produce different droop characteristics depending on dead band size, as displayed in Fig. 5.2(b).

$$\Delta P = \left((f^{ref} - f_{meas}) - f_d \right) K_p \tag{5.3}$$

$$K_p = \frac{(f^{ref} - f_a) - f_d}{\Delta P_{desired}} \tag{5.4}$$

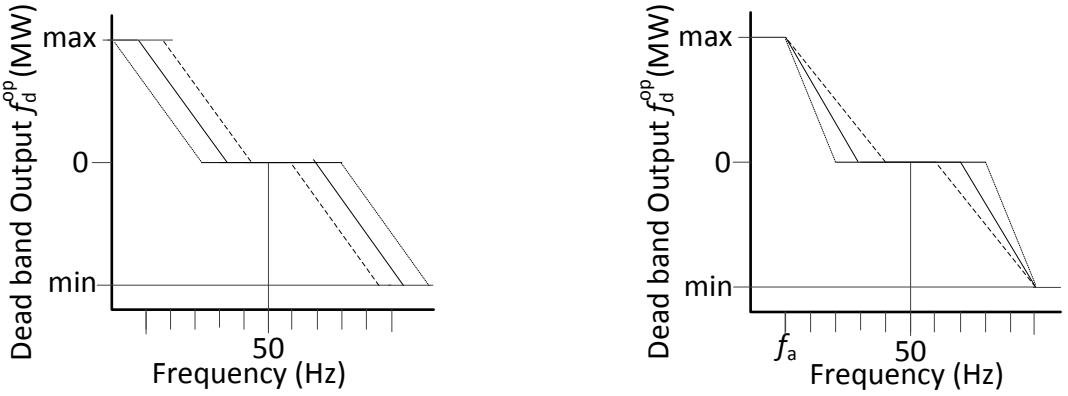

(a) (b)

Fig. 5.2. Continuous dead band operation. (a) fixed gain,
(b) variable gain dependent on dead band size

5.1.1.2 Discontinuous Dead Band

Discontinuous dead bands could not traditionally be implemented into a SG due to mechanical restrictions. The output of a SG cannot change instantaneously due to the inertia of the rotor and limits to the rate of change that the rotor can achieve. A discontinuous implementation would place undue mechanical stress on the rotor. However, power electronic interfaced energy sources are not subject to the same mechanical restrictions and can increase their output significantly faster. Although there are no mechanical constraints on the power electronics, there are thermal limits that need to be adhered to, and system inductance still limits the rate of change of current. Nevertheless, adjustment on a timescale of milliseconds is possible. For discontinuous dead band implementation, when the measured frequency exceeds the dead band limits, the output follows (5.5). Only the initial step varies as the dead band value increases as displayed in Fig. 5.3(a). However, the larger the dead band, the larger the initial step

change in output as the dead band is exceeded and the practical feasibility of this would have to be considered for the MMC operation.

$$\Delta P = (f^{ref} - f_{meas})\ K_p \tag{5.5}$$

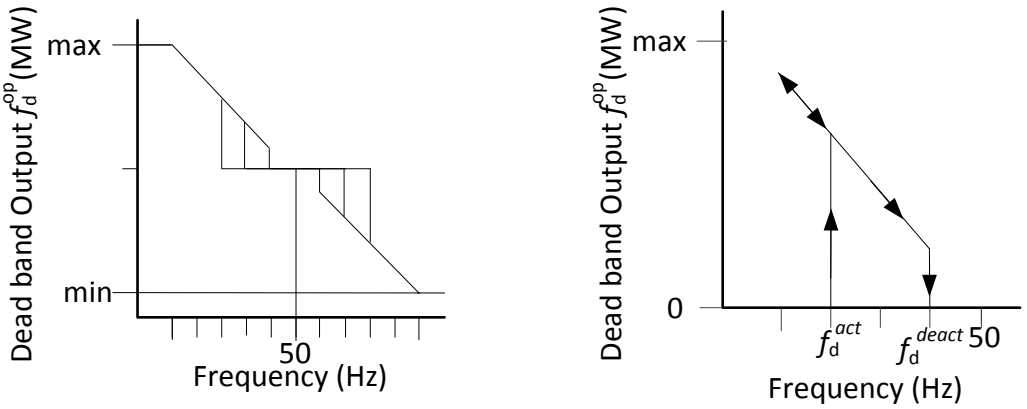

(a) (b)

Fig. 5.3. Discontinuous dead band operation

With this discontinuous dead band operation method, if the dead band size and disturbance size happen to align with the frequency deviating around the dead band threshold, there is the danger that the frequency containment response (FCR) may be constantly hunting. The controller would operate and return the frequency above the dead band value and be deactivated, allowing the frequency to drop back below the dead band again and so operating the controller. This undesired behaviour will be demonstrated later in the results.

To overcome this, a latching operation is introduced within this work with an activation dead band value (f_d^{act}) and a deactivation dead value $\left(f_d^{deact}\right)$. f_d^{act} is used to initiate the controller and then not until the frequency had recovered back to f_d^{deact} would the controller stop acting. With this method, as the frequency returns to a nominal value, the additional output value would reduce until f_d^{deact} was reached as displayed in Fig. 5.3(b). The implementation logic for this approach for a frequency drop would be as given in Fig. 5.4.

$$
\begin{aligned}
&IF\ \left(\Delta f \geq f_d^{act}\right)\ \&\ (flag == false)\\
&\qquad \Delta P = 0\\
&\qquad flag = false\\
&ELSEIF\ \left(\Delta f \leq f_d^{act}\right)\ \&\ (flag == false)\\
&\qquad \Delta P = (\Delta f)\, k_p\\
&\qquad flag = true\\
&ELSEIF\ \left(\Delta f < f_d^{deact}\right)\ \&\ (flag == true)\\
&\qquad \Delta P = (\Delta f)\, k_p\\
&\qquad flag = true\\
&ELSEIF\ \left(\Delta f \geq f_d^{deact}\right)\ \&\ (flag == true)\\
&\qquad \Delta P = 0\\
&\qquad flag = false\\
&END
\end{aligned}
$$

Fig. 5.4. Latched dead band logic implementation for a frequency drop

5.1.2 Analysis of Dead Band Implementations

The section presents the results from the investigation into the different dead band implementations in the supplementary frequency controller of an MMC. The MMC represents aggregated interconnector in-feed into the network and provides 8 GW steady state power and has a 10% capacity (800 MW) for frequency response. The impact that the current ramp rate limiter has on controller performance is also evaluated. The ramp rate limiter will be set to disabled, 1 GW/s, or 2 GW/s and the value used will be stated at each phase during the analysis. The generic four area system is used with the dispatch values and setup for this analysis provided in Appendix Section E.1.

5.1.2.1 Simulation Parameters

The five dead band sizes (f_d) for each implementation and the proportional gain parameter (K_{p3}) settings for each scenario are provided in Table 5.1. Gain parameter values displayed in Table 5.1 are given in SI units and in per unit. For the latching dead band scenarios, the deactivate dead band size is set to zero in order to view the best case recovery response from the MMC. This means that the latching behaviour will deactivate when the frequency returns to 50 Hz. However in a practical implementation the deactivation value may need to be larger than zero to account for measurement errors.

Table 5.1. Dead band and gain simulation values

Dead Band Type		Simulated Cases				
Continuous fixed gain	f_d (Hz)	0.1	0.2	0.3	0.4	0.5
	K_{p3} (GW/Hz)	1600	1600	1600	1600	1600
	K_{p3} (pu)	20	20	20	20	20
Continuous variable gain	f_d (Hz)	0.1	0.2	0.3	0.4	0.5
	K_{p3} (GW/Hz)	1600	2000	2666	4000	8000
	K_{p3} (pu)	20	25	33	50	100
Discontinuous non-latched	f_d (Hz)	0.1	0.2	0.3	0.4	0.5
	K_{p3} (GW/Hz)	1600	1600	1600	1600	1600
	K_{p3} (pu)	20	20	20	20	20
Discontinuous latched	f_d^{act} (Hz)	0.1	0.2	0.3	0.4	0.5
	f_d^{deact} (Hz)	0	0	0	0	0
	K_{p3} (GW/Hz)	1600	1600	1600	1600	1600
	K_{p3} (pu)	20	20	20	20	20

5.1.2.2 Continuous Dead Band Results

Results of the additional power output from the MMC following the disturbance for a fixed value of K_{p3} with varying dead band sizes that are provided in Table 5.1, is shown in Fig. 5.5(a). Similarly Fig. 5.5(b) displays the additional power output when K_{p3} is dependent on dead band size. The use of a variable K_{p3} value that is determined by the dead band size is shown to provide a greater response from the MMC as the dead band size increases. The maximum power injection values (P_{max}) for each dead band size when operating with a fixed gain and variable gain implementation are displayed in Table 5.2. The difference in maximum power injection (ΔP_{max}) displays the increase in power that the variable gain implementation provides over the fixed gain implementation.

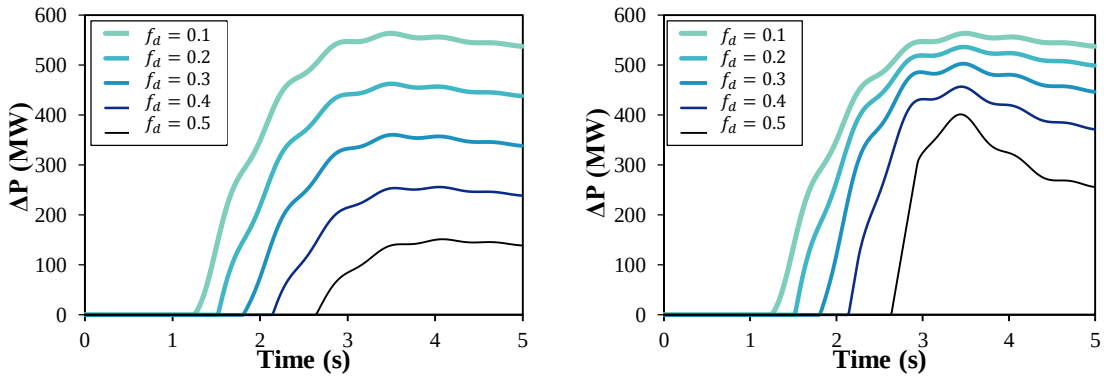

a) b)

Fig. 5.5. Continuous dead band operation. (a) fixed gain, (b) variable gain

Table 5.2. Comparison of maximum power injected between fixed and variable gain implementations

	f_d (Hz)	0.1	0.2	0.3	0.4	0.5
Fixed gain	P_{max} (MW)	563	462	360	255	151
Variable gain	P_{max} (MW)	563	536	502	456	401
	ΔP_{max} (MW)	0	74	142	201	250

A comparison of the system frequency for a dead band of 0.1 Hz and 0.5 Hz when operating with a fixed and variable gain implementation is displayed in Fig. 5.6(a) and Fig. 5.6(b). The pronounced effect of operating using a variable gain implementation compared to a fixed gain implementation is displayed in Fig. 5.7. It can be seen that as the dead band size is increased, the use a variable gain implementation becomes more beneficial. In this implementation of the dead band, the ramp rate limiter would not affect the output of the converter. The maximum rate of change observed from the supplementary frequency controller is 0.947 GW/s in the 0.5 Hz dead band scenario. This ramp rate falls below the MMC ramp rate limiter value of 1 GW/s and 2 GW/s that are implemented in this chapter.

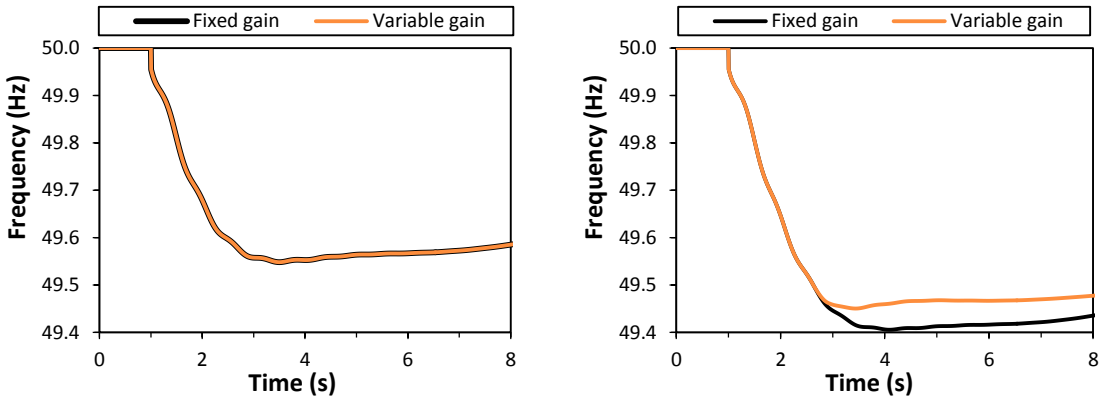

(a) (b)

Fig. 5.6. Comparison of system frequency. (a) dead band 0.1 Hz, (b) dead band 0.5 Hz

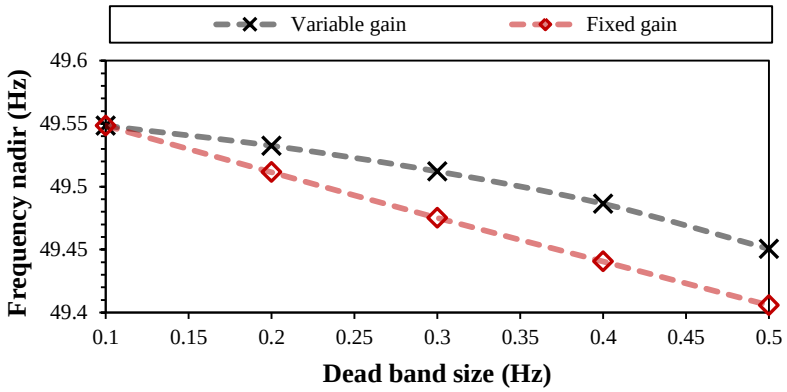

Fig. 5.7. Comparison of frequency nadir for continuous dead band

5.1.2.3 Discontinuous Non-latched Dead Band Results

When a discontinuous dead band is implemented using a dead band operating range given by f_d along with an infinite ramp rate (i.e. no ramp rate limit), the step increase in the output of the MMC is actuated, as can be seen in Fig. 5.8. As the dead band size, disturbance size and additional power injection coincide, it can be seen that the controller keeps activating as enough power is injected to recover the frequency above the dead band. The controller then deactivates and the frequency falls back below the threshold which activates the controller again. This unwanted continual operation could be detrimental to the converter and the system. Although the continual switching is only observed at dead bands of 0.4 Hz and 0.5 Hz in this simulation case, this action could occur at different dead bands depending on the size of the disturbance, the quantity of response available within the system, and the response characteristics of the additional ancillary services.

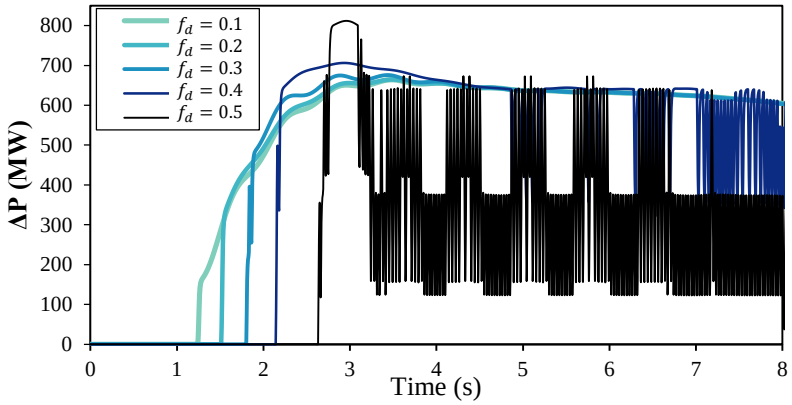

Fig. 5.8. Discontinuous non-latched dead band operation with no ramp rate limiter

To reduce the impact of the impulse caused by the discontinuous dead band, a ramp rate limiter can be utilised to constrain the rate of change of the converter output. As displayed in Fig. 5.9(a) and Fig. 5.9(b), the use of a ramp rate does reduce the hunting or switching behaviour of the converter around certain dead band sizes where the hunting behaviour occurs.

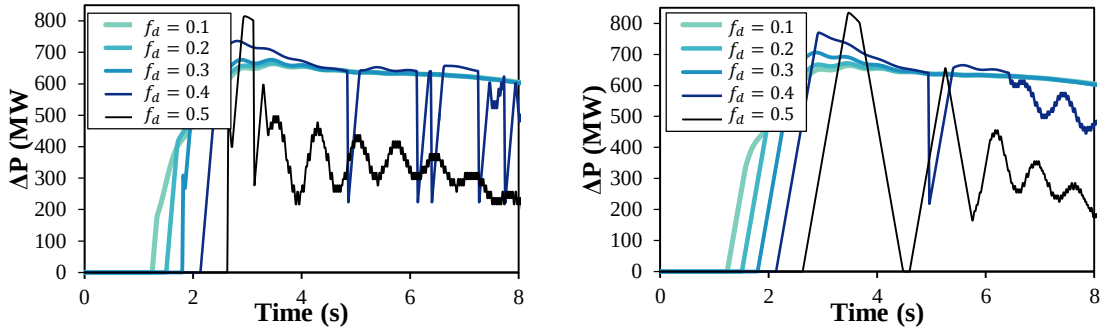

Fig. 5.9. Discontinuous non-latched dead band operation. (a) using a 2 GW/s ramp rate limiter, (b) using a 1 GW/s ramp rate limiter

The introduction of the ramp rate limiter does not completely eliminate the cycling behaviour as seen in in Fig. 5.9(a) and Fig. 5.9(b), however it does severely reduce the unwanted switching action. The incorporation of a ramp rate limiter reduces the power injection from the converter which leads to a reduced response. The use of a lower ramp rate limiter does reduce the speed of the converter and this could be reduced further below the 1 GW/s displayed in Fig. 5.9(b). However, to enable a fast response, particularly as the inertia reduces, a large ramp rate limit value would be more beneficial as it would enable the converter to reach its maximum power set point in a shorter time. The impact of the ramp rate limiter on the system frequency is displayed in

Fig. 5.10 where a 0.5 Hz dead band value is used. The use of a 2 GW/s ramp rate limiter leads to an increase (improvement) of 0.027 Hz in the frequency nadir over the 1 GW/s ramp rate implementation. This highlights that there is a trade-off between the speed of frequency response and the frequency nadir when implementing a ramp rate limiter in this implementation.

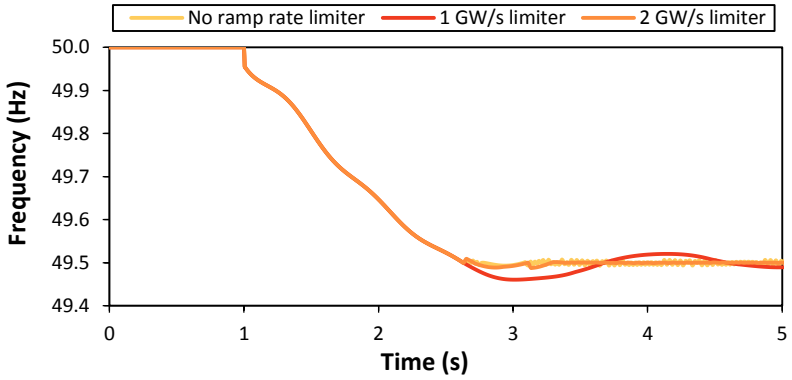

Fig. 5.10. Impact of the ramp rate limiter on the frequency response for a 0.5 Hz dead band implementation

5.1.2.4 Discontinuous Latched Dead Band Results

To overcome the hunting or limit cycling behaviour completely around a dead band, the use of different f_d^{act} and f_d^{deact} dead band values is shown in this work to be effective. The additional power output from the controller for this implementation of the dead band does not experience any hunting or switching behaviour across all dead band values when no ramp rate limiter is included as displayed in Fig. 5.11(a). The activation and deactivation values are displayed in the plots as $f_d = f_d^{act}/f_d^{deact}$, for example $f_d = 0.1/0$ refers to a frequency deviation activation value of 0.1 Hz and a frequency deviation deactivation value of 0 Hz. When a 2 GW/s ramp rate limiter is incorporated, the characteristic response is similar but it reduces the speed of power injection at the instant the frequency support is operated. The reduction in the speed of response from a converter would become a greater issue as systems experience faster rates of change of frequency. In Fig. 5.11(b) it is seen that when incorporating a 2 GW/s ramp rate limiter along with 0.5 Hz dead band, it takes the converter approximately 0.4 s to reach its maximum power injection following the disturbance. The impacts of the ramp rate limiter on the system response are explored in the next section.

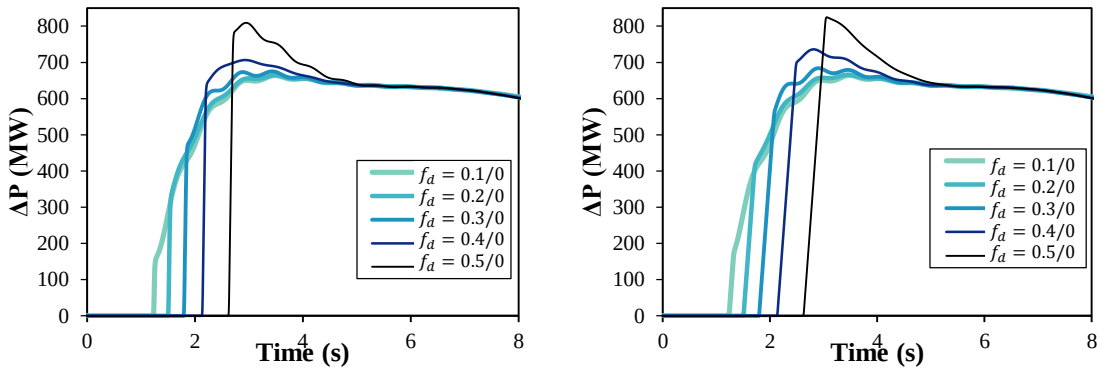

(a) (b)

Fig. 5.11. Discontinuous latched dead band operation. (a) no ramp rate limiter, (b) using a 2 GW/s ramp rate limiter

5.1.2.5 Discontinuous Dead Band Types Comparison

No significant difference in frequency nadir is seen between the two implementations of the discontinuous dead band (non-latched and latched) as shown in Fig. 5.12. No difference in nadir occurs because the response provided by the converter in both cases is similar, and any energy reduction due to converter switching in the non-latching implementation is negligible. A comparison of frequency nadirs for a discontinuous dead band with various ramp rate limiter values is displayed in Fig. 5.13 and is compared to the best case variable continuous dead band implementation. It can be seen that, in general, the larger the ramp rate limiter, the higher (better) the nadir and the less severe the frequency deviation. Even when a ramp rate limiter of 1 GW/s is used with the discontinuous dead band, this still proves to be more beneficial to the system than the continuous variable dead band implementation. For a 0.1 Hz dead band (that is the closest to the current operation requirement in GB) there is no difference between the discontinuous latched implementations that have different ramp rate limiter values. However the discontinuous latched dead band type does reduce the nadir by 0.4 Hz compared to the variable gain implementation. As the dead band size is increased, the ramp rate limiter starts to reduce the effectiveness of the latched discontinuous dead band implementation because of the large initial step when the frequency exceeds the dead band.

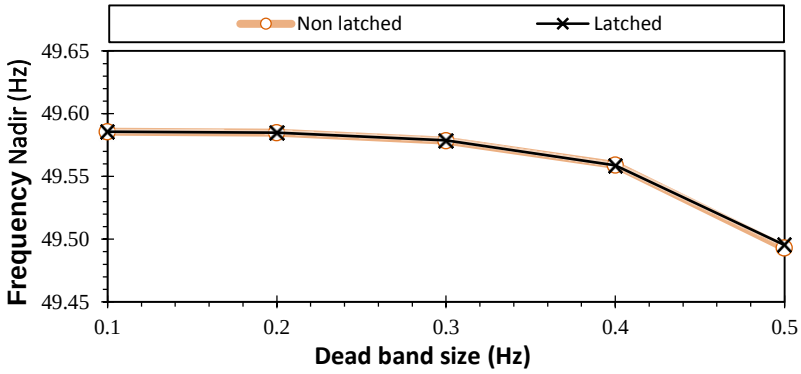

Fig. 5.12. Comparison of frequency nadir from non-latched and latched discontinuous dead band implementation with no ramp rate limiter

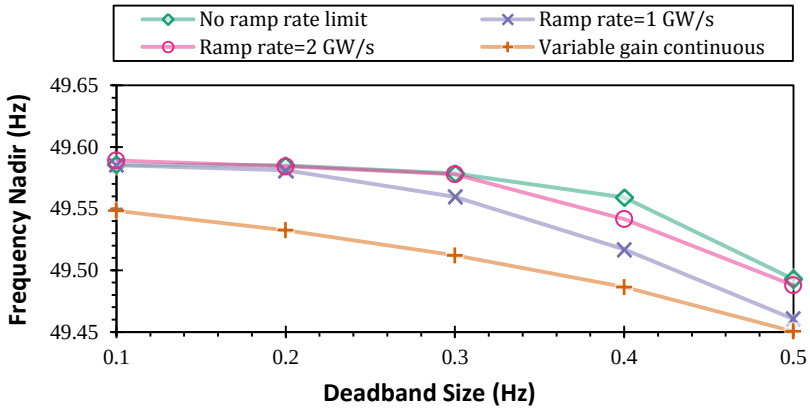

Fig. 5.13. Comparison of frequency nadirs

When using different activate and deactivate dead band values, the frequency recovery is shown to be improved for cases where the controller is acting around the dead band. Additionally, the response from the converter perspective is significantly improved. A comparison of frequency response following both implementations of the discontinuous dead band is displayed in Fig. 5.14(a) and Fig. 5.14(b) to highlight the improved recovery. Moreover, a discontinuous dead band implementation has already been shown to improve frequency nadir compared to a conventional continuous implementation, due to a higher immediate power injection that is achieved by a step as previously displayed in Fig. 5.8 and Fig. 5.9. The interrupted operation of the controller around the dead band value for a non-latched operation could be detrimental to the system as it prevents the frequency from recovering.

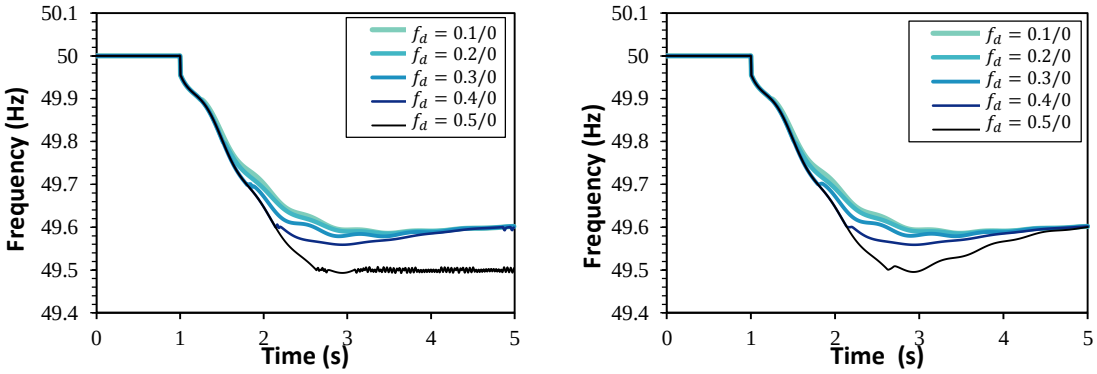

Fig. 5.14. Frequency response using discontinuous dead band with no ramp rate limiter. (a) non-latched, (b) latched

The maximum power injected for a discontinuous dead band implementation with different ramp rate limiter settings is displayed in Fig. 5.15. It can be seen that in these scenarios which use a large disturbance, there is minimal difference between the power injected when operating with different ramp rate limiter settings at dead bands of 0.1 Hz and 0.2 Hz. For dead band sizes of 0.3 Hz and 0.4 Hz it can be seen that a slower ramp rate limiter leads to a larger maximum power being injected from the MMC due to the frequency deviation being further. For a dead band size of 0.5 Hz the other system responses, namely the SG governors, have had to operate and constrain the frequency which leads to a reduced difference in the maximum power injection from the MMC.

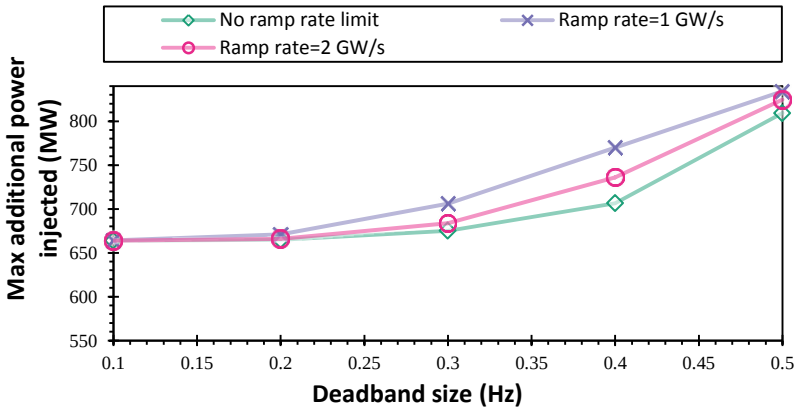

Fig. 5.15. Maximum power injected for discontinuous dead band implementation with different ramp rate limiter values

5.1.2.6 Dead Band Types Summary

During a continuous dead band implementation, the use of a variable gain that is dependent on dead band size has been shown to improve frequency response from the

MMC. The resulting frequency nadir was reduced compared to a fixed value of gain as the dead band size increases highlighting the benefit of the method. The second method was the discontinuous dead band implementation which was shown to improve frequency nadir over both versions of the continuous implementation. The discontinuous dead band with the variable activate and deactivate limits has been shown to eliminate the hunting action of the frequency controller when operating around the dead band value. It has also shown to improve frequency recovery as dead band limits increased making it the most effective option for frequency response in this study. The variable activation and deactivation limits on the dead band has been shown to enable an increased ramp rate limiter to be incorporated into the converter while leading to unwanted switching behaviour as the frequency containment is operated.

The cycle limit behaviour observed in this section arose when there was a large network disturbance and when the dead band size was greater than 0.4 Hz. This same situation could also occur when the dead band size is smaller and the network experiences a small disturbance where there is a large quantity of fast frequency response. The following section will investigate the potential for this behaviour to occur.

5.2 Detrimental System Behaviour

As the number of renewable energy sources connected using VSC technology increases, so will the potential to provide increased levels of fast frequency response. Schemes such as those ones presented in the previous section enable a faster response that reduce the frequency nadir which will be crucial in future low inertia systems following large disturbances. It will also be crucial to retain stability following smaller disturbance sizes. There is the need to provide fast frequency response with a sufficient amount of energy to contain the frequency following a large disturbance, without having a detrimental impact on the system frequency and rotor angle stability following a small disturbance.

In this section the occurrence of converter cycle limit behaviour under small network disturbances is investigated. Its aim is to investigate the potential detrimental system impact that fast frequency response can have. The study is necessary because previous literature has only focused on the improvements that fast frequency response had on stability following large disturbances. In future low inertia systems it will be crucial to retain frequency and rotor angle stability following a small disturbance without compromising the ability to contain the frequency after a large disturbance. This would

be necessary to allow scalability of fast frequency response (FFR) enabled devices and ensure that the frequency or rotor angle stability is not negatively impacted under large and small disturbances. Any such adjustment in the speed or quantity of response to reduce the small disturbance behaviour could adversely limit the speed of response of the FFR device and ultimately could reduce its effectiveness during the frequency containment process.

This section will first investigate the small disturbance converter behaviour and then introduce an adaptive frequency controller for a VSC frequency control loop. The overall aim of this controller is to enable the VSC to provide FFR without causing detrimental stability impacts, particularly with consideration of small disturbances. The FFR in this section refers to a fast frequency response using a proportional droop controller.

5.2.1 Frequency Controller

The proportional frequency control loop presented in Chapter 4 is used in this section alongside a continuous dead band implementation. Limiting factors affecting the response are the phase lock loop (PLL) which measures the system frequency, the gain component (K_{p3}), and potentially any other delays introduced from the signal processing. To improve the frequency response capability, the PLL bandwidth could be increased, or the value of K_{p3} could also be increased as displayed in the section 5.1. For large disturbances, increasing these parameters would be beneficial as a larger quantity of energy would be injected over shorter timeframes. However, for smaller disturbances, increasing these parameters could lead to unwanted oscillatory behaviour or limit cycling from the frequency control loop. Unwanted behaviour occurring from the converter control loop could be dependent on the value of K_{p3}, the system inertia, dead band settings, or the quantity of FFR operating in the system. It is likely to be a combination of these factors acting together. To highlight this behaviour, four scenarios described in Table 5.3 are used when the VSC is operating with the proportional controller described in Chapter 2. These scenarios are representative of different size disturbances in a transmission system that is approximately scaled to the GB power system operating with low inertia. The four area system presented in Chapter 2 is used for this analysis. These disturbances are all less than the maximum infeed loss for the GB system which is 1800 MW. The resultant outputs of the VSC frequency control loop (ΔP) for these scenarios are displayed in Fig. 5.16. This highlights the potential detrimental oscillatory behaviour when providing FFR under small disturbances. This

cycle limit behaviour occurs because the converter can provide a sufficient quantity of response to recover the frequency back above its operating dead band threshold. Once back in the dead band, the converter frequency response stops which leads to the frequency deviating outside of the dead band again, and so retriggering the converter frequency response. This oscillatory behaviour could lead to rotor angle stability concerns in the system - particularly in a low inertia system that will have a reduced quantity of damping. The frequency control in Scenario 1 operates first because the frequency exits the set dead band faster than the other scenarios, due to it being subject to the largest disturbance.

Table 5.3. Example oscillatory behaviour scenario parameters

Scenario	K_{P3} (pu)	Disturbance size (MW)	System inertia (GVA.s)
Scenario 1	150	300	120
Scenario 2	150	150	120
Scenario 3	150	150	90
Scenario 4	200	150	90

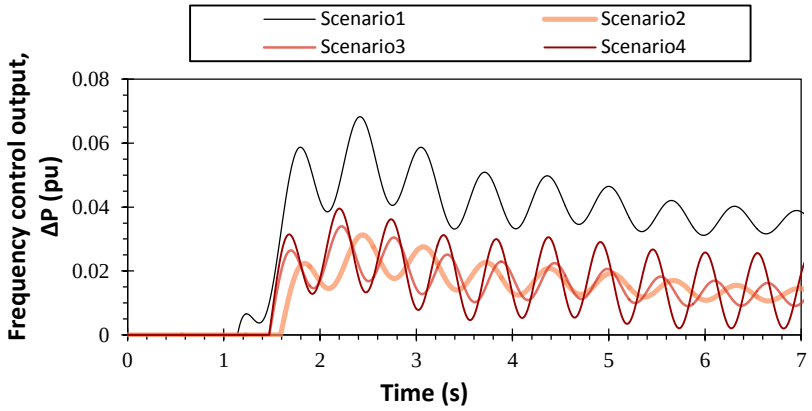

Fig. 5.16. VSC frequency control output behaviour

To prevent this unwanted oscillatory action from the converter due to the frequency control loop, the proportional droop gain could be reduced or the PLL bandwidth could be reduced. These both reduce the response from the converter leading to a lower impact from the FFR schemes. An alternative could be to introduce a first order lag filter for the measured frequency value as displayed in Fig. 5.17 to act as a band pass and limit the converter response to frequencies above a certain range. However, the introduction of a first order filter would reduce the FFR capability of the converter. Although this will have a positive impact for small disturbances in low inertia networks

when multiple devices are providing FFR, it would be unfavourable for large disturbances or when there is limited FFR connected.

The impact of the addition of a first order filter with a time constant of 0.5 s on the converter output and the system frequency for an example situation with a large disturbance is displayed in Fig. 5.18(a) and Fig. 5.18(b). In this setup, the introduction of the first order filter leads to an increase in the ROCOF (measured over the first 1000 ms) from 0.22 Hz/s to 0.25 Hz/s. The ability to provide FFR that is capable of being applied for large and small disturbances may become a challenge as the network changes and the number of FFR devices connected increases. Future practical implementations of FFR will need to be scalable without the need to be constantly retuned and without causing detrimental system impacts.

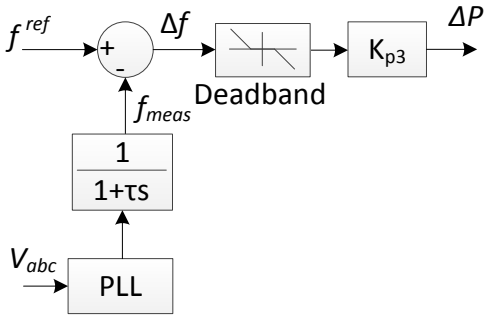

Fig. 5.17. Proportional control with a first order filter on the measured frequency

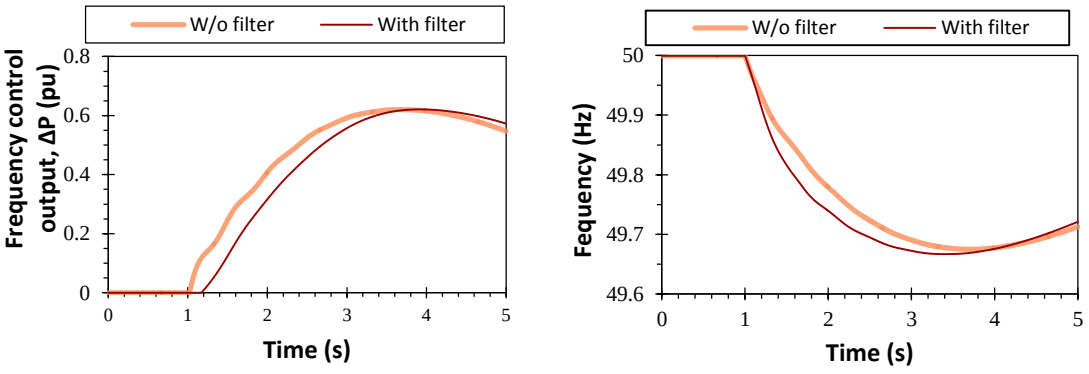

(a) (b)

Fig. 5.18. Impact of first order delay filter.
(a) converter response, (b) system frequency

5.2.2 Augmented Frequency Controller

To overcome the constraints and performance limiting behaviour of the converter when using a fixed time constant for the first order filter, an adaptive controller that

adjusts the time constant of a first order lag filter has been designed in this research. The aim of the adaptive controller is to prevent unwanted oscillatory frequency control behaviour without slowing down the speed of the converter response. This adaptive controller allows the converter to provide a fast acting response for large disturbances. At the same time, if oscillatory or limit cycle behaviour is detected, it varies the filter time constant to reduce or remove the undesirable behaviour. The method proposed in this thesis is displayed in Fig. 5.19 where the adaptive controller is shown inside the dashed box. The action of the adaptive controller is a corrective action instead of a preventative one. The adaptive controller detects any oscillating or limit cycle behaviour in the output of the frequency control loop and adjusts the time constant of the first order filter. The dominant frequency detected (the frequency with the largest magnitude) is used to determine a time constant for the first order filter. To prevent any sudden filter operation changes, the new time constant is ramped up to the new value with a gradient limit of 1 s/s. Once any output oscillations have settled down, the filter time constant is returned to its original value once again enabling the controller to respond as fast as possible to new disturbances.

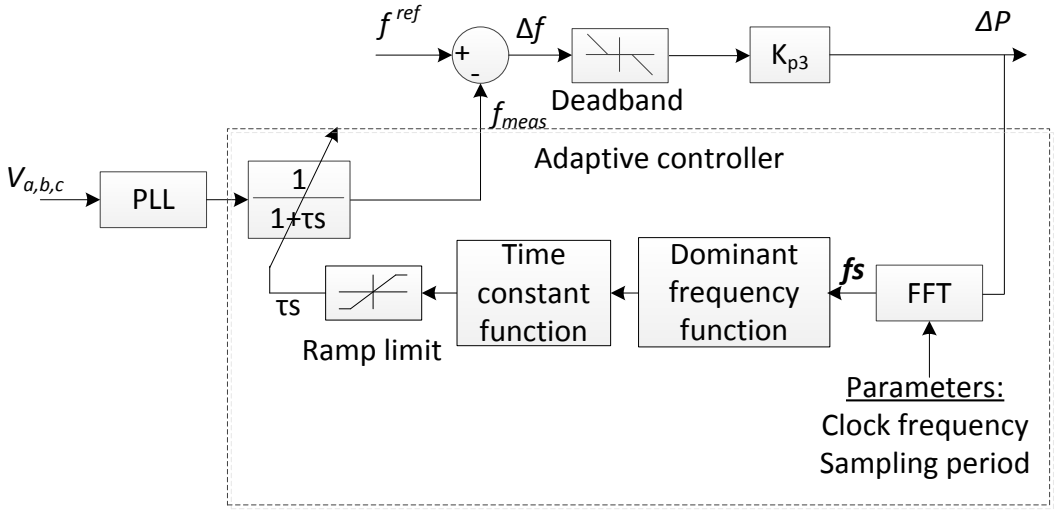

Fig. 5.19. Proposed FFR control method

Detecting any oscillations in the output of the frequency controller could be achieved using a number of different methods including a fast Fourier transform or a wavelet transform as described in [162]. In this research, the detection is completed using a discrete Fourier transform that can be given by (5.6) where k is an individual sample, N is the number of samples and T is the time sample separation.

$$\mathrm{F} = \sum_{k=0}^{N-1} f[k] e^{-jwkT} \tag{5.6}$$

To improve computing time, the discrete Fourier transform is achieved by applying a fast Fourier transform (FFT) algorithm. The chosen sampling rate is 500 Hz and the number of samples required to complete an FFT period is 500. These values are used because they offer a balance between frequency resolution and time taken to achieve a complete FFT period (which is 1s in this case). A greater frequency resolution would require a longer sampling period resulting in the FFT output action occurring later. The resolution of the FFT is determined by dividing the sampling frequency by the number of samples producing a resolution of 1 Hz in this case. The output vector from the FFT (f_s) that contains the transformed time domain signal information is passed to the *dominant frequency function* displayed in Fig. 5.20.

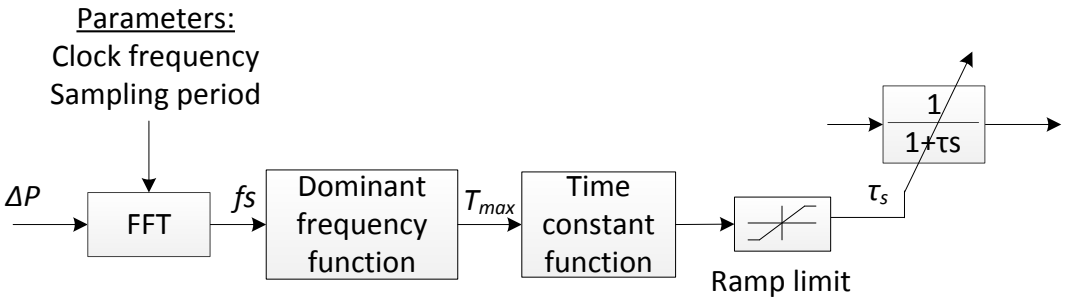

Fig. 5.20. Adaptive controller

The high frequency components from the measured frequency signal are expected to have been filtered out due to the PLL bandwidth, which does not have to be as large for the frequency measurement as for the converter synchronization. The *dominant frequency function* determines the frequency with the largest magnitude that is detected by the FFT (taken from the FFT frequency spectrum) and then determines the period of that frequency given as T_{max}. This time period is then passed to the *time constant function* that sets a time constant for the first order filter. The FFT output only occurs when the set number of samples has been processed. This requires a compromise between the speed that the adaptive control can adjust to any oscillations and the precision of the detected frequencies in the output. Taking this into consideration, the time constant function determines the filter time constant as (5.7). To overcompensate for any errors at the detection stage, there is a user specified denominator value, which is arbitrarily chosen as 2 in this case as the FFT has a limited resolution for detecting the value of T_{max}. For example, the detection of a 1 Hz oscillation from the FFT would lead

to a T_{max} value of 1 s and a resulting value for τ_s of 0.5 s. The value of τ_s is expected to be in the range of 0-2 s for most typical system oscillations, but is dependent on the system dynamics and damping. More elaborate methods could be applied at this point to improve the decision making and tuning of the value for τ_s if required.

$$\tau_s = \frac{T_{max}}{2} \tag{5.7}$$

5.2.3 Analysis

The four area generic system detailed in Chapter 2 is used to perform the analysis. In these simulations the integral time step used for the RMS simulation is changed from 10 ms to 1 ms. This allows a clock frequency of 500 Hz which is used for the FFT sampling signal. The VSC proportional gain value and disturbance size for all four test cases are displayed in Table 5.4.

Table 5.4. Test case gain and disturbance size parameters

Scenario	K_{P3} (pu)	Disturbance size (MW)	System inertia (GVA.s)
Case 1	150	150	120
Case 2	175	150	120
Case 3	150	1800	120
Case 4	150	500	120

5.2.3.1 Test Case 1

The first test case for comparison has a disturbance size of 150 MW and a VSC frequency control gain (K_{p3}) of 150 pu with a view of investigating how the controller can reduce oscillatory output behaviour due to the FFR. The VSC frequency control loop output (ΔP) is displayed in Fig. 5.21(a) and compares the output without the adaptive control and with the adaptive control. When the frequency control loop activates there is no difference in the initial speed of the response and both control types lead to an output oscillation at the beginning of the response. However, the adaptive control detects the oscillation in the output of the frequency controller and applies a new time constant to the first order filter, which reduces the frequency pass band of the filter. As the disturbance is relatively small, it can be seen that the overall frequency deviation is minimal. The adaptive control prevents the sustained injection of power oscillations

into the network and reduces the frequency oscillations as displayed in Fig. 5.21(b). Depending on network topology and rotor angle stability factors, these oscillations could lead to rotor angle stability issues.

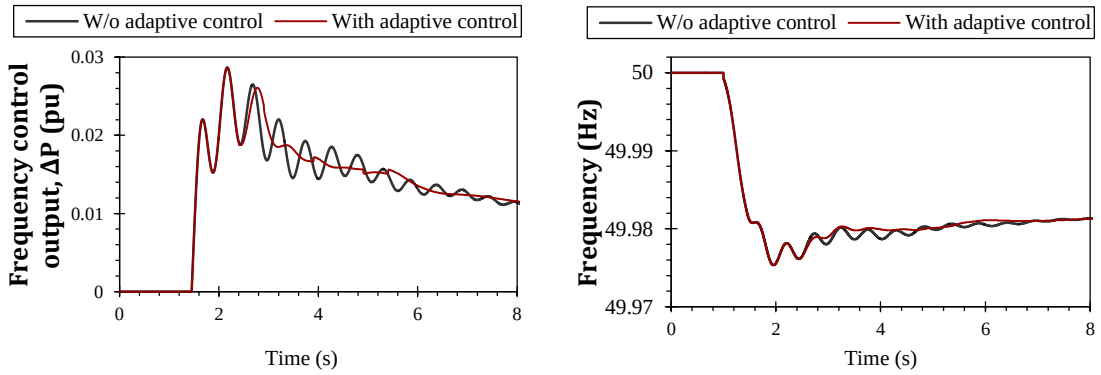

(a) (b)

Fig. 5.21. Test Case 1 response. (a) converter output, (b) system frequency

The first order filter time constant value is displayed in Fig. 5.22 and shows the value is increased via a ramp when the adaptive controller detects oscillatory behaviour. There is a delay between the converter responding and the time constant increasing due to the detection time taken by the FFT method. The filter value is reduced back to zero by the adaptive controller as the oscillations decrease. In this study the adaptive controller and FFT setup does not have the resolution to distinguish between the subtle frequency changes between each case, this leads to a similar filter time constant profile for each case.

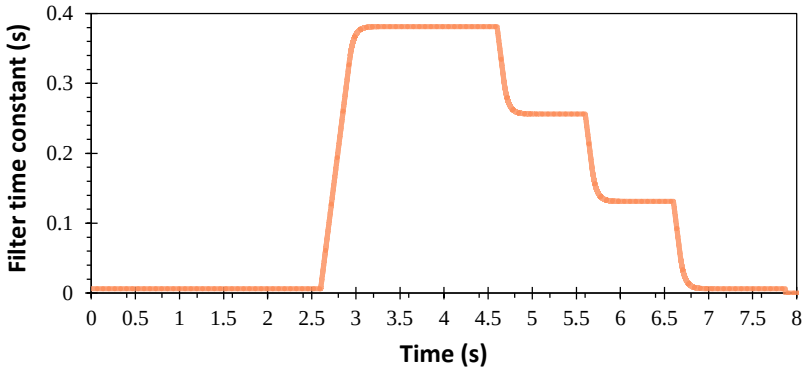

Fig. 5.22. Filter time constant for test Case 1

5.2.3.2 Test Case 2

For the second test case, the frequency control gain is increased to 175 pu but all other parameters are the same as test Case 1. In this test case, due to the larger value of

gain applied, the control action is larger leading to a greater oscillation magnitude without adaptive control implemented as displayed in Fig. 5.23(a). Similar to test Case 1, both the non-adaptive and adaptive control initially respond in the same manner until the adaptive control has detected the oscillations in the controller output. In this test case, without the adaptive frequency control, larger power oscillations would be injected into the network as displayed in Fig. 5.23(b) which would increase the risk of rotor angle stability issues. In this particular case, without the adaptive controller the oscillations do not reduce and are not damped.

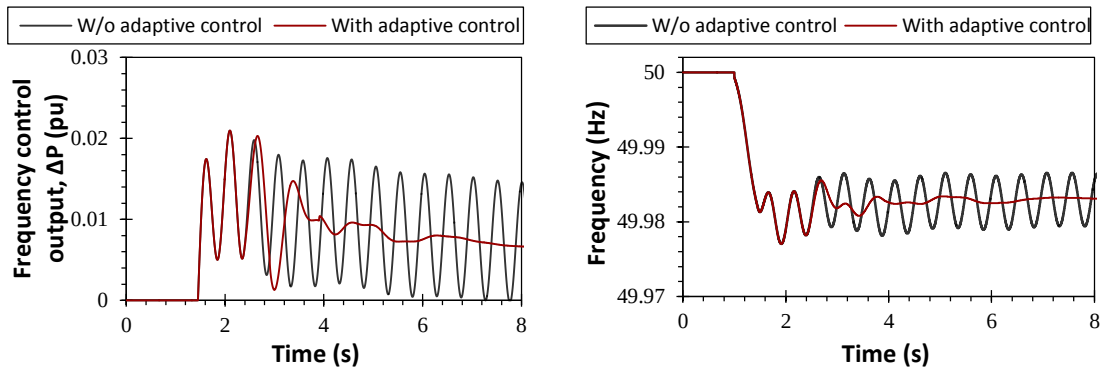

(a) (b)

Fig. 5.23. Test Case 2 response. (a) converter output, (b) system frequency

5.2.3.3 Test Case 3

This third test case investigates the influence of the adaptive control when a large disturbance occurs. The aim of the adaptive control is not reduce the speed of the response when a large disturbance occurs. This test case will examine if the adaptive control reduces the speed of response which could lead to an increased rate of change of frequency or worse frequency nadir. In this test case the disturbance size is 1800 MW and the VSC frequency control gain value is 150 pu.

In Fig. 5.24(a), the non-adaptive and the adaptive VSC frequency control outputs do vary slightly. The FFT has detected some small oscillatory action and has adapted the first order filter time constant. It is important to remember that although the frequency control loop output may be large, the converter output is limited by the inner and outer control loops, and depends on the available capacity. This detection of a slight oscillation and the subsequent change in the filter time constant does not reduce the ability of the converter to provide FFR for large disturbances as displayed in Fig. 5.24(b) where no difference in ROCOF or frequency nadir is seen. The impact of

FFR with and without adaptive control is also compared against a scenario where there is no FFR applied in order to show that the FFR does have a significant system impact.

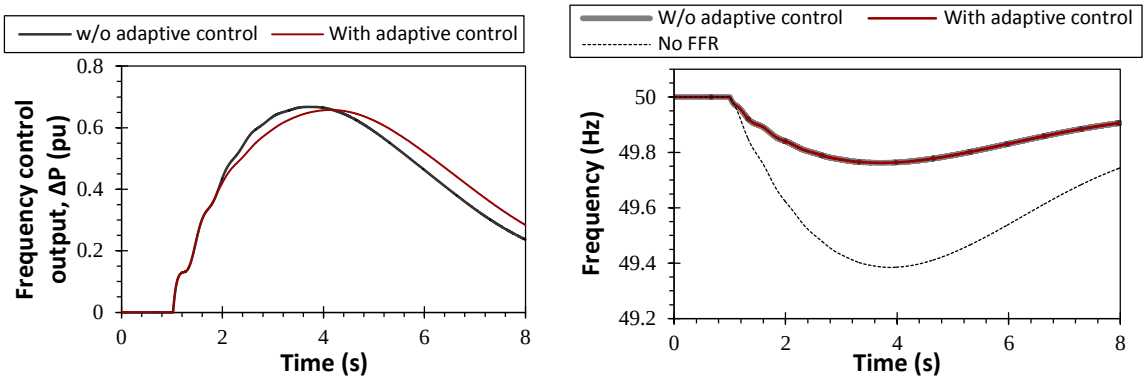

(a) (b)

Fig. 5.24. Test Case 3 response. (a) converter output, (b) system frequency

5.2.3.4 Test Case 4

The fourth test case is presented to highlight what impact the adaptive controller has when a medium size disturbance occurs on the network, and would represent a medium size in-feed loss such as non-nuclear SG or WPP. In this test case the disturbance size is 500 MW allowing the frequency deviation to be more significant than Case 1 and Case 2, but not as severe as Case 3.

It is observed in Fig. 5.25(a) that similar to test Case 1 and Case 2, due to the high gain value of the FFR, oscillations are introduced. In Fig. 5.25(b) the adaptive controller is shown to allow initial frequency containment the same as without the adaptive controller. This displays the adaptive controller does not reduce the speed or quantity of initial power injection. Following the initial containment, the adaptive frequency controller is shown to damp out any unwanted oscillations introduced by the FFR in Fig. 5.25(b). It is noted that the implementation of the adaptive controller within this work causes a discontinuous change in the frequency controller output when the adaptive controller operates. Although this discontinuous action does not impact the system frequency the sudden change of the filter constant would have to be considered further.

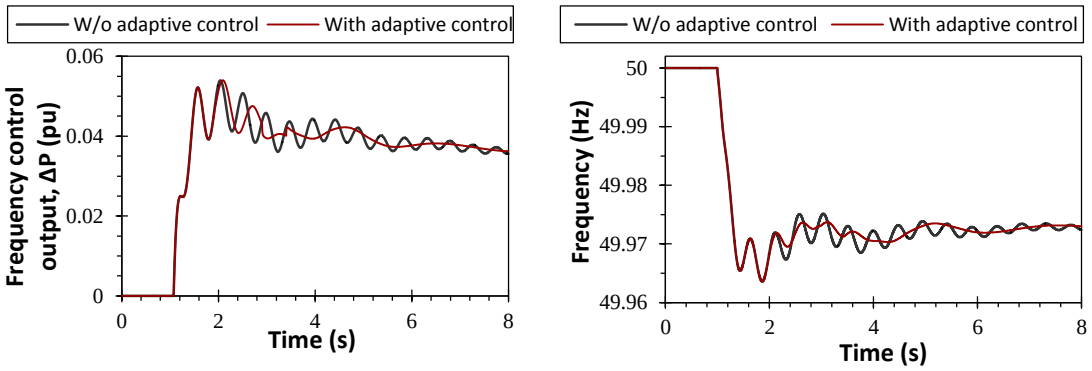

(a) (b)

Fig. 5.25. Test Case 4 response. (a) converter output, (b) system frequency

5.2.3.5 Analysis Discussions

The four test cases presented have highlighted how an adaptive frequency control scheme could be implemented, to allow a greater quantity of FFR to be connected to the network by limiting the impact following small disturbance scenarios. Although the detection method and time constant assignment are simple, they are still shown to be effective. More efficient algorithms to detect unwanted frequency control behaviour could be used as the FFT is limited by the sample frequency and number of samples. Improved techniques could also be used to produce more robust methods for assigning the filter time constant based on the detected oscillatory behaviour.

5.3 Summary

Within this chapter two VSC proportional frequency control adaptations have been presented. The first adaptation is designed to enhance the responsiveness of the proportional control scheme by using a discontinuous dead band implementation. The second adaptation is designed to reduce the impact that fast response schemes could have on the system by using an adaptive first order filter time constant.

To improve the frequency response capability from the VSC using a proportional control scheme, two dead band implementations were investigated: continuous and discontinuous. The continuous implementation is enhanced through the use of a variable gain component that is dependent on the dead band size. This ensures that the converter can provide a set quantity (power injection) of response by a certain frequency deviation, even when the dead band size is increased. The discontinuous dead band implementation is shown to enable the converter to respond faster and improve the frequency stability over the continuous dead band due to the initial step action. The

latched variant of the discontinuous dead band removes any hunting behaviour that may occur due to dead band size and quantity of frequency response. This latched version also improves the frequency recovery.

This chapter has also highlighted how large quantities of fast frequency response under small disturbances could lead to oscillatory behaviour. To enable larger quantities of FFR to be provided in future low inertia systems without leading to the situation where unwanted oscillatory action is introduced, a simple adaptive FFR control scheme for a VSC system is designed. The adaptive control process utilises a FFT method to detect oscillations in the output of the frequency controller. A resultant time constant determined by an adaptive algorithm is then applied to a first order filter on the frequency measurement signal in order to reduce the injection of oscillations by the frequency controller. This simple adaptive control method has been shown via simulation to enable the converter to respond quickly (the same as with no adaptive control) to large disturbances. Under small disturbances, the adaptive controller has been shown to reduce the unwanted power oscillations introduced. This research has displayed that improving future frequency stability is not just a case of increasing the speed or quantity of response. Consideration must be given to the system response under small disturbance situations.

This chapter has completed objectives 4 and 5. The research contributions from this chapter are the enhancement of the proportional control scheme and a mitigation scheme to reduce cycle limit behaviour.

The adaptation of the dead band within the frequency control enables a faster response. However a proportional control scheme still limits the shape of the response from the converter. However, using a VSC that does not have the same mechanical limitations as a SG enables it to be operated differently and provide unique frequency response. Instead of applying a simple proportional frequency control to improve frequency stability, the response could be tailored to provide a response to specifically address deficiencies of existing SG primary response. In the next chapter, the VSC frequency response will be developed to provide a response based on the deficiency of SG primary response (in terms of the delays present in their operation) schemes.

6 Innovative Frequency Containment Control

The previous chapter presented a proportional control scheme that used a discontinuous dead band to enable a faster frequency response. However, a proportional control scheme cannot be designed to provide a response that takes into account the deficiency and delays of traditional SG primary response schemes. For example, by injecting an initial large quantity of energy that decays as the primary response starts to operate. Being able to guarantee a set amount of frequency response by a certain frequency deviation would enable the system operator to be more confident when operating low inertia systems. This would reduce the need to over-contract for ancillary services. This cannot be achieved using traditional SG-based frequency containment due to the inherent delays in the actuation of the frequency containment response. Currently the GB system operator has specified the capacity for each type of frequency response service [16], but this does not provide a picture of how much response will actually operate after a specific magnitude of frequency deviation.

Primary response schemes are limited by the speed that they can respond due to the mechanical constraints and operational delays. In order to overcome the problems with primary frequency response and the potential for fast rate of change of frequency (ROCOF) caused by a reduction in the proportion of synchronous generation, there is a need for improved power electronics control schemes to fill the gap. However, the capability of power electronics and conventional synchronous generation is different. Significantly, the power electronics often used to connect the RES can be adapted to provide frequency response that is capable of being delivered faster than traditional primary response. However it can provide less overcurrent and typically has less stored energy. Direct comparison between both systems is therefore complex and an agreed common metric remains elusive.

The fast frequency response (FFR) scheme presented in this section aims to provide containment and ROCOF support while keeping the control complexity to a minimum. It provides a targeted fast response that does not exceed the system operator's expected total response and is easily integrated with existing control structures. In Chapter 5, the frequency containment schemes were designed to enable the VSC to respond quickly with a large quantity of response. Although providing a response as fast as possible is beneficial in certain system operating conditions, the SO may require the response to be limited and to take into account the existing primary response schemes as described in [16]. Instead of operating the converter to just provide a large quantity of fast response,

they could respond in a manner that more effectively takes into account the operation of existing primary response schemes.

In this chapter the different methods used to quantify the *amount* of primary response in a system are compared to highlight shortcomings and to identify the most meaningful quantification metric. Using the meaningful quantification metric, the difference between an ideal system response (assuming no thermal or mechanical delays in the system) and the actual system response is highlighted to show how the two differ. This difference is then used to develop a novel FFR controller that acts to reduce the difference between the ideal response and the actuated system frequency response. The proposed FFR controller provides a response that is analogous to an inertial response without requiring the direct calculation of the frequency derivative. The performance of this new controller is compared alongside different frequency containment schemes commonly used in the literature. The relative performance of each controller is quantified by calculating the average deviation from an ideal response. The research in this chapter completes thesis objective 6.

6.1 Frequency Stability Analysis Considerations

This section analyses the quantification of primary response in order to develop a meaningful quantification metric. In addition to the quantification metric, the difference between the expected quantity of primary response and the actual quantity of primary response from a SG is highlighted.

6.1.1 Primary Response Quantification

Before primary response has had time to act, the system inertia that is the synchronously connected rotational energy, limits the rate of change of frequency. The inertia can be determined by the sum of all SG apparent power ratings (S_{sys}) multiplied by their inertia constants (H_{sys}) leading to the units of GVA.s as given in (2.14). The use of H_{sys} alone does not describe the quantity of energy that is available; it only describes how long it would take to deplete all of the energy. However, when the total system inertia is reported or modelled, the same value of GVA.s can be achieved in multiple ways for example as given by Table 6.1. Although they have the same value of GVA.s and the initial ROCOF is the same, the frequency responses will diverge as the frequency deviation from nominal increases due to the non-linear swing equation [122]. However, the frequency deviations experienced during frequency stability studies are usually in the range of 0-1 Hz, because extreme system state control such as load

shedding will start to operate. During frequency deviations within this size, the frequency response is still approximately linear and it can be concluded that the value of GVA.s is sufficient to describe the quantity of system inertia.

As described in Chapter 2 and repeated here as a refresher, primary response is used to arrest and contain the frequency deviation following a disturbance. It is incorporated into the SG in the form of proportional control (droop control). They typically use a droop characteristic of between 3-5% (0.03-0.05), which is given by the symbol R [122]. In an ideal primary frequency response, where the governor control and physical action have no time delays, the response can simply be given as (6.1) where P_m is the mechanical power reference, $\Delta\omega$ is the difference in angular speed and α is the load reference. In this research the term *Ideal response* refers to primary response that is not restricted by thermal or mechanical governor or prime mover delays.

$$P_m = \Delta\omega \frac{1}{R} + \alpha \tag{6.1}$$

Using a single machine infinite bus (SMIB) system and the scenario data provided in Table 6.1, it can be seen that similar droop characteristics and inertia values can lead to different frequency responses (under ideal conditions). The significance of the scenario labels used will be explained at the end of this paragraph. Comparing scenario φ11200 and scenario φ12000 in Fig. 6.1, the frequency response is visibly different. It can also be seen that scenario φ14284 which has a less steep droop percentage of 7%, still provides the best response. From this it can be concluded that droop percentage is not an accurate measure for the operation of primary response because the quantity of response also relies on the rating of the SG. Although these scenarios are used just for illustration, it can be concluded that quantifying the primary response solely as either a capacity or based on the droop percentage, does not accurately reflect how well the frequency will be contained. It is more useful to quantify the primary response in MW/Hz, denoted in this work as φ or (φ/10 to improve the resolution to MW/0.1 Hz). The value of φ can be calculated using (6.2) where f_n is the nominal system frequency and S is the machine rating.

$$\varphi = \frac{S}{f_n R} \tag{6.2}$$

From this measure it becomes clearer that scenario φ14284 provides the greatest response to the system even though it has the lowest gradient droop. The measure of φ represents a response that does not take delays into account.

Table 6.1. Example inertia scenarios

Scenario	$S_{sys}\ (GVA)$	$H_{sys}\ (s)$	GVA.s	R	φ (MW/Hz)
φ11200	28	4.285	120	0.05 (5%)	11200
φ12000	30	4	120	0.05 (5%)	12000
φ14284	50	2.4	120	0.07 (7%)	14284

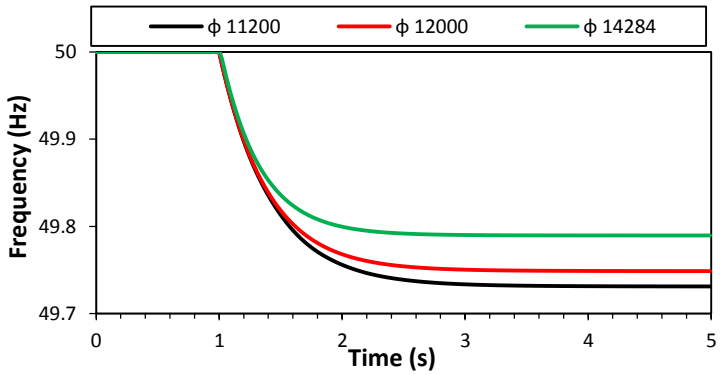

Fig. 6.1. System response with ideal primary response

6.1.2 Proportional and Realistic Primary Response

The frequency response in traditional power systems predominantly comes from SGs, and the actual primary response differs from the ideal proportional response because the governor control has physical restrictions that depend on the type of generator (e.g., steam, hydro etc.), and the type of governor control circuit. Inside the governor control circuit there exist intentional dead bands to prevent unwanted operation. There is also hysteresis associated to the mechanical components such as the valves in the turbine. The governor control that provides the mechanical power to the turbine (P_m) may be represented using a simple reduced order model. The model may be reduced by ignoring all time constants involved in the governor model apart from the dominant prime mover operation time constant. This allows the governor model to be represented by a dead band, droop gain, and a first order time constant (τ_{SG}) to represent the prime mover operation as given by Fig. 6.2 and outlined in [163, 164].

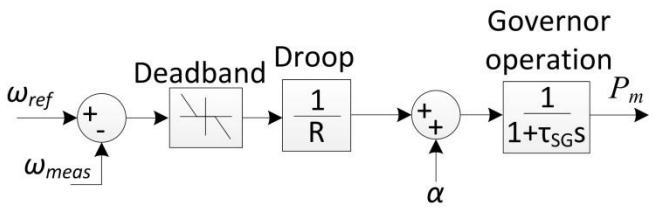

Fig. 6.2. Reduced governor model

Using parameters from scenario φ12000, a comparison between the ideal case and two non-ideal implementations given as Gov 1 and Gov 2 are displayed in Fig. 6.3, with the illustrative parameter values for each governor provided in Table 6.2. The values of τ_{SG} can be used to represent different turbine fuel types such as hydro, gas, and steam. The different fuel types and their associated governor models lead to different response times. For instance, hydro types are able to respond faster than gas and steam which would lead to a lower value of τ_{SG} [165]. In Fig. 6.3, it can be seen using these simplified reduced order models, how the limitations of the governor impact the frequency response and ultimately lead to a larger frequency deviation and a second order response from the SG.

The quantity of actual primary response that is supplied by each implementation for a given frequency deviation is displayed in Fig. 6.4. The plot is produced by quantifying the additional active power injection that occurs as the frequency deviation increases. In Fig. 6.4 it can be seen that the response from the ideal case matches the expected (calculated) MW/0.1 Hz deviation. It is also evident that the governor action has a significant impact on the quantity of frequency response provided by a certain frequency deviation when compared to the ideal case. From this it can be concluded that although there may be an expected value of φ (MW/Hz) response, the actual MW/Hz response is dependent on the governors within the system. So the actual response is different from the expected (ideal case) and should be taken into consideration for future frequency response schemes.

Table 6.2. Dead band and gain simulation values

Scenario	Dead band (mHz)	τ_{SG} (s)	R (%)	φ (MW/0.1 Hz)
Ideal	-	-	0.05 (5%)	1200
Gov 1	15	0.7	0.05 (5%)	1200
Gov 2	15	0.4	0.05 (5%)	1200

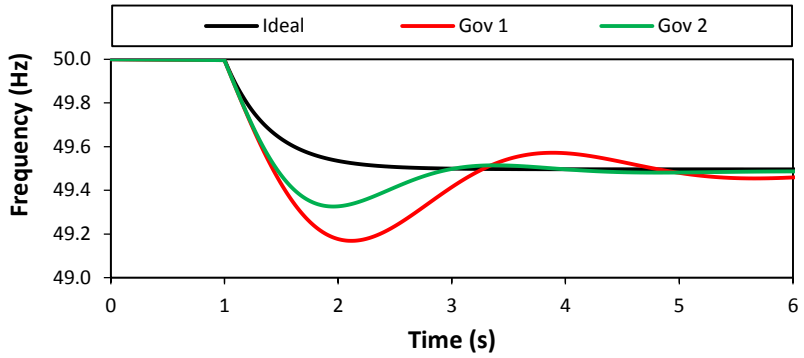

Fig. 6.3. Frequency responses for different governor parameters

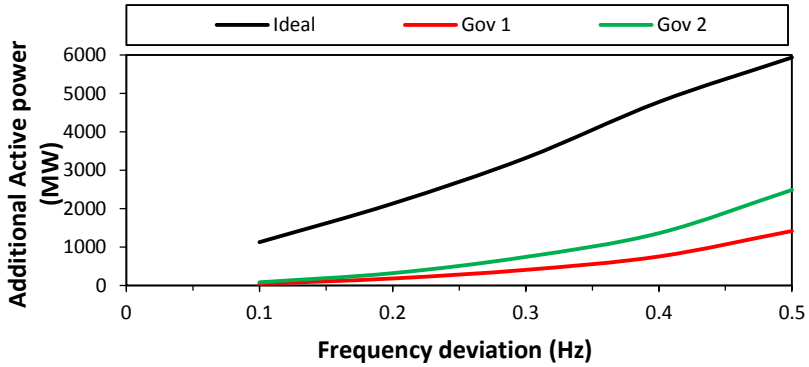

Fig. 6.4. Governor impact on the quantity of frequency response

6.1.3 Increasing the Quantity of Primary Response

In order to reduce the MW/Hz difference between ideal and actual frequency response, the power system operator would need to tender for an increased quantity of response. This is especially crucial as the system inertia reduces and there is more reliance on ancillary frequency control services to prevent frequency operating limits from being violated. The additional response may come from SG or from power electronic (PE) sources, with the significant difference between them being the anticipated operational time. The droop characteristic used is dependent on the network operator guidelines.

Additional fast frequency containment response may come from PE connected energy sources that can respond faster than a SG. These may have the same droop characteristic, but are not inhibited by mechanical delays resulting in a faster operational time. A simple reduced model of the droop scheme frequency response enabled PE energy source is displayed in Fig. 6.5, where τ_{conv} represents the power electronic converter operation delay. The additional power reference from the supplementary frequency control loop (ΔP) is added to the steady state power

reference (P^{ref}) to produce the unrestricted power reference (P^*). The reduced converter model also incorporates a limiting function to prevent sudden or large changes from occurring that is described in Chapter 4 and uses the ramp rate parameter P^{rr} that is provided in MW/s. The limiting function ramp rate is incorporated as given by (4.13) in Chapter 4 to determine $\hat{P}$. These reduced models allow the impact of the different crucial parameters for frequency stability to be investigated. This model differs from the one presented in Chapter 4 because it does not incorporate dq control or an average value MMC model. The converter is represented by a static generator and includes the proportional frequency control loop and the ramp rate limiter that was presented in Chapter 4.

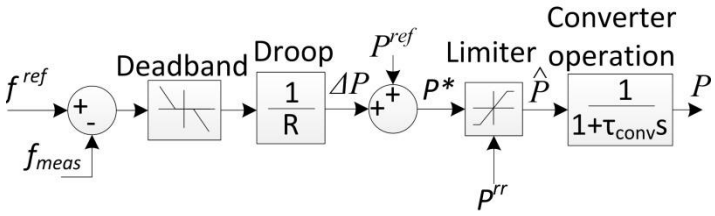

Fig. 6.5. Reduced PE frequency response enabled energy source

Using parameters given in Table 6.3, the same capacity of additional response from a SG (SG5000 scenario) and a PE device (PE5000 scenario), that both have an additional capacity of 5000 MW, are compared against the ideal case (Ideal) and the case where there is no additional response (Gov 1). The frequency response is displayed in Fig. 6.6 and the actual MW/Hz response for each case is displayed in Fig. 6.7. It can be seen that adding the same MW capacity and droop characteristic for a SG or for a PE device will result in an improvement in the frequency response, as expected. The PE deployment has a faster response due to lower operational delays. In this setup, in order to achieve the same MW/Hz response as the PE5000 scenario, the capacity and the droop characteristic of the PE device could be halved as given by the PE2500 scenario that has an additional capacity of 2500 MW (unlike with a SG). This would lead to the same MW/Hz response as displayed in Fig. 6.8. Halving the droop gain as in the PE2500 scenario may not be viable and would depend on the converter characteristics, the SO's requirements, and the network characteristics. This illustrates that the change in PE capacity alone has no effect on the frequency response as no inertial support is provided.

Increasing the capacity of MW/Hz frequency response, whether from a SG or a PE device, still leads to a deficit in power between the Ideal case and the actual response. The difference is due to the delayed operation that is associated with the prime mover time constant in a SG and with the operating time constant in the converter.

Table 6.3. Example scenario parameters

Scenario	Device	τ_{SG} (s)	τ_{conv} (s)	R (%)	Additional capacity (MW)	φ (MW/0.1 Hz)
SG5000	SG	0.7	-	0.05	5000	1400
PE5000	PE Droop	-	0.1	0.05	5000	1400
PE2500	PE Droop	-	0.1	0.025	2500	1400

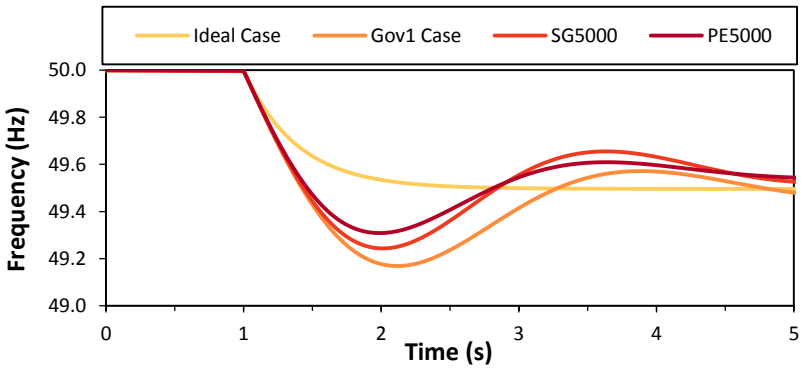

Fig. 6.6. System response comparing SG and PE frequency response

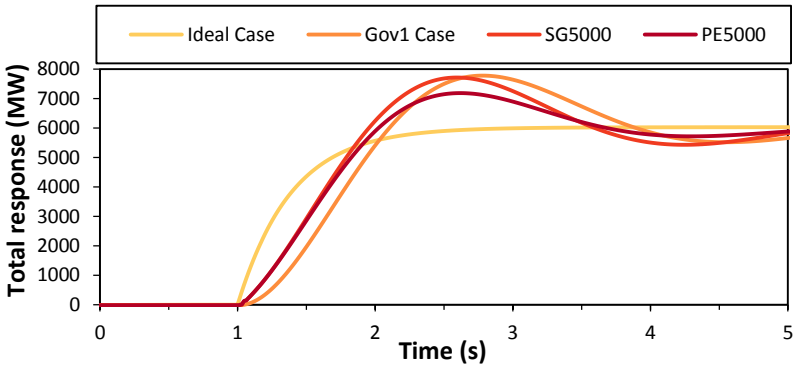

Fig. 6.7. System response comparing SG and PE active power response

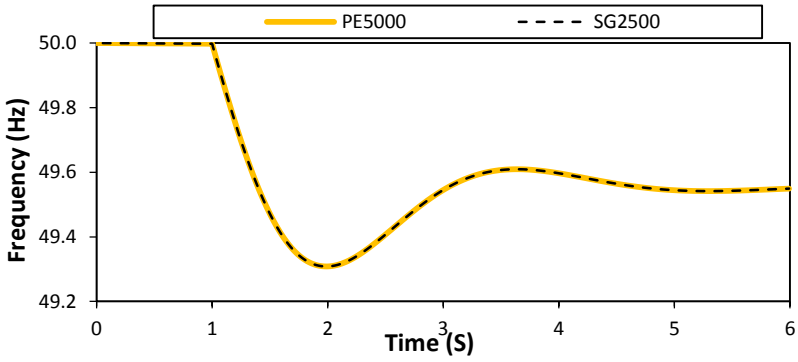

Fig. 6.8. Frequency response when applying two PE capacity and droop scenarios

The difference between the ideal and the actual response of the system as displayed in Fig. 6.7 can be quantified using an RMS measure denoted as $\varepsilon_{\Delta P}^{rms}$ as given by (6.3). In (6.3), the variable N is the number of samples, P_{actual} is the value of the total actual power response at the sampled time-step, and P_{ideal} is the Ideal power response that would occur at the sampled time-step if governors and prime movers were not subject to any time delays. The subscript i refers to a sampled value. Using this measure, the improvements in response can be quantified in relation to an Ideal response. The values of $\varepsilon_{\Delta P}^{rms}$ for the example scenarios are provided in Table 6.4. These values are calculated from the time period of the disturbance occurring to the time the frequency has settled to within 0.1% of the final steady state settling value given by f_{set} (i.e. from the time of the disturbance to the end of the considered time horizon for these simulations) using a sample resolution of 10 ms (i.e. the time-step of the dynamic simulation). It can be seen that using this measure enables a straightforward comparison measure of the different response types, which nonetheless captures a composite of factors including frequency nadir, speed of response, settling time etc. It shows that the average deviation of the PE droop scheme compared to the ideal response is lower and therefore that the response in PE5000 more closely tracks the ideal response.

$$\varepsilon_{\Delta P}^{rms} = \sqrt{\frac{1}{N}\sum_{i=0}^{f_{set}}\left(P_{actual\,(i)} - P_{ideal\,(i)}\right)^2} \tag{6.3}$$

Table 6.4. Illustrative scenario average deviation values

Scenario	$\varepsilon_{\Delta P}^{rms}$ (MW)
Gov 1case	1119.01
SG5000	912.29
PE5000	735.69

6.2 Proposed Difference Control Scheme

This section presents a power electronic control scheme that is designed using the information from the previous sections and is termed *difference* control. The presented controller is also compared to a derivative control scheme to view how susceptible their outputs are when subjected to noise in the frequency measurements. The scheme is compared to a derivative controller because the output can be seen as analogous to that of a derivative scheme.

6.2.1 Controller Design

The use of PE droop control and the ability to increase the droop characteristic has proven to be beneficial in Section 6.1.3. However, the frequency control within a PE device could be improved to reduce the difference between the expected and the actual value of φ frequency response. Unlike a SG, a PE device can be operated in faster time scales and it does not have the same mechanical restrictions, enabling it to be operated in a manner that is outside of the traditional proportional control operation. The improved PE frequency control presented in this research, denoted as *difference* controller, estimates the difference between an Ideal response and the Normal system response that was highlighted in the previous sections.

To enable the difference control scheme to reduce the difference between the Ideal and the estimated system response, some additional estimated system information is required. The first required value is the equivalent system droop coefficient (R_{sys}) given by (6.4) where S_i is the rating of the machine or PE device that provides frequency support and R_i is the droop coefficient of that machine or device.

$$\frac{1}{R_{sys}} = \frac{\sum_{i=1}^{n} S_i/R_i}{\sum_{i=1}^{n} S_i} \tag{6.4}$$

The second value is the equivalent estimated time constant of the frequency response controls (τ_{sys}) given by (6.5) where τ_i is the estimated operation time constant of the frequency response device and N is the number of machines and devices providing the response. The value of τ_i could be determined per governor type using techniques described in [166, 167]. The identification of governor parameters on real plant would be difficult, and as the plant ages these values will alter. Obtaining the values via a step test manner based on the type of governor (steam, hydro, gas) is proposed at this stage where the parameters for each type of governor can be found in [127]. The step input is

achieved by altering the load reference and the time constant is calculated from the response of P_m. The controller's sensitivity to this value will be examined later in Section 6.4.3.

$$\tau_{sys} = \frac{\sum_{i=1}^{n} \tau_i}{N} \tag{6.5}$$

The third value required is the ratio of the equivalent estimated MVA rating of all frequency response devices and machines (S_i) divided by the MVA rating of the PE devices operating using the difference scheme (S_{dif_i}) to produce PE_{ratio} as given by (6.6). The number of SG providing primary response is given as n_sg and the number of PE devices operating with the difference controller is given by n_dif. This is a gain component that acts to scale the difference control output to match the short fall in power immediately after the disturbance. It enables the converter to provide the power that is delayed from the SG due to governor operation. If the converter ratings are not sufficient to provide the energy deficit, then they will saturate.

$$PE_{ratio} = \frac{\sum_{i=1}^{n\_sg} S_i}{\sum_{j=1}^{n\_dif} S_{dif\_j}} \tag{6.6}$$

The control structure uses a dead band similar to other frequency response services to prevent unwanted operation and is implemented as (6.7), where $\hat{\Delta}\omega$ is the dead band output. The difference between the Ideal system response and the estimated system response is given by (6.8) and simplified to (6.9) where the dead band is omitted. In (6.9) it can be seen that the control structure mimics a high pass filter and this should be considered when configuring the frequency measurement device (envisaged to be a phase locked loop, PLL). The value of ΔP is subject to a low limit check against P_{Low} as given by (6.10) where P_{Low} will be set to zero to prevent the supplementary reference signal from going negative after the frequency nadir has been reached. The block diagram of the control scheme is displayed in Fig. 6.9.

$$\hat{\Delta}f = \begin{cases} \Delta f + f_d & \Delta f < -f_d \\ 0 & -f_d \leq \Delta f \leq f_d \\ \Delta f - f_d & \Delta f > f_d \end{cases} \tag{6.7}$$

$$\Delta P = PE_{ratio}(\hat{\Delta}f\ \frac{1}{R_{sys}} - \hat{\Delta}f\frac{1}{R_{sys}}\ \frac{1}{1+\tau_{sys}\ s}) \tag{6.8}$$

$$\Delta P = PE_{ratio}\hat{\Delta}f\ \frac{1}{R_{sys}}(\frac{\tau_{sys}\ s}{1+\tau_{sys}\ s}) \tag{6.9}$$

$$\hat{\Delta}P\ = \begin{cases} P_{Low}, & \Delta P \leq\ P_{Low} \\ \Delta P, & \Delta P > P_{Low} \end{cases} \tag{6.10}$$

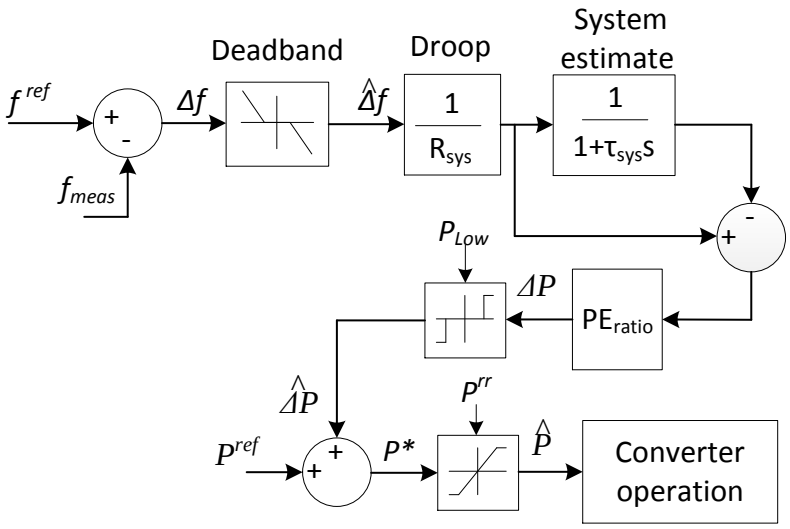

Fig. 6.9. Difference control structure

6.2.2 Noise Comparison with Derivative Control

The presented controller is subjected to noise response analysis to ensure that no detrimental behaviour occurs when the measured frequency contains noise components. In this analysis the noise component (f^n) is added to the frequency measurement that is used by the MMC frequency control loop as displayed in Fig. 6.10.

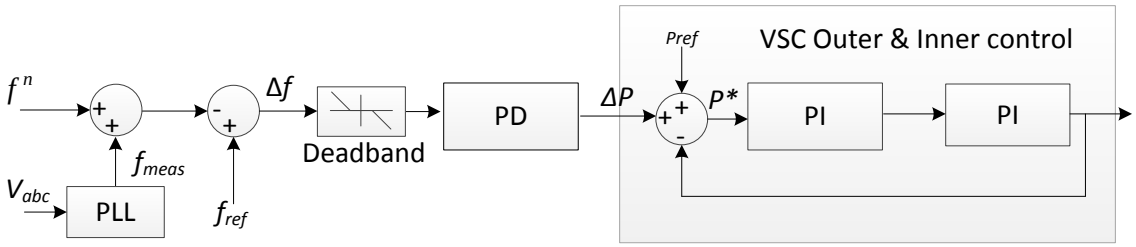

Fig. 6.10. VSC frequency controller with noise incorporation

To view how susceptible the difference controller is to noise in the frequency measurement, it is compared to the derivative controller. Both control schemes are

analysed when subjected to noise in the frequency measurements. The noise component is directly added to the frequency measurement. The noise signal has two components, amplitude $f^{n\alpha}$ and frequency of change in the noise signal $f^{n\beta}$ that are displayed in Fig. 6.11. The noise amplitude causes a change in the measured frequency in Hz which makes it deviate from its nominal value of 50 Hz. The amplitude of the noise signal also changes at a fixed rate or time step, this also can be viewed as a frequency change. To prevent confusion between the change in measured frequency and the rate that the noise signal is changing, the rate that the noise signal amplitude changes will be given in ms.

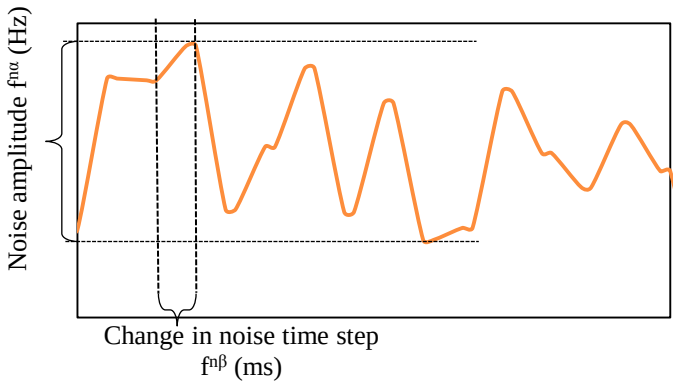

Fig. 6.11. Noise signal components

In Fig. 6.12(a) - Fig. 6.12(c) the control schemes are subjected to a noise profile that changes every 6.6 ms and has a maximum deviation of 0.05 Hz. The plot in Fig. 6.12(a) displays the addition of the noise component to the measured frequency. In Fig. 6.12(b) the active power error (P^*) that is before the current limiter in MMC control structure is displayed. The converter output that has been subject to the current limiter and the PI control loops is displayed in Fig. 6.12(c). Similarly, Fig. 6.12(d)-Fig. 6.12(f) display the results for both controllers when they are subjected to a noise component that changes every 10 ms with a maximum deviation of 0.25 Hz. The initial differences seen in the converter output is due to the noise signal been present when the initial conditions are determined for the simulation that occurs from -0.1 s to 0 s.

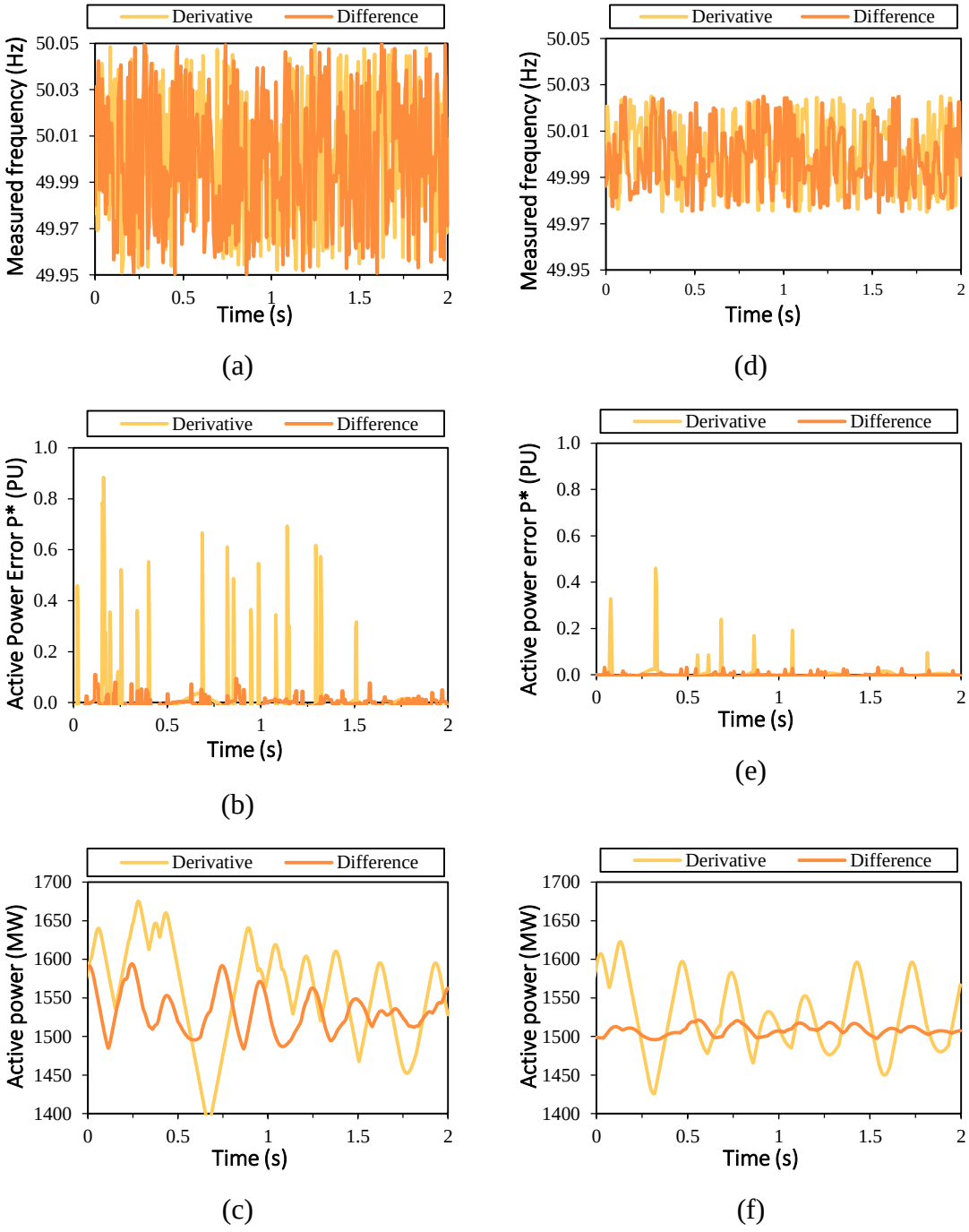

Fig. 6.12. Analysis of the difference and derivative control schemes when subjected to uniform noise. (a)-(f) 6.6 ms, 0.05 Hz deviation, (d)-(f) 10 ms, 0.025 Hz deviation

The analysis displays that both controllers are affected by noise in the frequency measurements. However, the difference controller is seen to be less susceptible to noise and that makes it more viable for implementation when inertial type responses are required.

6.3 Simulation Setup

The analysis in this chapter is performed using the SMIB and NETS systems that are described in Chapter 2 with the system parameters provided in Appendix Sections B3.1 and B3.2. The converter operation that encompasses the PE control is modelled using a non-rotating generator detailed in [138, 168] and is modified with a first order time delay (τ_{conv}) that represents converter operation delay. The PE control signal $\hat{P}$ presented in Fig. 6.5 and Fig. 6.9 is input into the PE device model to control the output power as displayed in Fig. 6.13. The time constant τ_{conv} representing all communication and operation delays of the converter is set to 0.1 s as it is expected that when all internal control loop bandwidths and delays are considered, the converter will effectively operate in this timeframe [169]. The frequency measurement is achieved using a PLL with the per unit values of K_p = 12.56 and K_i = 39.47. The ramp rate value P_{rr} is set at 2 GW/s to factor in future improvements in semiconductor technology and cooling ability that would take the value beyond the 1 GW/s value stated in [153]. The dead band used is set to 15 mHz as stated in [125].

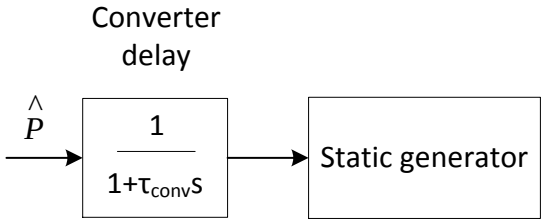

Fig. 6.13. PE device implementation

In the SMIB setup, there is a single PE device that has a capacity of 5 GW. For the NETS system, four PE devices each having either 50 MVA or 100 MVA ratings are implemented and located arbitrarily at buses 6, 16, 18, and 23. Separate setups are investigated for PE operating using droop (PE Droop) and difference (PE Dif). The PE parameters used in the analysis are given in Table 6.5.

Table 6.5. PE frequency control parameters

Scenario	*PE cap.(GW)*	R_{pe}	τ_{conv} (s)	τ_{sys} (s)	R_{sys}	PE_{ratio}
SMIB PE Droop	5	0.05	-	-	-	-
SMIB PE Dif	5	-	0.1	0.7	0.05	7.00
4x50 PE Droop	4×100	0.05	-	-	-	-
4x100 PE Droop	4×50	0.05	-	-	-	-
4x50 MVA PE Dif	4×100	-	0.1	0.7	0.05	17.75
4x100 MVA PE Dif	4×50	-	0.1	0.7	0.05	35.50

6.4 Analysis of FFR Control Scheme

This section investigates the improved difference scheme when it is implemented into a SMIB system and the NETS system using the control scheme presented in Fig. 6.9.

6.4.1 Evaluation of the FFR Scheme in the SMIB System

The time series evolution showing the additional power injected into the system by all energy sources, for the given frequency deviation following a disturbance, is displayed in Fig. 6.14. It displays how the power injection into the system changes over time as the frequency deviates. In this section *Normal* refers to a response where the SGs are operating with the WIESG1 turbine governor and there is no PE controller incorporated. The *Normal* response curves are due to the delayed reaction of the governor before reaching the settling frequency. The *Ideal* response does not experience a circular trajectory because there are no time delays present. Using the difference scheme, it can be seen that there is a greater initial power injection compared to the *Normal* and *PE Droop* responses and this acts to contain the frequency deviation quicker. In Fig. 6.15 the actual time series power response for each scenario is displayed and shows that the *FFR* implementation approximately follows the *Ideal* case and results in a lower second order response. The difference scheme does not completely match the *Ideal* system response due to the converter operational delays, the simplified representation and estimation of the system response, and the resultant network dynamics.

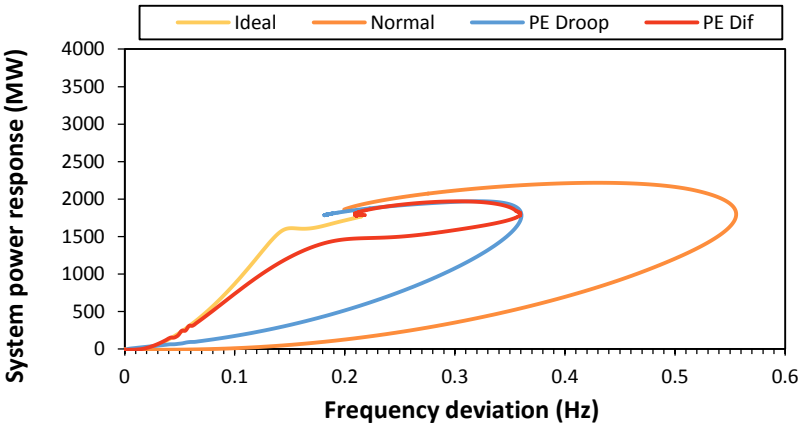

Fig. 6.14. Time evolution of the system response vs frequency deviation

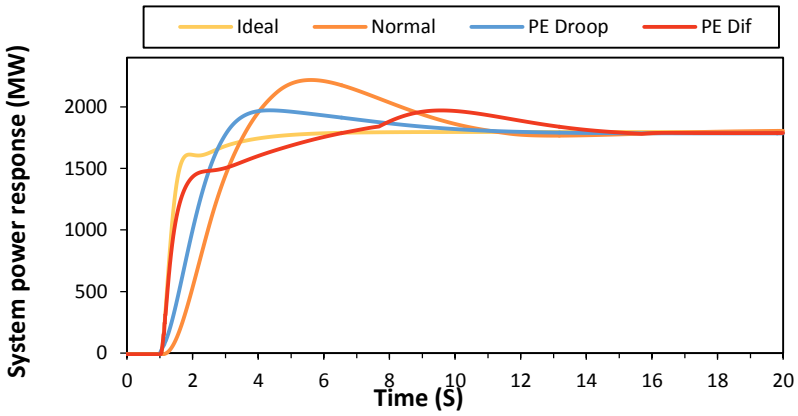

Fig. 6.15. Total system power response

For the PE Dif scenario, the portion of active power injected from both the SG and the PE device are displayed in Fig. 6.16 to highlight the portion of additional power from the PE Dif scheme. It can be seen that the difference controller provides support where the SG response has not had time to initiate or fully deploy. The power output from the difference controller returns to zero as the difference reduces and the low limit prevents the reference from going negative which would reduce the power transfer for assets such as interconnectors that operate with a steady state reference as well.

The frequency response for all scenarios is depicted in Fig. 6.17 and the corresponding ROCOF and nadir for each scenario is provided in Table 6.6. The ROCOF values are measured from the initiation of the disturbance and is taken over the first 1000 ms. Using the difference scheme, the nadir is improved by 0.2 Hz compared to the *Normal* scenario. The ROCOF after the first second is reduced by 0.169 Hz/s compared to the *Normal* scenario. The average deviation away from the Ideal response for each scenario is provided in Table 6.6 and displays that the PE Dif significantly reduces the deviation away from the ideal response case.

Table 6.6. Analysis of the frequency response schemes in the SMIB system

Scenario	1 s ROCOF(Hz/s)	Nadir (Hz)	$\varepsilon_{\Delta P}^{rms}$ (MW)
Normal	-0.355	49.44	373.65
PE Droop	-0.291	49.63	222.82
PE Dif	-0.186	49.64	116.41

Attempting to obtain a truly ideal response using the difference scheme would be complex due to the changing nature of a power system and would require large quantities of real time data. Although the parameter estimation used in this research is simple, it is still effective when coupled to this difference control scheme.

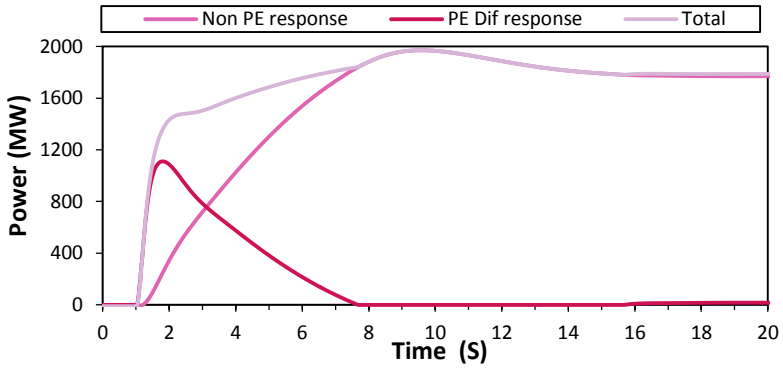

Fig. 6.16. Response for the PE Dif scenario from the SG and the PE

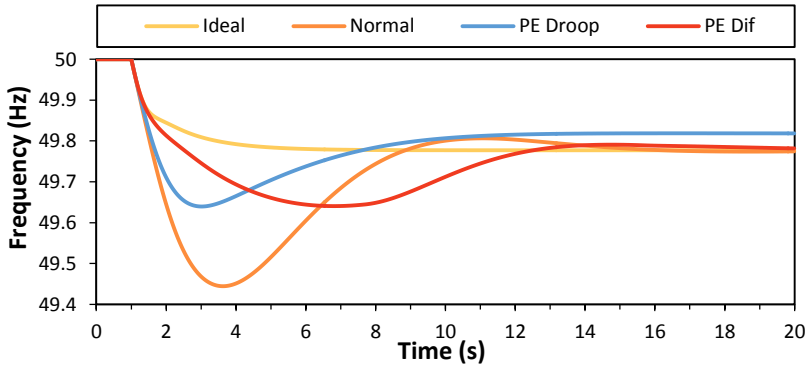

Fig. 6.17. Frequency response comparison for the SMIB setup

6.4.2 Impact of Available PE Capacity for the FFR Scheme in the SMIB

The amount of capacity or headroom is the combined quantity of power that can be provided from all PE devices operating using the difference control scheme. This is equivalent to power sources such as interconnectors operating with spare capacity for

the purpose of frequency response or battery storage where there may be limited power available. A reduction in the nadir over the *Normal* scenario nadir for different quantities of available PE capacity is displayed in Fig. 6.18. For the difference-based method presented, it can be seen that even when there is minimal capacity available, there are still system benefits. It can also be seen that beyond a certain amount of capacity for this difference method, there are no further system benefits and so there is a useful capacity operating range of between 0.03–1 GW for the considered system. Beyond a certain amount of capacity there is no further improvement to nadir. This is because the capacity has reached a level that is sufficient to provide the estimated difference in energy between the ideal case and the actual. The maximum capacity incorporated into a system would need to be evaluated based on the parameters presented in Section 6.2.

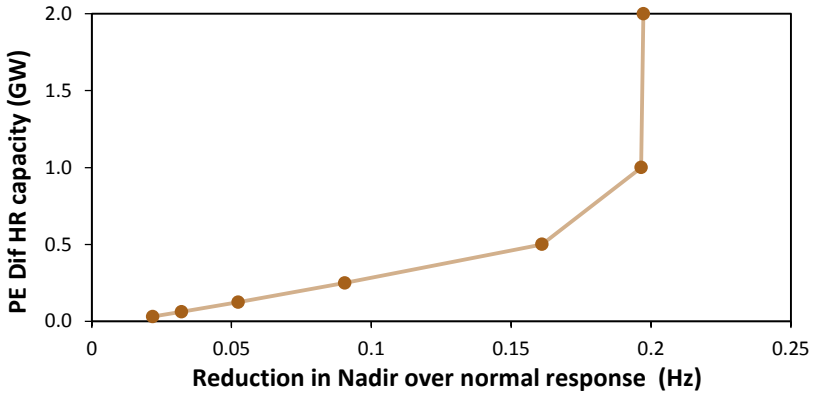

Fig. 6.18. Impact of capacity on maximum frequency deviation

6.4.3 Impact of Estimated Parameters for the Difference Scheme in the SMIB

The impact of the time constant estimation is investigated using three different values of τ_{sys} to highlight how sensitive the control scheme is to this value. The output response of the PE device is displayed in Fig. 6.19(a) and shows that an under estimation of τ_{sys} leads to a reduced initial power injection combined with a reduced power injection duration. The impact of this change on the system frequency is displayed in Fig. 6.19(b).

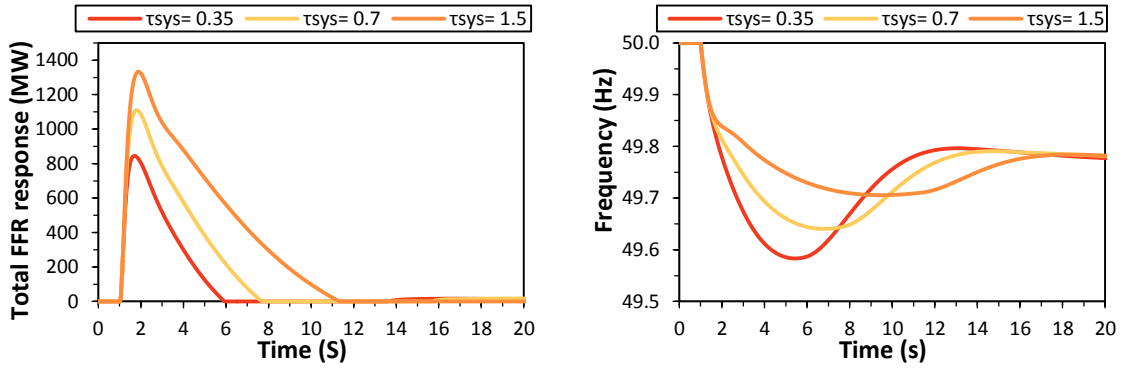

(a) (b)

Fig. 6.19. Impact of changing τ_{sys} . (a) difference controller power response, (b) system frequency

The differences displayed are due to the converter attempting to provide the deficit in power; therefore if the estimated system response is slow (larger value of τ_{sys}) then the converter would be required to provide greater power for longer. An under estimate would lead to a lower power injection over a shorter time period. The initial injection of power differs by 507 MW for a change in τ_{sys} of 1.15 s in the setup presented. To limit the potential large power injection into the system or prevent a response that is too large, the value of τ_{sys} could be reduced by a compensation factor to reduce the impact of any potential parameter over estimation.

Similarly, three distinct values for PE_{ratio} are used to investigate the impact of the estimated ratio between the amount of frequency response provided from difference and non-difference controlled devices. The results in Fig. 6.20(a) and Fig. 6.20(b) display that an over-estimation of the ratio (estimation that there is greater non-difference controlled or less difference controlled devices) lead to a greater initial difference controller response that is active for a longer duration.

Overall, changing the value of these parameters does not lead to any detrimental operation or system issues in terms of oscillatory behaviour that was highlighted in Chapter 5. Incorrect estimation could lead to a reduced or a greater impact on the system frequency, but does not cause extreme changes or introduce additional oscillatory behaviour. Indeed, in the future this scheme could be intentionally operated to provide response that does not aim to achieve an ideal response from the traditional primary response schemes. The parameters could be set to create a bespoke frequency response that has an initial maximum injection quantity and unique decaying response.

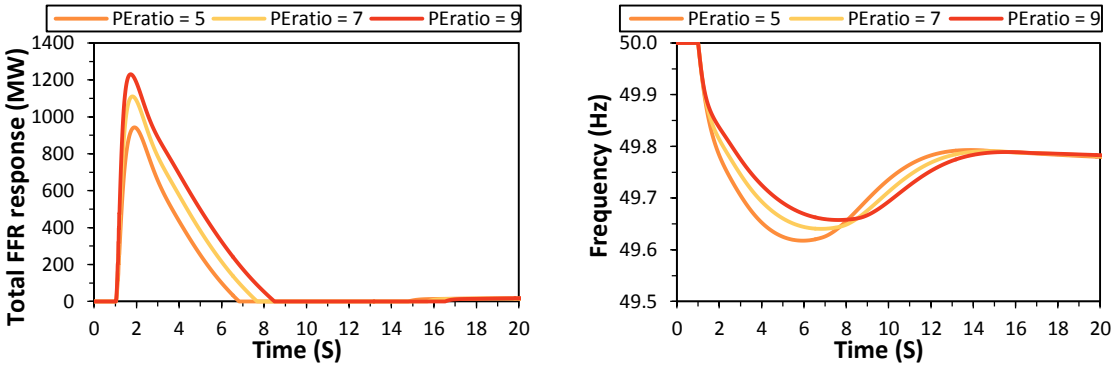

(a) (b)

Fig. 6.20. Impact of changing PE_{ratio}. (a) difference controller power response, (b) system frequency

6.4.4 Evaluation of the Difference Control Scheme in the NETS System

The difference control scheme is further evaluated in a larger more complex system than a SMIB to establish its effectiveness when there is additional system dynamics involved. The two chosen PE setups for the NETS system (100 MVA and 50 MVA units) are investigated. The total system power response is displayed in Fig. 6.21, where both cases are compared to a case with no PE response and PE droop schemes. Both PE Dif control setups enable an increased quantity of power injection immediately after the disturbance which reduces the nadir. The PE Dif case with four 50 MVA units totalling 26% of the disturbance size has limited capacity, but even with the reduced capacity the scheme still reduces the nadir by a significant 0.474 Hz compared to the case with no PE Dif incorporated. The ROCOF values after 1000 ms of the disturbance occurring, and the subsequent improvement in ROCOF is displayed in Table 6.7 and compared to the same PE cases operating with droop schemes. The average deviation away from the ideal response ($\varepsilon_{\Delta P}^{rms}$) is also provided in Table 6.7. The values display the reduction in average deviation away from the ideal response when using the difference controller scheme, confirming the benefit in using the method. Both difference-based schemes reduce the second order response of the active power output that is dominated by the SG governor delays.

Table 6.7. Analysis of the ROCOF in the NETS system

Scenario	1 s ROCOF (Hz/s)	Δ in 1 s ROCOF (Hz/s)	$\varepsilon_{\Delta P}^{rms}(MW)$
No FFR	-0.359	-	
4x50 PE Droop	-0.355	0.003	102.48
4x100 PE Droop	-0.347	0.012	84.44
4x50 MVA PE Dif	-0.304	0.055	67.80
4x100 MVA PE Dif	-0.256	0.103	64.37

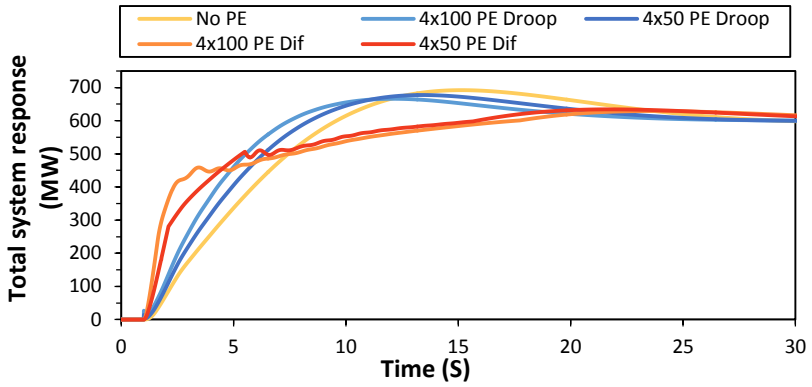

Fig. 6.21. Total system power response for the NETS system

The combined PE Dif control power output for both cases is displayed in Fig. 6.22 and highlights the similarity in response but with the limited capacity for the 50 MVA unit setup. In Fig. 6.22 it can be seen that there are oscillations in the difference controller output - these are due to the rotor angle oscillations occurring in the network. Depending on the severity of these oscillations, the PLL used to measure the frequency for the difference controller scheme could be tuned to minimize the impact of low frequency oscillations, or additional filtering could be applied. The severity of the output oscillations will be determined by the characteristics of the network and the ratio of the SGs to PEs and is a factor for the future.

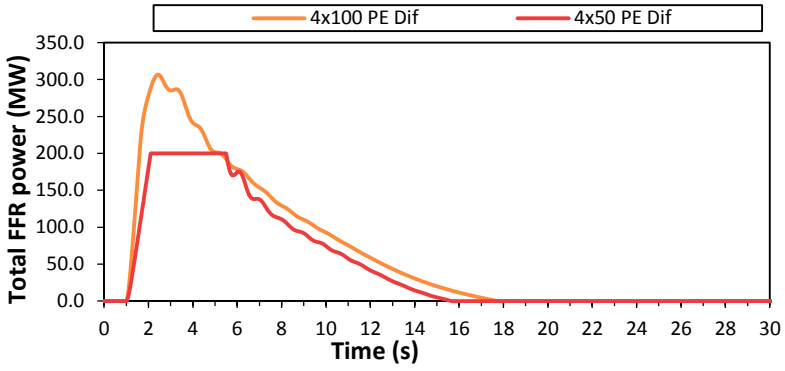

Fig. 6.22. FFR power output comparison

The difference control scheme presented in this research has used estimated values from the system to determine and limit the response from the PE device. However, this concept could be extended further by using bespoke values in place of R_{sys}, τ_{sys}, and PE_{ratio} to produce different response characteristics from the difference controlled capable device. Using bespoke values would require more care to be given when assigning or tuning the controller, but could be used to produce unique response characteristics to achieve specific target functionality.

6.5 Summary

Within this chapter, the quantification of frequency response in terms of MW/Hz is shown to be a more useful measure than capacity or droop alone. It is also shown that although there is an expected MW/Hz response based on defined controller parameters, the actual response will differ due to the mechanical delays.

To reduce the difference between the idealized proportional system response and the actual system response, this chapter has presented a difference control scheme (aimed at being a fast frequency response) for implementation into power electronic connected energy sources. The difference scheme enables an enhanced fast frequency response supplementary control signal. The control requires limited system information that does not have to be available in real time. The results demonstrate that the control can significantly reduce the frequency deviation, but cannot completely achieve an ideal response. This is due to the use of a reduced estimation of the system response to reduce complexity. An ideal response would also be unattainable because the action from the difference controller would cause the SG to alter their response and change the dynamics of the system.

The difference control scheme presented in this paper enables a faster response to frequency deviations that is analogous to an inertial response, without introducing the detrimental behaviour common with derivative control implementation. The scheme would allow the system operator to be more confident about the quantity of MW/Hz frequency response, potentially reducing the need to over-tender for the service.

The research from this chapter has completed objective 6. The controller presented in this chapter will be compared against other VSC frequency control options in Chapter 7 where they will be operated under various network operating scenarios that were highlighted in Chapter 3.

7 Evaluation of VSC-HVDC Frequency Response Scheme Deployment

The VSC-HVDC frequency response schemes previously presented in Chapters 5 and 6 are designed to reduce the nadir or ROCOF, or simply improve the overall frequency stability by injecting power. The schemes previously presented in the literature and in this research so far have not taken into consideration how various network factors may influence the effectiveness of certain VSC frequency control schemes. No consideration has been placed on understanding how network operation may change the effectiveness of the VSC frequency response. Their deployment could be better informed by taking into consideration various network and control operating factors. For instance, instead of simply designing and integrating a VSC frequency response scheme, the decision of which scheme to implement could be taken based on which frequency metric is of greater concern, nadir or ROCOF. As well as deciding which metric to target, the network operation should be taken into consideration as it may change the effectiveness of the implemented frequency control scheme, as shown in the previous chapter.

The VSC frequency response schemes that were reported in the literature in Chapter 1 were predominantly droop and derivative schemes. In Chapter 5 the droop scheme implementation was updated and in Chapter 6 a new *difference* controller was presented that adds to the potential number of VSC frequency controller options available. The difference between these control types in terms of frequency containment may be insignificant or only apparent in certain situations or network operating conditions. It is yet to be seen how these different controllers perform in relation to each other in different network operating scenarios.

In Chapter 3, certain network factors were shown to influence the frequency stability and impact the frequency stability metrics of nadir and ROCOF. This chapter will use the information about the network factors, and will build on that analysis by adding in a variety of VSC-HVDC frequency controllers. The aim of this chapter is to investigate how different VSC-HVDC frequency control types perform under different network and control operating scenarios, in order to evaluate their effectiveness. This component of research could lead to improved or targeted deployment of the VSC-HVDC frequency control services, where the service has a stronger influence on either the nadir or

ROCOF or a combination. The following four additional factors are investigated in this section:

1) VSC-HVDC frequency response capacity.
2) VSC-HVDC frequency response location.
3) Quantity of SG primary response in the system.
4) Quantity of system inertia.

Along with these factors, two different network setups that represent the best case and worst case operating scenarios found in Chapter 3 are used.

7.1 Test system details

The generic four area test system presented in Chapter 2 is used to perform the analysis with the incorporation of VSC-HVDC in-feed that can provide frequency response. In this chapter the frequency response is provided using a VSC-HVDC interconnector making the results only applicable to large VSC assets and not low voltage DC or medium voltage DC applications.

7.1.1 Modifications to the test network

The generic four area test system described in Chapter 2 is used to facilitate quantifiable network changes. In addition to the standard four area test system, VSC-HVDC in-feeds representing interconnectors are incorporated into Area1 and Area4 as displayed in Fig. 7.1. The disturbance size used for this analysis is 1.8 GW. Both of these VSC-HVDC in-feeds represent a connection to a large network where the sudden transfer of power would not destabilise the attached network. Only one VSC-HVDC in-feed will be enabled at a time to provide frequency response and when they are not operating in frequency sensitive mode, they will operate as constant power sources. The VSC-HVDC in-feeds operate with the dq current control presented in Chapter 4. The converter station connected to the four area test system operates in P, Q mode and the remote converter operates in V_{DC},Q mode. There will be two network topology configurations used throughout as displayed in Fig. 7.2, where T1 represents a highly meshed low impedance topology, and T6 represents a radial network with higher impedance between areas. The synchronous to non-synchronous generation ratio is set to 50% synchronous and 50% non-synchronous and this generation dispatch is unchanged throughout this analysis. Full dispatch detail is given in Appendix Section E.2.

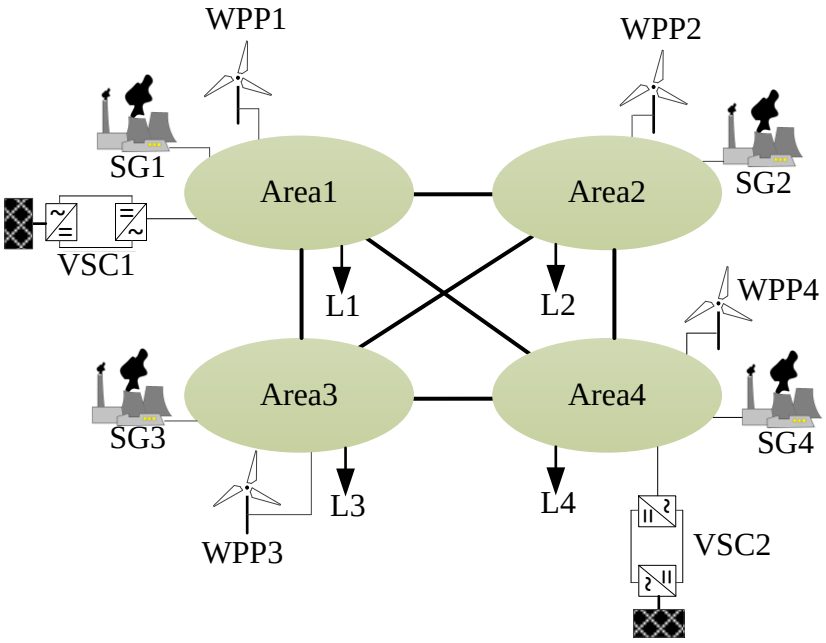

Fig. 7.1. Updated four area test system with VSC-HVDC in-feed incorporated in Area1 and Area4

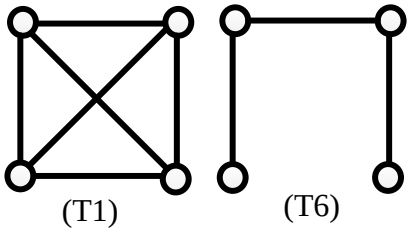

Fig. 7.2. Topology configurations used for this component of research

Four VSC frequency control schemes are considered and evaluated. The four schemes are droop, derivative, difference, and combined. They will be operated individually in the system and not together, so that the impact of each type can be isolated and examined. The four control schemes considered are described below.

Droop – the droop scheme is detailed in Chapter 4 and will operate with a 5% droop coefficient that is in-line with existing SG droop values. As the VSC-HVDC in-feed is a large power source similar to a large generator, a similar droop value has been used to enable the VSC to co-ordinate with the SGs. This will prevent too much reliance being placed on the VSC-HVDC to correct the power imbalance following the disturbance and should make it more co-operative with existing SGs.

Derivative – this derivative scheme is detailed in Chapter 4 and will operate with a 0.5 Hz/s ROCOF causing a 100% change in VSC active power output. As the VSC device considered is an interconnector, it will be operating with a steady state power injection that reduces the overall available capacity for frequency response. This means

the output is more likely to saturate when a ROCOF over a certain value occurs. It is noted that to the author's knowledge, this is the first time that a VSC derivative control that is designed such that a maximum ROCOF value leads to a 100% change in converter output has been implemented.

Difference – this control scheme is the innovative VSC frequency control scheme that was presented in Chapter 6 and is termed the *difference* controller to distinguish it from the other control types. This VSC frequency controller aims to provide the difference between the ideal system frequency response (assuming no thermal or mechanical delays in the system) and the actual system frequency response that is delayed due to SG mechanical delays. It can be seen as somewhat analogous to an inertial response that reduces in-line with the ROCOF.

Combined – this control scheme incorporates elements of both droop and derivative control, enabling it to target initial high ROCOF and then also provide power injection to improve nadir. The scheme presented is designed to use 50% droop and 50% derivative with the control scheme displayed in Fig. 7.3. The droop and derivative components are setup as the previously described droop and derivative controllers and their output is summed. Their output contribution is limited in this controller by the variables $\alpha 1$ and $\alpha 2$. These variables are multiplication factors that can be set between 0 and 1 where 0 sets that control component output to have a 0% contribution and 1 sets the control contribution to 100%. The values for these variables are both set to 0.5 allowing 50% of each control type to be used. The combination of these two control functions may make the VSC output more susceptible to saturating, but it will make better use of the available capacity than just droop or derivative alone.

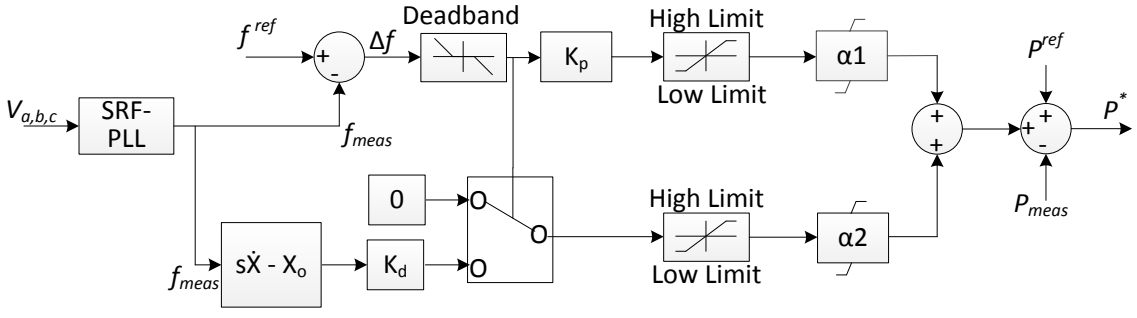

Fig. 7.3. Combined VSC frequency control scheme

Example open-loop responses from the four VSC frequency response schemes are displayed in Fig. 7.4(a) to highlight how each control option responds as the frequency changes. The frequency plots shown in Fig 7.4(b) are an illustrative time series plot for

each control option to aid visualisation for how each VSC frequency control type responds as the frequency changes. It is noted that each VSC control type would change the trajectory of the frequency and lead to a unique frequency plot if they were implemented in closed loop. It is also noted that the actual magnitude of the response from each control option will be different and based on the resulting frequency response of the system.

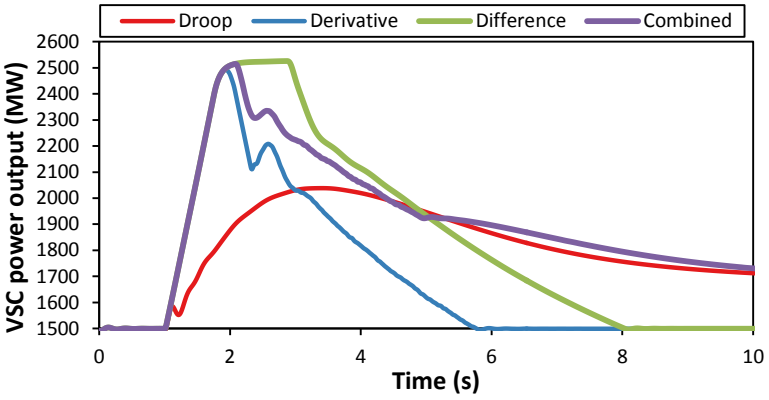

(a)

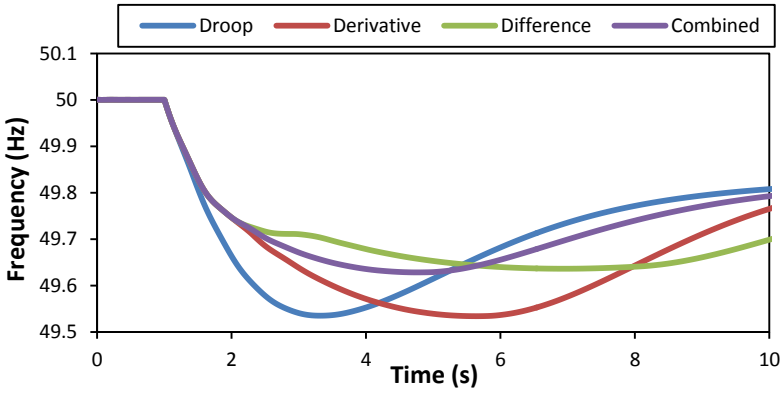

(b)

Fig. 7.4. Example illustrative responses for each VSC frequency control scheme compared to a general frequency plot to visualise the control response. (a) illustrative control response, (b) illustrative frequency

In droop based cases, unless the frequency deviation is sufficiently large, the converter is unlikely to saturate, but this would also depend on the available converter capacity. Conversely for derivative control, the output magnitude will be greater because the ROCOF experienced is closer to the maximum value of 0.5 Hz/s that causes a 100% output change. It can be seen from the response examples in Fig. 7.4(a) that the derivative and difference controller are shown to inject larger quantities of power

immediately following the disturbance, which should reduce the ROCOF experienced over a case where no VSC frequency response is provided. The droop option is shown to approximately provide maximum energy injection when the frequency nadir occurs and maintains a portion of the power injection sharing with the SGs in the system. The combined response controller displays elements of both droop and derivative control and it can be seen how the available capacity is better utilised.

7.1.2 System setup configurations

Two different system setups will be used throughout this component of research. The two setups are designed based on the analysis undertaken in Chapter 3 which highlighted the best and worst case network operating conditions. It was highlighted that high power flow into Area4 and network topology T6 both had a measurable impact on the frequency stability and these factors have been incorporated. The two network setups in this chapter are termed as ***strong*** and ***weak***. The *strong* system setup is designed to be a best case operating situation versus a *weak* network operating setup that represents a worst case situation. The best and worst case scenarios are in relation to each other and are not intended to be the absolute best and worst for a power system. It should be noted that the terms strong and weak are not related to the short circuit capacity of the system and do not refer to the voltage strength of the system. Setup details for the strong and weak system are displayed in Table 7.1.

Table 7.1. Load values used for the *weak* system setup

	Strong	Weak
Topology	T1	T6
Load 1 (MW)	12500	7500
Load 2 (MW)	12500	7500
Load 3 (MW)	12500	10000
Load 4 (MW)	12500	25000
H_{sys} (GVA.s)	119.63	93.93
Primary Response (MW/Hz)	12532	12532

7.2 Analysis

The four factors consisting of VSC frequency response capacity, VSC frequency response location, primary response quantity, and inertia quantity are analysed

separately for each type of VSC frequency controller. This analysis will be used to inform recommendations about the deployment of future VSC-HVDC frequency controllers based on the performance experienced.

7.2.1 Impact of VSC-HVDC Frequency Response Capacity

The first factor evaluated is the role that VSC-HVDC frequency response capacity has on the effectiveness of the four controller types. When providing frequency response using VSC-HVDC interconnectors there may be limited available capacity from an individual interconnector. To overcome this, aggregating the available capacity from each interconnector could produce a greater capacity for frequency response services. The capacities used in this section are considered as an aggregated quantity from multiple VSC-HVDC in-feeds to create the maximum available capacity. Five different available quantities of frequency response from the VSC-HVDC are investigated with the capacities displayed in Table 7.2. The capacities presented in Table 7.2 are not the rating of the VSC system or its steady state power injection, they are the additional quantities of power available before the converter limit is reached. The converter rating does not change as the capacity changes. This ensures the control schemes respond in the same manner irrespective of available capacity because the parameters may be dependent on the VSC rating. The converter output capacity is restricted using the current limit value I_d^{max} that is described in Section 4.1.2. Only the VSC installed in Area4 will be operated in frequency response mode in this part of the analysis.

Table 7.2. Available frequency response capacities for the VSC-HVDC

VSC available capacity	Pct. of loading	Pct. of primary response
200 MW	0.4%	1.5%
400 MW	0.8%	3.1%
600 MW	1.2%	4.7%
800 MW	1.6%	6.3%
1000 MW	2%	7.9%

The impact of having 200 MW and 1000 MW VSC capacity is investigated first in the *strong* system. The difference between the VSC operating using droop control and derivative control when having a 200 MW capacity is displayed in Fig. 7.5(a). The resulting frequency response from the two control types is compared to a case where no VSC frequency control is provided. Similarly, Fig. 7.5(b) compares the influence of the

VSC operating using droop and derivative modes but with 1000 MW of available capacity. In both cases of available capacity the VSC control schemes are shown to improve the nadir and the ROCOF over cases where no VSC frequency support is provided. However, in the case with a 1000 MW capacity, the influence of the droop and derivative control on the frequency causes it to diverge and shows that the derivative has a greater impact on improving the ROCOF.

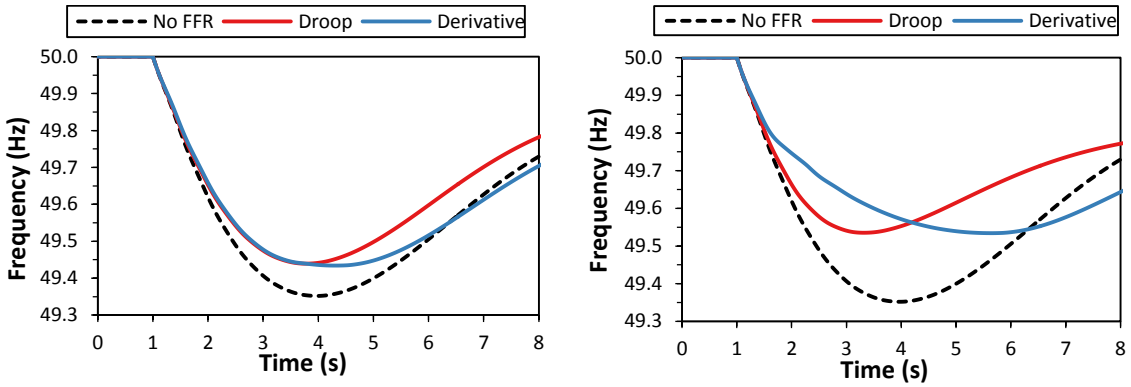

(a) (b)

Fig. 7.5. Comparison between VSC operating using droop and derivative control in a *Strong* system. (a) using 200 MW capacity, (b) using 1000 MW capacity

The difference that a VSC frequency controller has on improving the nadir and ROCOF over the base case that involves no VSC frequency support can be achieved using (7.1) and (7.2). Using (7.1), the difference in nadir (Δf_{nadir}) over the base case setup is calculated where f_n^{VSC} is the nadir experienced when the VSC is providing frequency response and $f_n^{non-VSC}$ is the nadir experienced in the case where no VSC frequency support is provided. A similar method is used to calculate the difference in ROCOF $\left(\Delta \frac{df}{dt}\right)$ given by (7.2) where $\frac{\Delta f^{VSC}}{\Delta t}$ is the ROCOF experienced when the VSC is providing frequency response and $\frac{\Delta f^{non-VSC}}{\Delta t}$ is the ROCOF experienced when no VSC response is provided.

$$\Delta f_{nadir} = f_n^{VSC} - f_n^{non-VSC} \tag{7.1}$$

$$\Delta \frac{df}{dt} = \frac{\Delta f^{non-VSC}}{\Delta t} - \frac{\Delta f^{VSC}}{\Delta t} \tag{7.2}$$

Using the described measures of Δf_{nadir} and $\Delta \frac{df}{dt}$ and isolating the use of VSC droop control for all five quantities of frequency response capacity, that are provided in

Table 7.2, the values for Δf_{nadir} and $\Delta \frac{df}{dt}$ are displayed in Table 7.3. The values in Table 7.3 can be used to produce the plot displayed in Fig. 7.6. In Fig. 7.6, the x-axis is the Δf_{nadir} (improvement in nadir over the case with no VSC response) and the y-axis is the $\Delta \frac{df}{dt}$ (improvement in ROCOF over the case with no VSC response). Each point represents a VSC frequency response capacity. In this plot, the further right the point then the greater the improvement in nadir (higher nadir value). The higher the point is in the plot then the better the improvement in ROCOF (lower ROCOF value). In Fig. 7.6 the improvement in ROCOF is calculated over the worst 200 ms period experienced as discussed in Chapter 2.

As the available capacity is increased there is a greater improvement in the nadir than the ROCOF between the case with no VSC frequency response. Above a certain value of capacity though (600 MW), there is no further improvement in the nadir when using the droop control. It is also observed that when capacity for droop control is increased to 1000 MW the nadir is improved by 0.09 Hz, but there is only a 0.005 Hz/s improvement in ROCOF (y-axis).

Table 7.3. Influence of capacity on frequency drop and 200 ms ROCOF in a strong system

Capacity (MW)	Δf_{nadir} (Hz)	$\Delta \frac{df}{dt}$ (Hz/s)
200	0.08695	0.04225
400	0.1568	0.048
600	0.1825	0.048
800	0.1825	0.048
1000	0.1825	0.048

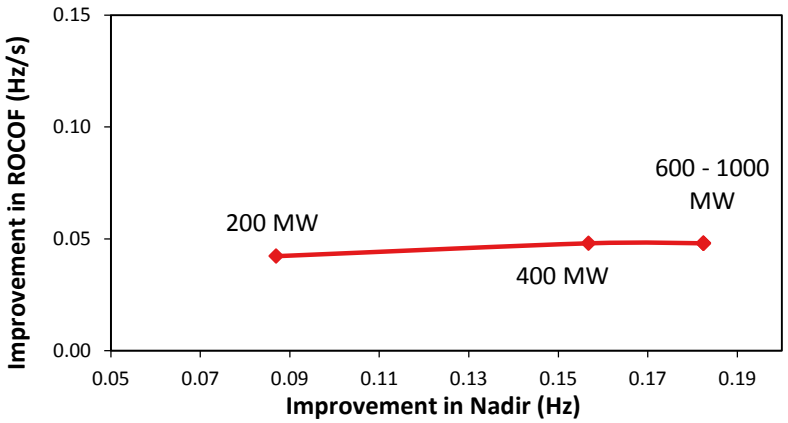

Fig. 7.6. Influence of capacity in *strong* system when operating using droop control

The impact that capacity has for all four VSC frequency control options is now assessed in the same way. The improvement of nadir and ROCOF for all control types when the capacity is increased and using a *strong* system setup is displayed Fig. 7.7(a). As the quantity of VSC frequency response capacity increases it can be seen that for each control type there is an improvement in the nadir and the ROCOF. For each control type the improvement in nadir and ROCOF between a 200 MW and 1000 MW capacity is provided in Table 7.4. A key finding is that as the capacity is increased when using derivative control, the greater the improvement in ROCOF. This increase is 0.076 Hz/s between the 200 MW and 1000 MW cases. There is also an improvement in nadir of 0.099 Hz with the derivative controller over the same cases. The difference and combined controllers are shown to provide a superior performance for nadir improvement over the droop and derivative controllers where they improve the nadir by 0.195 Hz and 0.187 Hz respectively over the same cases.

Similar analysis is undertaken to evaluate the impact of capacity when the four VSC control types are operated in a *weak* system setup. The results from the *weak* system are displayed in Fig. 7.7(b). The improvement in nadir and ROCOF between a 200 MW and 1000 MW VSC frequency response capacity in the weak system is provided in Table 7.4. In this instance it can be seen that an increase in capacity under all control types improves the nadir as in the *strong* system setup. However, the improvement in ROCOF in the *weak* system for all four VSC control types is loosely indistinguishable. This is due to the ROCOF being calculation over the worst 200 ms time period, which occurs at the start of the disturbance before any control options have had an impact. During this 200 ms period all four control types have not had time to respond sufficiently and have any effect on the ROCOF.

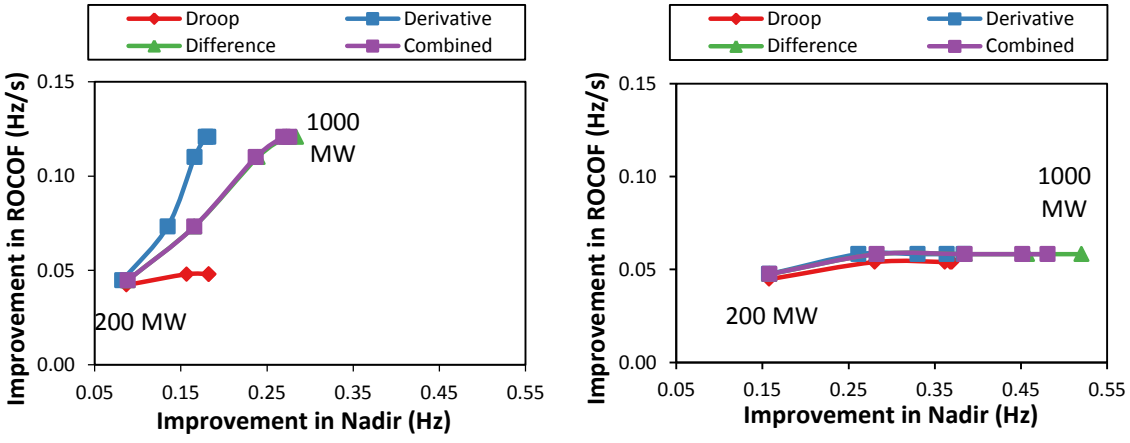

Fig. 7.7. Impact capacity has for each control type when using a 200 ms ROCOF measurement. (a) *strong* system setup, (b) weak system setup

Table 7.4. Improvement in nadir and 200 ms ROCOF between a VSC frequency capacity of 200 to 1000 MW in a strong and weak system

System	VSC control	Improvement in Δf_{nadir} (Hz)	Improvement in $\Delta \frac{df}{dt}$ (Hz/s)
Strong	Droop	0.095	0.005
	Derivative	0.099	0.076
	Difference	0.195	0.076
	Combined	0.187	0.076
Weak	Droop	0.211	0.009
	Derivative	0.226	0.010
	Difference	0.363	0.010
	Combined	0.332	0.010

The 200 ms ROCOF calculation does not capture the wider impacts that the different control types have on ROCOF. Therefore a ROCOF calculation over the first 500 ms following the disturbance is also used, as outlined in [170]. This is also the time period around which ROCOF relays are typically programmed to operate. Using this time period to calculate the ROCOF, the impact of VSC capacity for each control type in a *strong* system is re-calculated and displayed in Fig. 7.8(a) and similarly for a *weak* system as displayed in Fig. 7.8(b). The updated improvements in nadir and ROCOF between a 200 MW and 1000 MW VSC frequency response capacity for the strong and weak system is provided in Table 7.5.

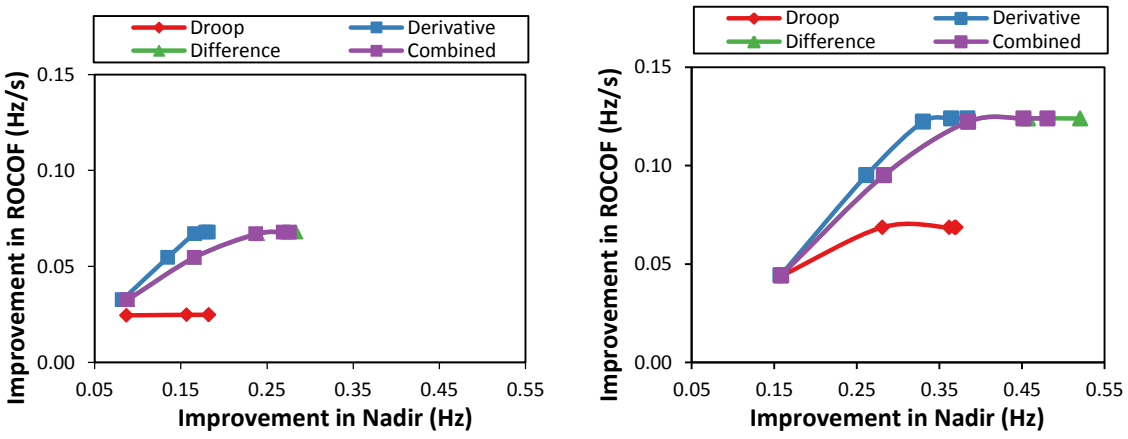

Fig. 7.8. Impact capacity has for each control type when using a 500 ms ROCOF measurement. (a) *strong* system setup, (b) *weak* system setup

Table 7.5. Improvement in nadir and 500 ms ROCOF between a VSC frequency capacity of 200 to 1000 MW in a strong and weak system

System	VSC control	Improvement in Δf_{nadir} (Hz)	Improvement in $\Delta \frac{df}{dt}$ (Hz/s)
Strong	Droop	0.095	0.000
	Derivative	0.099	0.035
	Difference	0.195	0.035
	Combined	0.187	0.035
Weak	Droop	0.211	0.039
	Derivative	0.226	0.079
	Difference	0.363	0.079
	Combined	0.332	0.079

In both system setups, a low available capacity (200 MW) results in no significant difference between the four VSC control types. As the available capacity increases, each control type starts to improve the nadir and ROCOF differently. The VSC active power output for each control type operating in the *strong* system setup with 200 MW capacity is displayed in Fig. 7.9(a). It displays that the converter saturates for each control type and they all inject the same amount of power (albeit for different time periods) which results broadly in the same impact. When the converter has a larger available capacity of 1000 MW the power injection for each control type differs as displayed in Fig. 7.9(b). It is evident in Fig. 7.9(b) that the speed of the initial response is faster for the derivative and difference controller and is limited by the current ramp rate limiter in the VSC outer control loop. The derivative and the difference control types also saturate the converter output at the maximum capacity. This is because the initial ROCOF experienced is sufficient enough to result in the use of all available capacity. The frequency deviation experienced is not sufficient enough to cause the same degree of change in the output which is why the droop control option injects a lower peak magnitude of power. The combined and difference control options are shown to have a higher average power injection over the first few seconds following the disturbance which restrains the ROCOF and allows time for the SG primary response to operate. The combined and difference controllers under large available capacity do not improve the ROCOF any more than the derivative because of converter saturation, but the nadir is significantly improved compared to the droop and derivative cases in both system setups. In the strong system the difference controller improves the nadir by 0.096 Hz

over the derivative scheme and the combined controller improves the nadir by 0.092 Hz. The combined controller improves the nadir but eventually injects the same amount of power as the droop control alone once the derivative action has ended.

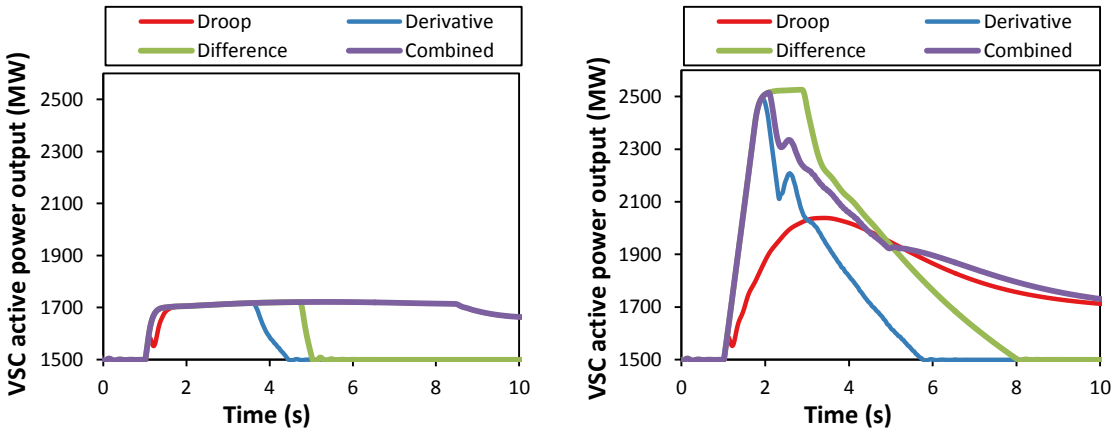

(a) (b)

Fig. 7.9. VSC active power output. (a) with 200 MW capacity, (b) with 1000 MW capacity

This investigation has highlighted the role the available VSC-HVDC frequency response capacity has when implementing different frequency controllers. The smaller the capacity the smaller the difference between each control type in relation to the improvement of ROCOF and nadir. As capacity increases, beyond a certain value for a given system setup when using droop or derivative, there is no further improvement in nadir or ROCOF. This emphasises that there must be maximum useful operating limits for these control types when operated individually. Therefore specific consideration should be given to employing multiple types of VSC frequency response to improve the overall effectiveness of the response.

7.2.2 Impact of location

The impact that location of VSC frequency response has on the frequency stability metrics is investigated in this section. The maximum available capacity of 1000 MW is used because that has been shown to maximise the distinctive impact of the different controllers. The VSC frequency response will be compared when it is located in either Area4 (where the 1800 MW disturbance occurs) or Area1. The resultant time series frequency responses when VSC droop control is implemented into Area4 and Area1 in a *weak* system is displayed Fig. 7.10(a). Calculation of Δf_{nadir} and $\Delta \frac{df}{dt}$ for the droop implementation in each area is achieved using (7.1) and (7.2) where they are compared

to the scenario with no VSC frequency response. The values calculated from (7.1) and (7.2) that are the resulting improvement in nadir and ROCOF for each location are displayed in Fig 7.10(b). In this plot it can be seen that the droop located in Area1 improves the nadir and ROCOF less than when it is implemented into Area4 (where the disturbance occurs).

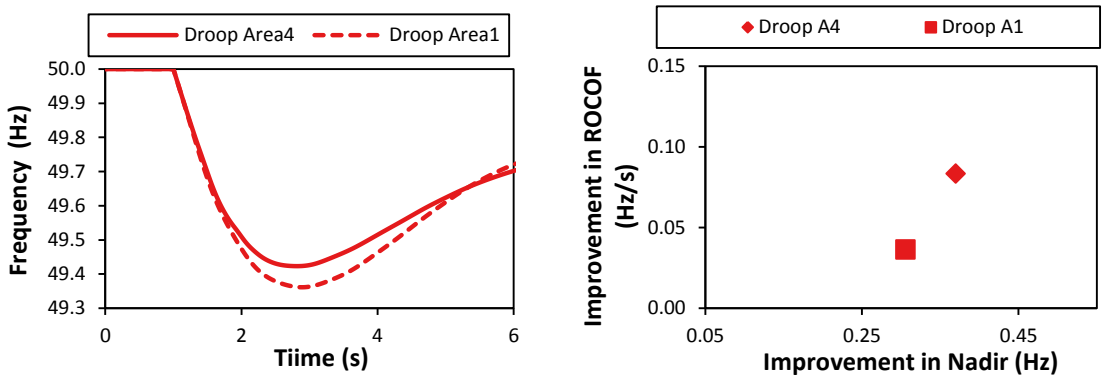

(a) (b)

Fig. 7.10. Impact of VSC operating using droop implemented in Area4 and Area1. (a) time series comparison, (b) reduction in nadir and 500 ms ROCOF

The difference in the improvement of nadir and ROCOF between the droop implemented control in Area4 and Area1 in a *weak* system is performed to determine how much of an impact location has on the frequency response. To achieve this, the difference between the improvements in nadir for droop in both Area4 and Area1 is calculated from Fig. 7.10(b) by applying the values to (7.3), where Δf_n^{Area4} and Δf_n^{Area1} are the Δf_{nadir} values from Fig. 7.10(b) that were calculated using (7.1). Similarly the difference in the improvement in ROCOF between the two droop cases where $\Delta \frac{df}{dt}^{Area4}$ and $\Delta \frac{df}{dt}^{Area1}$ are the $\Delta \frac{df}{dt}$ values from Fig. 7.10(b) that were calculated using (7.2). These values are then applied in (7.4) to determine the difference in ROCOF between the two location cases.

$$\hat{\Delta} f_{nadir} = \Delta f_n^{Area4} - \Delta f_n^{Area1} \tag{7.3}$$

$$\hat{\Delta} \frac{df}{dt} = \Delta \frac{df}{dt}^{Area4} - \Delta \frac{df}{dt}^{Area1} \tag{7.4}$$

The resultant difference in the improvement of nadir and ROCOF between the cases where VSC droop is implemented in Area4 and Area1 using the *weak* system setup is

displayed in Fig. 7.11. It shows that when droop control is implemented in Area4 there is a difference in the improvement (over the Area1 case) in nadir of 0.06 Hz and a difference in the ROCOF experienced of 0.05 Hz/s. It is these values that create the point displayed in Fig. 7.11.

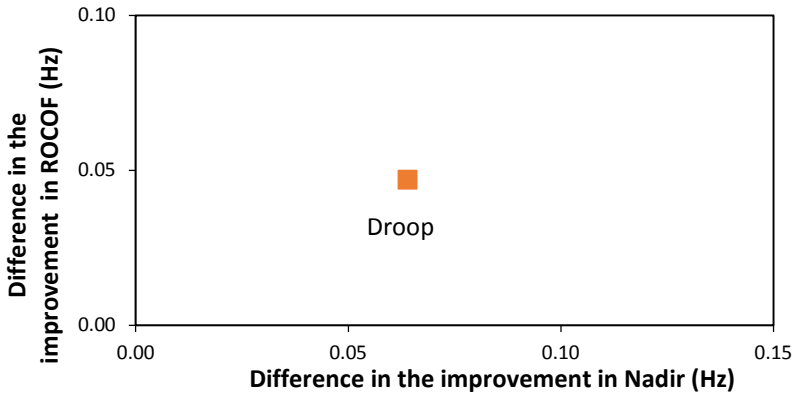

Fig. 7.11. Difference between the improvement of nadir and 500 ms ROCOF when droop control is implemented in Area4 and Area1 in a weak system

The differences in the improvement of nadir and ROCOF between VSC-HVDC frequency control injection located in Area4 and Area1 for all four different control options are now determined. This is performed in both the *strong* and *weak* system setups using the previously described method with the results displayed in Fig. 7.12. It is noted that the result values in Fig. 7.12 represent the difference between the improvement of nadir and ROCOF between Area4 and Area1. In this analysis it can be seen that when the network is setup as *strong* and the VSC frequency control response is moved to Area1 from Area4, there is no difference in the improvement of nadir or ROCOF when compared to response provided in Area4. When operating in *weak* network setup, moving the response to Area1 reduces the impact and its effectiveness for improving the nadir and ROCOF. In the *weak* system, when the VSC response is outside of the area of disturbance it does not contribute as much to stabilising the system.

The values for the improvement from the control types on nadir and ROCOF between an implementation in Area1 (that is outside of the disturbance area) and Area4 are provided in Table 7.6. There is a greater difference observed for the combined control type because it comprises droop and derivative components that both improve the nadir. The main cause for this observed difference is due to the electrical torque imposed on the SG in Area4. When the frequency response is further away, it has less

impact on reducing the electrical torque which determines the deceleration of the SG as described in Chapter 3. This will be expanded on further in Section 7.2.3. This suggests that there is a need to ensure frequency response schemes are located close to large SG in-feeds (i.e. possible grid disturbances) in weak systems.

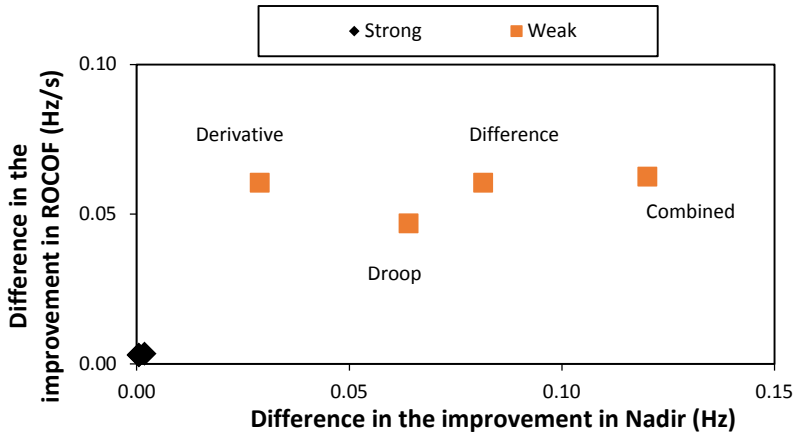

Fig. 7.12. Difference between the reduction of nadir and 500 ms ROCOF for each control type when implemented in Area4 and Area1. Analysis is performed in a *strong* and *weak* system setup

Table 7.6. Difference in nadir and 500 ms ROCOF between Area4 and Area1 implementation in a weak system setup

VSC control	$\hat{\Delta} f_{nadir}$ (Hz)	$\hat{\Delta} \frac{df}{dt}$ (Hz/s)
Droop	0.064	0.046
Derivative	0.029	0.060
Difference	0.120	0.062
Combined	0.081	0.060

7.2.3 Impact of Primary Response

Three different quantities of primary response are considered in this section as given in Table 7.7, where PR12532 is the system setup that has the minimum quantity of primary response and PR20886 has the largest quantity of primary response. This analysis is performed using the *strong* system setup with the VSC in Area4 operating to provide frequency response. In this analysis the system inertia and SG machine ratings do not change. A time series comparison between a scenario with no VSC frequency response and VSC operating using droop control under PR12532 primary response setup is displayed in Fig. 7.13(a). The same time series analysis for the VSC operating in droop mode is displayed for the PR20886 primary response setup in Fig. 7.13(b). It

can be seen that with no VSC frequency response, the PR12532 and PR20886 primary response setups have different nadirs as would be expected. However, in both conditions, the use of VSC frequency response improves the nadir. In the PR12532 setup, the nadir is improved by 0.19 Hz to 49.52 Hz. In the PR20886 setup the nadir is improved by 0.14 Hz to 49.6 Hz. From this it can be concluded that when the quantity of primary response in the system is lower, there is a greater improvement in nadir when operating the VSC with frequency droop control. Under conditions when the system has less primary response incorporated, the system frequency will deviate further and have a higher sustained ROCOF leading to a larger response from the converter.

Table 7.7. Primary response setup quantities

Primary response setup	G1 (R)	G2 (R)	G3 (R)	G4 (R)	Primary response (MW/Hz)
PR12532	0.05	0.05	0.05	0.05	12532
PR15665	0.04	0.04	0.04	0.04	15665
PR20886	0.03	0.03	0.03	0.03	20886

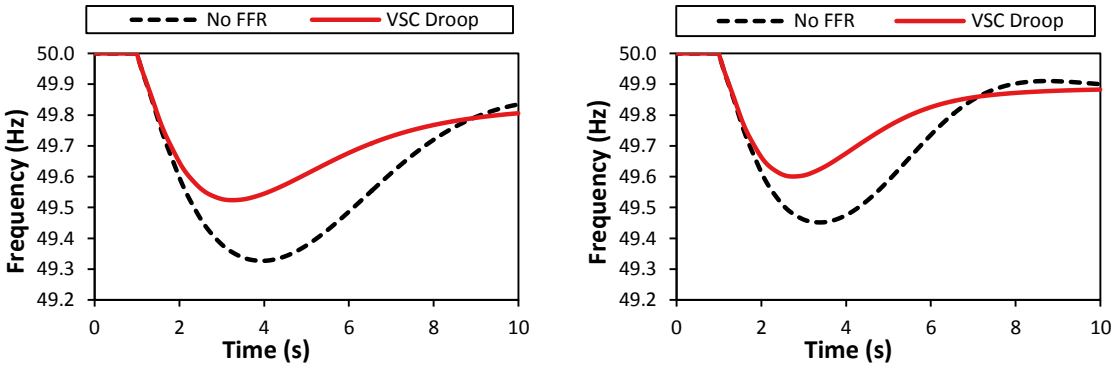

(a) (b)

Fig. 7.13. Impact of VSC operating using droop under different primary response conditions. (a) PR12532 setup, (b) PR20886 setup

Using the time series data displayed in Fig. 7.13, the improvement in nadir and ROCOF for the primary response quantity cases PR12532 and PR20886 is determined. The resultant values are displayed as Fig. 7.14 and provided in Table 7.8. The results show that when there is less primary response in the system, the VSC operating using droop control provides a greater improvement for the nadir (higher nadir).

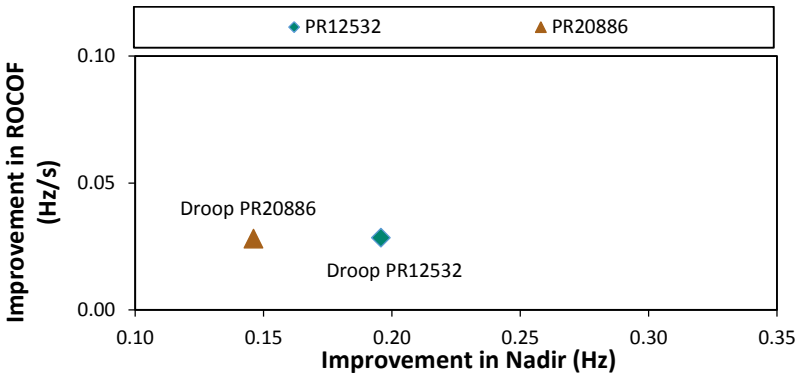

Fig. 7.14. Improvement in the nadir and 500 ms ROCOF when the VSC is operating with droop in primary response setups PR12532 and PR20886

Table 7.8. Improvement in nadir and 500 ms ROCOF for PR12532 and PR20886 setups

Scenario	Δf_{nadir} (Hz)	$\Delta \frac{df}{dt}$ (Hz/s)
PR12532	0.195	0.028
PR20886	0.146	0.028

Building on the previous comparison, the impact for each of the four VSC control types is analysed using the three primary response quantities (PR12532, PR15665, PR20886). The full analysis results for each VSC control type are displayed in Fig. 7.15(a)-(d). The full set of results is also provided in Table 7.9 for further clarity. This analysis reveals that as the quantity of primary response increase or decreases, the impact from derivative control remains almost entirely unchanged with a difference of 0.004 Hz in nadir and 0.3 mHz/s in ROCOF between the PR12532 and PR20886 setups. Droop control is shown to have its greatest impact when there is less primary response (PR12532 setup) compared to larger quantities of primary response (PR20886 setup) as discussed previously in this section. It is also shown that the impact from the combined controller increases as the primary response quantity decreases due to the droop component with a reported improvement in nadir and ROCOF of 0.049 Hz and 0.3 mHz/s between the PR12532 and PR20886 setups. The improvement in ROCOF between these two cases is very small. The difference controller is seen to be less susceptible to primary response changes where there is only a difference of 0.02 Hz and 0.3 mHz/s in nadir and ROCOF respectively between PR12532 and PR20886 setups, similar to the derivative controller.

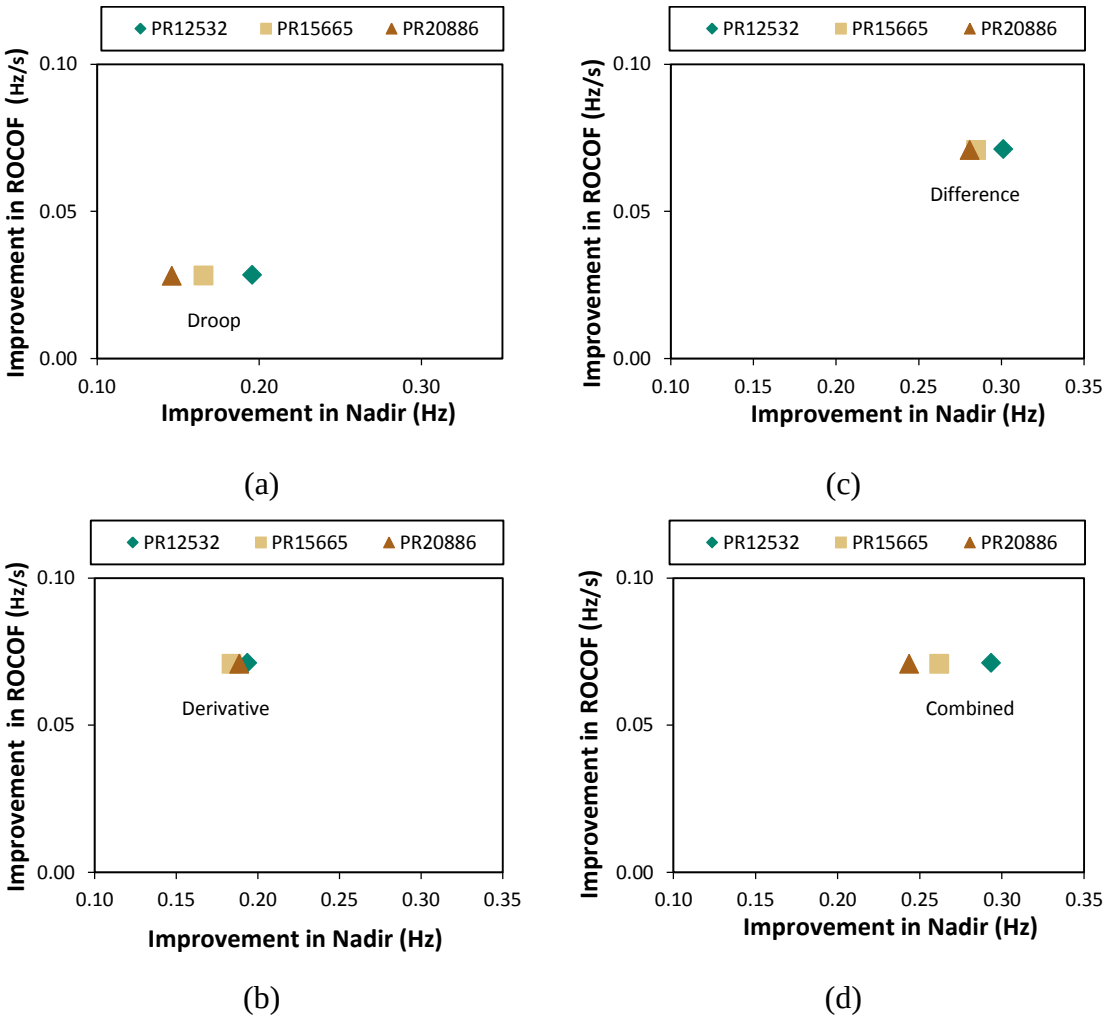

Fig. 7.15. Improvement in nadir and 500 ms ROCOF for each control type. (a) droop control, (b) derivative control, (c) difference control, (d) combined control

Table 7.9. Improvement in nadir and 500 ms ROCOF for each primary response scenario and control type

Scenario	Control	Δf_{nadir} (Hz)	$\Delta \frac{df}{dt}$ (Hz/s)
PR12532	Droop	0.19575	0.0284
	Derivative	0.1935	0.0712
	Difference	0.3013	0.0712
	Combined	0.2934	0.0712
PR15665	Droop	0.16575	0.0282
	Derivative	0.1839	0.0709
	Difference	0.2848	0.0709
	Combined	0.2619	0.0709
PR20886	Droop	0.1461	0.0281
	Derivative	0.1886	0.0709
	Difference	0.2809	0.0709
	Combined	0.2435	0.0709

The initial active power output from the VSC when operating using derivative control is displayed to be independent of the quantity of primary response in Fig. 7.16(b). This is due to the fact that the derivative control relies on the initial rate of change of frequency. This initial ROCOF is determined by the quantity of system inertia (which does not change between analysis scenarios in this section) and does not rely on the quantity of primary response schemes. This is expected because the primary response schemes have not had time to completely operate in the first second following the disturbance. The impact on nadir improvement when the VSC is operating in droop mode is seen to increase as the primary response reduces. When operating in droop mode, the VSC takes part in sharing the power that reduces the torque imbalance on the SG rotor. In turn, the VSC reduces the amount of mechanical input power required from the SG to achieve equilibrium. It is observed in Fig. 7.16(a) that the initial VSC active power response using droop control is identical, but under scenarios with less primary response, as in PR12532, the VSC provides more active power as there is less primary response to create the equilibrium. In this instance the converter plays a greater role in achieving the equilibrium that leads to the nadir.

Overall the droop controller in this condition injects more power as the primary response in the system reduces. This influence of the droop component improves the impact of the combined control on the nadir by 0.049 Hz between the PR20886 and the

PR12532. Conversely, between the PR20886 and the PR12532, the difference controller experiences a change in nadir of 0.020 Hz. The improvement of ROCOF remains small for the combined and difference control and is 0.3 mHz/s. From this analysis it can be seen that the difference controller provides limited additional benefit as the inertia reduces compared to the combined controller.

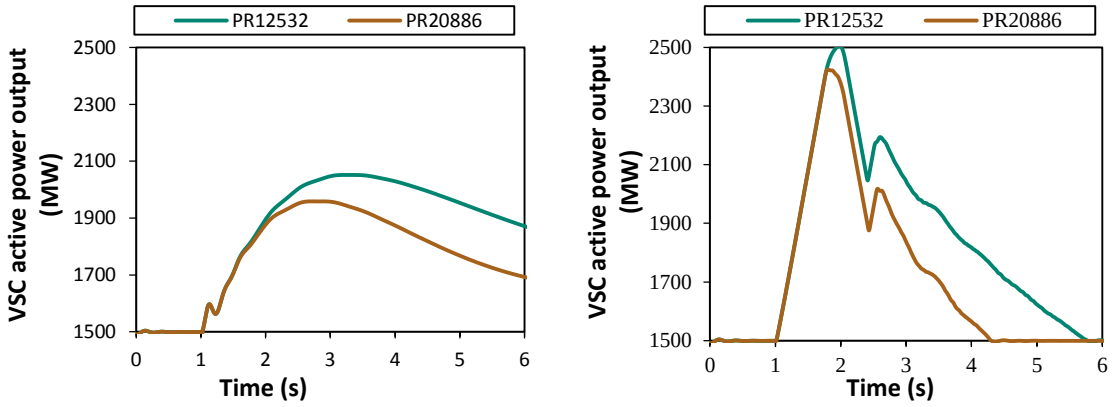

(a) (b)

Fig. 7.16. VSC active power output under the PR12532 and PR20886 primary response setups. (a) proportional control, (b) derivative control

To explain the difference further, the impact of the VSC frequency response on the mechanical torque of the SG in Area4 is shown in Fig. 7.17(a) for the droop and derivative cases. This compares cases when the VSC is operating using droop and derivative control types under the PR12532 primary response setup. It displays that when operating the VSC using derivative control, the increase in the initial mechanical torque is smaller than when using droop. However, as the derivative component reduces, the SG needs to increase its mechanical input to increase the mechanical power. From the same condition the *electrical* torque imposed onto the SG in Area4 is displayed in Fig. 7.17(b). Although the rotor oscillation obscures the data slightly, it can be seen that initial electrical torque imposed on the rotor is less when using derivative control. However, as the derivative reduces, the rotor is slowly electrically 'loaded up' leading to a further imbalance in torque. The electrical loading of the SG under VSC derivative control happens gradually and this gradual increase allows the primary response to operate and limit the ROCOF and nadir. When operating the VSC using droop control, it can be seen that the overall electrical torque imposed on the SG is less as the VSC provides a larger proportion of the power deficit. The impacts displayed here for the droop and derivative control on the SG torques is similar for the combined and difference controller. The impact from the difference controller on SG torque is

similar to the impact of the derivative controller, and the combined controller impact is between the droop and derivative controller. This highlights how the VSC frequency response interacts with the SGs in the system and is useful to help determine what type of interaction would be most beneficial for a certain network operating condition.

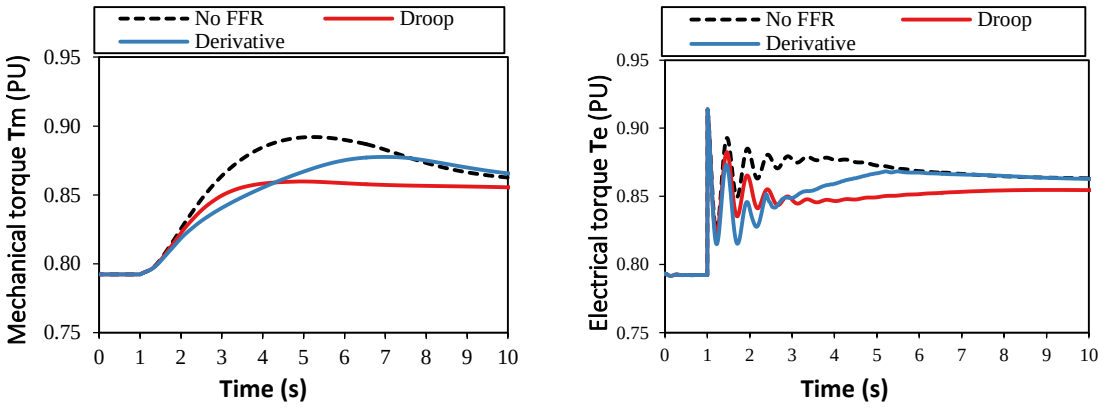

(a) (b)

Fig. 7.17. Impact on SG4 torque when using VSC operating with droop and derivative. (a) mechanical torque, (b) electrical torque

A key point observed from this section is that as the quantity of primary response reduces, the derivative control provides the same initial response due to its setup. The derivative control also reduces the initial electrical torque imposed on the SG following the disturbance. As the derivative component reduces in line with the rate of frequency change, the SG electrical torque gradually increases but at a rate that allows the primary response to operate. As the quantity of primary response reduces, the VSC operating in droop control has a greater impact on improving the nadir because the frequency deviation is greater. It should be noted that the droop plays a role in the power sharing whereas the derivative does not, so if there was limited primary response in the system then the operator may require more droop based response. The difference and combined controller options were shown to be superior over droop and derivative once again in Fig. 7.15. The combined controller has a greater impact as the inertia reduces over the difference controller. It should also be noted that the difference controller parameters rely on the existing SG (see Chapter 6), which mean that as SGs are decommissioned this type of control may start to have less impact.

7.2.4 Impact of Inertia

Using three different system inertia ratings given in Table 7.10, the four VSC frequency control options are evaluated using the *strong* system setup as the initial base

for the analysis. The VSC-HVDC in Area4 is set to provide the frequency response. The lower system inertia ratings will naturally lead to a greater ROCOF and a lower resulting nadir. Due to this the overall impact of all VSC control types will improve the nadir and ROCOF as the inertia reduces. The droop control will inject larger quantities of power due to the greater deviation in frequency and the derivative action will inject power over a longer time period because it will take longer to reach the nadir.

Table 7.10 Inertia quantification for the different scenarios

Scenario	Inertia (GVA.s)
H93	93
H119	119
H142	142

To begin and in order to explain the analysis methodology, a time series comparison between VSCs operating using droop and derivative control for inertia setups H119 and H93 are displayed in Fig. 7.18(a) and Fig. 7.18(b) respectively. In these figures the response when using droop and derivative is compared to a scenario where there is no VSC frequency response. In these cases where droop and derivative control are used, the resulting frequency response in terms of nadir in both system inertia setups is seen to be similar. The resulting nadir values are given in Table 7.11 and show that there are small differences in the nadir between droop and derivative of 0.035 Hz for the H119 setup and of 0.032 Hz for the H93 setup. The complete results for the improvement in nadir and ROCOF are provided later in Table 7.12. The similarity in response is in part due to the fact that the disconnection size remains the same at 1.8 GW and the available capacity of the VSC is 1000 MW. This will be explored further in the remaining part of this section.

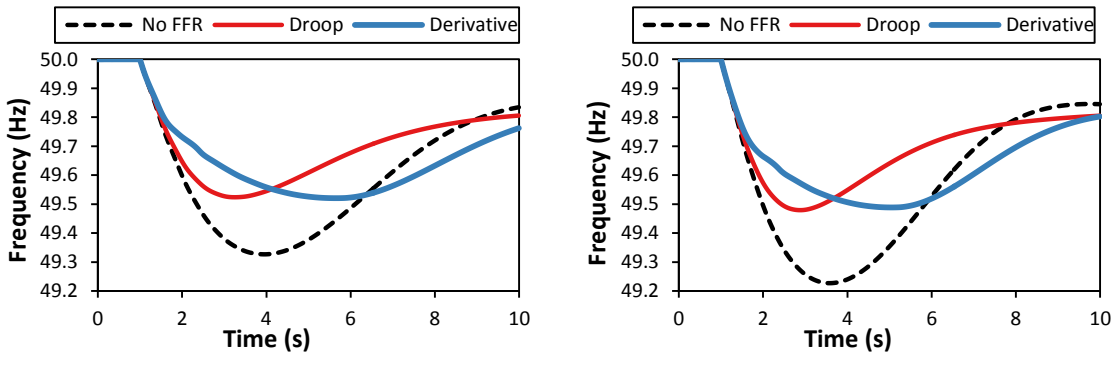

(a) (b)

Fig. 7.18. Impact of droop and derivative control under different system inertia values. (a) H119, (b) H93

Table 7.11. Resulting frequency nadir for droop and derivative control in H93 and H119 setups

Scenario	Control	f_{nadir} (Hz)
H119	Droop	49.523
	Derivative	49.520
H93	Droop	49.479
	Derivative	49.488

The resultant improvement in nadir and ROCOF for scenario H119 for all four VSC frequency control options is displayed in Fig. 7.19(a). It is seen that the droop and derivative control have a similar influence for improving the nadir. Similarly to previous analysis, the derivative control is seen to further improve the ROCOF over droop control implementations. Extending the analysis for all three inertia setups and four VSC controller types produces the results that displayed in Fig. 7.19(b), with the results also provided in Table 7.12. In all three system inertia quantities the derivative component initially responds the same (injects the same amount of power) because the ROCOF experienced in all cases is sufficient to cause a change in VSC output that saturates the converter. In this condition the converter is limited by the current ramp rate constraint. The derivative is seen to have more impact on improving the ROCOF as the inertia reduces with a difference in ROCOF of 0.026 Hz/s between the H142 and the H93 setups. This is in comparison to the difference in ROCOF of 0.015 Hz/s for the same case when using droop. The reduction in electrical torque reduces the SG imbalance that is a key factor determining how fast the machine decelerates. This is a key concern in low inertia networks that still operate with SGs in the system.

The derivative control also has a greater impact on nadir as the inertia reduces because it allows time for the SG primary response schemes to operate and reduces the deceleration of the SGs. Conversely, the derivative control is seen to have less impact in improving nadir and ROCOF when there is a higher level of system inertia. This is because the inertial response provided from the turbine rotors reduces the initial ROCOF and allows time for the primary response to operate. Due to the constrained ROCOF from the SGs in the higher inertia setups, the contribution from the VSC to the frequency containment process is lower.

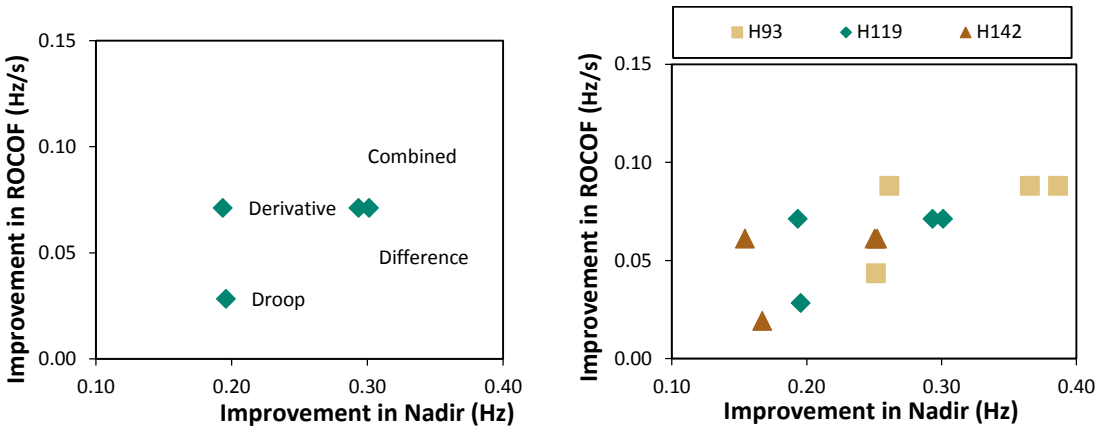

(a) (b)

Fig. 7.19. Improvement of nadir and 500 ms ROCOF for each VSC frequency control scheme. (a) H119 setup, (b) H93, H119, and H142setups

Table 7.12. Difference in nadir and 500 ms ROCOF for each inertia setup

Scenario	Control	Δf_{nadir} (Hz)	$\Delta \frac{df}{dt}$ (Hz/s)
H93	Droop	0.25155	0.0435
	Derivative	0.26135	0.088
	Difference	0.38645	0.088
	Combined	0.3656	0.088
H119	Droop	0.19575	0.0284
	Derivative	0.1935	0.0712
	Difference	0.3013	0.0712
	Combined	0.2934	0.0712
H142	Droop	0.1671	0.0192
	Derivative	0.15435	0.0611
	Difference	0.25235	0.0611
	Combined	0.25055	0.0611

It can be seen in Fig. 7.20(b) that the initial response when using the derivative control is the same for all inertia cases but the response lasts longer in cases where there is lower inertia because the frequency nadir takes longer to be achieved. The droop VSC scheme responses displayed in Fig. 7.20(a) show that a larger power injection occurs in lower inertia setups that is due to the greater frequency deviation before settling at the defined droop characteristic that is the same for all inertia setup cases.

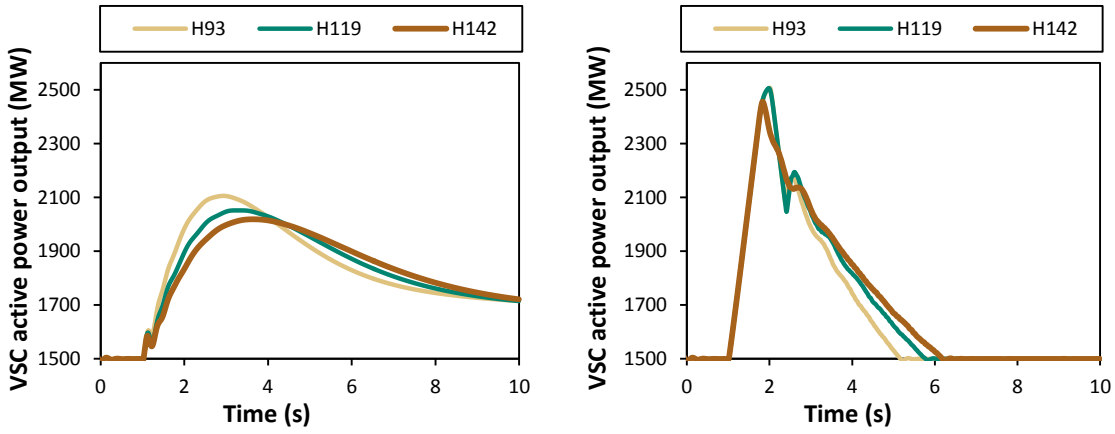

(a) (b)

Fig. 7.20. VSC active power output for different system inertia values. (a) VSC operating using droop (b) VSC operating using derivative

Isolating the comparison between the use of droop and derivative in the low inertia setup (H93) and the high inertia setup (H142) in Fig. 7.21, it is seen that the derivative starts have a greater effect on the nadir in low inertia conditions. In the high inertia setup (H142), the VSC droop control has a stronger impact on reducing the nadir than the derivative control. However, under a low inertia setup (H93) the derivative control has a stronger impact on improving the nadir. The reason for this has been described in Section 7.2.3 and is due to the derivative control alleviating the sudden electrical torque increase on the SG. Again under all inertia scenarios it has been seen that derivative control has a stronger impact on the ROCOF. However, in future low inertia systems the SO may want the droop gain characteristics of the large VSC-HVDC in-feeds gain values increased so they can start to have a stronger impact on ROCOF as well, although it is noted that it will never be the same as a derivative response or respond in the same manner.

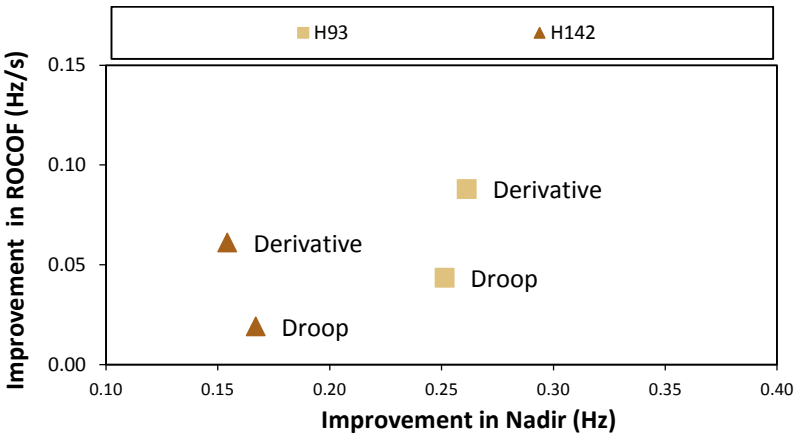

Fig. 7.21. Comparison between the VSC operating using droop and derivative control for H93 and H142 setups

The key points from the analysis of system inertia quantity is that as the inertia reduces, the use of derivative control starts to have a greater impact and improve both the nadir and ROCOF over cases where no VSC support is provided. It is shown that droop does not always improve nadir better than using derivative control. Although, the derivative control does start to have less impact in higher inertia setups because the control signal it acts on (df/dt) is not as severe. Determination of the boundary between a high and low inertia system is undefined and the description of what constitutes a low inertia system is out of the scope of this thesis. However, it is acknowledged that the quantity and availability of frequency response should be taken into consideration and not just the quantity of inertia.

7.3 Summary

This chapter has investigated the use of four different VSC-HVDC frequency controllers and evaluated their performance under different network and control operating conditions. An additional VSC frequency controller has been presented that incorporates the functions of droop and derivative control and is termed *combined* control in this thesis. The results provided from this component of research are general and broad with the intended application towards large scale VSC-HVDC assets, such as interconnectors that are operating with a steady state power injection and frequency response control.

Throughout the analysis, the derivative control is shown to be more effective at improving the ROCOF than droop control as expected. The use of derivative control also improves the nadir in similar manner to droop control. For all scenarios and system setups, the use of the difference and combined controllers provide the best frequency

containment for nadir and ROCOF. Out of the four control types investigated, there may be situations where using a certain control type is impractical. For example, using derivative control may not be possible if there is significant rotor angle stability issues in the system as the sudden injection of power from the derivative control could exacerbate the oscillations. The use of the difference controller may also be unfavourable in future systems that only have a small amount of traditional primary response, because its operation is determined by the ratio of SG to PE devices operating using the difference controller. When the system setup is configured as *weak*, all control types operating at each capacity have a greater impact on the frequency metrics over the same cases in a *strong* system setup. This confirms the effectiveness of all schemes. The conclusions from this component of research can be broken down and described by the following main points:

- For any system setup a low available capacity (200 MW, 0.4% of the system load) from the VSC-HVDC leads to minimal difference in the impact between VSC frequency control types. With a capacity between 200 MW – 600 MW (0.4% - 1.2% of the system load), droop control has a marginally greater impact on nadir, and the derivative control has a greater impact on the ROCOF. With a capacity of 1000 MW (2% of the system load), derivative has a far greater impact on ROCOF but both droop and derivative have the same impact on nadir.
- For a system setup defined as *strong*, relocating the VSC frequency response into Area1 (outside the area of disturbance) leads to no reduction in the effectiveness of the VSC frequency control schemes. When the system is setup as *weak*, relocating the VSC frequency response outside of the area of disturbance leads to a reduction in the impact that all four control schemes have on the frequency metrics. Therefore the deployment of frequency response services further away from large SG power in-feeds (i.e. possible disturbance sources) lead to a reduced impact on the effectiveness from the response. This means that frequency containment services in power systems would be better placed near the large SGs.
- As the available primary response in the system reduces, droop based VSC frequency response schemes have a stronger impact on the nadir than the derivative schemes. With the implementation of the derivative control used in this research, changes in available primary response do not lead to differences in

the derivative controller output. This is because the initial rate of change of frequency remains the same regardless of the available primary response.

- As the inertia reduces, the derivative control starts to improve the nadir more than droop. This is because the large initial injection of power alleviates the electrical torque on the SG more than droop control and this becomes more crucial to allow the primary response to operate as the inertia reduces.
- The use of the derivative and difference controllers reduces the initial torque imbalance on the SG by injecting a large initial amount of power, but as the ROCOF reduces so does the power injection from these controllers. Although this action reduces the initial electrical torque on the SG, there is still a requirement for some form of primary response service to operate to supply the missing generation following the disturbance.

These broad conclusions can be used to inform the deployment of frequency services within power networks using large scale VSC-HVDC assets. Overall the deployment will depend on the main priorities within the network or for the SO, such as under frequency relays and ROCOF relays or the need to increase primary response capacity if there is already sufficient additional fast responding services operating (battery or DSR) in the system. Overall the derivative control is not only useful for improving the ROCOF but it improves the nadir as well providing there is additional primary response available. The use of a combined or derivative control is seen throughout this analysis to have a stronger impact on improving the ROCOF and nadir. The difference control is designed to co-ordinate with existing SG and provide the initial deficit in expected energy, but does not provide any steady state power injection. In contrast, the combined control applies the benefits from both the droop and derivative schemes, including the droop-based steady state power injection.

From the research in this chapter, the use of a VSC-HVDC asset operating with the combined function of droop and derivative control is more beneficial than operating with a single control option. The difference control has been shown to be more beneficial than droop or derivative alone. However its response decays back to zero which prevents it from providing any of the power deficit following the disturbance requiring the need for additional droop based schemes. Due to this, the combined controller is the most beneficial because it improves the nadir and ROCOF without the need for additional control schemes to be implemented. The recommendations from this chapter would be to use the difference controller in a system that has a large percentage

of synchronous generation with an approximate percentage being at least 50% synchronous generator based generation. For a system that has less than 50% synchronous generation incorporated it would be recommended that the combined controller would be more suitable as it does not have to coordinate with synchronous generators in the system. The research undertaken in this chapter has addressed thesis objective 7.

8 Conclusions and Future Work

8.1 Conclusions

This thesis has firstly explored frequency stability in greater depth in relation to the network topology, power flow, and inertia and droop gain distributions. These factors are used to investigate frequency stability beyond the quantity of system wide inertia that is commonly used as the main factor. It has secondly provided improvements to VSC based frequency containment control. These have been achieved by altering the implementation of the dead band used within the frequency control structure and operating the converter based on the delay of SG primary response. Thirdly, this research has highlighted detrimental system impacts arising from fast frequency response. This thesis has fourthly investigated the deployment of different VSC frequency containment services within the network using various network operating conditions. The following sub sections provide a succinct formulation of the conclusions that have arisen from this research.

8.1.1 Factors Influencing Frequency Stability

The review of past literature highlighted that previous studies have predominantly focused on the impact that the quantity of system inertia has when performing frequency stability analysis. In the previous literature attention had been given to certain control elements such as the dead band size and droop coefficient, but not to the distribution of these elements, nor to the network operating conditions. The contribution from this thesis to this area of research is a thorough evaluation into the mechanisms and factors that govern the frequency drop and ROCOF in a power system. To undertake the analysis a generic four area system has been developed and addresses objective 1 (Develop a generic test system model that can be used to evaluate frequency stability and allow for discrete and quantifiable network alterations).

The analysis revealed how different network factors affect the time evolution of the frequency response and how specific parameters impact different frequency metrics. A new metric to describe network topology (λ) was presented and used to quantify the influence topology has on the ROCOF. A major finding was that the frequency stability is further influenced by the power flow around the system in relation to the area where the disturbance occurs. Moreover, the topology and power flow influence the operating points around the system which in turn determines the post fault torque imbalances (load pick up) for each SG. It has been shown that the power flow into the disturbance

area could be used as an elementary indicator of subsequent frequency performance. The greater the power flow into the area of disturbance, the greater the resulting frequency drop.

The location of the inertia reduction or the droop gain increase has also been shown to have a strong impact on the ROCOF and the frequency drop respectively. This work has shown the location-specific nature and distribution of these aspects and highlights that consideration should be given when deciding where to change these network factors.

Overall this component of research addresses objective 2 (Evaluate how network factors and system operating condition impact frequency stability beyond the well-established impact of inertia) and highlights that the frequency drop and ROCOF are influenced separately around the network. It displays that the factors governing them should be taken into consideration when allocating frequency response resources.

8.1.2 VSC Supplementary Frequency Control

The use of VSC to improve the frequency stability has already been proven in the literature to be beneficial as reported in Chapter 1. With the expected increase in VSC connected energy sources and the reduction of inertia in future power systems, the VSC will need to be more versatile in the frequency response that it can provide. It will also likely need to operate beyond the standard proportional control. A future concern is being able to respond fast enough to disturbances. The utilisation of the intrinsic energy in a VSC has been highlighted as a potential strategy to provide this fast response in previous literature. The use of this intrinsic energy has been analysed in this research to determine the quantity of energy available for frequency response and POD ancillary services. Contribution to knowledge provided in this thesis through the completion of objective 3 shows that the quantity of energy is insufficient for frequency response, and this quantity would be further reduced when converter limits are applied making it unviable. It was highlighted that for POD ancillary services the available calculated energy within the sub module operating limits is shown to have a minor effect on the damping. Although minor, the impact on the system damping could be scaled up through a co-ordinated response from multiple converters.

The most common VSC supplementary frequency controller is the proportional droop based control. This controller is easy to implement and operates in a similar manner to the governor control loop in a SG. This thesis has contributed to the improved implementation of this type of control loop and enabled it to respond faster through the use of a discontinuous dead band that is incorporated into the controller.

This element of research has addressed the research outlined in thesis objective 4 (Develop frequency control methods that improve the responsiveness of the VSC proportional control schemes). The operation of the VSC frequency controller when using a discontinuous dead band is further enhanced by the use of a latching component in the dead band. The latching component improves the frequency recovery by the use of different activation and de-activation limits enabling the converter to inject power over a longer period.

Due to the ability to operate a VSC in faster timeframes than the traditional SG, this opens up the potential for new frequency control strategies to be incorporated. The ability to provide fast response that can resemble an inertial response is introduced in the literature through the use of derivative control. This type of control is beneficial to limit the ROCOF but there are drawbacks due to the implementation of the derivative component. This thesis highlighted the difference between the idealized proportional system response and the actual system response in Chapter 6. To reduce the difference between ideal and actual response, an innovative controller is presented for implementation into power electronic connected energy sources. The difference-based control scheme enables an enhanced fast frequency response supplementary control signal that enables the converter to inject power when the primary response schemes have not yet had time to operate. This produces a large initial power injection due to the slow responding primary response schemes before decaying as the primary response increases. This type of response is analogous to an inertial response but does not require a derivative component on the measured frequency. This frequency control scheme requires limited system information that does not have to be available in real time. From the analysis of the scheme, results demonstrate that the control can significantly reduce the frequency deviation over non-PE and PE drop based schemes, but cannot completely achieve an ideal response. This is due to the use of a reduced estimation of the system response to reduce complexity. Overall the difference control scheme presented in this research completes objective 6 (Develop a frequency control method that operates based on the delays and limitations of traditional primary response schemes). The difference controller enables a faster response to frequency deviations that is analogous to an inertial response, without introducing the detrimental behaviour common with derivative control implementation. The scheme would also allow the system operator to be more confident about the quantity of MW/Hz frequency response and reduce the need to over-tender for primary response ancillary services.

8.1.3 Detrimental response

From the body of literature reviewed there was a focus on the improvements that fast VSC frequency response schemes have on the frequency stability under large disturbances. As the power system evolves it is inevitable that the quantity of system inertia will reduce making the frequency more vulnerable to deviations in either direction. Along with reduced levels of inertia, there will be more power electronic devices that can provide fast frequency response and stabilise the frequency following a severe disturbance, which is potentially extremely beneficial to the system. However, the fast frequency response schemes will need to operate following small disturbances as well as the large severe disturbances. Analysis provided in this thesis shows that when using a large quantity of fast frequency response and a small disturbance occurs in a low inertia system, oscillatory behaviour can occur due to the frequency controller interaction. This oscillatory behaviour or cycle limiting occurs because the quantity of frequency response is able to recover the frequency back above the operational dead band where the frequency controller is de activated, allowing the frequency to fall back below the dead band and re-trigger the frequency controller. To reduce this potential unwanted oscillatory behaviour, a contribution provided from this research is the use of an adaptive frequency controller. The adaptive controller enables the converter to respond in an unrestricted manner to disturbances of all size. However, it reduces the speed of response if oscillatory behaviour is detected in the frequency controller output. An additional feedback component in the supplementary frequency controller is used to determine the value of a first order time constant that is used on the measured frequency input. The time constant has an initial value of zero allowing fast response, but if oscillations through the use of an FFT are detected in the output then this time constant value is increased based on the frequency of the detected oscillation. The completion of this research has addressed objective 5 (Investigate detrimental system impacts created by incorporating fast frequency response schemes). This type of control would allow an increased number of fast frequency response schemes to be incorporated into the system while reducing the complexity of co-ordinating their responses.

8.1.4 Deployment of VSC Frequency Control

The use of individual VSC frequency control schemes has been shown to improve frequency stability from the literature and within this thesis. However, the use of a particular type of VSC frequency control can provide greater benefits if it is deployed under a certain network condition or in a specific network location. This would enable it

to target a specific frequency metric. Although different types of VSC control are implemented, there is currently no framework or consideration for which type of control should be deployed.

To evaluate the deployment of VSC frequency control, the implementation of different control types was performed for network operating scenarios that were derived from the initial network factors research. In addition to the different network scenarios, the location of the control type in relation to the network disturbance was also investigated. The contribution from this segment of research is the ability to improve the deployment of the VSC frequency control type by having a stronger focus on a specific frequency metric or a combined impact on both metrics. This contribution addresses objective 7 (Thoroughly investigate the impact of fast frequency response implementations under various network scenarios in order to provide operation guidance).

From the analysis it is shown that under limited VSC capacity the type of frequency control implemented has minimal impact on the frequency stability. With larger quantities of available VSC capacity the derivative controller is shown to have a stronger impact on ROCOF, but droop and derivative have the same impact on the frequency drop. It is seen that in scenarios involving lower system inertia and less available primary response, the use of proportional control has a stronger impact on reducing the frequency drop. The impact of VSC location is shown to be irrelevant in system scenarios that have high inertia and where the network topology is well meshed. For the opposing system scenarios though, the deployment of frequency response services further away from large SG power in-feeds (that influence the frequency) leads to a reduced impact on the effectiveness from the response. Overall the benefits from a specific type of VSC frequency control is shown to be dependent on the available capacity, location of the service, and the network operating conditions. These factors can be used to determine the optimal deployment strategy for the VSC frequency response deployment.

8.2 Future Work

From achieving the objectives set out in this thesis and expanding the understanding of frequency stability in general, a number of areas for future work have been highlighted. The future work derives from knowledge gained in this thesis and from expectations about the power system evolution. Future power systems are likely to progress by: 1) incorporating virtual synchronous machines (VSMs) [171], 2) real time

telemetry of generation output and connection status using Internet of Things (IoT) [172], 3) connection of low voltage (LV) [173], medium voltage (MV) [174], and HVDC energy sources, and 4) grid code changes including frequency containment limit and droop changes.

Taking these evolutionary factors into consideration, future work in the area of frequency stability can be broken into two main areas: system level analysis and converter level analysis.

8.2.1 System Level Analysis

During these studies the disconnection of a single generator was used to create a frequency disturbance, and the under frequency and ROCOF relays were not modelled. To improve the fidelity of the model, these relays need to be incorporated to enable active trip conditions if the frequency exceeds the trip limits. This would allow situations to be modelled where the initial generator disconnection can lead to a trip relay operating causing a second generator to trip. The situation where embedded distributed generation and two transmission level connected generators disconnected, has been highlighted as a crucial situation that led to large scale power cuts in the GB system [175]. This model configuration would allow cascading failure situations to be investigated and the frequency response services to be tested in extreme situations.

In this research a new network topology measure (λ) was introduced and describes how meshed and connected a network is. Future studies are required to investigate how this measure performs for larger more complex networks. Further studies are also required to quantify how a change in this value impacts the frequency stability metrics and determine if there is a linear relationship between λ and the frequency stability metrics. When analysing the data from the network factors in Chapter 3 certain correlations were found to be weak. There may have been considerable cross correlation between two or more signals, or the indicators used were not sufficient enough. To improve the conclusions drawn from the study, the analysis could be undertaken using different types of statistical analysis. The chosen methods could be compared to the Pearson correlation results provided in Chapter 3 to determine the most suitable statistical method.

This research has focused on the implementation of HVDC devices to provide the frequency containment services, but a real system will have a combination of DC in-feed assets from LV discussed in [173], MV as discussed in [174], up to HV that are discussed in Chapter 1. Due to this, analysis requires expanding to include a

combination of different rated DC assets that are capable of providing FFR. Each different rated DC asset may be required to perform different frequency response operations or contain the frequency over different timescales due to their size and capacity. Instead of isolating the impact of using HVDC assets such as interconnectors that have a high utilisation factor, additional asset types could be incorporated into the models including MV DC battery connections. This could then be used to determine the maximum quantity of fast frequency response that should be incorporated into the network to prevent the highlighted detrimental cycle limit behaviour (see Section 5.2). Analysis undertaken in Chapter 7 used an aggregated single VSC operating with a single frequency control type in the form of proportional, derivative control, or difference control (see Chapter 6). In reality there will need to be a combination of frequency response services including a proportion of all types. Future studies are required to determine the quantities and capacity of each frequency control type based on the system inertia and the additional SG based primary response.

Although in was shown in Chapter 7 that operating the MMC interconnectors with different frequency control strategies improved a specific frequency stability metric, this did not take into account the impacts on the remaining SGs in the system. As conventional SGs are decommissioned, more emphasis may be put on the large HVDC in-feeds to provide ancillary services in a similar manner to that provided by the SGs such as droop control. Evaluation is required to assess how the HVDC assets should be operated to enable them to co-ordinate the post fault power sharing with existing large generating assets. Studies should determine if a droop mode would be more beneficial for HVDC assets as they provide a large amount of power and could participate in the power sharing (pick-up), versus inertia style responses for smaller PE assets.

This thesis has focused on traditional operating principles and frequency response requirements that are designed to prevent under frequency and ROCOF relays from tripping. As technology and communication connectivity improves, the frequency response requirements will evolve and the influence of these changes needs to be understood. As all assets become connected using IoT or the traditional ROCOF relays are replaced with new technology, the requirements to contain the frequency may change. Improved communication connectivity between assets as highlighted in [172] could lead to the use of signals confirming an event such as SG disconnection rather than speculating that an event has occurred from the measured frequency. Every SG could be monitored in real time and pre-disconnection data could be used to co-ordinate the frequency response including the size of the response required from the remaining

generation. Moreover, if traditional relays are improved or IoT connectivity becomes commonplace, a determination of the frequency containment requirements would be required including values for the maximum permissible frequency drop and ROCOF.

Using HVDC interconnectors to provide frequency support is extremely beneficial for the disturbed network, but energy has to be extracted from the adjacent network where the sudden extraction could be detrimental to the attached network as outlined in [55]. Frequency response from interconnectors may have to be limited depending on the characteristics of the attached network and the factors that influence this could be VSC converter type, frequency response control technique, and attached network properties. Future studies are required to assess these limitations in depth and determine the maximum frequency response capabilities from HVDC interconnectors when they are bounded.

No optimal deployment of the VSC frequency containment response was provided in this thesis from the research undertaken in Chapter 7. Optimal deployment of the VSC frequency response could be determined based on the network factors and the control factors that were introduced in this thesis. Optimal deployment could combine all of the factors and research presented in this thesis and use it to determine frequency response deployment in large scale power systems.

This research has also highlighted that there is a need for an agreed or standardised ROCOF measurement window methodology. As of yet, no standard measured ROCOF window exists and this can lead to different values being reported. There are additional defined frequency response requirements that are changed by the SO on a semi regular basis currently, for instance through working groups as in [176]. This makes it difficult to define the best VSC frequency response conditions. There are several important questions that this research has highlighted in order to expedite future research into VSC frequency response from a network perspective. These are: 1) what size the VSC droop component should be to contain the frequency and provide power sharing, 2) what size should the VSC frequency controller dead band size be, 3) the maximum MW response that should be applied to each different size VSC device (currently in the UK the maximum is 50 MW), 4) is there a maximum realistic time the frequency response should last from different size VSC devices. In this thesis, a change in these requirements, for example the dead band size, has been shown to impact the frequency stability highlighting the need to define rigid criteria for each requirement in the future.

8.2.2 Converter Level Analysis

An evaluation of the effects that each VSC frequency response type has on the DC link voltage and overall converter stability is required. The impact of the frequency response type may affect converter stability and some future analysis is required to evaluate the resultant interaction between converter stations, circulating current changes, modulation, and capacitor balancing when the different frequency control schemes are implemented. Research presented in this thesis used an average value MMC model that does not take into account certain aspects of the converter operation and the frequency detection. Using a detailed MMC model would allow the converter limitations and frequency detection methods to be incorporated into the analysis. This would enable each VSC frequency type to be evaluated in detail to provide greater knowledge for the best type of control and where further limitations appear. Further to that, a detailed model implementation could be used to explore the detrimental behaviour witnessed in this thesis (see Section 5.2) that is due to the converter limit cycling. The knowledge could be used to improve the mitigation techniques for cycle limit behaviour in instances of large quantities of fast response combined with small disturbances. The detailed model would allow greater fast acting converter dynamics to be incorporated to determine how the cycle limit behaviour impacts the converter and not the grid as displayed in this thesis. The phenomena of cyclic limit behaviour also requires evaluation when using VSMs that are equipped with primary response controls.

There is significant research going into VSMs and although they are not incorporated into large scale power systems currently, it is expected that they will be in the future as in [171]. Therefore a detailed comparison of the frequency response between grid-following and grid-forming converter types is required to determine if a specific converter type should be operated with a specific role regarding frequency stability. The required investigation should evaluate the impact of different VSM control types in order to determine how the response from the converter would change as the network evolves. This future work would also need to evaluate the impact of the frequency response as the percentage in-feed of each converter type changes.

The use of derivative control was used in this thesis and several literature articles have implemented this type of control as in [46] and reported in Chapter 1. A further detailed evaluation and comparison for different derivative based control schemes is required. Derivative control may be implemented as an actual derivative scheme or as a lead/lag filter component and both may operate on the measured frequency or the difference in frequency. A comparison between techniques is required and further

analysis is needed to determine the best method to implement the derivative, especially the parameters for the derivative time and input signal filtering time constants.

To bridge the gap between theoretical simulation and real world implementation, further performance evaluation of the VSC frequency control schemes could be achieved using a real time digital simulator (RTDS) system. The use of RTDS would allow the VSC control schemes to be tested in greater depth, allowing the SOs to be confident about the capabilities of each control scheme.

References

[1] Department for Business, Energy and Industrial Strategy, "2018 UK Green House Gas Emissions, Provisional Figures," National Statistics Report, London: Crown Copyright, 2019.

[2] National Grid, "Future Energy Scenarios," Company Report, 2018.

[3] Department for Business, Energy and Industrial Strategy, "UK Energy Statistics, 2018 & Q4 2018," National Statistics Report, London: Crown Copyright, 2019.

[4] World Energy Council, "World Energy Trilemma Index | 2018," Institutional Report. [Online]. Available:https://trilemma.worldenergy.org/reports/main/2018/2018%20-Energy%20Trilemma%20Index.pdf. [Accessed 5th August 2019].

[5] P. Kundur *et al.*, "Definition and classification of power system stability IEEE/CIGRE joint task force on stability terms and definitions," *IEEE Transactions on Power Systems*, vol. 19, no. 3, pp. 1387-1401, 2004.

[6] National Grid, "GSR015: Normal Infeed loss Risk. National Electricity Transmission System Security and Quality of Supply Standards," Company Report, 2014.

[7] Z. Zhian *et al.*, "Power system frequency monitoring network (FNET) implementation," *IEEE Transactions on Power Systems*, vol. 20, no. 4, pp. 1914-1921, 2005.

[8] A. Ulbig, T. S. Borsche, and G. Andersson, "Impact of Low Rotational Inertia on Power System Stability and Operation," *IFAC Proceedings Volumes*, vol. 47, no. 3, pp. 7290-7297, 2014.

[9] P. Tielens and D. Van Hertem, "The relevance of inertia in power systems," *Renewable and Sustainable Energy Reviews*, vol. 55, pp. 999-1009, 2016.

[10] J. Machowski, J. Bialek, J. Bumby, *Power system Dynamics: Stability and Control*. UK: John Wiley and Sons, 2008.

[11] H. Gu, R. Yan, and T. K. Saha, "Minimum Synchronous Inertia Requirement of Renewable Power Systems," *IEEE Transactions on Power Systems*, vol. 33, no. 2, pp. 1533-1543, 2018.

[12] A. S. Ahmadyar, S. Riaz, G. Verbič, J. Riesz, and A. Chapman, "Assessment of minimum inertia requirement for system frequency stability," in *IEEE International Conference on Power System Technology*, Wollongong, Australia, 2016

[13] P. Wall and V. Terzija, "Simultaneous Estimation of the Time of Disturbance and Inertia in Power Systems," *IEEE Transactions on Power Delivery*, vol. 29, no. 4, pp. 2018-2031, 2014.

[14] P. M. Ashton, C. S. Saunders, G. A. Taylor, A. M. Carter, and M. E. Bradley, "Inertia Estimation of the GB Power System Using Synchrophasor Measurements," *IEEE Transactions on Power Systems*, vol. 30, no. 2, pp. 701-709, 2015.

[15] E. Orum, M. laasonen, M. Laasonen, A. I. Bruseth, E. A. Jansson, et al, "Future system inertia," European Network of Transmission System Operators for Electricity (entsoe) Technical Report, 2015.

[16] National Grid, "Product Roadmap: For frequency response and reserve," Company Report, Warwick, 2017.

[17] National Grid, "Operability Strategy Report," Company Report, Warwick, 2019.

[18] M. Nedd, K. Bell, and C. Booth, "Containing Loss Risk in a Low Inertia GB Power System," in *IEEE International Conference on Environment and Electrical Engineering and IEEE Industrial and Commercial Power Systems Europe*, Palermo, Italy, 2018.

[19] A. Berizzi, "The Italian 2003 blackout," in *IEEE Power Engineering Society General Meeting, Denver, USA*, 2004.

[20] Australian Energy Market Operator "Black System South Australia 28 September 2016," Company Report, 2017.

[21] F. Chengwei, W. Xiaoru, T. Yufei, and W. Wencheng, "Minimum frequency estimation of power system considering governor deadbands," *IET Generation, Transmission & Distribution*, vol. 11, no. 15, pp. 3814-3822, 2017.

[22] G. Kou, P. Markham, S. Hadley, T. King, and Y. Liu, "Impact of Governor Deadband on Frequency Response of the U.S. Eastern Interconnection," *IEEE Transactions on Smart Grid*, vol. 7, no. 3, pp. 1368-1377, 2016.

[23] I. Egido, F. Fernandez-Bernal, P. Centeno, and L. Rouco, "Maximum Frequency Deviation Calculation in Small Isolated Power Systems," *IEEE Transactions on Power Systems,* vol. 24, no. 4, pp. 1731-1738, 2009.

[24] P. Vorobev, D. M. Greenwood, J. H. Bell, J. W. Bialek, P. C. Taylor, and K. Turitsyn, "Deadbands, Droop, and Inertia Impact on Power System Frequency Distribution," *IEEE Transactions on Power Systems,* vol. 34, no. 4, pp. 3098-3108, 2019.

[25] Y. Bian, H. Wyman-Pain, F. Li, R. Bhakar, S. Mishra, and N. P. Padhy, "Demand Side Contributions for System Inertia in the GB Power System," *IEEE Transactions on Power Systems,* vol. 33, no. 4, pp. 3521-3530, 2018.

[26] H. Huang and F. Li, "Sensitivity Analysis of Load-Damping Characteristic in Power System Frequency Regulation," *IEEE Transactions on Power Systems,* vol. 28, no. 2, pp. 1324-1335, 2013.

[27] M. P. Bahrman and B. K. Johnson, "The ABCs of HVDC transmission technologies," *IEEE Power and Energy Magazine,* vol. 5, no. 2, pp. 32-44, 2007.

[28] J. Yu *et al.*, "Reliable control and protection system for the Tian-Guang HVDC transmission project," in *International Conference on Power System Technology*, Kunming, USA, 2002.

[29] P. L. Francos, S. S. Verdugo, H. F. Álvarez, S. Guyomarch, and J. Loncle, "INELFE — Europe's first integrated onshore HVDC interconnection," in *IEEE Power and Energy Society General Meeting*, San Diego, USA, 2012.

[30] O. E. Oni, I. E. Davidson, and K. N. I. Mbangula, "A review of LCC-HVDC and VSC-HVDC technologies and applications," in *IEEE 16th International Conference on Environment and Electrical Engineering*, Florence, Italy, 2016.

[31] N. Flourentzou, V. G. Agelidis, and G. D. Demetriades, "VSC-Based HVDC Power Transmission Systems: An Overview," *IEEE Transactions on Power Electronics,* vol. 24, no. 3, pp. 592-602, 2009.

[32] N. Ha Thi, Y. Guangya, A. H. Nielsen, and P. H. Jensen, "Frequency stability improvement of low inertia systems using synchronous condensers," in *IEEE International Conference on Smart Grid Communications*, Sydney, Australia, 2016.

[33] H. T. Nguyen, G. Yang, A. H. Nielsen, and P. H. Jensen, "Combination of Synchronous Condenser and Synthetic Inertia for Frequency Stability Enhancement in Low Inertia Systems," *IEEE Transactions on Sustainable Energy,* vol. 10, no. 3, pp. 997-1005, 2018.

[34] M. Nedd, C. Booth, and K. Bell, "Potential solutions to the challenges of low inertia power systems with a case study concerning synchronous condensers," in *52nd International Universities Power Engineering Conference*, Heraklion, Greece, 2017.

[35] Think Grid. "Synchronous condensers for better grid stability." 2016. [Online]. Available: https://www.think-grid.org/synchronous-condensers-better-grid-stability. [Accessed 21st July August 2019].

[36] A. F. Meyabadi and M. H. Deihimi, "A review of demand-side management: Reconsidering theoretical framework," *Renewable and Sustainable Energy Reviews,* vol. 80, pp. 367-379, 2017.

[37] M. T. Muhssin, L. M. Cipcigan, S. S. Sami, and Z. A. Obaid, "Potential of demand side response aggregation for the stabilization of the grids frequency," *Applied Energy,* vol. 220, pp. 643-656, 2018.

[38] P. Babahajiani, Q. Shafiee, and H. Bevrani, "Intelligent Demand Response Contribution in Frequency Control of Multi-Area Power Systems," *IEEE Transactions on Smart Grid,* vol. 9, no. 2, pp. 1282-1291, 2018.

[39] I. Beil, I. Hiskens, and S. Backhaus, "Frequency Regulation From Commercial Building HVAC Demand Response," *Proceedings of the IEEE,* vol. 104, no. 4, pp. 745-757, 2016.

[40] F. Teng, M. Aunedi, D. Pudjianto, and G. Strbac, "Benefits of Demand-Side Response in Providing Frequency Response Service in the Future GB Power System," *Frontiers in Energy Research,* vol. 3, no. 36, 2015.

[41] M. Marzband, M. M. Moghaddam, M. F. Akorede, and G. Khomeyrani, "Adaptive load shedding scheme for frequency stability enhancement in microgrids," *Electric Power Systems Research,* vol. 140, pp. 78-86, 2016.

[42] K. Seethalekshmi, S. N. Singh, and S. C. Srivastava, "A Synchrophasor Assisted Frequency and Voltage Stability Based Load Shedding Scheme for Self-Healing of Power System," *IEEE Transactions on Smart Grid*, vol. 2, no. 2, pp. 221-230, 2011.

[43] F. Shokooh *et al.*, "Intelligent Load Shedding," *IEEE Industry Applications Magazine*, vol. 17, no. 2, pp. 44-53, 2011.

[44] R. Ofir, U. Markovic, P. Aristidou, and G. Hug, "Droop vs. virtual inertia: Comparison from the perspective of converter operation mode," in *IEEE International Energy Conference*, Limassol, Cyprus, 2018.

[45] M. Dreidy, H. Mokhlis, and S. Mekhilef, "Inertia response and frequency control techniques for renewable energy sources: A review," *Renewable and Sustainable Energy Reviews*, vol. 69, pp. 144-155, 2017.

[46] M. Yu *et al.*, "A review of control methods for providing frequency response in VSC-HVDC transmission systems," in *49th International Universities Power Engineering Conference*, Cluj-Napoca, Romania, 2014.

[47] S. A. Alsharafi, H. A. Besheer, and M. H. Emara, "Primary Frequency Response Enhancement for Future Low Inertia Power Systems Using Hybrid Control Technique," *Energies*, vol. 11, no. 4, 2018.

[48] Y. Ye, Y. Qiao, and Z. Lu, "Revolution of frequency regulation in the converter-dominated power system," *Renewable and Sustainable Energy Reviews*, vol. 111, pp. 145-156, 2019.

[49] R. Eriksson, N. Modig, and K. Elkington, "Synthetic inertia versus fast frequency response: a definition," *IET Renewable Power Generation*, vol. 12, no. 5, pp. 507-514, 2018.

[50] A. Bucurenciu, M. Ndreko, M. Popov, and M. A. M. M. v. d. Meijden, "Frequency response using MTDC grids: A comparative study of common methods," in *IEEE Eindhoven PowerTech*, Eindhoven, Netherlands 2015.

[51] A. S. Elansari, S. J. Finney, J. Burr, and M. F. Edrah, "Frequency control capability of VSC-HVDC transmission system," in *11th IET International Conference on AC and DC Power Transmission*, Birmingham, UK, 2015.

[52] C. Du, M. H. J. Bollen, E. Agneholm, and A. Sannino, "A New Control Strategy of a VSC-HVDC System for High-Quality Supply of Industrial Plants," *IEEE Transactions on Power Delivery*, vol. 22, no. 4, pp. 2386-2394, 2007.

[53] C. Du, E. Agneholm, and G. Olsson, "Comparison of Different Frequency Controllers for a VSC-HVDC Supplied System," *IEEE Transactions on Power Delivery*, vol. 23, no. 4, pp. 2224-2232, 2008.

[54] K. Rouzbehi, Z. Jiebei, Z. Weiyi, G. B. Gharehpetian, A. Luna, and P. Rodriguez, "Generalized voltage droop control with inertia mimicry capability - step towards automation of multi-terminal HVDC grids," in *International Conference on Renewable Energy Research and Applications, Palermo, Italy*, 2015.

[55] C. E. Spallarossa, Y. Pipelzadeh, and T. C. Green, "Influence of frequency-droop supplementary control on disturbance propagation through VSC HVDC links," in *IEEE Power & Energy Society General Meeting*, Vancouver, Canada, 2013.

[56] T. M. Haileselassie, R. E. Torres-Olguin, T. K. Vrana, K. Uhlen, and T. Undeland, "Main grid frequency support strategy for VSC-HVDC connected wind farms with variable speed wind turbines," in *IEEE Trondheim PowerTech*, Trondheim, Norway, 2011.

[57] D. Zeng, "A generalized power control strategy with droop feedback for VSC-HVDC," in *IEEE Power and Energy Society General Meeting*, San Diego, USA, 2012.

[58] B. Silva, C. L. Moreira, L. Seca, Y. Phulpin, and J. A. P. Lopes, "Provision of Inertial and Primary Frequency Control Services Using Offshore Multiterminal HVDC Networks," *IEEE Transactions on Sustainable Energy*, vol. 3, no. 4, pp. 800-808, 2012.

[59] S. Li, M. Barnes, R. Preece, and J. Milanović, "Frequency stabilisation using VSC-HVDC," in *IEEE Power and Energy Society General Meeting*, Boston, USA, 2016.

[60] A. G. Endegnanew and K. Uhlen, "Global analysis of frequency stability and inertia in AC systems interconnected through an HVDC," in *IEEE International Energy Conference*, Leuven, Belgium, 2016.

[61] J. V. d. Vyver, J. D. M. D. Kooning, B. Meersman, L. Vandevelde, and T. L. Vandoorn, "Droop Control as an Alternative Inertial Response Strategy for the Synthetic Inertia on Wind Turbines," *IEEE Transactions on Power Systems*, vol. 31, no. 2, pp. 1129-1138, 2016.

[62] R. Shah, R. Preece, and M. Barnes, "Dual-loop primary frequency regulation controller for VSC-HVDC system," in *IEEE Manchester PowerTech*, Manchester, UK, 2017.

[63] I. M. Sanz, P. D. Judge, C. E. Spallarossa, B. Chaudhuri, and T. C. Green, "Dynamic Overload Capability of VSC HVDC Interconnections for Frequency Support," *IEEE Transactions on Energy Conversion*, vol. 32, no. 4, pp. 1544-1553, 2017.

[64] D. M. Greenwood, K. Y. Lim, C. Patsios, P. F. Lyons, Y. S. Lim, and P. C. Taylor, "Frequency response services designed for energy storage," *Applied Energy*, vol. 203, pp. 115-127, 2017/10/01/ 2017.

[65] Y. Phulpin, "Communication-Free Inertia and Frequency Control for Wind Generators Connected by an HVDC-Link," *IEEE Transactions on Power Systems*, vol. 27, no. 2, pp. 1136-1137, 2012.

[66] Y. Rink, L. Held, S. Wenig, M. Suriyah, and T. Leibfried, "On implementation of primary frequency control in MMC-HVDC transmission systems," in *IEEE PES Innovative Smart Grid Technologies Conference Europe*, Torino, Italy, 2017.

[67] J. E. S. de Haan, C. Escudero Concha, M. Gibescu, J. van Putten, G. L. Doorman, and W. L. Kling, "Stabilising system frequency using HVDC between the Continental European, Nordic, and Great Britain systems," *Sustainable Energy, Grids and Networks*, vol. 5, pp. 125-134, 2016.

[68] W. Wang, Y. Li, Y. Cao, U. Häger, and C. Rehtanz, "Adaptive Droop Control of VSC-MTDC System for Frequency Support and Power Sharing," *IEEE Transactions on Power Systems*, vol. 33, no. 2, pp. 1264-1274, 2018.

[69] K. Jose, O. Adeuyi, J. Liang, and C. E. Ugalde-Loo, "Coordination of fast frequency support from multi-terminal HVDC grids," in *IEEE International Energy Conference*, Limassol, Cyprus, 2018.

[70] O. D. Adeuyi, M. Cheah-Mane, J. Liang, and N. Jenkins, "Fast Frequency Response From Offshore Multiterminal VSC–HVDC Schemes," *IEEE Transactions on Power Delivery*, vol. 32, no. 6, pp. 2442-2452, 2017.

[71] E. Rakhshani, D. Remon, A. M. Cantarellas, and P. Rodriguez, "Analysis of derivative control based virtual inertia in multi-area high-voltage direct current interconnected power systems," *IET Generation, Transmission & Distribution*, vol. 10, no. 6, pp. 1458-1469, 2016.

[72] T. Kerdphol, F. S. Rahman, M. Watanabe, Y. Mitani, D. Turschner, and H. Beck, "Enhanced Virtual Inertia Control Based on Derivative Technique to Emulate Simultaneous Inertia and Damping Properties for Microgrid Frequency Regulation," *IEEE Access*, vol. 7, pp. 14422-14433, 2019.

[73] A. E. Leon, "Short-Term Frequency Regulation and Inertia Emulation Using an MMC-Based MTDC System," *IEEE Transactions on Power Systems*, vol. 33, no. 3, pp. 2854-2863, 2018.

[74] J. Zhu, C. D. Booth, G. P. Adam, A. J. Roscoe, and C. G. Bright, "Inertia Emulation Control Strategy for VSC-HVDC Transmission Systems," *IEEE Transactions on Power Systems*, vol. 28, no. 2, pp. 1277-1287, 2013.

[75] F. M. Gonzalez-Longatt, "Activation schemes of synthetic inertia controller for full converter wind turbine generators," in *IEEE Eindhoven PowerTech*, Eindhoven, Netherlands, 2015.

[76] E. Rakhshani and P. Rodriguez, "Inertia Emulation in AC/DC Interconnected Power Systems Using Derivative Technique Considering Frequency Measurement Effects," *IEEE Transactions on Power Systems*, vol. 32, no. 5, pp. 3338-3351, 2017.

[77] M. Rezkalla, A. Zecchino, S. Martinenas, A. M. Prostejovsky, and M. Marinelli, "Comparison between synthetic inertia and fast frequency containment control based on single phase EVs in a microgrid," *Applied Energy*, vol. 210, pp. 764-775, 2018.

[78] M. Hajiakbari Fini and M. E. Hamedani Golshan, "Determining optimal virtual inertia and frequency control parameters to preserve the frequency stability in islanded

microgrids with high penetration of renewables," *Electric Power Systems Research,* vol. 154, pp. 13-22, 2018.

[79] O. D. Adeuyi *et al.*, "Frequency support from modular multilevel converter based multi-terminal HVDC schemes," in *IEEE Power & Energy Society General Meeting*, Denver, USA, 2015.

[80] C. Barker, A. Adamczyk, G. Garcia Soto, "Low Frequency Active Power Oscillation Damping Using A MMC-VSC HVDC link," in 13th *IET International Conference on AC and DC Power Transmission*, Manchester, UK, 2017.

[81] A. Junyent-Ferr, Y. Pipelzadeh, and T. C. Green, "Blending HVDC-Link Energy Storage and Offshore Wind Turbine Inertia for Fast Frequency Response," *IEEE Transactions on Sustainable Energy,* vol. 6, no. 3, pp. 1059-1066, 2015.

[82] P. D. Judge and T. C. Green, "Modular Multilevel Converter With Partially Rated Integrated Energy Storage Suitable for Frequency Support and Ancillary Service Provision," *IEEE Transactions on Power Delivery*, vol. 34, no. 1, pp. 208-219, 2019.

[83] I. Trintis, S. Munk-Nielsen, and R. Teodorescu, "A new modular multilevel converter with integrated energy storage," in *37th Annual Conference of the IEEE Industrial Electronics Society*, Melbourne, Australia, 2011.

[84] M. Vasiladiotis and A. Rufer, "Analysis and Control of Modular Multilevel Converters With Integrated Battery Energy Storage," *IEEE Transactions on Power Electronics,* vol. 30, no. 1, pp. 163-175, 2015.

[85] Z. Jiebei, C. D. Booth, G. P. Adam, and A. J. Roscoe, "Inertia emulation control of VSC-HVDC transmission system," in *International Conference on Advanced Power System Automation and Protection*, Beijing, China, 2011.

[86] G. Delille, B. Francois, and G. Malarange, "Dynamic Frequency Control Support by Energy Storage to Reduce the Impact of Wind and Solar Generation on Isolated Power System's Inertia," *IEEE Transactions on Sustainable Energy*, vol. 3, no. 4, pp. 931-939, 2012.

[87] H. Liu and Z. Chen, "Contribution of VSC-HVDC to Frequency Regulation of Power Systems With Offshore Wind Generation," *IEEE Transactions on Energy Conversion,* vol. 30, no. 3, pp. 918-926, 2015.

[88] T. M. Haileselassie, R. E. Torres-Olguin, T. K. Vrana, K. Uhlen, and T. Undeland, "Main grid frequency support strategy for VSC-HVDC connected wind farms with variable speed wind turbines," in *IEEE Trondheim PowerTech*, Trondheim, Norway, 2011.

[89] Y. Li, Z. Xu, J. Østergaard, and D. J. Hill, "Coordinated Control Strategies for Offshore Wind Farm Integration via VSC-HVDC for System Frequency Support," *IEEE Transactions on Energy Conversion*, vol. 32, no. 3, pp. 843-856, 2017.

[90] Z. Miao, L. Fan, D. Osborn, and S. Yuvarajan, "Wind Farms With HVdc Delivery in Inertial Response and Primary Frequency Control," *IEEE Transactions on Energy Conversion*, vol. 25, no. 4, pp. 1171-1178, 2010.

[91] P. Kou, D. Liang, Z. Wu, Q. Ze, and L. Gao, "Frequency Support From a DC-Grid Offshore Wind Farm Connected Through an HVDC Link: A Communication-Free Approach," *IEEE Transactions on Energy Conversion,* vol. 33, no. 3, pp. 1297-1310, 2018.

[92] F. Gonzalez-Longatt, E. Chikuni, and E. Rashayi, "Effects of the Synthetic Inertia from wind power on the total system inertia after a frequency disturbance," in *IEEE International Conference on Industrial Technology*, Cape Town, South Africa, 2013.

[93] L. Ruttledge and D. Flynn, "Emulated Inertial Response From Wind Turbines: Gain Scheduling and Resource Coordination," *IEEE Transactions on Power Systems,* vol. PP, no. 99, pp. 1-9, 2016.

[94] N. Miller, R. Delmerico, and M. Cardinal, "GE Wind Plant Dynamic Performance for Grid and Wind Events," In *AEE Techwindgrid*, Madrid, Spain, 2009.

[95] Y.-K. Wu and K.-T. Tang, "Frequency Support by BESS – Review and Analysis," *Energy Procedia*, vol. 156, pp. 187-191, 2019.

[96] Y. Kim, "Experimental study of battery energy storage systems participating in grid frequency regulation," in *IEEE/PES Transmission and Distribution Conference and Exposition*, Dallas, Texas, 2016.

[97] M. Ramírez, R. Castellanos, G. Calderón, and O. Malik, "Placement and sizing of battery energy storage for primary frequency control in an isolated section of the Mexican power system," *Electric Power Systems Research*, vol. 160, pp. 142-150, 2018.

[98] A. Adrees, J. V. Milanović, and P. Mancarella, "The Influence of Location of Distributed Energy Storage Systems on Primary Frequency Response of Low Inertia Power Systems," in *IEEE Power & Energy Society General Meeting*, Portland, USA, 2018.

[99] Y. Yang, W. Zhang, J. Jiang, M. Huang, and L. Niu, "Optimal Scheduling of a Battery Energy Storage System with Electric Vehicles' Auxiliary for a Distribution Network with Renewable Energy Integration," *Energies*, vol. 8, no. 10, 2015.

[100] R. Alvarez, M. Pieschel, H. Gambach, and E. Spahic, "Modular multilevel converter with short-time power intensive electrical energy storage capability," in *IEEE Electrical Power and Energy Conference*, London, Canada, 2015.

[101] E. Spahic, C. P. S. S. Reddy, M. Pieschel, and R. Alvarez, "Multilevel STATCOM with power intensive energy storage for dynamic grid stability - frequency and voltage support," in *IEEE Electrical Power and Energy Conference*, London, Canada, *2015*.

[102] E. Spahic, K. Frey, G. Beck, and V. Hild, "Inertia in the System and First Swing Frequency-Description and Mitigation Possibilities," in *IEEE/PES Transmission and Distribution Conference and Exposition*, Denver, USA, 2018.

[103] EirGrid. "System Services Compliance." [Online]. Available: http://www.eirgridgroup.com/customer-and-industry/general-customer-information/-grid-code-compliance-test/compliance-testing/system-services-testing/index.xml. [Accessed 4th April 2019].

[104] Y. Mu, J. Wu, J. Ekanayake, N. Jenkins, and H. Jia, "Primary Frequency Response From Electric Vehicles in the Great Britain Power System," *IEEE Transactions on Smart Grid*, vol. 4, no. 2, pp. 1142-1150, 2013.

[105] F. Teng, Y. Mu, H. Jia, J. Wu, P. Zeng, and G. Strbac, "Challenges on primary frequency control and potential solution from EVs in the future GB electricity system," *Applied Energy*, vol. 194, pp. 353-362, 2017.

[106] J. Dai, Y. Phulpin, A. Sarlette, and D. Ernst, "Coordinated primary frequency control among non-synchronous systems connected by a multi-terminal high-voltage direct current grid," *IET Generation, Transmission & Distribution*, vol. 6, no. 2, pp. 99-108, 2012.

[107] A. Llaria, O. Curea, J. Jiménez, and H. Camblong, "Survey on microgrids: Unplanned islanding and related inverter control techniques," *Renewable Energy*, vol. 36, no. 8, pp. 2052-2061, 2011.

[108] A. Ghafouri, J. Milimonfared, and G. B. Gharehpetian, "Coordinated Control of Distributed Energy Resources and Conventional Power Plants for Frequency Control of Power Systems," *IEEE Transactions on Smart Grid*, vol. 6, no. 1, pp. 104-114, 2015.

[109] M. Imhof and G. Andersson, "Power system stability control using Voltage Source Converter based HVDC in power systems with a high penetration of Renewables," in *Power Systems Computation Conference*, Wroclaw, Poland, 2014.

[110] I. Y. Chung, W. Liu, D. A. Cartes, E. G. Collins, and S. I. Moon, "Control Methods of Inverter-Interfaced Distributed Generators in a Microgrid System," *IEEE Transactions on Industry Applications*, vol. 46, no. 3, pp. 1078-1088, 2010.

[111] B. K. Poolla, D. Gross, and F. Dörfler, "Placement and Implementation of Grid-Forming and Grid-Following Virtual Inertia and Fast Frequency Response," *IEEE Transactions on Power Systems*, pp. 1-1, 2019.

[112] H. Pulgar-Painemal, Y. Wang, and H. Silva-Saravia, "On Inertia Distribution, Inter-Area Oscillations and Location of Electronically-Interfaced Resources," *IEEE Transactions on Power Systems*, vol. 33, no. 1, pp. 995-1003, 2018.

[113] B. K. Poolla, S. Bolognani, and F. Dörfler, "Optimal Placement of Virtual Inertia in Power Grids," *IEEE Transactions on Automatic Control*, vol. 62, no. 12, pp. 6209-6220, 2017.

[114] H. Bevrani, T. Ise, and Y. Miura, "Virtual synchronous generators: A survey and new perspectives," *International Journal of Electrical Power & Energy Systems,* vol. 54, pp. 244-254, 2014.

[115] Q. C. Zhong and G. Weiss, "Synchronverters: Inverters That Mimic Synchronous Generators," *IEEE Transactions on Industrial Electronics,* vol. 58, no. 4, pp. 1259-1267, 2011.

[116] A. Fathi, Q. Shafiee, and H. Bevrani, "Robust Frequency Control of Microgrids Using an Extended Virtual Synchronous Generator," *IEEE Transactions on Power Systems,* vol. 33, no. 6, pp. 6289-6297, 2018.

[117] F. Wang, L. Zhang, X. Feng, and H. Guo, "An Adaptive Control Strategy for Virtual Synchronous Generator," *IEEE Transactions on Industry Applications,* vol. 54, no. 5, pp. 5124-5133, 2018.

[118] V. Karapanos, P. Kotsampopoulos, and N. Hatziargyriou, "Performance of the linear and binary algorithm of virtual synchronous generators for the emulation of rotational inertia," *Electric Power Systems Research,* vol. 123, pp. 119-127, 2015.

[119] M. Guan, W. Pan, J. Zhang, Q. Hao, J. Cheng, and X. Zheng, "Synchronous Generator Emulation Control Strategy for Voltage Source Converter (VSC) Stations," *IEEE Transactions on Power Systems,* vol. 30, no. 6, pp. 3093-3101, 2015.

[120] A. D. Paquette and D. M. Divan, "Virtual Impedance Current Limiting for Inverters in Microgrids With Synchronous Generators," *IEEE Transactions on Industry Applications,* vol. 51, no. 2, pp. 1630-1638, 2015.

[121] P. W. Sauer and M. A. Pai, *Power System Dynamics and Stability*. Prentice Hall, 1998.

[122] P. Kundur, *Power System Stability and Control*. New Delhi: McGraw Hill, 1994.

[123] DIgSILENT GmbH, "Technical Reference Documentation: Synchronous Generator Model," 2017.

[124] J.Glover, M. Sarma, and T. Overbye, *Power System Analysis and Design*. USA: Cengage, 2012.

[125] National Grid, "The Grid Code," Technical Report Issue no. 5, 2017.

[126] G. Kou, S. W. Hadley, and Y. Liu, "Dynamic Model Validation with GovernorDeadband on the EasternInterconnection," Oak Ridge National Laboratory, Technical Report, Oak Ridge, 2014.

[127] Task Force on Turbine Governor Modelling, "Dynamic Models forTurbine-Governors in Power System Studies", IEEE Technical report PES-TR1, 2013.

[128] S. Mohajeryami, A. R. Neelakantan, I. N. Moghaddam, and Z. Salami, "Modeling of deadband function of governor model and its effect on frequency Response characteristics," in *North American Power Symposium,* Charlotte, USA, 2015.

[129] Siemens PTI, "BOSL Controllers – Standard 1," 2008, [Online]. Available: https://www.energy.siemens.com/us/pool/hq/serv-ices/power-transmission-distribution-/power-technologies-international-/software-solutions/BOSL_Controllers_Standard-1_2008_03_13.pdf. [Accessed 23rd August 2019].

[130] "IEEE Recommended Practice for Excitation System Models for Power System Stability Studies," *IEEE Technical Standard Std 421.5-2005 (Revision of IEEE Std 421.5-1992),* 2006

[131] L. Rodríguez-García, S. Pérez-Londoño, and J. Mora-Flórez, "Measurement-based exponential recovery load model: Development and validation," *DYNA,* vol. 82, pp. 131-140, 2015.

[132] D. J. Hill, "Nonlinear dynamic load models with recovery for voltage stability studies," *IEEE Transactions on Power Systems,* vol. 8, no. 1, pp. 166-176, 1993.

[133] J. V. Milanovic and I. A. Hiskens, "Effects of load dynamics on power system damping," *IEEE Transactions on Power Systems,* vol. 10, no. 2, pp. 1022-1028, 1995.

[134] M. K. Al-Nussairi, R. Bayindir, S. Padmanaban, L. Mihet-Popa, and P. Siano, "Constant Power Loads (CPL) with Microgrids: Problem Definition, Stability Analysis and Compensation Techniques," *Energies,* vol. 10, no. 10, 2017.

[135] DIgSILENT Gmbh, "Technical reference documentation, Static Generator," Gomaringen, Germany, 2017.

[136] E. Muljadi, N. Samaan, V. Gevorgian, L. Jun, and S. Pasupulati, "Short circuit current contribution for different wind turbine generator types," in *IEEE Power and Energy Society General Meeting*, Providence, USA, 2010.

[137] Power System Dynamic Performance Committee, "Benchmark Systems for Small-Signal Stability Analysis and Control," in "IEEE Technical Report PES-TR18," 2015.

[138] DIgSILENT Gmbh, "DIgSILENT PowerFactory User manual 2017," Gomaringen, Germany, 2017.

[139] National Grid, "Electricity Ten Year Statement 2017," Company report, 2017.

[140] Z. A. Obaid, L. M. Cipcigan, L. Abrahim, and M. T. Muhssin, "Frequency control of future power systems: reviewing and evaluating challenges and new control methods," *Journal of Modern Power Systems and Clean Energy*, vol. 7, no. 1, pp. 9-25, 2019.

[141] V. V. Terzija, "Adaptive underfrequency load shedding based on the magnitude of the disturbance estimation," *IEEE Transactions on Power Systems*, vol. 21, no. 3, pp. 1260-1266, 2006.

[142] F. Milano, *Power system modelling and scripting*. Springer, 2010.

[143] M. E. J. Newman, *Networks: An introduction*. USA; Oxford University Press, 2010.

[144] A. Edwards, *An Introduction to Linear Regression and Correlation*. USA: W. H. Freeman and Company, 1976.

[145] K. Sharifabadi, L. Harnefors, H.-P. Nee, S. Norrga, and R. Teodorescu, "Design, Control and Application of Modular Multilevel Converters for HVDC Transmission Systems," in *Design, Control and Application of Modular Multilevel Converters for HVDC Transmission Systems*. UK: John Wiley & Sons Ltd, 2016.

[146] Siemens, "ULTRANET" [Online]. Available: https://www.siemens.com/press/pool/de/-feature/2016/energymanagement/2016-04-ultranet/presentation-ultranet-e.pdf. [Accessed 27th July 2019].

[147] M. López, F. Briz, A. Zapico, D. Diaz-Reigosa, and J. M. Guerrero, "Operation of modular multilevel converters under voltage constraints," in *IEEE Energy Conversion Congress and Exposition, Montreal, Canada*, 2015.

[148] M. Davies, M. Dommaschk, J. Dorn, J. Lang, D. Retzmann, D. Soerangr, "HVDC PLUS – Basics and Principle of Operation," Siemens Technical Report, Germany, 2009.

[149] S. Debnath, J. Qin, B. Bahrani, M. Saeedifard, and P. Barbosa, "Operation, Control, and Applications of the Modular Multilevel Converter: A Review," *IEEE Transactions on Power Electronics*, vol. 30, no. 1, pp. 37-53, 2015.

[150] Cigre working Group B4.57, "Guide for the development of models for HVDC converters in a HVDC grid," Technical Report, 2014.

[151] H. Yang, Y. Dong, W. Li, and X. He, "Average-Value Model of Modular Multilevel Converters Considering Capacitor Voltage Ripple," *IEEE Transactions on Power Delivery*, vol. 32, no. 2, pp. 723-732, 2017.

[152] J. Peralta, H. Saad, S. Dennetiere, J. Mahseredjian, and S. Nguefeu, "Detailed and Averaged Models for a 401-Level MMC–HVDC System," *IEEE Transactions on Power Delivery*, vol. 27, no. 3, pp. 1501-1508, 2012.

[153] T. Beddard, "Factors Affecting the Reliability of VSC-HVDC for the Connection of Offshore Windfarms," Ph.D. Thesis, The University of Manchester, 2014.

[154] R. F. Mochamad and R. Preece, "Impact of model complexity on mixed AC/DC transient stability analysis," in *13th IET International Conference on AC and DC Power Transmission*, Manchester, UK, 2017.

[155] W. Wang, A. Beddard, M. Barnes, and O. Marjanovic, "Analysis of Active Power Control for VSC–HVDC," *IEEE Transactions on Power Delivery*, vol. 29, no. 4, pp. 1978-1988, 2014.

[156] A. D. Giles, L. Reguera, and A. J. Roscoe, "Optimal controller gains for inner current controllers in VSC inverters," in *International Conference on Renewable Power Generation*, Beijing, China, 2015.

[157] S. Golestan and J. M. Guerrero, "Conventional Synchronous Reference Frame Phase-Locked Loop is an Adaptive Complex Filter," *IEEE Transactions on Industrial Electronics*, vol. 62, no. 3, pp. 1679-1682, 2015.

[158] S. P. Teeuwsen, "Modeling the Trans Bay Cable Project as Voltage-Sourced Converter with Modular Multilevel Converter design," in *IEEE Power and Energy Society General Meeting*, Detroit, USA, 2011.

[159] R. Majumder, C. Bartzsch, P. Kohnstam, E. Fullerton, A. Finn, and W. Galli, "Magic Bus: High-Voltage DC on the New Power Transmission Highway," *IEEE Power and Energy Magazine*, vol. 10, no. 6, pp. 39-49, 2012.

[160] National Grid. "Mandatory Frequency Response," [Online]. Available: http://www2.-nationalgrid.com/uk/services/balancing-services/frequency-response/mandatory-frequency-response/. [Accessed 2nd November 2016].

[161] T. Wescott, *Applied Control Theory for Embedded Systems*. USA: Newnes, 2006.

[162] G. Bachman, L. narici, E. beckenstein, *Fourier and Wavelet Analysis*. New York: Springer, 2002.

[163] A. D. Hansen, P. E. Sørensen, L. Zeni, and M. Altin, "Frequency control modelling - basics," DTU Technical Report, 2016.

[164] P. M. Anderson and M. Mirheydar, "A low-order system frequency response model," *IEEE Transactions on Power Systems*, vol. 5, no. 3, pp. 720-729, 1990.

[165] L. Grigsby, *Power System Stability and Control*. Florida: CRC Press, 2012.

[166] D. Dinh Thuc, K. Uhlen, and E. A. Jansson, "Estimation of hydro turbine-governor system's transfer function from PMU measurements," in *IEEE Power and Energy Society General Meeting*, Boston, USA, 2016.

[167] C. Fan, Y. Teng, J. Xie, and X. Wang, "Steady frequency prediction algorithm for power system with governor deadband," *International Transactions on Electrical Energy Systems*, vol. 28, no. 1, 2018.

[168] OFGEM. "Changes to the Distribution Code and Engineering Recommendation G59: Frequency Changes during Large Disturbances and their Impact on the Total System." Technical Report, [Online]. Available: https://www.ofgem.gov.uk/sites/default/files/-docs/2014/07/gc0035_authority_decision_0.pdf. [Accessed 7th April 2019].

[169] C. Wang, L. Xiao, X. Zheng, L. Lv, Z. Xu, and X. Jiang, "Analysis, Measurement, and Compensation of the System Time Delay in a Three-Phase Voltage Source Rectifier," *IEEE Transactions on Power Electronics*, vol. 31, no. 8, pp. 6031-6043, 2016.

[170] European Network of Transmission System Operators for Electricity (entsoe), "*Rate of Change of Frequency (ROCOF) withstand capability"*, European Network of Transmission System Operators for Electricity (entsoe) Technical Report, Brussels, Belgium, 2018.

[171] European Network of Transmission System Operators for Electricity (entsoe), "Need for synthetic inertia (SI) for frequency regulation," European Network of Transmission System Operators for Electricity (entsoe) Technical Report, Brussels, 2017.

[172] J. Höller, V. Tsiatsis, C. Mulligan, S. Karnouskos, S. Avesand, and D. Boyle, "*From Machine-To-Machine to the Internet of Things*, Oxford: Academic Press, 2014.

[173] SP Energy Networks. "LV Engine." Network innovation Competition Proposal, [Online]. Available: https://www.ofgem.gov.uk/system/files/docs/2017/11/lv_engine-_2017_nic_full_resubmission_-_clean_redacted.pdf. [Accessed 2nd September 2019].

[174] J. Yu, K. Smith, M. Urizarbarrena, N. MacLeod, R. Bryans, and A. Moon, "Initial designs for the ANGLE DC project; converting existing AC cable and overhead line into DC operation," in *13th IET International Conference on AC and DC Power Transmission*, Mancehster, UK, 2017.

[175] National Grid, "Interim Report into the Low Frequency Demand Disconnection (LFDD) Following Generator Trips and Frequency Excursion on 9 Aug 2019' Company Report, [Online]. Available: https://www.nationalgrideso.com/document-/151081/download. [Accessed 10th September 2019].

[176] National Grid. "Frequency Response Technical Sub-Group Report." Technical Report, [Online]. Available: https://www.nationalgrideso.com/document/10336/download. [Accessed 10th September 2019].

[177] W. Wang, "Operation, Control and Stability Analysis of Multi-Terminal VSC-HVDC Systems," Ph.D Thesis, The University of Manchester, 2015.

Appendix A Introductory data

A.1 List of Existing and Planned Interconnection in the GB Network

Table A.1. List of existing and proposed In-feed interconnection in the GB System

Name	Installed Capacity (GW)	Technology	Connections
BritNed	1.2	LCC-HVDC	UK – Netherlands
IFA1	2	LCC-HVDC	UK – France
Moyle	0.5	LCC-HVDC	UK – Ireland
EWIC	0.5	VSC-HVDC	UK – Ireland
NEMO Link	1	VSC-HVDC	UK – Belgium
IFA2	1	VSC-HVDC	UK – France
North Sea Link	1.4	VSC-HVDC	UK – Norway
Viking	1.4	VSC-HVDC	UK – Denmark
FABLink	1.4	VSC-HVDC	UK – France
Green Link	3	VSC-HVDC	UK – Ireland
Northconnect	1.4	VSC-HVDC	UK – Norway
AQUIND	2	VSC-HVDC	UK – France
ElecLink	1	VSC-HVDC	UK – France
Neuconnect	1.4	VSC-HVDC	UK - Germany
GridLink	1.4	VSC-HVDC	UK - France

Appendix B Model parameters

B.1 Synchronous Generator Construction

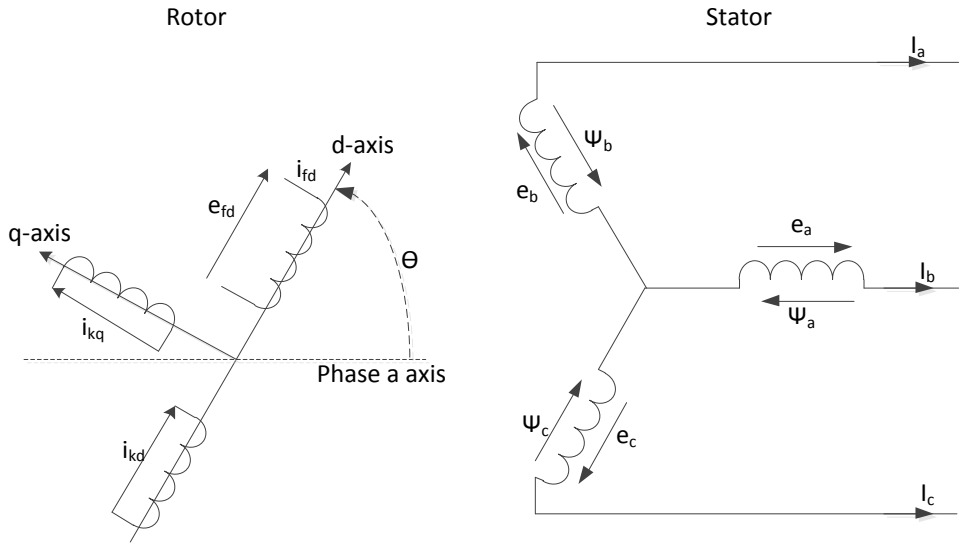

Fig. B.1.Synchronous generator rotor and stator circuits

B.2 Synchronous Generator Model Equations

B.2.1. Sixth Order Equations

$$\frac{d}{dt}E'_d = \frac{1}{T'_{qo}}-E'_d + \left(X_q - X'_q\right)\left\{I_q - \frac{X'_q - X''_q}{\left(X'_q - X_{lk,s}\right)^2}\psi_{2q} + \left(X'_q - X_{lk,s}\right)I_q + E'_d\right\} \quad \text{(B.1)}$$

$$\frac{d}{dt}E'_q = \frac{1}{T'_{do}}-E'_q + \left(X_d - X'_d\right)\left\{I_d - \frac{X'_d - X''_d}{\left(X'_d - X_{lk,s}\right)^2}\psi_{1d} + \left(X'_d - X_{lk,s}\right)I_d + E'_q\right\} \quad \text{(B.2)}$$

$$\frac{d}{dt}\psi_{1d} = \frac{1}{T''_{do}}\left[-\psi_{1d} + E'_q - \left(X'_d - X_{lk,s}\right)I_d\right] \quad \text{(B.3)}$$

$$\frac{d}{dt}\psi_{2q} = \frac{1}{T''_{qo}}\left[-\psi_{2d} + E'_d - \left(X'_q - X_{lk,s}\right)I_q\right] \quad \text{(B.4)}$$

$$\frac{d}{dt}\Delta\omega_r = \frac{1}{2H}\lfloor P_m - P_e - \mathrm{D}\Delta\omega_r\rfloor \quad \text{(B.5)}$$

$$\frac{d}{dt}\delta = \left(\omega_r - \omega_{syn}\right)\Delta\omega_r \quad \text{(B.6)}$$

$$V_t = \sqrt{{V_d}^2 + {V_q}^2} \quad \text{(B.7)}$$

$$P_t = V_d I_d + V_q I_q \tag{B.8}$$

B2.2. Second Order SG Equations

$$\frac{d}{dt}\Delta\omega_r = \frac{1}{2H}\lfloor P_m - P_e - \mathrm{D}\Delta\omega_r \rfloor \tag{B.9}$$

$$\frac{d}{dt}\delta = \left(\omega_r - \omega_{syn}\right)\Delta\omega_r \tag{B.10}$$

B2.3. Sixth order SG Model Parameters

Table B.1. Sixth order SG parameters

Parameter	xd	xq	xd'	xq'	xd''	xq''	Td'	Tq'	Td''	Tq''
Value	2.13	2.07	0.308	0.906	0.234	0.234	6.08	1.653	0.052	0.343

B2.4. SG WEISG1 Governor and IEEE Type1 Exciter Parameters

Table B.2. WESIG1 governor parameters excluding the droop gain coefficient

Parameter	T1	T2	T3	K1	K2	T5	K3	K4	T6	K5	K6	T4	T7	K7	K8
Value	0.2	1	0.6	0.3	0	7	0.25	0	0.8	0.3	0	0.6	1	0.15	0

Table B.3. IEE Type1 excitation parameters

Parameter	Tr	Ka	Ta	Ke	Te	Kf	Tf	E1	Se1	E2	Se2
Value	0.02	200	0.03	1	0.2	0.05	1.5	3.9	0.1	5.2	0.5

B.3 Network Data

B3.1. Single Machine Infinite Bus (SMIB) Parameters

Table B.4. SMIB parameters

	G1	WPP	PE	L1
S (GVA)	30	-	5	-
H (S)	4	-	-	-
Output (GW)	20	10	-	30
Inertia (GVA.s)	120	-	-	-
Droop (R)	0.05	-	0.05	-

B3.2. New England Test System (NETS) Aggregated Parameters

Table B.5. NETS aggregated parameters

	Generation	Load
S (GVA)	8.10	-
H (S)	4.09	-
Output (GW)	6.14	6.09
Inertia (GVA.s)	33.2	-
Droop (R)	0.05	-

B3.3 Four Area Generic Test System Parameters

Table B.6. General dispatch for the four area system with no VSC in-feed

	Area1	Area2	Area3	Area4	Total
SG (MW)	7500	7500	7500	7500	30000
WPP (MW)	5000	5000	5000	5000	20000

Transmission line data: resistance: 0.015 Ω/km, reactance: 0.15 Ω/km, length = 50 km

Appendix C Network Analysis data

C.1 Network Data

Four area test system y_{bus} is given by (C.1). The matrix becomes sparser as the network topology becomes more radial and less connected. To enable the sparse matrices to be inversed the, the Moore-Pernrose pseudoinverse MatLab function is used as given by (C.2).

$$y_{bus} = \begin{bmatrix} y_{11} & y_{12} & y_{13} & y_{14} \\ y_{21} & y_{22} & y_{23} & y_{24} \\ y_{31} & y_{32} & y_{33} & y_{34} \\ y_{41} & y_{42} & y_{43} & y_{44} \end{bmatrix} \quad \text{(C.1)}$$

$$Z_{bus} = pinv(\, y_{bus}) \quad \text{(C.2)}$$

Network analysis simulation data scenarios used in Chapter 3 are displayed in Table C.1 – Table C.3.

Table C.1. Droop gain distribution scenarios

	AREA1	AREA2	AREA3	AREA4
Droop dist. 1 (pu)	20	20	20	20
Droop dist. 2 (pu)	25	20	20	20
Droop dist. 3 (pu)	33	20	20	20
Droop dist. 4 (pu)	20	25	20	20
Droop dist. 5 (pu)	20	33	20	20
Droop dist. 6 (pu)	20	20	25	20
Droop dist. 7 (pu)	20	20	33	20
Droop dist. 8 (pu)	20	20	20	25
Droop dist. 9 (pu)	20	20	20	33

Table C.2. Loading distribution scenarios

	AREA1	AREA2	AREA3	AREA4
Loading L 1 (MW)	15000	12500	12500	10000
Loading L2 (MW)	15000	12500	10000	12500
Loading L3 (MW)	15000	10000	10000	15000
Loading L4 (MW)	12500	10000	10000	17500
Loading L5 (MW)	10000	10000	10000	20000
Loading L6 (MW)	7500	10000	10000	22500
Loading L7 (MW)	7500	7500	10000	25000
Loading L8 (MW)	15000	15000	12500	7500

Table C.3. Inertia distribution scenarios

	AREA1	**AREA2**	**AREA3**	**AREA4**
Inertia dist. 1 (GVA.s)	30000	30000	30000	30000
Inertia dist. 2 (GVA.s)	26250	30000	30000	30000
Inertia dist. 3 (GVA.s)	22500	30000	30000	30000
Inertia dist. 4 (GVA.s)	30000	26250	30000	30000
Inertia dist. 5 (GVA.s)	30000	22500	30000	30000
Inertia dist. 6 (GVA.s)	30000	30000	26250	30000
Inertia dist. 7 (GVA.s)	30000	30000	22500	30000
Inertia dist. 8 (GVA.s)	30000	30000	30000	26250
Inertia dist. 9 (GVA.s)	30000	30000	30000	22500

Appendix D MMC data

D.1 MMC Parameters

The parameters for the MMC system used in the RMS studies are given in Table D.1. Certain parameters are changed during the analysis with any changes explicitly stated. For a detailed implementation a detailed parameter set can be obtained in [177].

Table D.1. MMC parameters

MMC main data	Rated Apparent power	S	5000 MW
	Rated DC voltage	V_{DC}	800 kV
	Rated AC voltage	V_{AC}	400 kV
Arm data	Arm resistance	R_{arm}	6 Ω
	Arm inductance	L_{arm}	60 mH
	Number of Sub modules per arm	n_{sm}	200
Sub module data	Sub module capacitance	C_{sm}	9000 μF
Power controller	Proportional gain	K_{p1}	0.12 pu
	Integral gain	K_{i1}	100 pu
	Maximum current reference	I_d^{max}	1 pu
	Minimum current reference	I_d^{min}	0 pu
	Maximum current ramp rate	I_d^{rr}	2 GW/s
Current controller	Proportional gain	K_{p2}	1 pu
	Integral gain	K_{i2}	111 pu
	Current limit high	I_d^{max}	1 pu
	Current limit low	I_d^{min}	0 pu
DC voltage controller	Proportional gain	K_{p1}	4
	Integral gain	K_{i1}	140
Synchronisation PLL	Proportional gain	K_p^{PLL}	90 pu
	Integral gain	K_i^{PLL}	600 pu
Frequency control PLL	Proportional gain	K_p^{PLL}	12.56 pu
	Integral gain	K_i^{PLL}	39.47 pu

D.2 Sub Module Capacitance Calculation

This section expands the calculation of sub module capacitance that is used in Section 4.2 where the generic formulae are presented. Average submodule voltage can be given by (D.1) where the number of submodules per arm is 200 and the DC link voltage is 400 kV.

$$V_{sm} = \frac{400k}{200} = 2\ kV \tag{D.1}$$

Using a value of 30 kJ/MVA rating, the energy requirement per MVA for a sub module can be given by (D.2).

$$E_{sm} = \frac{30k\ (400)}{6\ (200)} = 10\ kJ \tag{D.2}$$

The capacitance per sub module can now be given by (D.3).

$$C_{sm} = \frac{10k}{0.5(2k)^2} = 10\ kJ \tag{D.3}$$

It can be seen how altering the sub module voltage impacts on the energy stored within it. This would have implications when operating the MMC to provide ancillary services as discussed in Section 4.2.

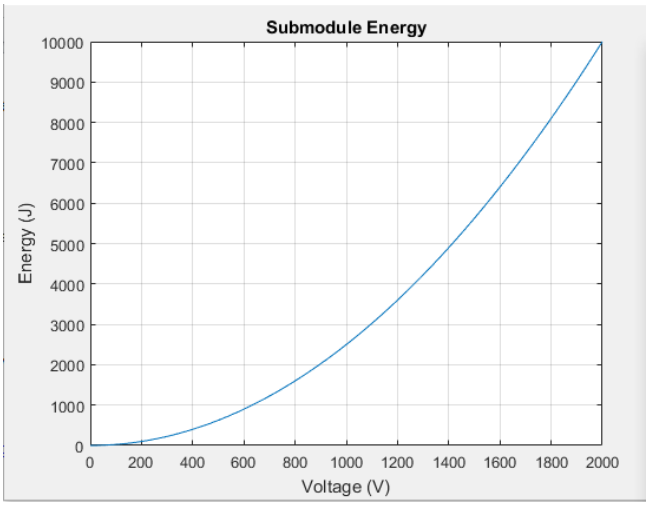

Fig. D.1.Sub module energy versus voltage magnitude

D.3 Frequency Controller Phase Locked Loop

The parameters used for the phase locked loop that measures the frequency for the supplementary VSC frequency controller is described here. The phase locked loop diagram given in Fig. 4.9 can approximated to the second order transfer function given by (D.4). From this the values proportional and integral functions can be obtain as (D.5) and (D.6). Using a damping factor (ζ) of 1 and a bandwidth of 50 Hz which is 1 per unit, the resulting ω_n value is 6.28 or 2π.

$$\frac{\theta_{pcc}}{\theta_m} = \frac{K_P^{PLL} + K_i^{PLL}}{s^2 + K_P^{PLL} + K_i^{PLL}} \tag{D.4}$$

$$K_P^{PLL} = 2\zeta\omega_n = 12.56\ pu \tag{D.5}$$

$$K_i^{PLL} = {\omega_n}^2 = 39.47\ pu \tag{D.6}$$

D.4 Derivative Controller Gain Calculation

The derivative based frequency controller presented in Section 4.1.3.2 uses a philosophy that is analogous to a droop based control scheme where a certain rate of change causes a determined change in the converter output. The value of derivative gain can be calculated as (D.7). The crucial rate of change (σ) that causes a 100% change in converter output is 0.5 Hz/s in this thesis. Converting 0.5 Hz/s into per unit using a base frequency of 50 Hz produces a value for σ of 0.01 pu/s and a converter output of 1 pu.

$$K_d = \frac{\Delta P}{\sigma} = \frac{1}{0.01} = 100\ pu \tag{D.7}$$

The derivative time step calculation used in the simulation is 0.02 s and not 1 s so the derivative gain needs to be scaled by (D.8) using K_t. This ensures that the maximum rate of change over that time period reflects the 0.5 Hz/s. The unitless multiplication factor can then be used to scale the derivative gain up as given in (D.9).

$$K_t = \frac{1}{\Delta t} = \frac{1}{0.02} = 50 \tag{D.8}$$

$$K_d = \frac{\Delta P}{\sigma} K_t = 100\ (50) = 5000\ pu \tag{D.9}$$

Although a crucial rate of change value of 0.5 Hz/s is used for σ in this thesis, this value may be deemed too responsive especially if there is a large quantity of noise measurement. The impact of reducing the value of σ on the converter output is displayed in Fig. D.2. This figure highlights how the converter output responds based on the measured output and it can be seen that for small values of measured ROCOF, the output is similar. However, as the measured ROCOF increases, the 0.5 Hz/s value for σ provides a greater response.

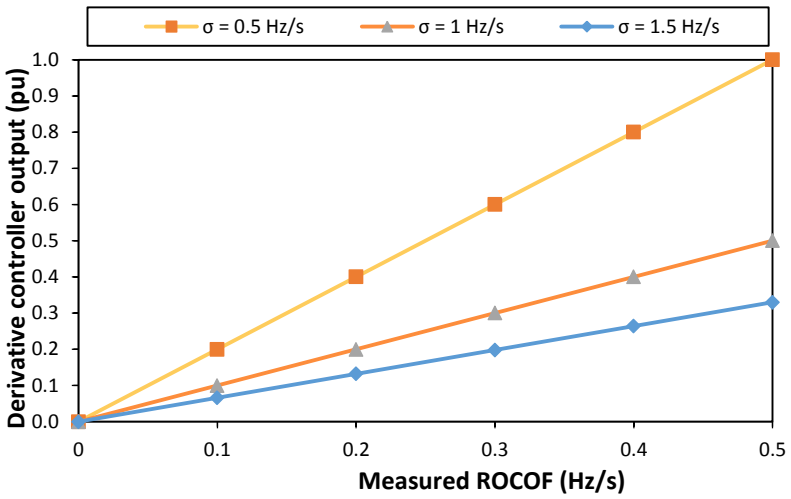

Fig. D.2.Comparison between different derivative operating values

Appendix E VSC frequency Controller Improvements

E.1 Proportional Controller Improvements

The following dispatch profile is used in the generic four area system for the analysis undertaken in Section 5.1.

Table E.1. Dispatch generation and loading for a single aggregated MMC interconnector

	Area1	Area2	Area3	Area4	Total
SG dispatch (GW)	6.25	6.25	6.25	6.25	25
SG rating (GVA)	8	8	8	6.5	30.5
WPP dispatch (GW)	5	5	5	2	17
HVDC dispatch (GW)	0	0	0	8	8
Inertia (GVA.s)	24	24	24	26	98
Load (GW)	12.5	12.5	12.5	12.5	50

Table E.2. Dispatch generation and loading for two MMC interconnector in-feeds

	Area1	Area2	Area3	Area4	Total
SG dispatch (GW)	6.5	6.5	6.5	5.5	25
SG rating (GVA)	8	8	8	6.5	30.5
WPP dispatch (GW)	6	6.5	6.5	3	22
HVDC dispatch (GW)	1.5	0	0	1.5	3
Inertia (GVA.s)	24	24	24	26	98
Load (GW)	12.5	12.5	12.5	12.5	50

Appendix F Python Code Segments

Useful segments of Python code and examples are provided in this section that enable interaction between DIgSILENT and Microsoft Excel. These are not completed scripts and should be viewed as reference for future users.

F.1 Python Script Example

The following example changes the dispatch of all SGs and runs the simulation followed by extracting the simulation results data to CSV:

```
import powerfactory
import csv
app = powerfactory.GetApplication()

GenObj = app.GetCalcRelevantObjects("*.ElmSym")
for Synchronous_Machine in GenObj:
Synchronous_Machine.pgini = 100

ldf = app.GetFromStudyCase("ComLdf") #Load Flow
ldf.Execute()
inc = app.GetFromStudyCase("ComSim") #RMS simulation
inc.Execute()

comRes = app.GetFromStudyCase('ComRes');
comRes.f_name = Example.csv';
comRes.ExportFullRange();
```

F.2 Useful Python Segments

The following segment enables data transfer between Python and Microsoft Excel in xlsx format using the *openpyxl* library.

```
import openpyxl
datapath = "C:/Users/example.xlsx"
workbook = openpyxl.load_workbook(datapath,data_only=True)
sheet = workbook["Sheet1"]
readcell = ["A1"]
read_data = sheet[readcell].value
writecell = ["B1"]
worksheet[writecell] = "data"
```

The following segment is used to change a parameter in a SG governor control.

```
GenObj = app.GetCalcRelevantObjects("*.ElmDsl")
for Common_Model in GenObj:
      if Common_Model.loc_name == "IEEEG1":     #checks for governor model
         df = (Common_Model.params)             # reads in the parameter set
         df[0]=float(5)                         # replaces first parameter with the value 5
          Common_Model.params=df                # writes the updated parameter set back
```

Altering a simulation event time in DIgSILENT can be achieved using the following segment.

```
folder = app.GetFromStudyCase('IntEvt')
eventSet = folder.GetContents("my event")
evt = eventSet[0]
evt.time = 1.5
```